Development and assessment of volume resolving velocimetry for turbomachinery test facilities

Dissertation zur Erlangung des akademischen Grades eines
Doktors der Ingenieurwissenschaften (Dr.-Ing.)

Vorgelegt im Fachbereich Elektrotechnik und Informatik
der Universität Kassel

Referent: Prof. Dr. rer. nat. habil. Hartmut Hillmer
Koreferent: Univ.-Prof. Dr.-Ing. Martin Lawerenz

von
Herrn Joachim Klinner

Datum der Einreichung: 2017/06/30
Datum der Disputation: 2017/10/16

Abstract

The present thesis assesses the applicability of volume resolving velocimetry for turbo machinery test facilities.

Tomographic particle image velocimetry has been implemented in a transonic cascade wind tunnel. Assessment is based on 3D-3C measurements of the passage vortex in an axial compressor cascade at subsonic inflow (Ma_1=0.6). Results show broad consistency with stereoscopic PIV with improved depth resolution. A novel Fast Multiplicative Algebraic Reconstruction Technique (FMART) enables significantly faster computations of particle reconstructions in comparison to a state-of-the-art procedure (simultaneous MART) while maintaining similar accuracies.

The second part describes the development of tomographic shadowgraphy for 3-D measurements of spatial fuel spray distributions and droplet velocities. This novel approach is based on simultaneous imaging from different directions with pulsed LED inline illumination. Assessment is based on 3D-3C measurements of the airblast atomization of a single kerosene jet in a swirl flow at air pressures between 4-7 bar and air temperatures between 440-570 K inside a spray test facility. The minimum resolvable droplet diameter is 10 μm under the given experimental conditions. Validation against PDA data revealed consistency at size classes $d = 10\,\mu$m and 15 μm.

transonic flow, tomographic reconstruction, PIV, pulsed LED, shadowgraphy, sprays, airblast atomization, swirled flow

Zusammenfassung

Es wird die Eignung instationärer volumenauflösender Geschwindigkeitsmessverfahren für Turbomaschinenprüfstände untersucht.

Tomographische Particle Image Velocimetry (TPIV) wurde in einem transsonischen Gitterwindkanal implementiert. Die Erprobung erfolgte anhand der 3D-3C Messung des Passagenwirbels eines Axialverdichter Leitradgitters bei subsonischer Anströmung (Ma_1=0.6). Ergebnisse zeigen weitgehende Übereinstimmung mit stereoskopischem PIV bei verbesserter Tiefenauflösung. Eine neue schnelle Multiplikative Algebraische Rekonstruktionstechnik (FMART) ermöglicht deutlich verkürzte Auswertezeiten im Vergleich zur herkömmlichen simultanen MART (SMART) bei ähnlichen Genauigkeiten.

Der zweite Teil beschreibt die Entwicklung der tomographischen Schattenbildtechnik zur 3-D Vermessung von räumliche Sprayverteilungen und Tropfengeschwindigkeiten. Dieser neuartige Ansatz basiert auf der simultanen Abbildung aus verschiedenen Richtungen mit gepulster LED-Inline-Beleuchtung. Beschrieben wird die 3D-3C Messung eines Kerosin Jets in einer Drallströmung im Sprayprüfstand bei Luftdrücken zwischen 4-7 bar und Lufttemperaturen zwischen 440-570 K. Der kleinste auflösbare Tropfendurchmesser ist 10 μm unter den gegebenen experimentellen Bedingungen. Die Validierung anhand von PDA Daten zeigt gute Übereinstimmung für die Größenklassen $d = 10\,\mu$m und $d = 15\,\mu$m.

transsonische Strömung, tomographische Rekonstruktion, PIV, gepulste LED, Schattenbildtechnik, Sprays, Airblast Zerstäubung, Drallströmung

Acknowledgements

This thesis was written in the scope of my work for the Department Engine Measurement Systems of the DLR Institute of Propulsion Technology Köln.

First of all, I would like to thank my doctorate advisor at Kassel University, Professor Hartmut Hillmer, for accepting me as an external doctoral candidate and for his friendly supervision and advice throughout the entire time of doctoral studies.

I also would like to thank my committee members, Professor Martin Lawerenz, Professor Bernd Witzigmann and Professor Peter Lehmann for their comments on my thesis and feedback.

I gratefully acknowledge my supervisor at DLR, Christian Willert, for his invaluable support. This thesis would not have been feasible without numerous helpful ideas, fruitful discussions and advice. Furthermore, provision of the PIV4D C/C++ library was extremely helpful. Through this source code I learned a lot about efficient programming.

Part of the work presented is supported by the EU-project AFDAR (Advanced Flow Diagnostics for Aeronautical Research, project no. 265695) of the 7th Framework programme whose support is gratefully acknowledged.

I am grateful to my colleagues Alexander Hergt and Sebastian Grund who helped me a lot to get through the challenging implementation of planar and volume resolving PIV in the transonic cascade wind tunnel (TGK) at the DLR Köln. My special thanks goes to Manfred Beversdorff for his help in the mechanical design of the light sheet probe.

I would also like to thank my colleagues Melanie Voges and Michael Schroll for the nice working atmosphere and their availability and support during the TGK experiments.

I am thankful to Daniel Schanz and Sebastian Gesemann of the Department Experimental Methods of the DLR Institute of Aerodynamics and Flow Technology for providing the SMART implementation and the corresponding Matlab calibration routine as well as indispensable advice regarding operation of

both.

I would like to thank Stefan Freitag and Christoph Hassa for the productive discussions on implementation and results of volumetric spray measurements in the Optical Swirling Spray Injector (OSSI) test rig as well as Ingo Otterpohl for reliable operation of the facility.

My very sincere thanks goes to Thomas Kusserow from Kassel university for both friendly advice and encouragement as well as the very comfortable lodging during visits to Kassel.

Last but not least, I would like to thank my family, my wife Anja Klinner and my parents Karin and Ulrich Klinner for their love and patience. Thank you for your continued support during these years.

Nomenclature

a	droplet radius
$\tilde{a}$	normalized droplet radius ($= \sqrt{2}a/\chi$)
C_D	drag coefficient
C_{II}	cross-correlation coefficient
C_I	autocorrelation coefficient
D_0	diameter of the injection nozzle
d	diameter
d_A	diameter of the Airy disc
D_I	particle image density
f	focal length
$f_\#$	f-number
$\tilde{i}$	normalized image intensity
$I_{\mathrm{f,max}}$	maximum continuous forward current
l	characteristic length
M	magnification
n	volume number density, number of objects per unit volume
p	pressure
r	radial droplet image coordinate
$\tilde{r}$	normalized radial droplet image coordinate($= \sqrt{2}r/\chi$)
R	gas constant
Δt	delay between two illumination pulses
T	temperature
t_p	pulse duration
q	liquid-to-air momentum flux ratio ($= \rho_k U_k^2/(\rho_a U_a^2)$)
Q	quality factor
U,V,W	velocity components along x, y, z
x,y,z	measurement coordinates
$\delta x_p, \delta y_p, \delta z_p$	absolute deviation of reconstructed particle position
Δpix	side length of a pixel element
$\Delta X, \Delta Y, \Delta Z$	displacement components along x, y, z
$\delta X, \delta Y, \delta Z$	absolute deviation between displacement estimates and reference (e.g. synthetic flow field)

ε	reprojection error
λ	wavelength of light
ν	kinematic viscosity
ρ	mass density
ξ_p	particle relaxation length
κ	heat capacity ratio of ideal gases
σ	standard deviation or surface tension
τ	contrast coefficient
τ_p	particle relaxation time
χ	half-width of the point-spread function
φ	camera yaw angle (rotation about y axis)
ψ	camera pitch angle (rotation about new x axis)

Subscripts

1	inlet plane
2	exit plane
a	air condition
I	basis for image space
k	kerosene condition
p	particle or pulse condition
PDA	basis for PDA vector space
t	total, stagnation value
TS	basis for tomographic shadowgraphy vector space
UV	based on axial and tangential velocity components

Dimensionless numbers

Ma	Mach number ($= U_a/\sqrt{\kappa R T_a}$)
Re	Reynolds number ($= U_a l/\nu$)
St	particle Stokes number ($= \tau_p U_a/l$)
We	Weber number ($= \rho_a U_a^2 l/\sigma$)

Acronyms

AVDR	Axial Velocity Density Ratio ($= (\rho_2 u_2 sin\beta_2)/(\rho_1 u_1 sin\beta_1)$)

CDF	Cumulative Distribution Function
DOF	Depth of Field
FMART	Fast Multiplicative Algebraic Reconstruction Technique
FOV	Field of View
FWHM	Full Width at Half Maximum
IDL	Interactive Data Language
IPR	Iterative Particle Reconstruction
LSF	Line Spread Function
MART	Multiplicative Algebraic Reconstruction Technique
MLOS	Multiplicative Line of Sight
OGV	Outlet Guide Vane
OSSI	Optical Swirling Spray Injector (test facility)
OTF	Optical Transfer Function
PDA	Phase Doppler Anemometry
PDF	Probability Density Function
PIV	Particle Image Velocimetry
ppp	particles per pixel (unit of particle image density)
PSF	Point Spread Function
RMS	Root Mean Square
ROI	Region of Interest
SMART	Simultaneous MART
SPIV	Stereoscopic PIV
TGK	Transonic Cascade Wind Tunnel (Transsonischer Gitterwindkanal)
TPIV	Tomographic PIV

Contents

Chapter 1

Introduction

1.1 Motives for volume resolving velocimetry in turbomachinery test facilities

Nowadays, the optimization of gas turbines in terms of balancing of efficiency, operational safety and emission of pollutants is one of the great challenges. For example, in 2001, the Advisory Council for Aeronautical Research in Europe (ACARE) formulated a need for research by 2020 that included a 50% reduction in CO_2 emissions per passenger kilometer, a 50% reduction in fuel consumption, an 80% reduction in nitrogen oxide emissions as well as a noise reduction to one half [1]. Research projects that optimize the gas turbine design with regard to such demanding goals frequently involve experimental validation of advanced 3-D computer fluid dynamic (CFD) methods which model the extremely complex flows found in modern aero engines or stationary gas turbines. In order to assess the performance of CFD models in realistic applications, velocity data must also be obtained from turbomachinery test facilities that are capable of capturing the rather comprehensive range of effects at realistic operation conditions found inside different components of the gas turbine (e.g. compressor, combustion chamber and turbine).

To date, optical particle-based velocimetry in duct flows of turbomachinery test facilities is still challenging for several reasons. Realistic operation conditions usually involve high primary flow velocities above 100 m/s as well as

elevated air temperatures and pressures. Experimental constraints typically include limited optical access and harsh experimental conditions in terms of test rig vibrations, window contamination over time by tracer deposition, thermal variations and/or high sound pressure levels. Regarding optical accessability, point-wise techniques (e.g. *Laser-two-Focus* (L2F) [147]) are less demanding and require only a single observation window. On the other hand, in terms of facility operating hours point-wise techniques can be rather costly if the flow has to be mapped volumetrically. Here, planar techniques as *Particle Image Velocimetry* (PIV) come into play which can provide instantaneous velocity fields at typical accuracies of 1% of the full velocity range and 10^3 to 10^5 vectors per sample [158, 128]. In the past years the technique has been successfully applied to axial or radial compressor and turbine flows [166, 187, 167] as well as in reacting flows in gas turbine combustion test rigs [181, 182, 184, 149].

Three-dimensional velocity fields can be obtained from planar PIV by stacking of successively captured time-averaged velocity fields over volume depth. The main drawback of this method is that unsteady flow structures as moving wakes or vortices are smoothed and may remain recognizable only in higher order statistics (e.g. RMS values). Moreover, only four to six of nine terms of the instantaneous velocity gradient tensor can be obtained by planar PIV. Thus, components of vorticity and strain rate can not be fully resolved by planar velocimetry techniques. Hence, if the flow itself is unsteady, three-dimensional three-component velocimetry becomes attractive to evaluate the organization and motion of the turbulent structures. Experimental studies in the present work are aiming at the application of volume resolving velocimetry in two different types of duct flows in turbomachinery test facilities as described below.

The schematic view in Fig. 1.1 provides some insight into the three-dimensional secondary flow field near the hub and the tip of a rotating turbine blade passage. The figure shows the rolling up of the incoming boundary layer into the "horseshoe" vortex as well as the formation of tip wall and hub wall passage vortices and the formation of tip-leakage vortices due to the finite clearance between rotor and wall (for a detailed description see [14]). Similar flow fields can be found in axial compressor blade rows, whereby the flow turning is typically

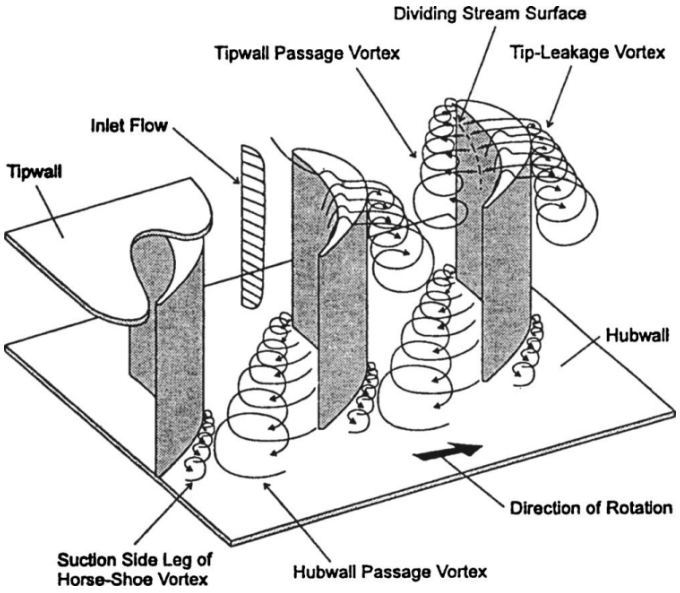

Figure 1.1: Schematic view of the secondary flow development inside a turbine rotor, reprinted from Sjolander [152]

much lower and the additional rise in static pressure increase the possibility of flow separations near the end walls. Those flow separations have influence on the flow turning near the wall and lead to blockage effects which limit the mass flow capacity of the passage. Secondly, flow separation induces strong shear and velocity fluctuations which are responsible for a large proportion of pressure losses in an axial compressor. The accurate prediction of the unsteady corner flow and the separation region in CFD is indispensable for compressor blade designing. Thus, instantaneous volume resolving velocimetry of the secondary flow structures within the corner flow of the blade passage could help to validate the underlying turbulence and transition models (c.f. [200]).

The second type of flow that is subject to experimental studies is related to the kerosene atomization process in aero-engine fuel injectors. Instead of gas velocimetry, the target application is aiming at instantaneous measurements of three-dimensional droplet velocities and the spatial distribution of the liquid fuel in a volume. By way of illustration Fig. 1.2 shows schematically a staged aero-engine burner that employs lean direct injection (LDI). Both pilot and main stage apply air-blast atomization of thin kerosene films that are injected through annular fuel channels. At the exit section, the liquid sheet extrudes into the gas phase and breaks up very quickly via turbulence, cavitation, shear or a combination of these mechanisms [31]. The liquid sheet is exposed to either coaxially counter-rotating (high shear rate) or co-rotating (wide spray

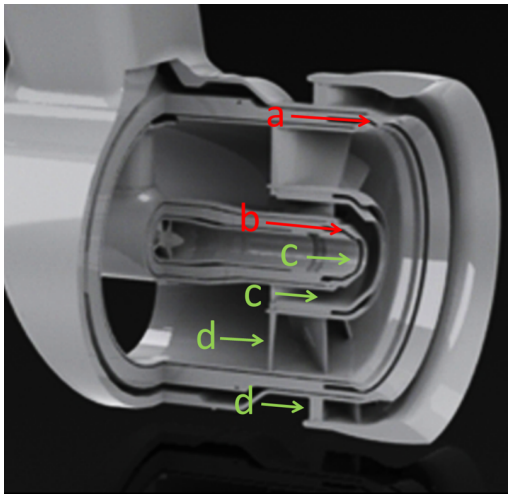

Figure 1.2: Modern Rolls Royce lean direct injection burner (LDI) employing kerosene atomization in between swirling air streams in both pilot and main stage; a: main fuel flow; b: pilot fuel flow; c: pilot air flow; d: main air flow (adopted from Meier et al. [102]).

angle) air flows that have direct influence on the atomization and dispersion processes. In contrast to wide-spread Rich-Quench-Lean (RQL) combustion chambers, the majority of air enters the combustion chamber through the LDI burner while fuel and air have to be premixed rapidly before the mixture enters the reaction zone [102]. The optimization of the mixing process of such complex swirl injectors can benefit from diagnostic methods capable of mapping the instantaneous three-dimensional distribution of liquid fuel and droplet velocities at a fixed time. Results could be used to improve estimates of liquid kerosene volume fraction by taking into account the three-dimensional variation of the spray placement at a fixed time which is not possible by planar techniques as Mie visualizations or laser induced planar fluorescence of kerosene.

1.2 Techniques for tracer-based three component velocimetry in a volume

To date, several methods are known for volume resolving velocimetry within 3-D air flows. These techniques typically base on pulsed volume illumination of moving tracer particles while the velocity is obtained from tracer displacements captured at two or multiple fixed time steps.

In general, the spatial resolution of volume resolving velocimetry improves with the capability to recover as many tracer positions and displacements as possible from a set of images. The ratio of the number of particle images

to the number of pixel elements (particle images per pixel, ppp) can be used to compare resolution capabilities of different techniques. For *digital holographic PIV* (DHPIV) [193, 122, 98, 6, 25, 151, 156, 83] the number of particle holograms per pixel depends on the minimal detectable ratio between interferogram intensity and speckle noise (Meng et al. [108]). A literature survey regarding experimental DHPIV studies by Ooms [120] revealed typical record densities in the range of 300 - 3200 particles per Mpixel ($0.0003 - 0.0032$ ppp). A drawback of digital holographic PIV is the restriction to small measurement volumes of less than a cubic centimeter [108] which is due to the limited resolution of the sensor regarding fringe spacing. Other techniques as classical *particle tracking velocimetry* (PTV) rely on determination of particle coordinates from triangulation (Maas et al. [95]). Malik et al. [99] were able to triangulate up to 1000 particles with a three-camera system at a image size of approximately 600^2 pixel (0.0028 ppp). For time-resolved particle tracking much higher particle image densities in the order of 0.05 ppp are feasible [142]. Particle number densities up to 0.02 ppp can be resolved by *Defocusing Digital PIV* (DDPIV) (Willert and Gharib [186]) if the technique is extended to multiple cameras. Pereira et al. [123] applied DDPIV to simultaneously measure velocities and size distribution of bubbles in a propeller flow. The authors used three cameras of $1k \times 1k$ pixel and recovered approximately 16000 bubbles which translates to 0.016 ppp. Except holographic PIV, each of the aforementioned techniques base on a reliable distinction of particle images. Elsinga et al. [46, 42] introduced *tomographic particle image velocimetry* (TPIV) which does not necessarily require identification of individual particles and thus can operate at high image densities. In TPIV, multiple cameras simultaneously capture images of moving particles from different viewing directions at least in two time steps. The 3-D particle distribution is represented by a 3-D intensity array over discrete voxels which is recovered using algorithms which often originate from computer tomography. After reconstruction, the volumetric velocity field is obtained by three-dimensional cross-correlation of sub volumes, so-called interrogation volumes (details on TPIV are provided in the following chapter). Recent TPIV studies on the basis of four simultaneous camera views operated at particle image densities in the range $0.005 - 0.07$ ppp (see Scarano [136] and Table 1.1).

Three-dimensional three-component velocimetry techniques that only use a single camera are of great interest to applications in duct flows of restricted optical access. On the other hand, due to the limited angular aperture, single camera techniques typically involve much higher uncertainties for out-of-plane[1] components in comparison to in-plane components . For example, digital inline holograms suffer from a low axial resolution due to the limited hologram aperture ("depth-of-field problem" ([107, 150]) which leads to a severe elongation of particle reconstructions. A few other techniques exist that apply a single camera but also involve a relatively high uncertainty on out-of-plane components in comparison to in-plane components. *Astigmatic Particle Tracking Velocimetry* (APTV) (Cierpka et al. [28]) introduce elliptical particle image distortions by placing a cylindrical lens in the rear of the camera lens. The shape and orientation of elliptical particle images can be related to the depth position [27]. Buchmann et al. [22] applied APTV to a transonic particle-laden jet in a measurement domain of $8 \times 7 \times 5\,\mathrm{mm}^3$. The authors specified particle location uncertainties of $5\,\mu$m in-plane and of $140\,\mu$m for out-of-plane positions. The uncertainty in out-of-plane velocity was estimated to be 3-7 times larger compared to in-plane velocity components. The application of single plenoptic cameras for volumetric velocimetry has been reported by Fahriger et al. [48]. Regarding particle location, the uncertainty on depth position was estimated to be 15.6 times larger compared to lateral positions for a plenoptic camera of 16 Mpixel [48]. The authors specified an uncertainty on the out-of-plane velocity component that was 5-10 times larger than both in-plane components.

Consequently, multi camera setups have a clear advantage in terms of depth resolution compared to single camera setups, because they can work at a wider range of viewing angels. For example, a TPIV setup of four cameras each at a $30°$ viewing angle (to the left, to the right, upward and downward) can provide uncertainties on depth components of velocity that are only 1.6 times larger in comparison to lateral components [42]. On the other hand, the TPIV technique is experimentally challenging and requires a stable camera setup including an accurate assignment between physical 3-D world coordinates and 2-D pixel coordinates of each camera. Thus, most applications of TPIV are

[1] In this context 'plane' means 'image plane')

Table 1.1: Tomographic PIV studies in high speed air flows

	Ma_∞ u_∞ [m/s]	Volume size [mm^3]	no. cameras Image size [pixel]	Pulse energy [mJ]	Interrogation vol. Vector spacing [mm^3]	Tracer
Humble et al. [75]	2.1 510	$70 \times 40 \times 10$	4 2048×1212	400	$2.1 \times 2.1 \times 2.1$ $0.5 \times 0.5 \times 0.5$	TiO_2 n_p=2mm^{-3} D_I=0.05ppp
Elsinga et al. [43]	2.1 510	$70 \times 35 \times 6.5$	4 2048×2048	400	$2.0 \times 2.0 \times 2.0$ $0.5 \times 0.5 \times 0.5$	TiO_2 n_p=3mm^{-3} D_I=0.05ppp
Avalone et al. [9]	7.5 1030	$31 \times 23 \times 2.5$	3 1376×1040	200	$1.89 \times 1.08 \times 0.67$ $0.47 \times 0.27 \times 0.17$	TiO_2 D_I=0.03ppp
Wernet et al. [171]	1.4 763	$180 \times 180 \times 10$	4 1376×1040	200	$1.75 \times 1.75 \times 1.75$ $0.88 \times 0.88 \times 0.88$	Al D_I=0.005 - 0.045ppp

conducted in water or wind tunnels with good optical access and under stable laboratory conditions (for a survey of TPIV applications see Scarano [136]). Very few publications can be found on application of TPIV in high-speed air flows at high mass flow rates as they occur in turbomachinery test facilities. Table 1.1 provides an overview of scant studies that involve tomographic PIV in high-speed flows.

Another issue is the problem of ambiguity of particle field reconstruction on the basis of a few projections, termed 'ghost particles' [45]. In tomographic PIV the suppression of those ghost particles strongly depends on the applied algorithms for particle field reconstruction (e.g. direct, algebraic or particle based) as will be described in detail in the following chapter. Recent developments in the field of time-resolved particle tracking provide efficient suppression of ghost particles over track length at image densities in the order of those applied for tomographic PIV ('Shake-the-Box' algorithm [142]). Subsequent interpolation of these 3-D Lagrangian particle tracks on a Cartesian grid enables application of regularization strategies using fluid mechanic constraints as mass and momentum conservation to further increase accuracy [146, 58]. On the other hand, temporally well-resolved image data at a sufficient pixel count is currently unavailable in high-speed flows ($U > 100\,\mathrm{m/s}$), from the technical point of view. Time resolved particle velocities using present high-speed cameras would require acquisition rates in the order of $0.5 - 1\,\mathrm{MHz}$ accompanying with a significant reduction of the pixel count from $3 - 5\,\mathrm{Mpixel}$ (typical double-

frame PIV cameras) down to about $30 - 50\,\mathrm{Kpixel}$. Multi-pulse 3-D particle tracking techniques for high-speed flows involve at least four coherent samples from multiple viewing angles (Novara et al. [119]) and thus require not less than 2×3 double-frame cameras (Geisler et al. [56]). Installation of such large camera arrays is hardly feasible if considering the limited optical access in gas turbine test rigs.

It follows from the above considerations that implementation of tomographic PIV on the basis of 3-4 double-frame cameras is a reasonable (first) step towards volume resolving velocimetry in high-speed flows in turbomachinery test facilities.

1.3 Optical spray diagnostics - from pointwise to volumetric measurements

While the first part of the thesis is dedicated to application and assessment of TPIV in a cascade wind tunnel the second part is aiming for instantaneous measurements of three-dimensional spatial spray distributions and droplet velocities in fuel sprays. In contrast to TPIV which relies on diffraction limited imaging of small and homogeneously distributed tracer particle, a 3-D reconstruction of sprays has to deal with pronounced spatial variations of droplet size, number density and shape.

The current body of literature describes a wide variety of optical techniques for the characterization of sprays and an adequate description is beyond the scope of this thesis. The techniques range from point-wise methods to two-dimensional (image-based) methods and even volume resolving approaches. Point-wise methods base on phase-Doppler interferometry [11, 40], analysis of diffraction patterns [160], refractometry [72] or time-shift techniques [35, 141] and are particularly well suited to obtain statistical quantities such as droplet size and even droplet velocity. Imaging methods can provide two-dimensional projections or slices of the three-dimensional droplet distributions and can be roughly separated into optical imaging using inline illumination [17, 50] and side scattering approaches using planar (laser) light sheet illumination. The

latter can be extended to provide droplet size information either by additionally measuring the spray fluorescence (laser sheet drop-sizing) [90, 79, 87, 113] or by interferometry (interferometric laser imaging for droplet sizing, ILIDS) [60, 97, 84]. By traversing the light sheet normal to the viewing axis recovers the time- or phase averaged three-dimensional spray distribution. None of the aforementioned techniques is capable of providing the instantaneous three-dimensional spray and velocity distribution which is the main goal of the herein proposed tomographic technique.

In this regard considerable work has been done in the field of holographic imaging. Inline film-based holography has been used to infer droplet position and size [80]. Droplet size and velocity in an impinging jet spray was investigated simultaneously using a double reference beam holographic setup with two pulses staggered in time [82]. Focused image holography with side lighting was used to image the complex ligament formation near the spray nozzle exit [134]. More recently digital inline holography was used to investigate the liquid breakup of aerated water injectors in cross-flow [110]. Multiple exposure recordings obtained with a similar inline setup were used to recover three-dimensional droplet velocities in sprays [94, 192]. Inline holographic approaches work well for sparsely populated droplet volumes but suffer from strong reference beam attenuation and speckle noise in high particle density regions. As mentioned above, the limited angular aperture of digital inline holograms results in ellipsoidal and elongated reconstructions of spherical particles [107]. This effect can be reduced by combining the inline reference beam with a side scattered object wave which improves the contrast of the recorded diffraction patterns and therefore increases axial resolution [25] or by crossing several inline holographic setups [156]. However these dual- or multi-beam interferometric setups require a higher instrumentation effort. In order to obtain information on droplet velocity multi-pulsed lasers are required.

Whereas holography has been used quite extensively for the investigation of sprays, the literature reports very few applications of tomography for three-dimensional spray reconstruction. Ultrafast X-ray tomography technique was used by Cai et al. [24] and Liu et al. [93] for the transient, near-field spray characterization of an multi-hole injector at frame rates of about 48 kHz. Tomo-

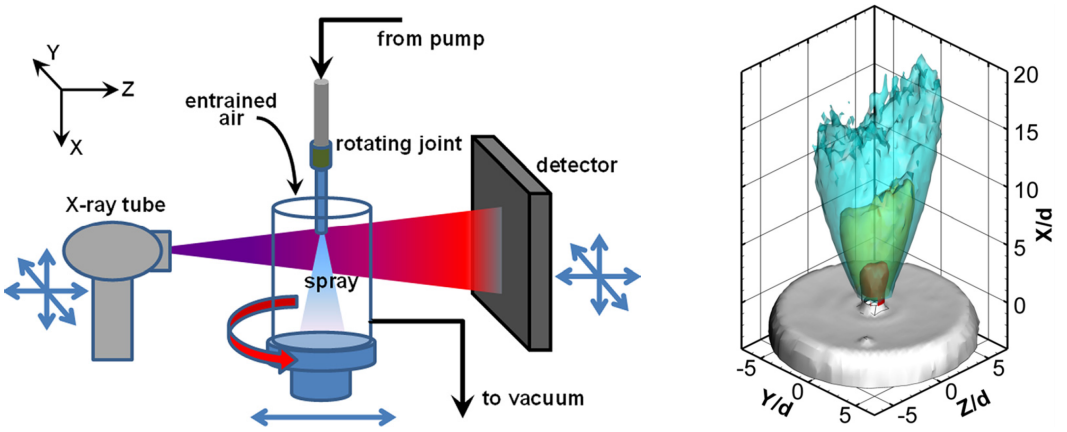

Figure 1.3: Setup for scanning X-ray tomography in sprays (*left*) and a result showing iso-surfaces of time-averaged concentration levels at 20%, 5% and 2.5% of a full-cone atomizer (*right*); reprinted from Coletti et al. [31]

graphic reconstruction of the instantaneous, phase-averaged spray distribution was achieved through rotation ($\approx 1°$ steps on $180°$) and vertical translation of the injector in the X-ray imaging path. Compared to optical imaging, X-ray imaging has the advantage that the recorded radiation intensity mainly depends upon the absorption in the liquid, since scattering can be neglected at small wavelengths. Thus quantitative measurements of the local fuel mass fraction are feasible [31]. On the other hand, all of the above mentioned tomographic techniques rely on sequential recording of several projections and thus are limited to providing time- or phase-averaged data.

If the spray is less dense, instantaneous optical tomography on the basis of a few simultaneous projections might be feasible. The herein proposed spray reconstruction technique termed *tomographic shadowgraphy*[2] relies on simultaneously acquired shadow images of a spray field obtained from different views using inline illumination with pulsed LED light for each view. Subsequent to image preprocessing, the reconstruction of droplet distributions relies on similar techniques compared to tomographic PIV.

[2]The term *shadowgraphy* is frequently used to describe shadow images of refractive index gradients in gases but describes images of droplet shadows projected onto the image plane just as well.

1.4 Objectives of the thesis

1.4.1 Implementation of Tomographic PIV in a transonic cascade wind tunnel

The first objective is the assessment of the technique's potential of instantaneously resolving secondary flow structures within the corner region of a highly loaded compressor cascade. A comparison between tomographic and stereoscopic PIV [5, 125] at selected planes will enable additional assessments of measurement accuracy. Preparatory work involves characterization of the applied seeding in terms of tracer response. The processing time for both particle field reconstruction and velocity recovery becomes critical if a large number of samples have to be evaluated to achieve convergence of velocity fluctuations in turbulent flow regions. Hence, a central goal is the development of a computational efficient 3-D particle reconstruction for TPIV.

1.4.2 Implementation of tomographic shadowgraphy for fuel sprays at elevated pressure and temperature

The second objective is aiming for instantaneous three-dimensional droplet velocities and spray distributions using a novel approach, namely tomographic shadowgraphy. Associated work involves the characterization of the technique regarding the depth of field and the smallest visible droplet diameter on the basis of experimental parameter as well as the development of concepts for camera calibration for spray volumes of a large depth-to-width aspect ratio. Different tomographic reconstruction techniques will be compared regarding their suitability to determine the three-dimensional instantaneous spray distribution on the basis of hollow cone water sprays. Finally, tomographic shadowgraphy is applied under rough operating conditions in a non-reacting kerosene spray in a high pressure environment with preheated airflow which is representative of air-blast atomization under realistic conditions. The consistency of experimental results will be assessed by comparison to PDA.

1.5 Outline

The following chapter describes the working principles of volumetric PIV including camera calibration, aspects of imaging, techniques for data processing as well as the current state of research. Chapter 3 introduces two novel approaches for fast particle volume recovery from multiple views. Their performance will be compared against a conventional reconstruction technique on the basis of synthetic images of particles conveyed through a prescribed flow field. Chapter 4 describes preparatory experimental work on the implementation of PIV in a transonic cascade wind tunnel as well as in-situ characterization of tracer response. Furthermore, laser energy requirements for volume resolving PIV are assessed. Implementation details and comparative results of tomographic and stereoscopic PIV of the corner flow of a compressor cascade are given in chapter 5. The second part of the thesis is dedicated to development and assessment of tomographic shadowgraphy. Chapter 7 deals with aspects of camera calibration and introduces a methodology to characterize the resolution capabilities of the technique in terms of the smallest visible droplet size over the depth-of-field. Furthermore, a comparative study on spray reconstruction techniques is conducted on the basis of experimental data of flat fan and hollow cone water sprays under atmospheric conditions. Chapter 7 provides implementation details and results of the first application of tomographic shadowgraphy in the non-reactive flow of the generic aero engine burner model in a pressurized test vessel at elevated air temperature. In the last chapter, main results and conclusions of the thesis are summarized while future directions are discussed to further improve volume resolving techniques proposed in this work. The appendix Chap. A provides additional details on the applied camera models.

Chapter 2

Fundamentals of tomographic particle image velocimetry and state of the art

2.1 Operating principle of tomographic PIV

Fig. 2.1 shows schematically the measurement chain of conventional tomographic PIV as originally proposed by Elsinga in 2005 [46]. The method relies on pulsed volume illumination and photogrammetric imaging of particles which are added to the flow under investigation. Typically three or four cameras simultaneously capture images of the moving particles from different viewing directions at two or multiple time steps, whereby additional cameras improve the spatial resolution [42]. After image acquisition and image preprocessing, a 3-D intensity array over discrete voxel elements is recovered using algorithms which often originate from computer tomography [42, 8, 59, 162] hence the name *tomographic PIV*. Usually, these reconstruction algorithms iteratively find a source intensity distribution in a volume of discrete voxel elements which minimizes the differences between the recorded pixel intensity and the integrated intensity along the corresponding line of sight. Camera calibration provides the mapping between voxel and pixel coordinates. Depending on the reconstruction technique, weighting coefficients have to be parameter-

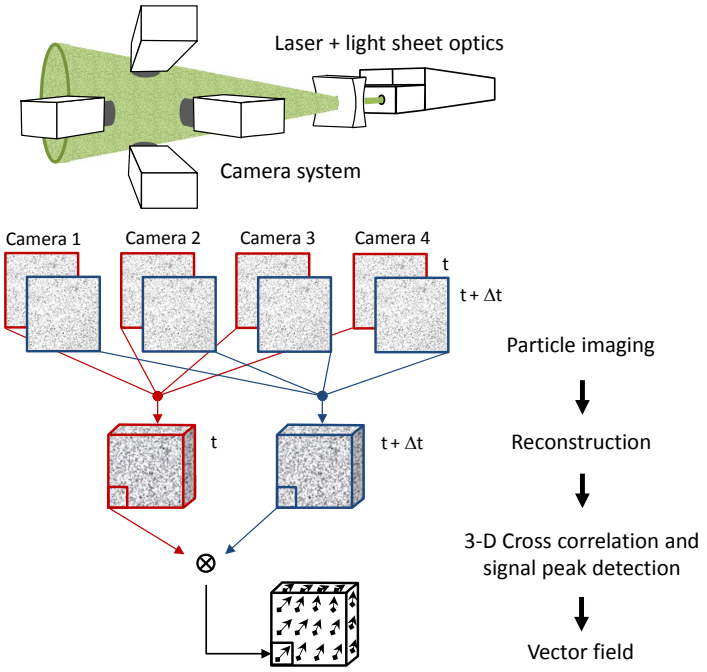

Figure 2.1: Measurement chain of conventional tomographic particle image velocimetry (adapted from Elsinga et al. [42])

ized which represent the intensity contribution of each pixel that observes a particular voxel. After reconstruction, the volumetric velocity field is typically obtained by three-dimensional cross-correlation of sub volumes.

2.2 Camera calibration

The reconstruction of 3-D particle intensity distributions from several projections relies on accurate mappings between physical 3-D world coordinates and 2-D pixel coordinates of each camera. In the present work different camera models have been applied with the aim of comparing their performance with regard to reconstruction accuracy. Thus, a brief overview will be given next to the applied camera models, most of which have been extensively documented in literature [133, 64].

A basic camera model that have been applied during this work is the direct linear transformation (DLT) developed by Abdel-Aziz and Karana [10]. The model bases on central projection, ignoring lens distortions and other non-linear imaging effects. The mapping of world-coordinates onto image coordinates $F : \mathbb{R}^3 \rightarrow \mathbb{R}^2$ is obtained by the following homogeneous matrix equation:

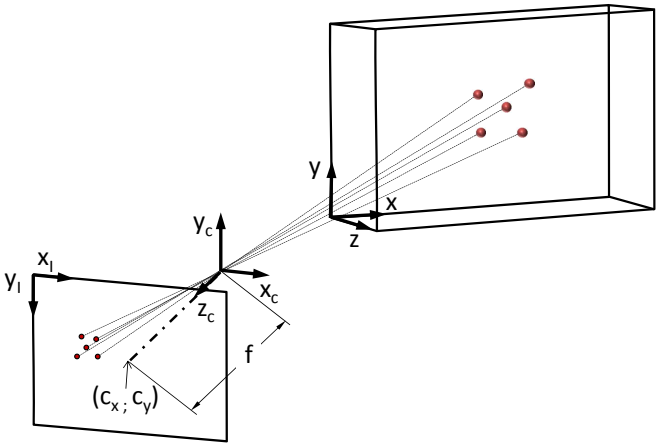

Figure 2.2: Projection of particle positions onto the image plane using a pinhole camera model

$$w_1 \begin{bmatrix} x_I \\ y_I \\ 1 \end{bmatrix} = \begin{bmatrix} a_{11} & a_{12} & a_{13} & a_{14} \\ a_{21} & a_{22} & a_{23} & a_{24} \\ a_{31} & a_{32} & a_{33} & a_{34} \end{bmatrix} \begin{bmatrix} x \\ y \\ z \\ 1 \end{bmatrix} . \tag{2.1}$$

The image coordinates are obtained by eliminating w_1:

$$\begin{aligned} x_I &= \frac{a_{11}x + a_{12}y + a_{13}z + a_{14}}{a_{31}x + a_{32}y + a_{33}z + a_{34}} \\ y_I &= \frac{a_{21}x + a_{22}y + a_{23}z + a_{24}}{a_{31}x + a_{32}y + a_{33}z + a_{34}} . \end{aligned} \tag{2.2}$$

A few reconstruction techniques require a inverse mapping from image to world coordinates. For a fixed z - coordinate the inverse function describes a mapping between two planes, a so-called homography:

$$w_2 \begin{bmatrix} x \\ y \\ 1 \end{bmatrix} = \mathbf{H}_z \begin{bmatrix} x_I \\ y_I \\ 1 \end{bmatrix} \tag{2.3}$$

where H_z is a 3×3 matrix, which can be obtained by explicit inversion of the reduced DLT matrix:

$$\mathbf{H}_z = \begin{bmatrix} a_{11} & a_{12} & z\,a_{13} + a_{14} \\ a_{21} & a_{22} & z\,a_{23} + a_{24} \\ a_{31} & a_{32} & z\,a_{33} + a_{34} \end{bmatrix}^{-1} \tag{2.4}$$

The parameters of the DLT matrix Eq. (2.1) are estimated from a set of cal-

ibration points representing correspondences between world and image coordinates. A detailed description of DLT parameter estimation is provided in the appendix A.2.1. The parameter of the DLT matrix have no direct physical meaning but can be decomposed into so-called intrinsic and extrinsic camera parameter of a pinhole model [105, 57]. The intrinsic parameter are the pixel size, the focal length f in pixel units and the intersection of optical axis and image plane (c_x, c_y) as illustrated in Fig. 2.2. The extrinsic parameter describe the orientation of the camera coordinate system (x_c, y_c, z_c) with respect to the world coordinate system (x, y, z) on the basis of a rotation matrix and a translation vector.

The DLT is frequently used to initialize multi-step photogrammetric camera models in computer vision (e.g. Tsai camera model [164], Zhang's method [194], Heikkilä and Silvén's four-step method [66]). These models additionally account for lens distortions but have at least the following two disadvantages with regard to tomographic applications in fluids: a back-projection from image to world coordinates is not provided in a closed-form and additional distortions from windows or fluid interfaces that lie between the volumetric measurement domain and the lens are not included in the model. Thus, in the present investigations, two additional camera models are implemented and tested using empirical mapping functions similar to those described by Willert [179] and Soloff [153]. These empirical camera models compensate for optical distortions by polynomial mapping functions involving higher order terms up to the 3$^{\text{rd}}$ degree. Although these types of mapping functions were originally proposed for stereoscopic PIV, they can easily be extended to 3-D mapping functions for both, world-to-image and image-to-world mappings, as shown in the appendix A.2.2.

Some of the experimental results in this thesis are obtained from a reconstruction algorithm that make use of a two-plane camera model [101, 169]. As the name indicates, the model is calibrated on the basis of point correspondences that originate from two planes that coincide with the front and back side of the volumetric measurement domain (plane A and B). For a given z coordinate, points in between both planes are calculated by linear interpolation between the intersections of the line of sight with plane A and plane B assuming a lin-

ear dependence of the mapping between the two planes. Basically, the model involves two perspective projection equations that map normalized image coordinates onto plane A respectively plane B. In the particular implementation, as provided by S. Gesemann from the DLR Institute of Aerodynamics and Flow Technologies, these planar mappings also involve non-linear terms to correct for distortions.

For volumetric imaging, the requirements on calibration accuracy are considerably higher than those for stereoscopic PIV [136]. All lines of sight of pixels that observe a particle have to intersect precisely and misalignments larger than a fraction of the particle image diameter will lead to rapid degradation of the intensity of an actual particle [42]. Possible sources of such misalignments are mechanical instabilities of camera and lens holders, thermal variations and image shifts due to structural vibrations of the test facility or even vibrations of the camera cooling system. Typically, static misalignments are compensated by a volumetric self-calibration procedure that involves triangulation of particle positions as described by Wieneke [176]. The average particle disparities, obtained during the self-calibration procedure, are used to iteratively correct the mapping functions. The author reports that the disparity error should be reduced to $0.1 - 0.2$ pixel for a reliable tomographic reconstruction.

2.3 Aspects of volume imaging of small particles

2.3.1 Particle image size

In high-speed air flows a fast response to sudden velocity changes (e.g. shock waves) requires tracer particle of a low Stokes number[1] of $St << 1$ resulting in particle diameter in the order of one micrometer or below [106, 137, 76, 129]. For such small particles the image size is usually determined by the point spread function of the imaging system rather than the geometric image [3].

[1] The dimensionless Stokes number relates the drag-based time constant in the exponential decay of particle's velocity to the velocity of the medium and the characteristic length of an obstacle.

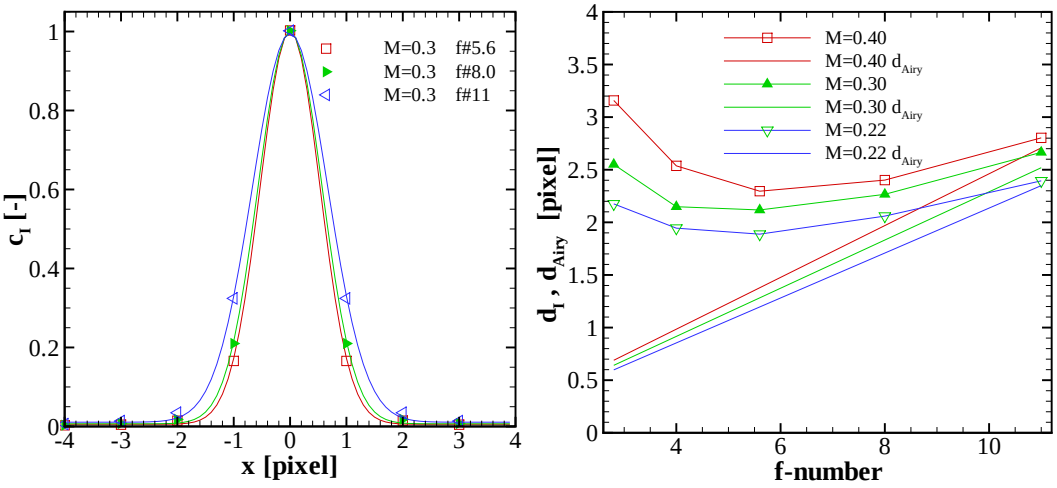

Figure 2.3: Characteristics of focussed particle images (Nikkor Micro lens $f = 55\,\mathrm{mm}$ + PCO2000 camera) at $\lambda = 532\,\mathrm{nm}$; *Left*: shape of particle images and Gaussian Fit; *Right*: diameter of the Gaussian particle images ($d_I = 4\sigma$) and of the Airy disc Eq. (2.5)

For a diffraction-limited[2] imaging system the particle image size can be estimated from the first zero of the diffraction pattern of a point source imaged through an annular aperture, also known as diameter of the Airy disk [3, 103]

$$d_A = 2.44\lambda f_{\#}(M+1)\,. \tag{2.5}$$

The diffraction-limited spot size Eq. (2.5) is a rough estimate of the lower bound of the particle image size. The latter can be significantly larger, depending on sensor resolution, optical lens aberrations or even aero-optical distortions [41]. The left subfigure of Fig. 2.3 shows the particle image shape obtained by autocorrelation of particle images at a light-sheet thickness of 0.5 mm and a laser wave-length of 532 nm. The right subfigure of Fig. 2.3 compares the particle image diameter obtained by a Gaussian fit to the diameter of the Airy disc obtained from Eq. (2.5). Up to a f-number of 8 the particle image size is significantly larger than the diameter of the Airy function for the given imaging setup, meaning that the particle signal is spread over a significant larger area as predicted by Eq. (2.5).

However, in tomographic PIV the reconstruction result can be improved by a

[2]The diffraction-limit describes the theoretical resolution limit in the absence of other optical distortions

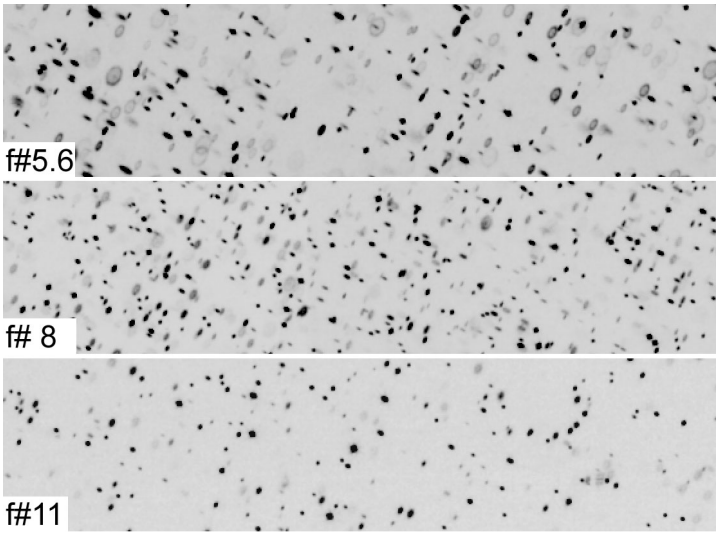

Figure 2.4: Particle image distortions due to off-normal imaging through perspex windows (viewing angle $\approx 30°$, window thickness 16 mm, M$\approx$ 0.34, volume depth 4 mm)

priori knowledge of the particle image shape as obtained from calibration (see Schanz et al. [144]). This is particularly the case if the particle image shape is non-uniform or elliptical. Fig. 2.4 shows an example of particle images undergoing elliptical distortions when imaged through a thick window under an angle of 30° between optical and window axis. Orientation and size of the elliptic images change with respect to their depth position. Fortunately these distortions can be reduced by closing the lens aperture which coincides with the requirement of a large depth of focus.

2.3.2 Depth of focus

During volumetric particle imaging, lens apertures have to be stopped down to maintain a sufficiently large depth of focus. The combination of both, small lens apertures and a thick light sheets can lead to a considerably weaker particle signal in comparison to planar PIV. To give an example: if the lens f-number is increased from 5.6 to 11 and the light sheet thickness is enlarged by a factor of five, then the laser radiance has to be increased by a factor of 20 to maintain the same signal strength. This implies an optimization of balancing the lens aperture with respect to the signal strength recorded by the sensor. For volumetric imaging, particle images should be in focus over the entire volume and should exhibit a sufficiently high intensity. Some basic optical relations can be used to estimate the depth of focus given the assumption that

particles represent point sources of scattered light.

Following Born and Wolf [18] and Meinhart et al. [104], the intensity of the Fraunhofer diffraction pattern of a point source imaged through a circular aperture reduces to a squared sinc function along the optical axis:

$$I(u) = I_o \,\mathrm{sinc}\left(\frac{m}{4}\right)^2, \tag{2.6}$$

where m is the dimensionless diffraction variable along the optical given by

$$m = \frac{2\pi z}{\lambda}\left(\frac{D_{EP}}{2a}\right)^2. \tag{2.7}$$

Here, D_{EP} denotes the diameter of the circular aperture and a the distance between particle and lens.

The axial image intensity $I(u)$ in Eq. (2.6) approaches 80% of its center intensity if $m = \pi$. By equating $m = \pi$ in Eq. (2.7) and by inserting the thin lens formula $f(1 + M) = a/M$ and $f_\# = f/D_{EP}$ one obtains the diffraction based depth of focus δz_d:

$$\delta z_d = 4\lambda f_\#^2\left(1 + \frac{1}{M}\right)^2. \tag{2.8}$$

When considering the three-dimensional intensity distribution of the diffraction pattern (c.f. Meinhart et al. [104] and Born and Wolf [18]) the diameter of particle images which lay within δz_d can be seen as constant. Thus, Eq. (2.8) is used as an estimation of the diffraction limited depth of field of a particle image (c.f. Adrian [3]).

Beyond the focal depth, particle images are blurred and estimation of a tolerable blur circle diameter d_b (e.g. $2 - 3$ pixel) helps to estimate the working f-number at which out-of-focus effects are sufficiently reduced to an acceptable level for tomographic imaging. According to Naumann and Schröder [114], for near field imaging ($0.1 \leq M \leq 1$) the geometric depth of field can be estimated by equating

$$\delta z_b = 2d_b f_\#\left(\frac{1 + M}{M^2}\right). \tag{2.9}$$

Following Scarano [136], both Eq. (2.8) and Eq. (2.9) can be combined to estimate the minimum f-number that is required to have all particles within a

given volume depth in focus. The f-number can be estimated from

$$f\# = \min\left[\frac{M}{M+1}\sqrt{\frac{\Delta z}{4\lambda}}, \frac{\Delta z M^2}{2d_b(M+1)}\right], \tag{2.10}$$

where Δz denotes the required depth of the volume. For example, given a working distance of a=400 mm, a focal length of $f = 100\ mm$, a magnification of $M \approx (a/f - 1)^{-1} = 0.33$, a wavelength of $\lambda = 532\,\text{nm}$ and a volume depth of 4 mm the f-number should not be smaller than 11 according to Eq. (2.8). On the other hand, if a blur circle of $d_b = 3\,\text{pixel}$ is seen as sufficient at a pixel pitch of 7.4 μm (PCO2000 camera) the lens aperture could be opened to $f_\# = 8$ which clearly increases the image intensity of particles.

2.3.3 Viewing geometry and particle elongation

Another aspect of tomographic particle imaging is the dependency of depth resolution on the angle between the lines of sight (see [42, 136]). The smaller the angle, the more elongated is the particle reconstruction. This effect is depicted in Fig. 2.5, where two images of the actual particle are back-projected into the volume, forming a double-cone shaped hull upon the circular reference shape. For a voxel-to-pixel ratio of unity, the depth resolution δz_e can be estimated from:

$$\delta z_e = \frac{d_I^*}{\sin(\frac{\beta}{2})}, \tag{2.11}$$

where d_I^* denotes the particle image diameter in pixel and β is the angular aperture of the system given by the planar angle between the optical axes of the outermost cameras of the viewing system. Elsinga et al. [42] investigated the effect of the angular aperture size on the reconstruction quality for a linear tomographic imaging setup consisting of three cameras. The authors reported best results near 60° and a sufficiently high reconstruction quality for a angular aperture ranging between 30° and 90°. Further increase of the angular aperture would reduce reconstruction quality due to a increasing intersection between the line of sight and the particle volume, leading to higher particle image densities (see Eq. (2.12)) .

A few approaches are known from literature that intend to compensate for

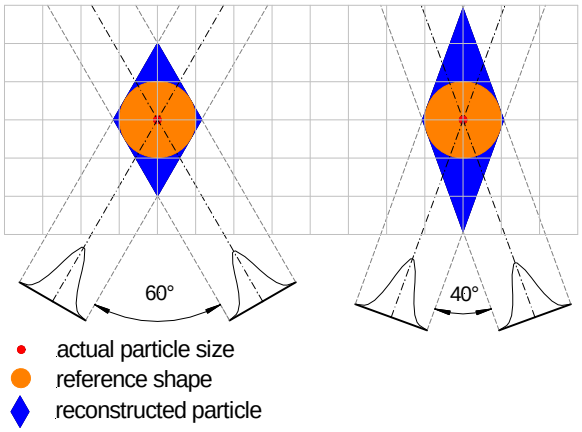

Figure 2.5: Influence of viewing geometry on reconstructed particle image shape (according to Scarano [136])

particle elongation. Discetti et al. [38] applied anisotropic Gaussian filtering during particle volume reconstruction. Wang et al. [168] proposed a method that shrink elongated particles by subtracting a fraction of the second-order derivative along z (inverse diffusion). Both authors reported marginal improvements of the velocity accuracy during their experiments. The reason might be, that both approaches expect elongations that are parallel with the volume z-axis, which is not always the case even if the camera arrangement is symmetrical.

2.3.4 Scattering behaviour

During the design of a multiple view camera setup consideration must be given to the fact that the signal strength of the scattered light strongly depends on the viewing direction and the particle size parameter $k_p = \pi\, d_p/\lambda$. As already mentioned above, in high-speed flows particle diameter of about one micron or less are required. Fig. 2.6 illustrates the angle-dependency of the particle signal of micron-sized particles and shows the scattered intensity of polarized laser light ($\lambda = 532\,\mathrm{nm}$) by spherical glycerin droplets in air. The scattered intensity is computed for a droplet size distribution of $d_p = 1 \pm 0.2\,\mu\mathrm{m}$ using *MiePlot 4.5* [88]. For example, if the cameras are placed symmetrical around $\theta = 90°$ and the angle between cameras is $60°$ strong differences can occur between the forward and backward scattering particle signal. If the laser light polarization is parallel to the scattering plane than the forward-scattered signal ($\theta = 60°$) would be about three times stronger compared to the back-scattered

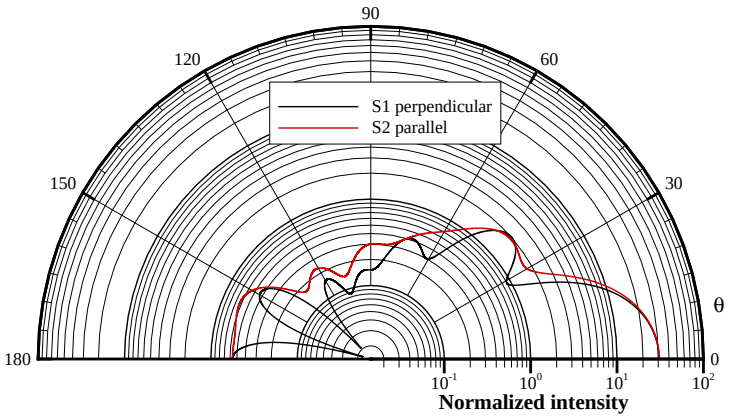

Figure 2.6: Angular intensity distribution of polarized light scattered by spherical oil droplets of $d_p = 1 \pm 0.2\,\mu$m in air

signal ($\theta = 120°$). This effect can partially be compensated by intensity normalization over each image and/or between cameras [176].

2.3.5 Seeding density

The seeding density or number of particles per volume unit strongly affects the spatial resolution of the velocity field. For planar PIV, usually a number of 10 particles per interrogation window results in a strong cross-correlation signal from which the mean displacement can be estimated [85]. For tomographic PIV, at least five particle per interrogation box are required because the loss-of-pairs phenomenon is less relevant in a volume in comparison to planar PIV configurations [136]. On the other hand, the particle field reconstruction may fail or produce ambiguous results at high seeding density due to a increasing overlap of particle images and/or reduction of particle image contrast by multi-scattering[3].

The following quantities are used frequently to evaluate the capability of a tomographic PIV measurement system to produce accurate results with regard to high seeding densities. The mean number of particle images per pixel (ppp) is given by the particle image density D_I which can be estimated from:

$$D_I = n_p \, \Delta z \left(\frac{\Delta \text{pix}}{M} \right)^2 , \tag{2.12}$$

[3]Multi-scattering refers to the phenomenon where photons scattered from single particles are re-scattered from neighboring particles prior to reaching the camera sensor. Hence, the directly scattered particle signal is decreased leading to a contrast reduction of particle images

where n_p denotes the particle number density and Δz the fraction of the line of sight that is covered by the measurement volume. The maximum particle image density for which a tomographic PIV system accurately recover a velocity field also determines the maximum depth of the volumetric domain at a given number density. A thinner volume may increase the reconstruction accuracy or alternatively, may enable higher particle number densities and a higher spatial resolution [7]. Another important quantity is the source density which determines the mean area per pixel that is covered by particle images [85]. The source density N_s can be obtained from particle image density by [136]

$$N_s = D_I \frac{\pi}{4} \left(\frac{d_I}{\Delta \text{pix}} \right)^2 , \tag{2.13}$$

where $d_I/\Delta\text{pix}$ denotes the particle image diameter in pixel units (d_I^*). For tomographic experiments in air flows, particle image densities typically range between $0.03 - 0.08\,\text{ppp}$ corresponding to source densities of $0.1 - 0.25$ at a particle image diameter of $2\,\text{pixel}$.

2.4 Particle field reconstruction

2.4.1 The ambiguity problem

The particle field reconstruction from a limited number of views is a underdetermined problem which potentially involves ambiguities. For example, Fig. 2.7 indicates three solutions (A, B, C) of a particle field reconstruction using a two camera system. The formation of non-physical particles or so-called *ghost particles* is caused by intersections of the lines of sight of different particles with each other [42, 8]. However, it is mainly due to the highly discrete nature of the imaged particle field that for a relatively small number of projections satisfactory results are feasible.

The occurrence of ghost particles in particle-based flow field measurements has already been observed during earlier 3-D PTV studies. Maas et al. [96] stated, that the number of ambiguous particle for a stereoscopic PTV system grows approximately with the square of the number of particles and linearly with the

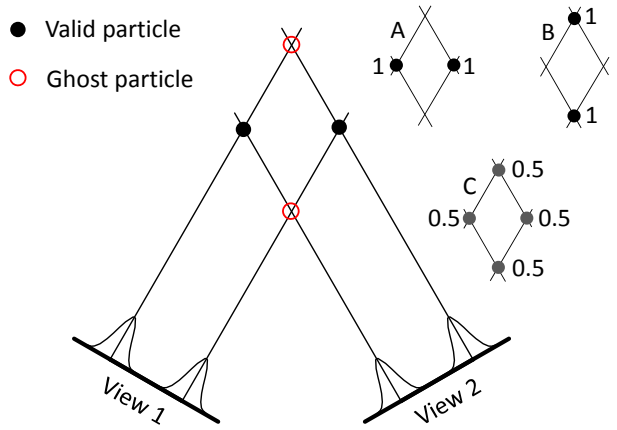

Figure 2.7: Ambiguity problem in tomographic PIV, according to [44]

length of the line of sight and can be reduced by using additional cameras. For a given number of cameras, Elsinga [44] and Novara [117] formulated a basic model to estimate the relative amount of ghost particle N_g with respect to the number of particle N_p for voxel-to-pixel ratio of unity:

$$\frac{N_g}{N_p} = D_i^{N_c-1} \, A_p^{N_c-2} \, \Delta l \, d_I^* \tag{2.14}$$

where N_c is the number of cameras, $A_p = \pi/4(d_i^*)^2$ denotes the representative area of a particle image in pixel, Δl is length of the line of sight in voxel and d_I^* is the typical particle image diameter in pixel units. According Eq. (2.14), a tomographic PIV system of four cameras, a volume depth of 160 voxel and a particle image diameter of $d_i^* = 3$ pixel would exhibit about five times more ghost particles than valid particles at a particle image density of 0.06 ppp and a voxel-to-pixel ratio of unity. However, this does not necessarily imply a erroneous velocity measurement, because typically the intensity of ghost particles is considerably lower than that of valid particles [136]. This effect is depicted in Fig. 2.8: if not all intersecting lines of sight originate from a particle image maximum, than the ghost particle holds significantly smaller energy compared to that of a valid particle.

The suppression of ghost particle intensity is strongly influenced by the reconstruction method and the way how particle images are weighted during back-projection. A short literature survey on reconstruction techniques is given in the following two subsections.

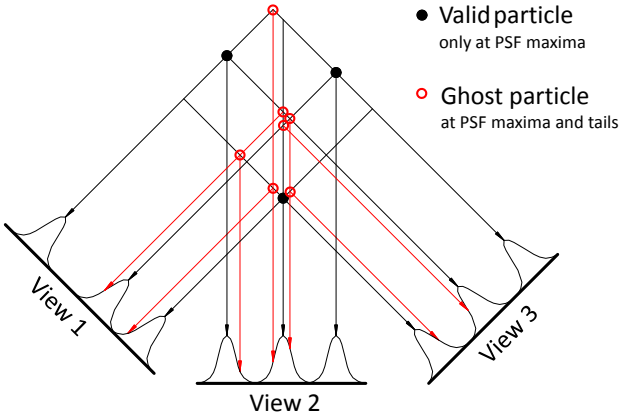

Figure 2.8: Incidence of ghost particle of weak intensities at LOS intersections involving particle image tails

2.4.2 Algebraic reconstruction techniques

In tomographic PIV, algebraic reconstruction techniques [62, 71] are the most common tools to obtain 3-D particle distributions from a limited number of arbitrary, non-collinear views. These techniques iteratively find the source intensity distribution in a volume of discrete voxel elements by solving a set of linear equations of the form $A\,x = b + \epsilon$, where A is the *projection matrix* and b is a vector of recorded pixel intensities. The solution x minimize the difference ϵ between recorded and projected pixel intensities. In the discretized form, each linear equation represents the projected intensity $\widehat{I}_i$ at a pixel i spatially integrated along the corresponding line of sight:

$$\widehat{I}_i = \sum_{j \in N_j} w_{ij}\, E_j\,, \tag{2.15}$$

where the weighting coefficient w_{ij} represents the contribution of a voxel j to a pixel i and the 3-D intensity array E_j is unknown in these equations. Typically, the intensity value of each voxel is iteratively refined until the difference between the recorded pixel intensity I_i and the projected intensity $\tilde{I}_i$ is minimized. In most cases, the volumetric reconstruction is a ill-posed reconstruction problem with multiple possible solutions. For tomographic PIV, the strategy that is mainly used to select a particular solution is the *maximum entropy* approach. For example, solution 'C' in Fig. 2.7 provides a superposition of all possible solutions which maximizes the entropy and best represents the set of measured projections.

The most widespread reconstruction approach is the *Multiplicative Algebraic Reconstruction Technique* (MART) [62, 42]. An earlier study by Verhoeven [165] already identified MART to be the algebraic reconstruction technique that is well suited to limited-data reconstruction of spike-like objects with steep intensity gradients. During iterative refinement MART involves a multiplicative update of voxel intensities based on the ratio between projected and recorded pixel intensities (further details are provided in Sect. 3.1.3). The voxel intensity correction is conducted separately for each of the views. The related *Simultaneous Multiplicative Algebraic Reconstruction Technique* (SMART) [112] performs simultaneously the iterative voxel correction for all views based on the product of the ratios of recorded to projected pixel intensities. SMART was first applied in tomographic PIV by Atkinson and Soria [8] with the intention of accelerating the reconstruction process. Further details on SMART intensity computation are given in Sect. 3.1.2.

2.4.3 Concepts for improved computational efficiency

Algebraic reconstruction techniques such as MART or SMART are computationally expensive and thus various modifications have been proposed in the past years to improve computational efficiency: Worths and Nickels [188] applied a *Multiplicative First Guess* (MFG) procedure for a initial detection of voxel that hold zero intensity values. Atkinson and Soria [8] proposed a similar but more efficient *Multiplicative Line of Sight* technique (MLOS), with the difference that a calculation of the weighting matrix is not required. After initialization, voxel that hold zero intensity are excluded from the iterative algebraic reconstruction procedure (e.g. SMART) which significantly reduces the dimensionality of the problem. Based on synthetic images at 0.05 ppp Atkinson and Soria obtained a speed 5.5 times faster of MLOS-SMART than that of MART while maintaining the same reconstruction quality. Turbulent boundary layer measurements of Atkinson et al. [7] confirmed negligible differences between the velocity fields obtained from MART and MLOS-SMART but a 11 times faster processing due to the MLOS-initialization at image densities ranging from $0.02 - 0.07$ ppp.

Discetti et al. [37] proposed a *Multi - Resolution* (MR) approach that applies $1-3$ MART iterations on images with reduced resolution during volume initialization. Further MART iterations at high resolution are conducted to improve ghost intensity suppression. The computational speed was estimated at 4.5 times faster than that of MART for a image density of 0.07 ppp and a source density of 0.5 without a loss of accuracy.

In order to simplify and accelerate the particle reconstruction process Bilsky et al. [16] applied the *Maximum Entropy Technique*[4] (MENT) for tomographic PIV. MENT seems to offer a number of advantages with respect to the more established methods as MART or SMART. Foremost MENT can significantly increase reconstruction speed because it operates on 2-D arrays and does not involve a iterative 3-D voxel correction step (details are provided in Sect. 3.1.1). The computational complexity is low and is limited to the calculation of products, sums and ratios of intensities, whereas MART and SMART require exponentiation and elaborate calculation of weighting factors. Bilsky et al. [15] have found MENT to converge already after 2 to 3 iterations while MLOS-SMART requires on the order of 10 to 20 iterations to achieve similar convergence levels. The authors found MENT to perform slightly less accurate then MLOS-SMART but stated a 14 times faster processing.

Another algebraic approach is the block-iterative MART (BIMART) by Byrne [23] that represents a generalization between MART and SMART, whereby each image is divided into a subset of blocks. With regard to tomographic PIV, the technique was assessed on the basis of synthetic data by Thomas et al. [162]. The authors stated a speed gain of 50% in comparison to MART while maintaining a equivalent accuracy. A comparative study of MART, BIMART and SMART and hot-wire data on the basis of a turbulent boundary layer experiment was conducted by Martin et al. [100] and confirms the speed gain results by Thomas et al.. Regarding experimental data, Martins et al. found the mean axial velocity obtained by tomographic PIV in good agreement to the hot-wire measurements up to a wall-normal distance of about 16 wall units

[4] In their paper, the technique is entitled with 'MENT' in accordance with Minerbo [111] who mathematically described the algorithm at first. Although most algebraic reconstruction techniques base on concepts which maximize the entropy, here the abbreviation MENT is kept in compliance with literature.

corresponding to 2 mm or approximately 29 voxel. With regard to velocity fluctuations, the MART, BIMART and SMART techniques exhibited very similar deviations from the hot-wire data.

Given a lack of implementation and hardware details, the results obtained from the above mentioned papers are not comparable among each other regarding computational speed but indicate only minor differences of MART, SMART or BIMART in terms of velocity measurement accuracy and a slightly lower accuracy for MENT. A proper initialization of the algorithm has huge influence on the computation time. The MENT reconstruction technique seems to be a promising approach regarding a increase of computational speed.

2.4.4 Particle based iterative reconstruction

Recent research focus on the reconstruction of sets of particles that are represented by their 3-D position and intensity rather than a discretized 3-D domain of voxel containing anonymous blob intensities. This particle based approach originates from *Particle Tracking Velocimetry* (PTV) [95, 12, 124] , where particle positions are tracked over time and space by matching techniques, using nearest neighbour or neural network or relaxation techniques to finally measure particle velocities and Lagrangian trajectories. Conventional PTV performs well for relatively low seeding densities. To increase robustness at higher densities, Akhmetbekov et al. [4] proposed a multi set PTV triangulation based on four cameras that allowed matching of particle images at typical image densities of 0.04 ppp during experimental verification. Velocity deviations in the order of 10% occurred between multiset PTV and tomographic PIV. The authors identified the uncertainty of the 3-D particle position as the largest error source. This problem has been addressed by the hybrid *Iterative Particle Reconstruction* (IPR) technique proposed by B. Wieneke [177], where the particle position error is corrected by a image matching scheme and particle intensities are corrected by a MART-like procedure. The image matching procedure relies on small step-wise variations of the 3-D particle position in space ('shaking') and simultaneous computation of the local residuum between the reprojected and the measured particle intensity distribution. The residuum

is fitted as a function of the step-wise particle displacements. If present, the minimum of the fit represents the corrected position. Based on synthetic data, a comparison between IPR and MART ([178]) revealed a smaller positioning error of IPR while maintaining similar levels of ghost suppression for image densities up to 0.05 ppp ($d_i^* = 2$ pixel, $N_s = 0.16$). For IPR, the computation of the local particle reprojection requires a-priori knowledge of the shape of the *point spread function* (PSF) that can be obtained by calibration of the optical transfer function (OTF) as described by Schanz et al. [143, 144]. Both, IPR and OTF calibration provide the basis for 'Shake-the-box' (STB), a multi-pulse technique for time-resolved PTV, proposed by Schanz et al. [142] that recently has been shown applicable also to four-pulse image recordings [**?**] in high-speed flows. The STB technique can provide Lagrangian particle tracks and particle source intensity over multiple exposures. The combination of both, track length and intensity have shown to be an efficient discriminator to distinguish between valid particles and ghosts [47]. During experimental assessment, Schanz et al. applied STB to measure 3-D particle trajectories in a free water jet. For a 3-camera setup and image densities of 0.035 ppp the authors found particle tracks to converge after 11-30 sequential exposures while exhibiting very low noise level. However, when applied to two-pulse image data, a combination of SMART followed by STB seems to be promising as well. During the previous PIV challenge contest (Case C: 'Resolution/accuracy of tomographic-PIV') [81], SMART-STB has outperformed solitary SMART and MART reconstruction techniques regarding ghost intensity suppression and spatial resolution.

Yet another promising approach to obtain a computational efficient particle based reconstruction is the *Particle Volume Reconstruction* (PVR) proposed by Champagnat et al. [26]. In contrast to IPR, PVR does not adjust particle positions by 'shaking' but iteratively corrects the intensity using SMART together with a PSF-based Gaussian weighting function. Sparse point-like particles in a voxel space are finally converted to a set of particles by searching local maxima. Recently, Cornic et al. [32, 33] proposed the application of a *Compressive Sampling Matching Pursuit* (CoSaMP) algorithm [115] in combination with PVR to further improve computational efficiency of the reconstruction. Instead of using a algebraic reconstruction technique to solve a

set of linear equations, CoSaMP solves a so-called constrained least-squares problem by minimizing the residual $\| A\,x - b \|$ as subject of a sparsity parameter. The accuracy assessment of PVR - CoSaMP with regard to displacement estimation on the basis of experimental data is subject of ongoing research.

By being relieved of the time-consuming process of reconstruction of large discrete voxel volumes, particle based reconstruction techniques as IPR, STB and PVR are promising concepts with regard to computational efficiency by taking into account the sparsity of a 3-D particle field. Especially STB provides a big step towards ghost particle removal due to the high discrimination power of particle track length and source intensity. On the other hand, turbo machine test facilities typically operate at high axial gas velocities of $u > 100\,\mathrm{m/s}$ and thus time-resolved particle tracking measurements on the basis of multiple subsequent recordings is technical hardly feasible. Thus, within the present work, a particle based reconstruction technique has been implemented, similar to the PVR technique (implementation details are provided in Sect. 3.1.3) which provides a expandable basis for advanced IPR or STB techniques.

2.5 Particle displacement estimation

In the present work, the estimation of particle displacements relies on a classical double-frame technique instead of emerging 3-D PTV multi-pulse techniques which require at least four coherent samples from multiple views (see Novara et al. [119]). The reason is that in high-speed flows ($U > 100\,\mathrm{m/s}$), as they occur in turbo machine test facilities, both temporally and spatially well-resolved image data is hardly feasible from the technical point of view, even if the limited optical access of those facilities is taken into account. The latter constraint impedes the installation of large camera arrays which enable the acquisition of at least four sequential exposures from multiple views (c.f. Geisler et al. [56]). Moreover, time resolved particle velocities using high-speed cameras would require acquisition rates in the order of $0.5\,\mathrm{MHz}$ accompanying with a significant reduction of the image resolution from $3-5\,\mathrm{Mpixel}$ (for typical double-frame PIV cameras) down to about $30-50\,\mathrm{Kpixel}$ for modern high-speed cameras.

Particle displacement recovery from two subsequent recordings is obtained by state-of-the-art cross-correlation analysis between small interrogation volumes. To improve spatial sampling, a overlap between adjacent interrogation volumes of 50 - 75% is applied. The 3-D interrogation algorithm can be considered as an extension of the well-established FFT based 2-D cross-correlation techniques for PIV (c.f. Willert [185]). According to Nogueira [116], the general cross correlation coefficient between two sub volumes **A** and **B** for a cubic interrogation box of W^3 elements reads as:

$$C_{II} = \frac{\sum_{i,j,k=1}^{W} \mathbf{w}_{i,j,k}^2 (\mathbf{A}_{i,j,k} - \mu_A)(\mathbf{B}_{i+l,j+m,k+n} - \mu_B)}{\sqrt{\sum_{i,j,k=1}^{W} \mathbf{w}_{i,j,k}^2 (\mathbf{A}_{i,j,k} - \mu_A)^2 \sum_{i,j,k=1}^{W} \mathbf{w}_{i,j,k}^2 (\mathbf{B}_{i+l,j+m,k+n} - \mu_B)^2}}. \tag{2.16}$$

where $\mathbf{w}_{i,j,k}$ are the coefficients of the weighting window, μ_A and μ_B are the mean intensities and m, n, k are the integer offsets between both interrogation volumes. The quantities in the denominator are actually the variances of A and B pre-multiplied with the weighting factors. For a top hat weighting function, the correlation coefficient becomes the ratio of the sample covariance of **A** and **B** divided by the standard deviations of **A** and **B**. Due to this normalization, the resulting correlation coefficients will fall in the range $-1 \leq C_{II} \leq 1$. The cross-correlation peak represents the resulting displacement estimate. Sub-voxel accuracy is achieved for example by a Gaussian curve fit around the element of the correlation table that holds the highest value. In common practise, multi-resolution techniques [155, 174, 139] are applied to compute offsets between both interrogation volumes and thereby extending the measurable dynamic range. Fractional instead of integer window offsetting can further improve the measurement dynamic range at the cost of an additional sub-voxel interpolation of interrogation volumes [91, 140]. In curved and shear flows the particle pattern within sub volume **A** is subject to deformations in sub volume **B** in terms of translation, rotation, shearing and dilation. The adoption of the iterative image deformation technique [74, 77, 140] provides a remedy to that problem and improves matching of interrogation volumes while the correlation peak height is increased. According to Scarano and Poelma [138], each deformation step involves sub-voxel sampling of both volumetric

intensity fields by the relations:

$$\begin{aligned} E_A^{k+1}(x,y,z) &= E_A(x-\Delta x^k/2, y-\Delta y^k/2, z-\Delta z^k/2) \\ E_B^{k+1}(x,y,z) &= E_B(x+\Delta x^k/2, y+\Delta y^k/2, z+\Delta z^k/2)\,, \end{aligned} \tag{2.17}$$

where the local displacement $(\Delta x^k, \Delta y^k, \Delta z^k)$ at the kth iteration is obtained by trilinear interpolation of the predictor field from the previous iteration. Low pass filtering of the predictor respectively the corrector field can reduce numerical instabilities of the iterative process especially if the overlap between adjacent interrogation volumes exceeds 50% and no window weighting is applied [148].

The computation effort for 3-D displacement field recovery can easily reach that of particle volume reconstruction. A few approaches to computation cost reduction are known from literature. Discetti and Astarita [36] proposed pre-calculation of terms of the correlation coefficient Eq. (2.16) on cubic blocks smaller than a interrogation volume. In this way, the overhead of computations due to overlapping interrogation volumes is reduced to a minimum. To further speed up processing, the authors made use of sparse direct cross-correlation for evaluation of residual sub-voxel displacements while FFT based correlation is applied during multi-step processing of the predictor displacement field.

2.6 Motion-based suppression of ghost particles

Whether or not a ghost particle distorts a velocity measurement depends on how it contributes to the cross-correlation signal. The worst case is that several ghost particles build coherent pairs in both interrogation boxes and establish a dominant peak in the cross-correlation signal. In case of non-coherent motion, ghost particles produces additional peaks in the cross-correlation plane at the expense of the strength and/or sharpness of the valid cross-correlation signal. Ghost particles are often connected to true particle which, at best, can support a valid correlation signal. The latter is unlikely in the presence of shear flows.

Novara et al. [118] proposed the recursive *Motion Tracking Enhancement* (MTE) technique in combination with MART to iteratively exclude ghost particles

from reconstruction that exhibit non-coherent motion. Initially, a velocity predictor is obtained by cross-correlation between uncorrected MART reconstructions. According to the predictor, the first exposure is deformed toward the second time step and the second exposure is deformed toward the first time-step. The deformed volumes and the initial MART reconstruction are averaged whereby the intensity of non-coherent ghost particles is reduced. The result serves as first guess for the next MART iteration. The authors stated that MTE-MART could enable a two to three times higher seeding density while maintaining a similar reconstruction quality.

Chapter 3

Fast algebraic reconstruction for tomographic PIV

A tomographic reconstruction process involves computation of the particle source intensity over a discretized 3-D domain of voxels from a set of images. Iterative algebraic methods are often used, such as the multiplicative algebraic reconstruction technique (MART), which is well suited to reconstruct discrete objects from a limited number of arbitrary non-coaxial projections [165, 42]. The processing is computationally intensive and can be time-consuming depending on the required resolution and available computing power. To give an example: The conventional algebraic reconstruction of two time steps each of 0.6 Gvoxel from four images of 4 Mpixel can take in the order of 20 minutes on a 12-core workstation. The processing time consumption becomes even more serious if a large number of samples have to be evaluated (e.g. to achieve convergence of velocity fluctuations in turbulent flow regions). Especially in high-speed flows, of the kind typically encountered within turbo machine test facilities, typically several thousand samples have to be evaluated. Thus, an accurate and computational efficient reconstruction technique is crucial.

This chapter describes the implementation of two algebraic reconstruction techniques, namely the maximum entropy technique (MENT) and a fast multiplicative algebraic reconstruction technique (FMART), which both are optimized in terms of high data throughput within a short computation time. These techniques are compared against a conventional simultaneous multi-

plicative algebraic reconstruction technique (SMART) that uses a multiplicative line of sight initialization (MLOS). Atkinson and Soria [8] first applied MLOS to minimize the number of active voxels during a SMART reconstruction. Although SMART typically needs more iterations to obtain a reconstruction quality similar to MART, the authors found MLOS-SMART to perform 4-5 times faster than MART depending on the seeding density. As part of the overall assessment of the various techniques the present work includes a comparison between FMART, MENT and MLOS-SMART in terms of ghost suppression, accuracy of displacement estimates and computation speed using sets of synthetic images, generated from randomly distributed 3-D particle positions at various number densities. Particle displacements are obtained from a predetermined synthetic flow field.

The following section describes the implementation of all tested reconstruction techniques and provides details about measures applied to speed up the reconstruction process. Section 3.2 explains the synthetic imaging setup as well as the synthetic flow field and gives details on the procedures used for performance assessment. In section 3.3.1 the convergence of all algorithms is compared in terms of the number of required iterations. Next, the suppression of ghost particles is assessed on the basis of intensity histograms. In section 3.3.3 the accuracy of the reconstructed particle positions and the accuracy of velocity estimates of all tested algorithms are compared. Finally, the computation speed is evaluated from reconstructions at various particle image densities.

3.1 Applied reconstruction techniques

3.1.1 The maximum entropy technique (MENT)

The maximum entropy technique (MENT) [111] was first applied in tomographic PIV by Bilsky et al. [16] in order to simplify and accelerate the reconstruction procedure. Algebraic reconstruction techniques correct the intensity of a 3-D voxel usually under the hypothesis that the pixel intensity and the intensity integral along the line of sight are equal (see Eq. (2.15)). For MENT,

the basic idea is that instead of computing the line of sight integral in 3-D, the intensities are summed along the 2-D epipolar line, which is the projection of the line of sight in corresponding images. The main advantage is that the computation and storage of voxel intensities is not required during the iterative refinement process. Instead, the MENT algorithm reconstructs the three-dimensional intensity distribution in two steps. The first step is depicted in Fig. 3.1, left and calculates two-dimensional discrete functions or so-called pseudo images h_j for each view j [16]. Following Minerbo [111], the pseudo images h_j are first initialized using:

$$\begin{aligned} h_j^0(x_I, y_I) &= 1 \quad \text{if } p_j(x_I, y_I) > 0 \\ h_j^0(x_I, y_I) &= 0 \quad \text{if } p_j(x_I, y_I) = 0\,. \end{aligned} \tag{3.1}$$

Subsequently, in order to calculate pseudo image intensities, the coordinates x_I, y_I of each pixel of view j are projected into the volume, giving the coordinates of the line of sight L as a function of x_I, y_I, z. The coordinates of all members of the line of sight $L(z)$ are then projected onto each image $i \neq j$ in order to obtain coordinates of the epipolar lines of x_I, y_I. The intensities h_{il}^k along each epipolar line are found by image interpolation. At this state of work bilinear interpolation of the 4-neighborhood in h_i^k is applied. In order not to undersample epipolar intensities during step no. 1, the discretization increment Δz_1 was chosen to be $0.5\Delta z_2$ with Δz_2 being the voxel depth at the final reconstruction. The denominator in Eq. (3.2) is given by the product of h_{il}^k of each view $j \neq i$ summated along L. Finally, the new value of h_j^{k+1} is calculated by the ratio of the measured pixel intensity p_j divided by the sum of intensity products along the epipolar lines:

$$h_j^{k+1} = \frac{p_j}{\frac{1}{V}\sum_{l \in L}\prod_{i \neq j} h_{il}^k} \tag{3.2}$$

The aim of this optimization is that the measured intensity at $p_j(x_I, y_I)$ equals the summation of intensities along the line of sight in the reconstructed volume. This state is expected if Eq. (3.2) converges to Eq. (3.3). Here the measured intensity at $p_j(x_I, y_I)$ equals the line-of-sight sum along L of the products of

intensities of h at the corresponding epipolar lines plus a residuum ϵ.

$$p_j = \left(h_j \frac{1}{V} \sum_{l \in L} \prod_{i \neq j} h_{il} \right) + \epsilon \tag{3.3}$$

Finally, voxel intensities are recovery after the residuum ϵ is minimized. The 3-D intensities at each voxel position x, y, z are found by multiplication of pseudo image intensities at the corresponding pixel positions x_I, y_I (see Fig. 3.1, right and 3.4). The pseudo image intensities at x_I, y_I are interpolated bilinearly from the 2×2-neighborhood. For storage the intensity product is finally scaled to 16bit unsigned integers.

$$E(x, y, z) = \frac{1}{V} \prod h_j(x_I, y_I) \tag{3.4}$$

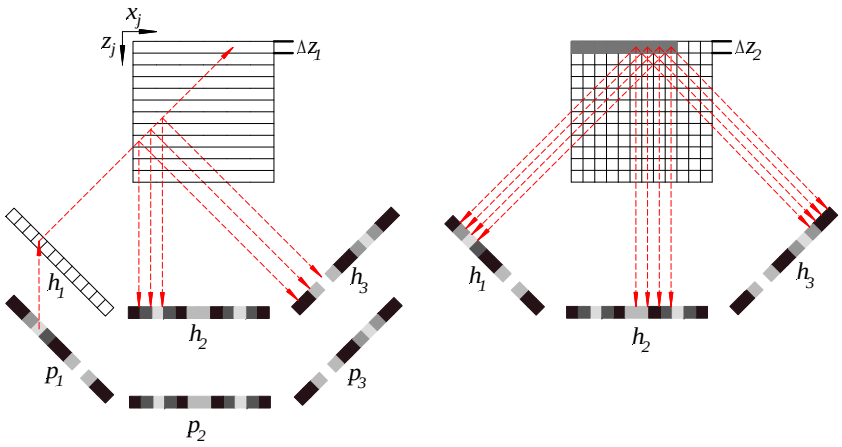

Figure 3.1: Reconstruction of the 3-D particle distribution with MENT (c.f. Bilsky et al. [15]): generation of pseudo images (left), volume recovery (right)

Compared to MART or SMART the memory demand of MENT is much lower. The processing of so-called pseudo images h is based on $nx_j \times ny_j$ arrays with nx_j and ny_j being the width and height of each view j. Conventional algebraic reconstruction techniques as MART or SMART need images and all 3-D intensities above zero as well as associated weighting factors to be stored in RAM during processing. MENT recovers the volume intensities only in the second step. Thus the processed $x-y$ slices can directly be transferred to non-volatile storage (e.g. hard disc). In the present work, MENT is implemented in C/C++ using additional libraries such as *OpenCV* [20] for image process-

ing and *OpenMP* [121] for parallelization. Parallel processing is achieved by distributed computation of rows of each pseudo image. To further speed up reconstruction during volume recovery, the processing of $x - y$ slices is also distributed on several processor cores.

3.1.2 The simultaneous multiplicative algebraic reconstruction technique (SMART)

Within this work, SMART is used as a benchmark for a comparison of reconstruction techniques in terms of accuracy and computation time requirement. The applied SMART algorithm was developed and implemented by D. Schanz and S. Gesemann of the DLR Dept. Experimental Methods of the DLR Institute of Aerodynamics and Flow Technology [144].

SMART calculates the voxel update simultaneously from intensities of all pixels which observe the voxel. According to Mishra [112] the simultaneous iterative refinement of voxel intensities is

$$E_j^{k+1} = E_j^k \prod_{i \in N_i} \left[\left(\frac{I_i}{\tilde{I}_i} \right)^{\mu w_{ij}} \right]^{1/N_i} , \tag{3.5}$$

where N_i denotes the total number of pixel that observe a given voxel j, I_i is the recorded pixel intensity and $\tilde{I}_i$ is the reprojected intensity (see Eq. (2.15)). The weighting coefficient w_{ij} represents the contribution of a voxel j to a pixel i and μ denotes a relaxation parameter. Typically, SMART requires more iterations to achieve a reconstruction quality similar to MART. Atkinson and Soria [8] reported improved convergence of SMART at $\mu = 2$ and $D_I = 0.05\,\mathrm{ppp}$. In order to check whether the iterative performance of the present SMART implementation can be improved, the relaxation parameter was tested within a range of $1 - 2$. As proposed by Atkinson and Soria [8] a MLOS procedure is applied initially to obtain a first guess of all voxels that hold a intensity above zero.

3.1.3 The fast multiplicative algebraic reconstruction technique (FMART)

In the field of tomographic PIV, the Multiplicative Algebraic Reconstruction Technique (MART) was first introduced by Elsinga [42] and is nowadays a common tool for the reconstruction of particle intensity distributions in volumetric domains. MART iteratively finds the intensity distribution in a volume of discrete voxels by solving a set of linear equations. Each equation represents the projected pixel intensity $\tilde{I}(x_i, y_i)$ spatially integrated along the corresponding line of sight (see Eq. (2.15)). MART involves a multiplicative update of voxel intensities using the following equation:

$$E_j^{k+1} = E_j^k \left(\frac{I_i}{\tilde{I}_i} \right)^{\mu w_{ij}} , \tag{3.6}$$

where $0 < \mu \leq 2$ is a relaxation parameter which influences convergence rate and numerical stability [8, 162]. In the present work, μ is set to unity as originally proposed by Elsinga et al. [42].

In the literature different projection models can be found which calculate the weighting coefficients w_{ij} either based on the intersection of geometrical objects (e.g. cylindrical line of sight and spherical voxel) or on bilinear or Gaussian weighting functions. The effect of these models on the quality of algebraic reconstruction is assessed by Thomas et al. [162] who found a Gaussian weighting function as well as a disc-intersect (intersection of a spherical voxel and a circular pixel) to be the most favorable for an algebraic reconstruction technique. Here, Gaussian weighting is used because of its similarity to physical imaging models involving a Gaussian approximation of the point spread function (PSF). Furthermore, such a PSF approach enables modelling of optical distortions as defocussing (Gaussian width depends on the source location) or even astigmatism (elliptical Gaussian functions, see [144]). The Gaussian projection model in the current implementation is depicted in Fig. 3.2 and is similar to a model proposed by Cornic et al. [32, 26]. Given the assumption that the spreading of voxel intensities is determined by the weighting function h, Eq. (2.15) becomes

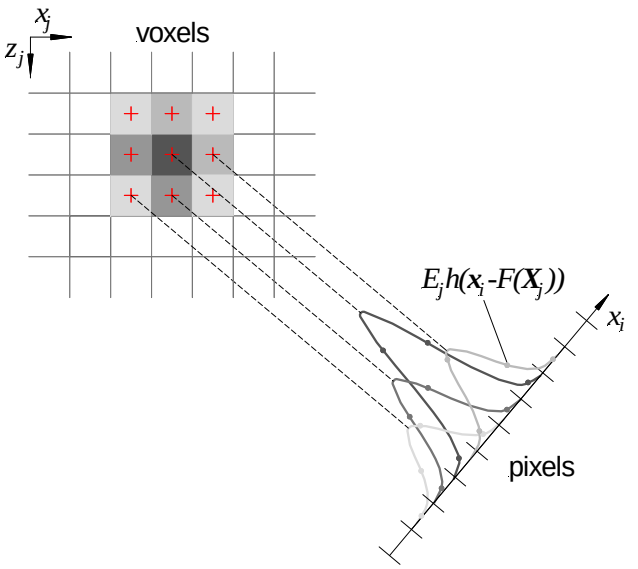

Figure 3.2: Projection of voxel intensities onto a sensor plane using a Gaussian point spread function h

$$\tilde{I}(\mathbf{x}_i) = \sum_{j \in N_j} E_j \, h(\mathbf{x}_i - F(\mathbf{X}_j)) \tag{3.7}$$

where $\mathbf{x}_i = (x_i, y_i)$ and $\mathbf{X}_j = (x_j, y_j, z_j)$ respectively represent the pixel and voxel position. The mapping function $F : \mathbb{R}^3 \rightarrow \mathbb{R}^2$ denotes the projection from 3-D space to the image plane where the pixel position of each voxel's center $F(\mathbf{X}_j)$ is $\mathbf{x}_j = (x_j; y_j)$.

For example, discretization of an elliptical Gaussian weighting function h gives the following weighting coefficients

$$w_{ij} = A \, \exp(-(a \, (x_i - x_j)^2 - 2b \, (x_i - x_j) \, (y_i - y_j) + c \, (y_i - y_j)^2)) \tag{3.8}$$

where the parameter A,a,b and c in principle can be calibrated for a set of sub volumes and for each view using for example the OTF calibration technique by Schanz et al. [143] or more simple by the slanted edge technique proposed by Reichenbach et al. [131] and Champagnat et al. [26] (see also Sect. 6.4).

The processing flow of the current C/C++ implementation of FMART is depicted in Fig. 3.3. In a first step, the volume is initialized by back-projection of each image onto each z plane. Following Atkinson and Soria [8], the back-projected image intensities are multiplied to obtain a first guess of all non-zero voxels (MLOS technique). The initialization is parallelized by distributed pro-

cessing of volume z-slices on several cores. Usually the initialized volume matrix is very sparse and only a small fraction of the voxels need to be evaluated during MART. Former simulations indicate that for a four camera setup, a particle image density of 0.06 ppp and a particle image diameter of 3 pixel as little as 4% of all voxels is occupied with non zero intensities. Thus, it is computationally efficient not to hold the entire volume matrix of $nx \times ny \times nz$ voxel in memory but a vector of data structures (so-called 'voxel listing') containing the integer volume position and the floating point intensity of each occupied voxel. During initialization the intensities of all non-zero voxel candidates are set to one and all recorded images are normalized to obtain a mean intensity of one for all non-zero pixels. Precalculation of the floating point image positions $\mathbf{x}_j^m = (x_j^m; y_j^m)$ of each voxel in each view m is implemented to avoid computationally intensive evaluation of mapping functions during each voxel projection and voxel update step. After initialization, the intensities of all voxel candidates are refined iteratively. Each iteration step consists of successive projection and voxel update. During projection, the intensity of each voxel candidate is distributed by the Gaussian weighting function over a patch size of p^2 pixel around the voxel's image position $\mathbf{x}_j$. The edge length of the patch is set to $p = \text{ceil}(4\sigma)$ where σ is the standard deviation of the Gaussian weighting function. The projection involves summation over the Gaussian distributions from all voxel candidates. Afterwards, the ratio $R^m = I^m / \tilde{I^m}$ is calculated which can be considered as the residual image of the actual and the projected image. For the intensity correction of the j^{th} voxel from the m^{th} view, the update factor P_j^m is calculated by multiplying all samples of the residual image within a region of p^2 pixel around the image position $\mathbf{x}_j$ of the voxel center:

$$P_j^m = \prod_{i \in N_i} R_{ij}^{\mu w_{ij}}, \tag{3.9}$$

where $N_i = p^2$. The FMART processing is parallelized by distributing projection and update of subsets of the voxels on several cores.

In order to further speed up the reconstruction process the weights w_{ij} are precalculated and accessed from lookup table (LUT), because they are evaluated frequently during projection and update of voxel intensities. For example, if a circular particle image of constant size is assumed, Eq. (3.8) simplifies and

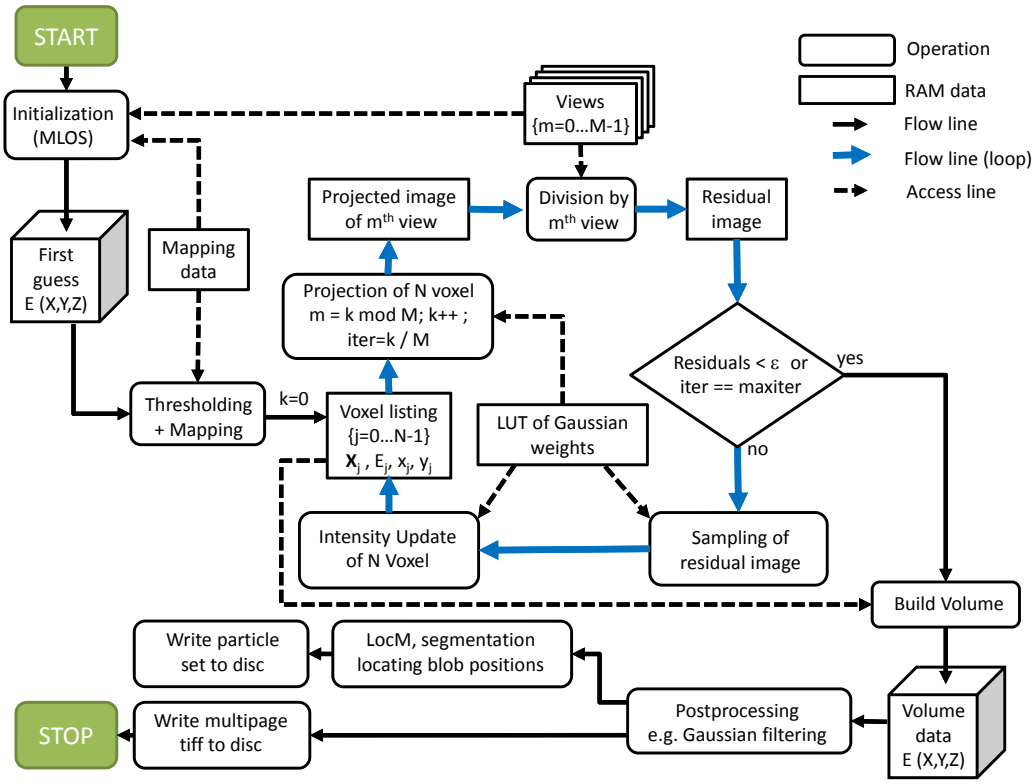

Figure 3.3: Processing chart of FMART

can be rewritten as

$$w(i,j) = A\,\exp(-a\,(x_i - x_j)^2)\,\exp(-a\,(y_i - y_j)^2) \tag{3.10}$$

where the parameter $A = 0.5/\pi\sigma^{-2}$ and $a = 0.5\sigma^{-2}$ are constant. Thus, the precalculation of both exponential terms involves only a single LUT where the number of columns is given by the kernel size p and the number of rows is given by the required accuracy of sub-pixel shifts. For example, a sub-pixel accuracy of 100 corresponds to a step width of 0.01 pixel in a range of $0 - 0.99$ pixel.

The iterative refinement of voxel intensities stops if the mean residual over all pixels is below a given threshold or if the maximum number of iterations is reached. Afterwards, the volumetric matrix of $nx \times ny \times nz$ voxel short integer elements is allocated and filled with the converted intensity entries of the voxel listing. Further post processing involves optional smoothing and evaluation of particle positions for particle tracking. These 3-D particle positions are recovered after a local maximum detection (LocM) and 3-D segmentation

of each coherent cluster of voxel, whereby the latter is implemented by evaluating the intensity of adjacent voxels of each local maximum within a given cluster size. Voxels are added to a cluster if they have intensities above a given threshold. The reconstructed volume is finally transferred to nonvolatile storage either as multipage TIFF file and/or as a file containing cluster positions (center-of-mass), sizes and intensities.

The fast MART algorithm is implemented in C/C++ using additional libraries such as *OpenCV* [20] for image processing, *OpenMP* [121] for parallelization and the in house library *PIV4D* for storage and handling of volumetric image data. All measures to speed up the computational time demand of a FMART reconstruction can be summarized as follows:

- Storage and access of the sparse volume using a 1-D voxel listing,
- Precalculation of pixel positions for each voxel entry in the list,
- Access of exponential terms of the Gaussian weights using lookup table,
- Parallelization of initialization, voxel projection, voxel update and post-processing using OpenMP.

3.2 Numerical setup and data evaluation

3.2.1 Synthetic images and flow field

The reconstruction accuracy of the previously described algorithms is assessed on the basis of synthetic images of randomly distributed 3-D particle positions and a synthetic swirl flow. Therefore, the predetermined particle positions inside of a $10 \times 10 \times 3\,\mathrm{mm}^3$ volume were projected onto four virtual cameras using a pinhole camera model. The model applies central projection and can be described as follows:

$$w \cdot \begin{bmatrix} x_I \\ y_I \\ 1 \end{bmatrix} = \begin{bmatrix} f/\Delta\mathrm{pix} & 0 & c_x \\ 0 & f/\Delta\mathrm{pix} & c_y \\ 0 & 0 & 1 \end{bmatrix} \cdot \begin{bmatrix} \mathbf{R} | \ \mathbf{t} \end{bmatrix} \cdot \begin{bmatrix} x \\ y \\ z \\ 1 \end{bmatrix}. \tag{3.11}$$

Table 3.1: Synthetic test parameter

Volume size		$10 \times 10 \times 3$	mm^3
Number of virtual cameras		4	
View angles around y-axis	φ	$-42° ; -14° ; 14° ; 42°$	
focal length	f	100	mm
Pixel pitch	Δpix	7.4	μm
Camera resolution		512×512	pixel
Approx. magnification	M	0.38	
Sub-pixel image accuracy		0.01	pixel
Particle image density	D_I	$0.03 - 1.30$	ppp
Particle image dia. (4σ)	d_I	3	pixel
Source density based on Eq. (2.13)	$0.21 - 0.92$		
Voxel size		19.5	μm (1 voxel/pixel)
Reconstructed volume size		$512 \times 512 \times 160$	voxel

The 3×3 matrix, which is frequently referred to as camera matrix $\mathbf{A}$ [21], contains the parameter s which describes the sensor resolution in pixel/mm, while f is the focal length in mm, and c_x, c_y describe the intersection between optical axis and senor in pixel. This intersection was placed at the center of each synthetic image. The translation vector $\mathbf{t}$ points from world coordinates origin toward the center of projection (location of lens principal point). Rotation matrix $\mathbf{R}$ and translation vector $\mathbf{t}$ form the 3×4 projection matrix $\mathbf{W}$. The views are arranged in a linear imaging configuration with respect to the y-axis (see Fig. 3.4, right). Thus, the rotation matrix $\mathbf{R}$ can be calculated from the sensor yaw (φ around the y axis) as follows:

$$\mathbf{R} = \begin{bmatrix} cos\,\varphi & 0 & -sin\,\varphi \\ 0 & 1 & 0 \\ sin\,\varphi & 0 & cos\,\varphi \end{bmatrix} \tag{3.12}$$

Particle number densities are adjusted according to image densities ranging from $0.03 - 0.13$ ppp. Particle images consist of 2-D Gaussian distributions of a radius of $r_p = 2\sigma = 1.5$ pixel. Sub-pixel positions are discretized with a step width of 0.01 pixel. Parameters are summarized in Table 3.1.

Tracer advection consists of a synthetic flow field of planar Taylor-Green vortices aligned parallel with the $x - z$ plane and a helical displacement along the y-axis (see Fig. 3.4). The predetermined particle displacement $\Delta X, \Delta Y, \Delta Z$

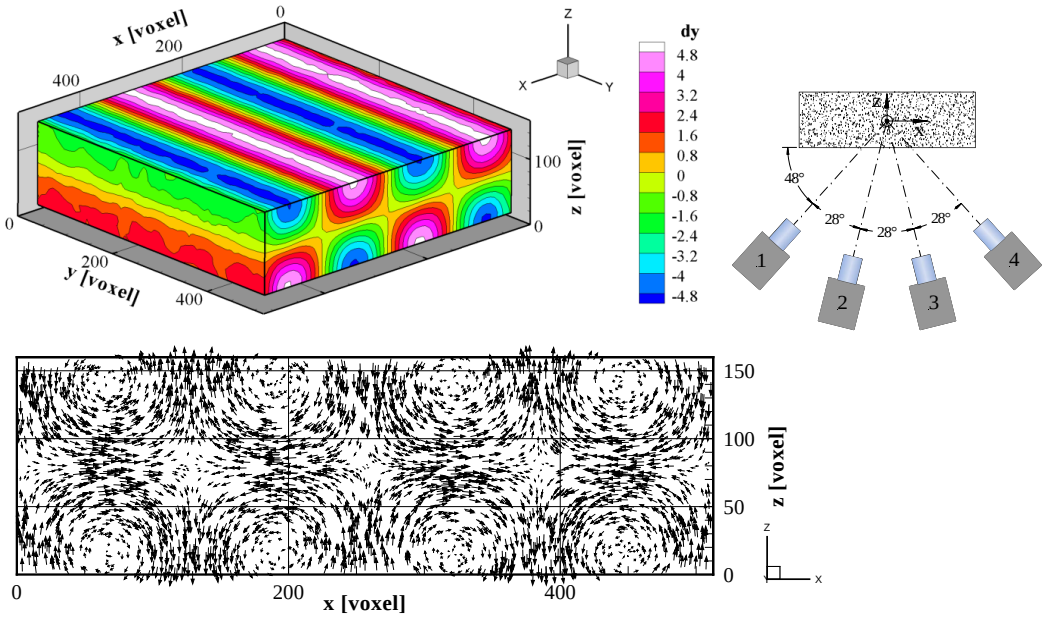

Figure 3.4: Synthetic flow field of $512 \times 512 \times 160$ voxel ($10 \times 10 \times 3$ mm) for accuracy assessment; *left:* synthetic flow field; *right:* viewing geometry

between two time steps is

$$\begin{aligned} \Delta X = &\quad A\ sin\left(\frac{2\pi}{p}x\right)\ cos\left(\frac{2\pi}{p}z\right) \\ \Delta Y = &-A\ sin\left(\frac{2\pi}{p}x\right)\ sin\left(\frac{2\pi}{p}z\right) \\ \Delta Z = &-A\ cos\left(\frac{2\pi}{p}x\right)\ sin\left(\frac{2\pi}{p}z\right), \end{aligned} \tag{3.13}$$

where A denotes the maximum displacement amplitude which was set at 5 voxel and p is the period taken equal to $0.5\,l$ where l is the edge length of the volume (512 voxel).

3.2.2 Procedure of quality evaluation

The quality of each reconstruction is assessed through several quantities:

Ghost Intensity suppression Intensity and number of reconstruction ambiguities (so-called 'ghost particles') is compared against the number and intensity of valid particle positions using histograms. Particle reconstructions consist of clusters of multiple voxel. Thus, the intensity near valid positions

is evaluated within a elliptical region around the valid position. The diameter of this region is set to the particle image diameter of 3 voxel in x, y and to 4.5 voxel in z. The larger diameter along volume depth was chosen to encounter the oblique viewing of the cameras which elongates the reconstructed particle shape in z direction according to Eq. (2.11). Subsequently, the true region diameters are used to calculate 3-D binary masks in order to distinguish between ghost and true intensities. After masking, the mean intensities of ghost particles are obtained by 3-D segmentation. Connected component labeling of true and ghost intensities (IDL routine *label_region*) enables the statistical evaluation of average intensities per voxel of each single 3-D blob.

Reconstruction signal-to-noise ratio Ghost particles can occur outside the particle volume at ambiguous intersections of lines of sight. Thus, on the basis of intensity profiles, the spatially averaged intensity level outside the particle volume border is evaluated against the signal strength inside the particle volume to obtain a rough indicator of the reconstruction signal-to-noise ratio (c.f. [136]).

Quality factor The reconstruction quality and convergence is assessed by the degree of correlation between synthetic volume (ground truth) and reconstruction. The ground truth volume consists of 3-D Gaussian particles each with 3 voxel diameter (equal to particle image diameter). The degree of correlation is computed by means of the normalized cross-correlation coefficient also referred to as quality factor or reconstruction quality [42]

$$Q = \frac{\sum\limits_{j \in N_j} E_j \, G_j}{\sqrt{\sum\limits_{j \in N_j} E_j^2 \sum\limits_{j \in N_j} G_j^2}}, \tag{3.14}$$

where E_j and G_j denote the reconstruction respectively ground truth intensity and N_j denotes the number of voxel per interrogation volume. A quality factor of unity indicates identical volumes. At an edge size of 64^3 voxel and a step size of 32^3, in total $15 \times 15 \times 4$ positions of the reconstructed and ground truth particle field were cross-correlated and then averaged. In particular FMART tends to produce spiky particle reconstructions after a few iterations. Thus, during postprocessing a constant Gaussian smoothing with a sigma of

$0.68 \times 0.68 \times 0.1$ voxel is applied to all FMART reconstructions which maximizes the degree of correlation between the reconstruction and the ground truth.

Position accuracy of reconstructed particles As already mentioned by Schanz et al. [144], the quality factor may lead to misinterpretation if reconstructed particles are much wider or even smaller than an arbitrary selected size of the ground truth. Moreover, no statements about the position accuracy of reconstructed particles can be drawn from the quality factor. Especially in PTV and PIV, the 3-D positioning error directly influences the accuracy of a velocity measure. Thus, 3-D particle positions are additionally recovered after a 3-D local maximum detection (LocM) and 3-D segmentation of the reconstructed volume. The position is estimated from the center of mass of each segmented blob. In the present investigation, a particle is considered as true if its center falls within the radial distance of $1.5 \times 1.5 \times 1.8$ voxel around a known position. The absolute positioning errors $\delta x_p, \delta y_p, \delta z_p$ of each particle are computed from the difference between center of mass of the detected blob and the true particle position.

Accuracy of PIV displacement estimates Apart from the accuracy estimates of individual particles the accuracy of displacement estimates of particle ensembles is determined as a function of increasing particle image density. The displacement field is estimated from 3-D cross-correlation of interrogation volumes at both 'time steps' containing 10 particles. Standard 3-D cross-correlation is applied as described in Sect. 2.5. A multi-grid algorithm is used, which employs a coarse-to-fine resolution pyramid that starts at a grid size of 64 voxel and ends at a grid size ranging from $38 - 23$ voxel depending on the given global particle number density. Once the final spatial resolution is reached, volume deformation based on third-order B-splines [161] is applied twice to further improve the match between volumes and thereby improving the displacement estimates by minimizing the influence of strong displacement gradients. The deviations $\delta X, \delta Y, \delta Z$ of each displacement component bases on the absolute deviation between the measured displacement component and the analytical solution of the synthetic flow (see Eq. (3.13)) taken at the center of the interrogation volume. Global error distributions of velocity estimates are computed over all interrogation boxes excluding boundary cells.

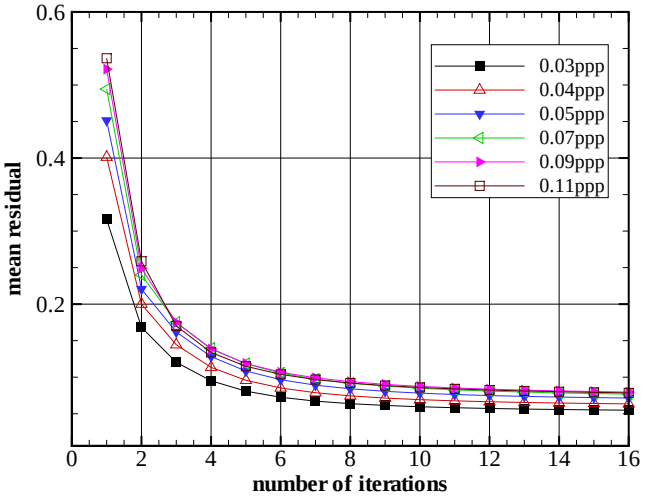

Figure 3.5: Convergence of the multiplicative intensity correction for FMART at various particle image densities

3.3 Results

3.3.1 Required number of iterations

Prior to evaluation of the reconstruction accuracy of each algorithm, the appropriate number of iterations was determined to ensure convergence. Fig. 3.5 shows the mean intensity update factor for FMART, which is obtained by averaging the multiplicative corrections P_j (defined in Eq. (3.9)) over all active voxels at each iteration. Depending on the particle image density, FMART requires 4-8 iterations until the mean multiplicative intensity update reduces to $5 - 10\%$.

In order to have a joint basis of assessment, the iterative performance of all tested algorithms is compared by the degree of correlation between reconstruction and ground truth. Therefore, the evolution of the quality factor Eq. (3.14) or 'reconstruction quality' [42, 8, 162] is computed.

Fig. 3.6 presents a comparison of the reconstruction quality of FMART, MENT and MLOS-SMART with increasing number of iterations at particle image densities ranging from $0.03 - 1.13$ ppp. For particle image densities of 0.03, 0.05 and 0.07 ppp, FMART reaches a maximum correlation coefficient of 0.98, 0.95 and 0.94 after 4, 7 and 10 iterations. Further iterations decrease the correlation coefficient because FMART tends to reduce the diameter of reconstructed blobs with increasing number of iterations. This leads to more and more spiky

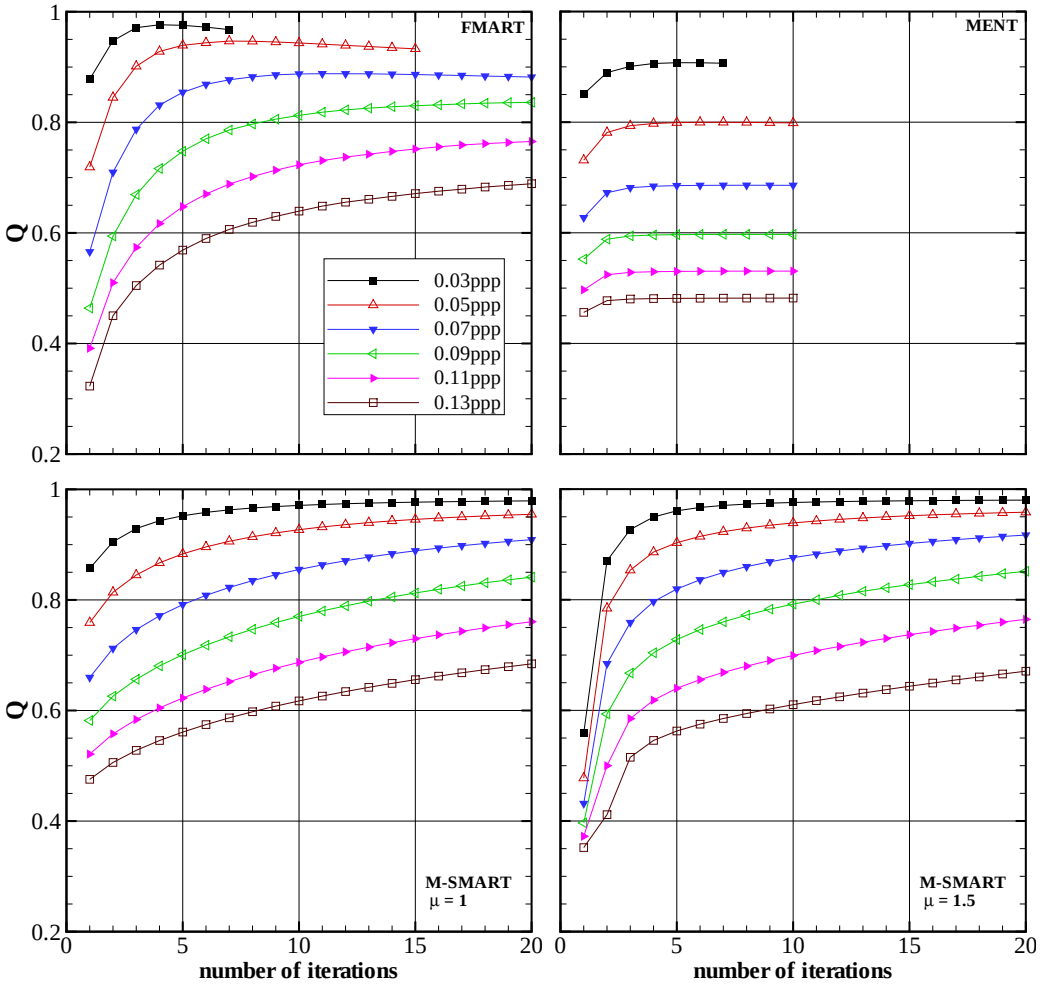

Figure 3.6: Evolution of the reconstruction quality Q over the number of iterations; *top left:* FMART ($\mu = 1$), *top right:* MENT, *bottom left:* MLOS-SMART($\mu = 1$); *bottom right:* MLOS-SMART ($\mu = 1.5$)

particle reconstructions which have a smaller diameter compared with the ground truth. A similar curve of convergence of MART was published by Thomas et al. [162] for particle images of a diameter of 6 pixel, a circular camera viewing geometry and a particle image density of 0.05 ppp. The authors found MART to reach its maximum reconstruction quality after 8 iterations ($q_{max} = 0.955$) and to decrease slightly at further iterations.

The convergence of MLOS-SMART is shown in Fig. 3.6 (bottom). An increase of the relaxation parameter from 1.0 to 1.5 leads to a higher iterative performance after $2-3$ iterations but only minor improvements of the reconstruction quality in a nearly converged state at 20 iterations. Moreover, at a maximum

particle image density of 1.3 ppp the reconstruction quality of MLOS-SMART oscillates within the first two iterations for $\mu = 1.5$. If the relaxation parameter value is slightly increased, the algorithm diverges severely. After 20 iterations, MLOS-SMART yields a reconstruction quality similar to FMART with correlation coefficients of 0.98, 0.96 and 0.92 at particle image densities of 0.03, 0.05 and 0.07 ppp. MENT (see Fig. 3.6 top, left) exhibits no further improvements of reconstruction quality after 4 iterations and the correlation coefficient in general is considerably lower than for FMART or MLOS-SMART. This indicates a weak ghost suppression in comparison to both other techniques.

Elsinga et al. [42] used a cut-off value of $Q = 0.75$ to decide whether a reconstruction is considered sufficiently accurate in terms of ghost intensity suppression. Based on this cut-off value a particle density limit can be estimated in the absence of additional error sources and if only noise from ghost particle is considered: The limits are 0.05 ppp for MENT and 0.11 ppp for both FMART and MLOS-SMART.

If not stated otherwise within this chapter, the number of iterations is adjusted in accordance with Fig. 3.6 and in such a way, that the correlation coefficient is maximized but the number of iterations does not exceed 20 for FMART and MLOS-SMART and does not exceed 5 for MENT.

3.3.2 Ghost intensity suppression

Fig. 3.7 shows an exemplary comparison of the particle field reconstruction within a single $x-z$ slice obtained from MENT, FMART and MLOS-SMART at a particle image density of 0.03 ppp. The upper left slice indicates Gaussian regions around particle positions which are accepted as true and of which binary masks were computed to distinguish between ghost and valid particle. The top row shows the reconstruction which is divided into valid particle positions (middle row) and ghost particle (bottom row) using those binary masks. The MENT reconstruction contains more ghost particles in comparison with FMART or MLOS-SMART which both exhibit a strong noise suppression. The FMART reconstruction shows more spiky blobs and slightly more ghosts than MLOS-SMART. On the other hand, the MLOS-SMART reconstruction

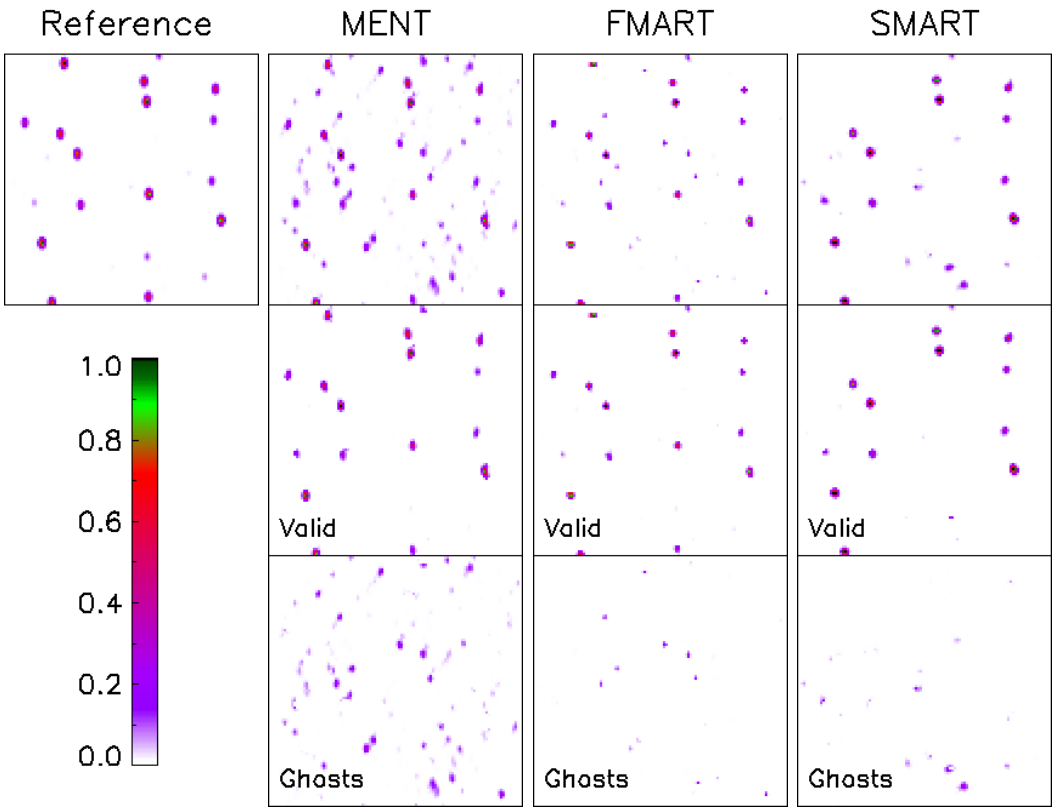

Figure 3.7: Region of $100 \times 1 \times 100$ voxel of a single x-z slice at a particle image density of 0.03 ppp ; *top:* Ground truth and reconstruction, *middle:* valid particle positions, bottom: ghost particles

seems incapable of recovering all valid particles in comparison to the reference.

In order to obtain a more quantitative comparison of ghost suppression, histograms are built, involving the distribution of the mean intensity per voxel over all reconstructed blobs. The intensities are standardized to the average intensity per voxel of all valid blobs and counts are standardized to the total number of valid blobs found.

Fig. 3.8 compares intensity distributions of a MENT reconstruction to that of a single pass MLOS reconstruction (so-called direct reconstruction). In contrast to MLOS, the valid intensity distribution obtained with MENT does not overlap with the ghost intensity distribution. MENT exhibits a trend to reduce ghost intensities and to form a Gaussian-like distribution of valid blob intensities in the histogram. This behaviour is observed for all tested algebraic reconstruction techniques and has also been reported in literature

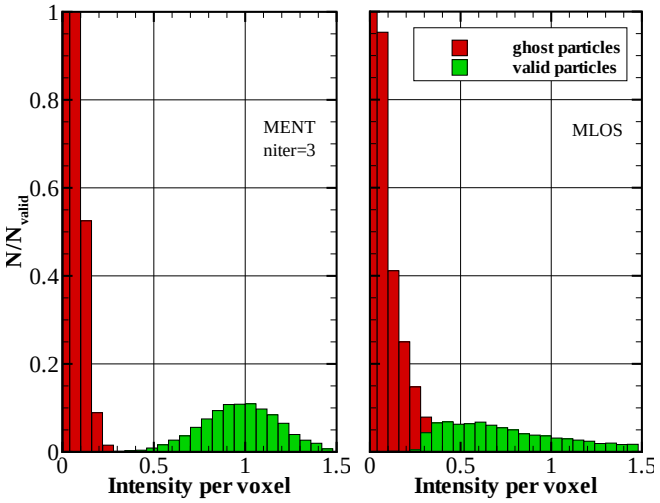

Figure 3.8: Mean blob intensities of true and ghost particles at a moderate particle image density of 0.03 ppp; left: MENT, right: MLOS

(c.f. results of PIV challenge case 'C' [81]). In contrast, MLOS exhibits wide and overlapping intensity distributions for both valid and ghost particle.

Fig. 3.9 compares intensity distributions obtained with MENT (top), FMART (middle) and MLOS-SMART (bottom) from images containing intermediate particle image densities of $D_I = 0.06\,\text{ppp}$. With such high image densities, MENT is not able to iteratively refine the intensity distribution of true particles by means of improving the signal. This is probably because MENT builds the integral sum of voxel intensities along their projection or epipolar line instead of summing the integral directly along each line of sight (see Eq. (3.7)). Those 2-D epipolar lines intersect more frequently at high particle image densities leading to incorrect results. If the number of iterations increase, both FMART and MLOS-SMART show a narrowing of intensity distributions of valid particles while the intensity of ghost particles is more and more reduced. After 10 iterations FMART begins to exhibit a slightly narrower intensity distribution of valid particles in comparison with MLOS-SMART. This is probably because FMART particle reconstructions are slightly more spiky (as also visible in Fig. 3.7) in comparison to MLOS-SMART. On the other hand, MLOS-SMART shows a better ghost intensity suppression in comparison to FMART. For example, a comparison of intensity distributions at 10 iterations (see Fig. 3.9, middle) reveals four times more ghost particles for FMART in comparison to MLOS-SMART within the interval $0.06 - 0.12$. In turn, the MLOS-SMART reconstruction suppresses a fraction of valid particles (about 5%) which is, to some extent, also visible in Fig. 3.7.

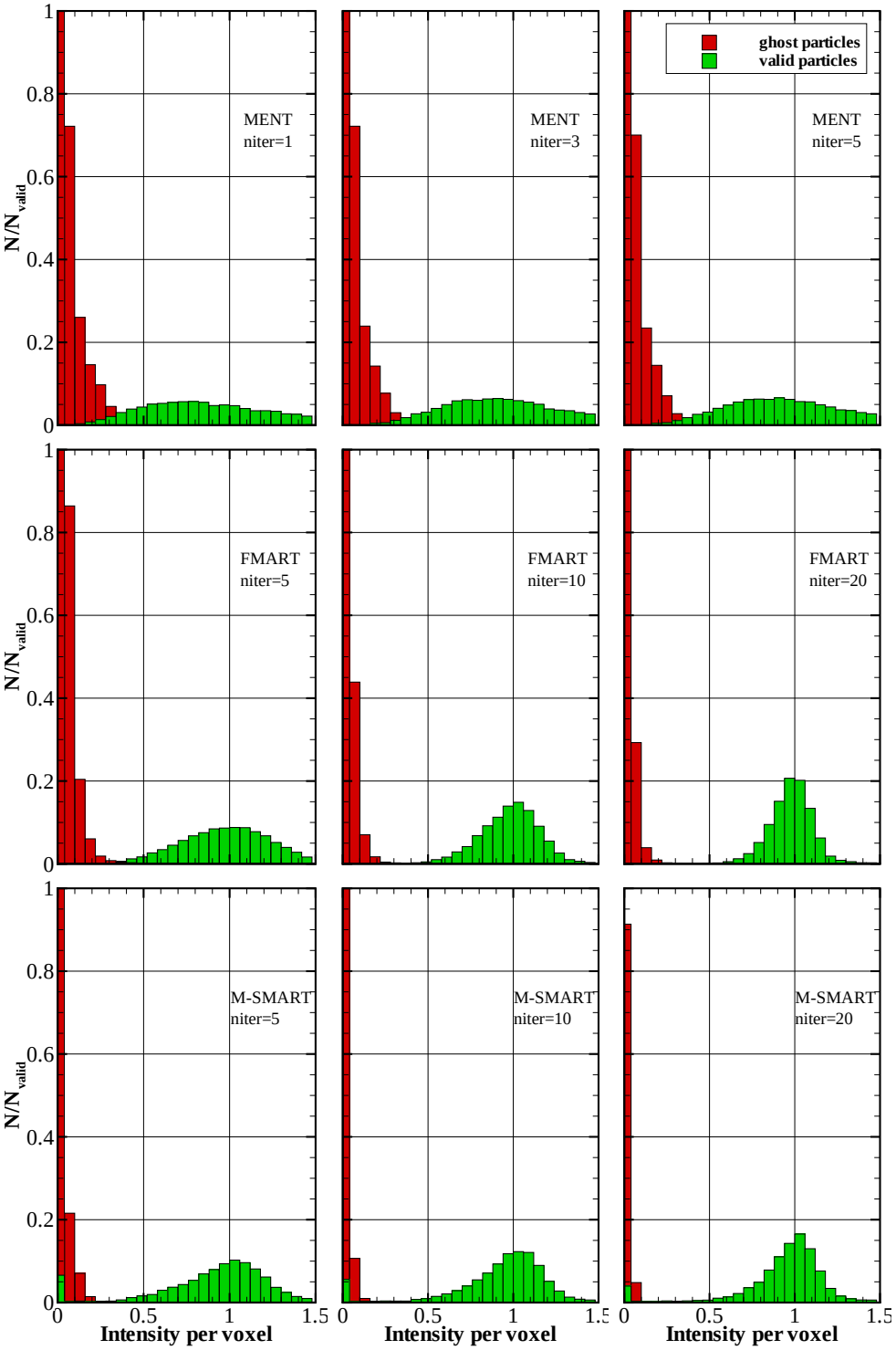

Figure 3.9: Intensity distributions of valid and ghost particles with increasing number of iterations at a particle image density of 0.06 ppp; *top*: MENT, *middle*: FMART; *bottom*: MLOS-SMART

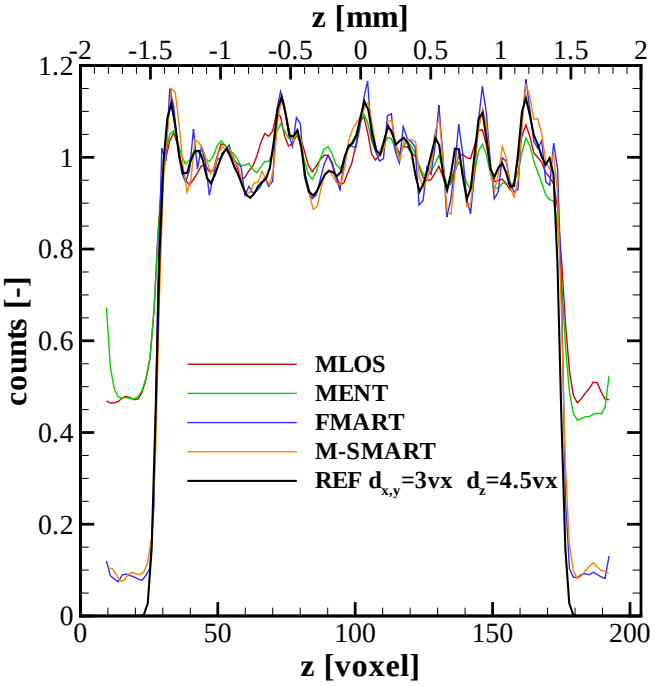

Figure 3.10: Normalized intensity within a slice of $400 \times 400 \times 1$ voxel obtained from reconstructions of synthetic particle images at a density of 0.06 ppp and from a reference volume containing Gaussian blobs at valid positions

The reconstruction signal-to-noise ratio (RSNR) can be obtained from Fig. 3.10, which shows a z-profile of the normalized intensity within slices of $400 \times 400 \times 1$ voxel obtained from reconstructions of synthetic particle images at $D_i = 0.06$ ppp. The noise level is gathered from regions which lay immediately outside of the synthetic particle volume ($z > |\pm 1.8|$). As shown in Fig. 3.10, the RSNR is equal to 2.17 for MLOS and MENT and significantly improves if techniques as FMART or MLOS-SMART are applied. For both techniques the RSNR is approximately 11.

Fig. 3.11 presents the evolution of number and intensity of valid and ghost particles with increasing seeding density for FMART. For the present numerical setup, the number of ghost particles grows approximately quadratic in the range 0.03-0.09 ppp. The relative amount of ghost particle with respect to valid particle is about 2.9 at a image density of 0.05 ppp and rises strongly towards 5.0 at a particle image density of 0.1 ppp. On the other hand, the mean intensity of valid particle reconstructions with regard to the intensity of ghost particle is about 20 times larger at 0.05 ppp and at least 12 times larger at 0.1 ppp. To what degree the noise contribution of ghost particles affects the accuracy of velocity measurements is evaluated in the next section.

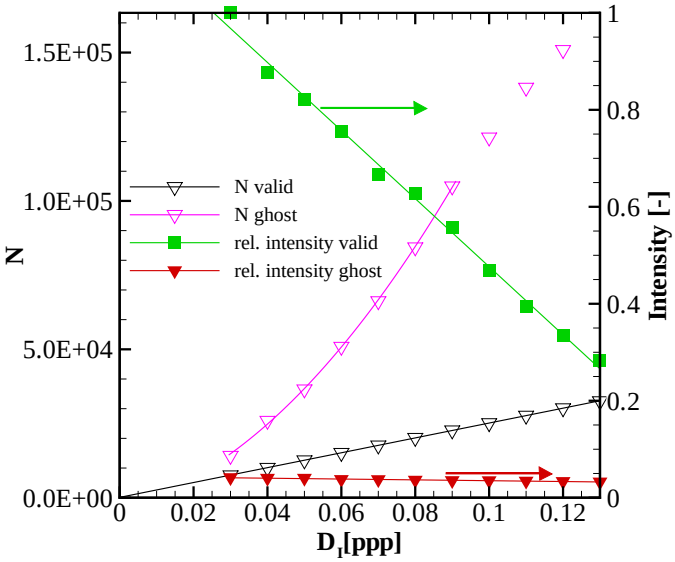

Figure 3.11: Amount and intensity of valid particles and of ghost particles as a function of particle image density for FMART; a quadratic increase of ghost particle is indicated by the fit

3.3.3 Accuracy of particle position and of displacement recovery

So far, the previous section has described the noise contribution of ghost particles at various particle number densities. Now the question arises to what extent the accuracy of particle position estimates is reduced as the number of ghost particle increases. Fig. 3.11 indicates, that the occurrence of ghost particles increases quadratically with increasing image density while the signal, namely the intensity of valid particle, decreases. This signal loss has influence on the position detectability. Fig. 3.12 presents the positioning error of reconstructed particles obtained by volume segmentation whereby the sub-voxel position is calculated through the center of mass of each reconstructed blob. The varying width of the error distributions in $\delta x_p, \delta y_p, \delta z_p$ stems in particular from the specific viewing geometry causing different spatial extensions of the reconstructed blobs. Back-projection of particle images does not preserve their circular shape which is primarily due to the viewing geometry and the limited number of projections. Thus, the back-projected reconstructed blobs are slightly elongated along x. Furthermore, particle reconstructions are elongated along volume depth z due to the limited viewing aperture of the system (as described in Sect. 2.5). Thus, at a particle image density of 0.05 ppp, the fluctuations of the y-position are the lowest ($y_{RMS} = 0.207$ voxel) while the RMS values for x ($x_{RMS} = 0.238$ voxel) and z-position ($z_{RMS} = 0.207$ voxel)

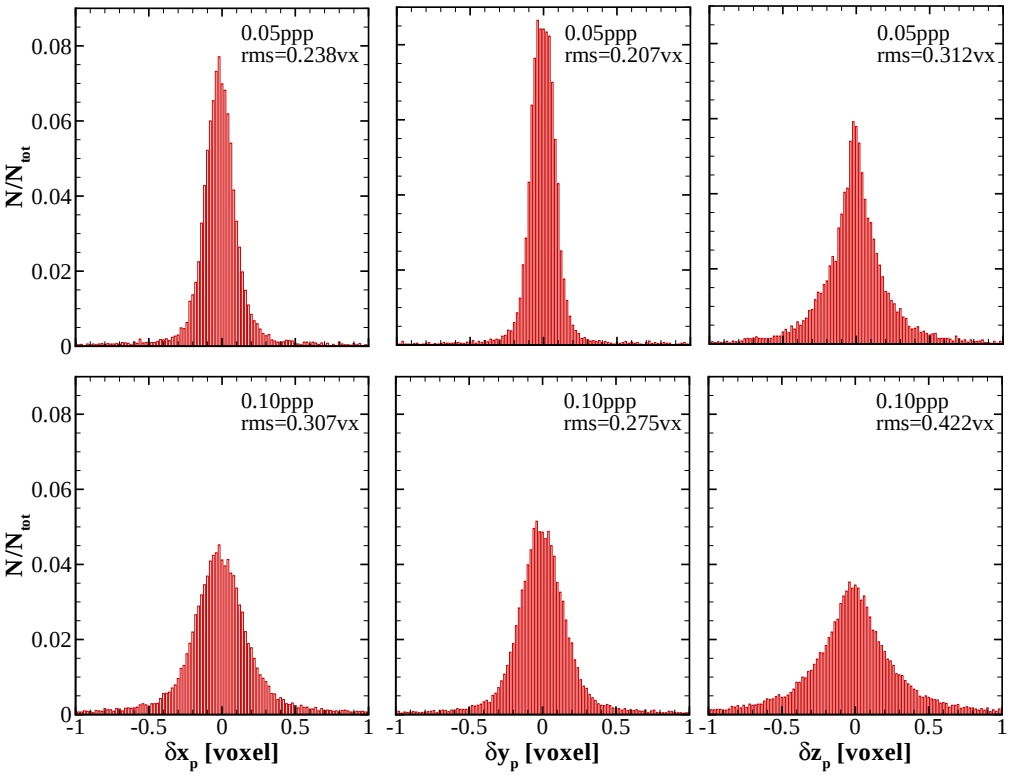

Figure 3.12: Global PDFs of the absolute deviation between the true particle position and the center-of-mass of each reconstructed blob for FMART; *top*: 0.05 ppp; *bottom*: 0.10 ppp

are 15% respectively 50% larger. A doubling of the particle image density from 0.05 ppp to 0.1 ppp decreases the signal at each particle position and thus increases the positioning error, here by $29 - 35\%$.

At 0.05 ppp the positioning error along x and y is comparable to the mean positioning error of 0.21 voxel for tomographic PIV and MART, reported by Wieneke [178] for a square-like viewing geometry, whereby the paper neither provides information on the absolute error components $\delta x_p, \delta y_p, \delta z_p$ nor the sub-voxel detection type. Furthermore, the present source density at 0.05 ppp is $N_s = 0.35$ ($d_i = 3$ pixel) while simulations reported by Wieneke were based on a lower source density of $N_s = 0.16$ ($d_i = 2$ pixel, $D_i = 0.0512$ ppp). Wieneke also reports a higher mean positioning accuracy for the iterative particle reconstruction (IPR) of 0.17 voxel, indicating that particle based reconstruction (see Sect. 2.4.4) can further improve the particle positioning accuracy.

The dependency of the position error on the discretization level of weights

(Eq. (3.10)) has been investigated additionally at $D_I = 0.05$ ppp for FMART. For this purpose, the weighting coefficients w_{ij} were computed at sub-pixel increments ranging between 1/10th and 1/100th of a pixel. To a sub pixel accuracy of 1/40th pixel and finer the positioning error did not deviate more than ± 0.001 voxel. Thus, for all tests, a sub-pixel accuracy of 1/50th of a pixel was applied.

Although relevant for 3-D particle tracking, the positioning error of single particles does not apply directly if displacements are evaluated by cross-correlation of small interrogation volumes at two time steps. Thus, the error of displacement estimates, as evaluated with classical TPIV, will be discussed next.

The particle displacement field of the previously described synthetic flow field is evaluated by 3-D cross correlation of both time steps of the synthetic flow field using small interrogation volumes (see Sect. 3.2). At each image density the interrogation volume size has been adjusted to contain on average 10 particles. Hence the interrogation volume size decreases with increasing number density. The sub voxel peak detection is implemented using a three-point Gaussian peak fit [185]. Fig. 3.13, top, shows the noise-free displacement field (red) and the displacement field obtained from FMART reconstructions (black) at 0.05 ppp. Fig. 3.13, middle and bottom compares the differences of both vector fields at 0.05 ppp and at 0.10 ppp. The latter exhibits partially larger displacement error magnitudes, but clearly below 0.5 voxel while the maximum displacement amplitude was set at 5 voxel. Bias errors due to ghost-particles become visible in the differential vector field, indicating coherent motion of those reconstruction ambiguities. In contrast, a merely statistical displacement error would result in a fully random difference vector field. The bias error occurs if the ghost particle correlation signal interferes with that of the actual particles (see Atkinson et al. [7] and Scarano [136]). When present, underestimation of velocity gradients can occur. The error source, namely ghost particles, is inherent to the tomographic reconstruction approach in general but might be more or less severe depending on the applied algorithm. Thus, probability density distributions are computed over the entire flow field in order to quantify the displacement error of FMART, MENT and MLOS-SMART reconstructions.

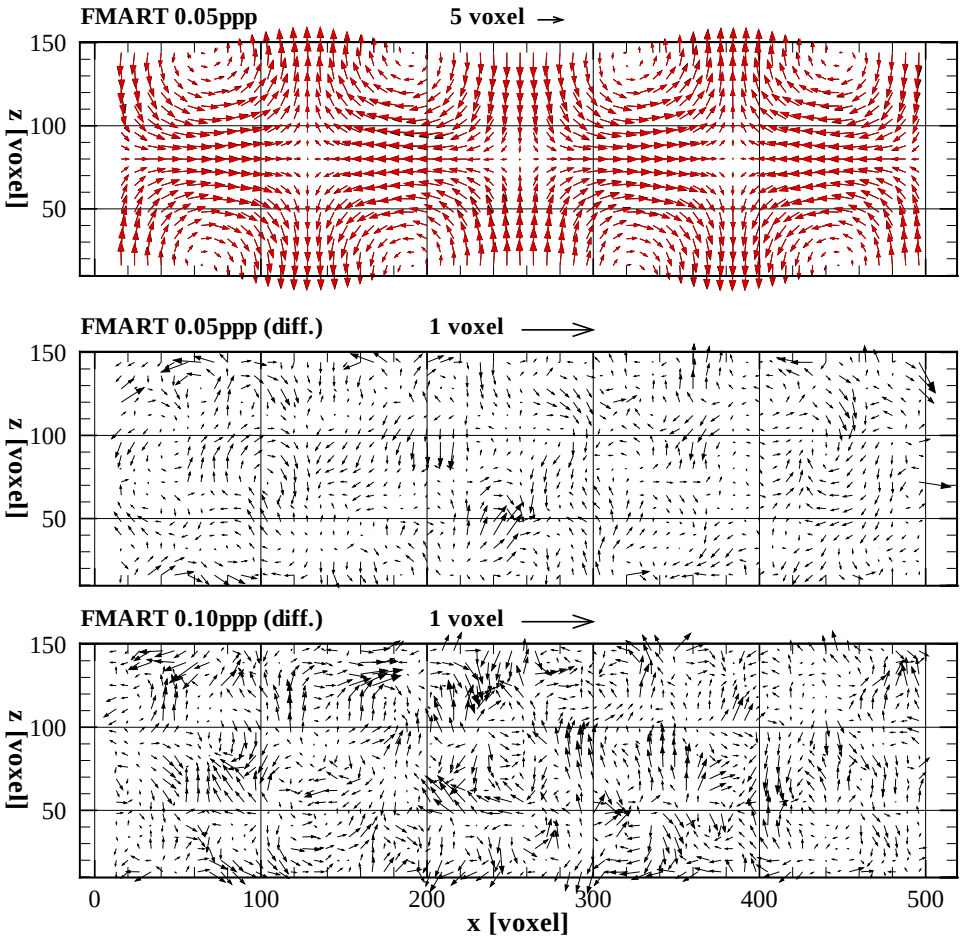

Figure 3.13: Displacement components in x and z and differences between FMART and the noise free ground truth within a single slice located at $y = 128$ voxel ; *Top:* FMART (*black*) and ground truth (*red*) at 0.05 ppp; *Middle:* differences at 0.05 ppp; *bottom:* differences at 0.10 ppp

Fig. 3.14 presents a comparison of the probability density distributions of displacement estimates at 0.05 ppp for the noise-free ground truth (green) and each tested reconstruction technique (red). The error distributions δX, δY and δZ are computed from the absolute deviation between the cross correlation result and the analytical solution of the flow field at the 3-D position of each interrogation volume (see Eq. (3.13)). The reference (see Fig. 3.14, top) is obtained from cross-correlation of two time-steps of the noise free ground truth using the same interrogation volume size and grid spacing as for the reconstructions. These reference distributions partially involve bimodal distributions in δX and δZ. The reason for this deviation from a bell-shaped curve

is probably the presence of large velocity gradients along x and z where Taylor-Green vortices are present (see Fig. 3.4). In these vortex regions, where the velocity frequently exhibit large variations within the interrogation volume, a systematic under- or overestimation is observed. However, bimodal distributions are less evident and hardly noticeable in the error distributions from the reconstructions, which is probably due to the presence of additional noise. The y -component shows the smallest error due to the absence of strong shear in the helical displacement field. MENT exhibits the highest displacement due to the weakest ghost intensity suppression. Cross-correlation results obtained from FMART and MLOS-SMART reconstructions indicate a almost similar accuracy for displacement components along x and z.

Fig. 3.15 presents the evolution of the Global RMS error over all displacement estimates in the measurement domain as a function of the particle image density. The RMS values obtained from cross-correlation of the noise-free ground truth are indicated as dashed lines delineating the accuracy limit. The error of the displacement magnitude, is shown additionally. Although MLOS-SMART performs slightly more accurate up to moderate image density of 0.05 ppp, the algorithm seems to be slightly less accurate at higher particle image densities. Especially the uncertainty of the z-component grows faster in comparison to FMART for particle image densities above 0.05 ppp. For example, the RMS values of the displacement magnitude at 0.05 ppp respectively 0.10 ppp are 0.10 and 0.14 voxel for MLOS-SMART and 0.12 and 0.13 voxel for FMART. At similar particle image densities, MENT is less accurate and reaches errors of 0.14 and 0.25 voxel for the displacement magnitude.

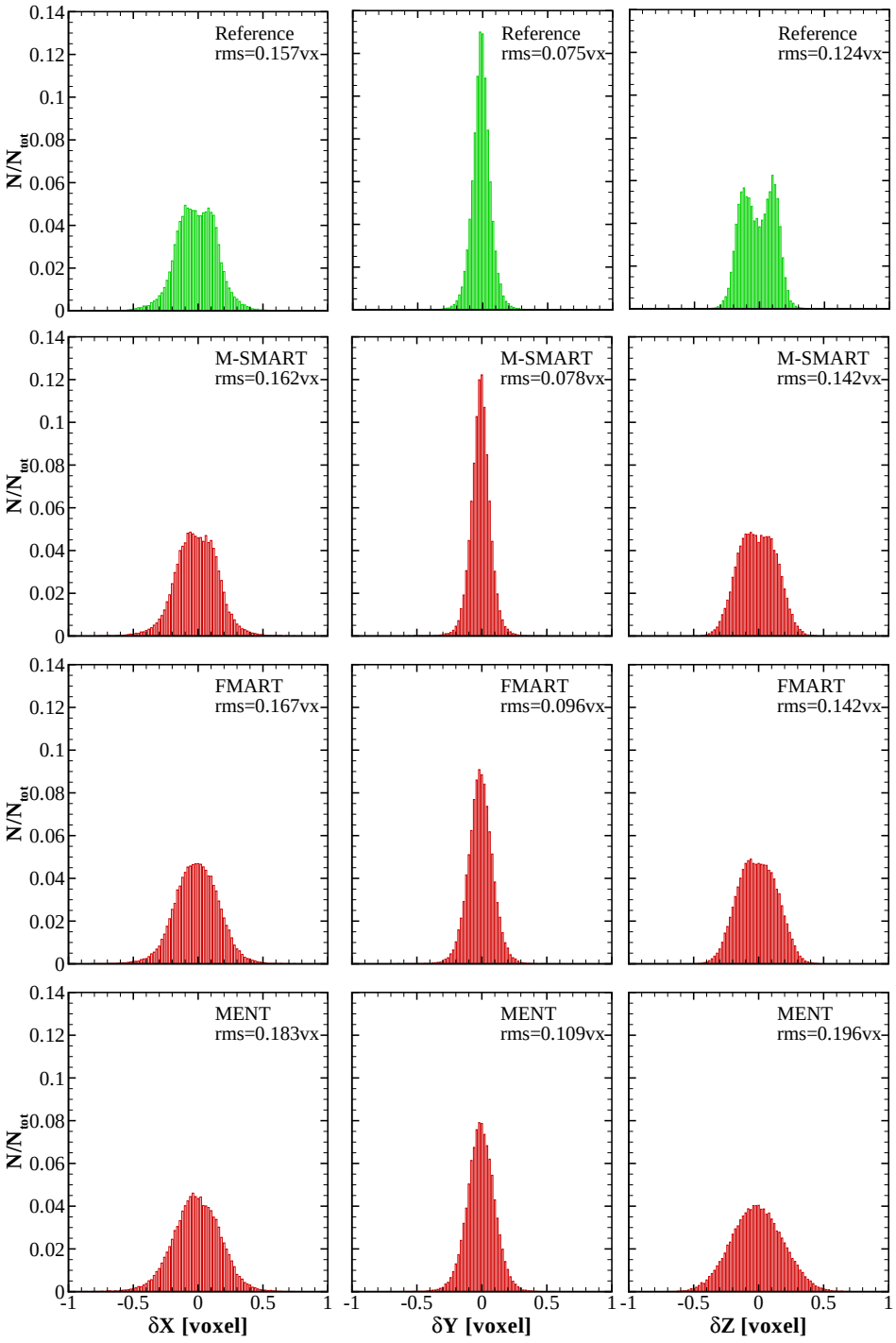

Figure 3.14: Global PDFs of the absolute deviation between displacement estimates by TPIV and the synthetic flow field ($D_I = 0.05$ ppp, 10 particles per interrogation volume); *from top to bottom:* Reference obtained from cross-correlation of ground truth (*green*); MLOS-SMART; FMART; MENT

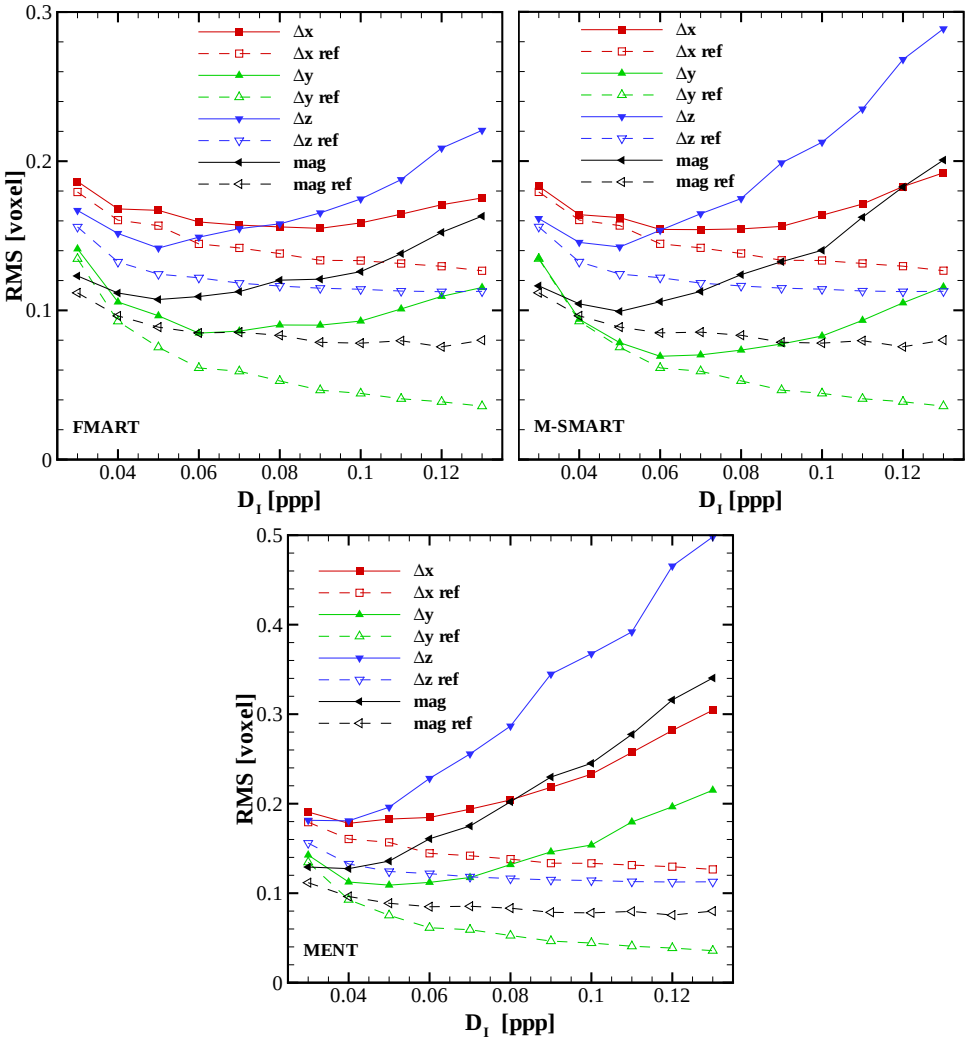

Figure 3.15: Evolution of the global RMS error of TPIV and of the noise free ground truth (ref) for interrogation volumes containing 10 particles; *top left:* FMART; *top right:* MLOS-SMART; *bottom:*MENT

3.3.4 Reconstruction speed

As part of the overall assessment of 3-D reconstruction methods the computation time of particle field reconstructions is evaluated. Tests are performed on a windows server workstation containing 24 GByte RAM and two Intel Xeon E5645 CPUs with 12 physical cores running at 2.4 GHz. Time measurements are averaged over 20 computations and are provided excluding the time needed for particle volume storage.

Fig. 3.16 presents the computation time as a function of particle image den-

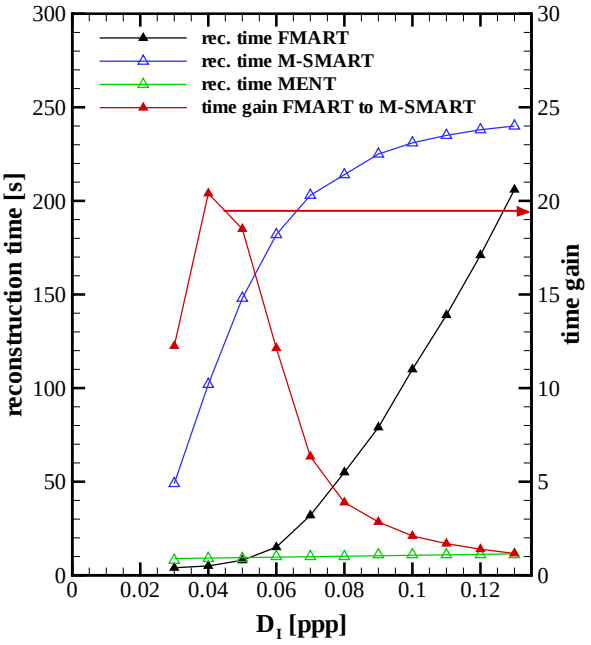

Figure 3.16: Computation time as a function of particle image density for particle volume reconstructions obtained with FMART, MLOS-SMART and MENT

sity for the previously described synthetic four camera setup. During this particular evaluation, the number of iterations is adjusted in such a way, that the correlation coefficient is maximized but the number of iterations does not exceed 20 for FMART and MLOS-SMART. At a particle image density of 0.04 ppp FMART reaches its maximum time gain relative to MLOS-SMART performing 20 times faster than MLOS-SMART. Moreover, the FMART reconstruction speed is at least 12 times faster than MLOS-SMART at 0.03 ppp respectively 0.05 ppp. With increasing particle image density the computation time of a FMART reconstruction approaches more and more that of a MLOS-SMART reconstruction. At high densities of 0.1 ppp FMART is still two times faster than MLOS-SMART. As the image density further increases, both algorithms require approximately the same computation time. For example, at 0.13 ppp the FMART reconstruction is only 16% faster in comparison to MLOS-SMART.

For the sake of completeness, the computation time for a MENT reconstruction is also evaluated although the previous subsection indicates less accurate displacement estimates in comparison to both MLOS-SMART and FMART. For the previously described synthetic test case, a MENT reconstruction requires $8-12$ sec depending on the particle image density (see Fig. 3.16), whereby not more than 4 iterations are conducted. Additional iterations do not improve the

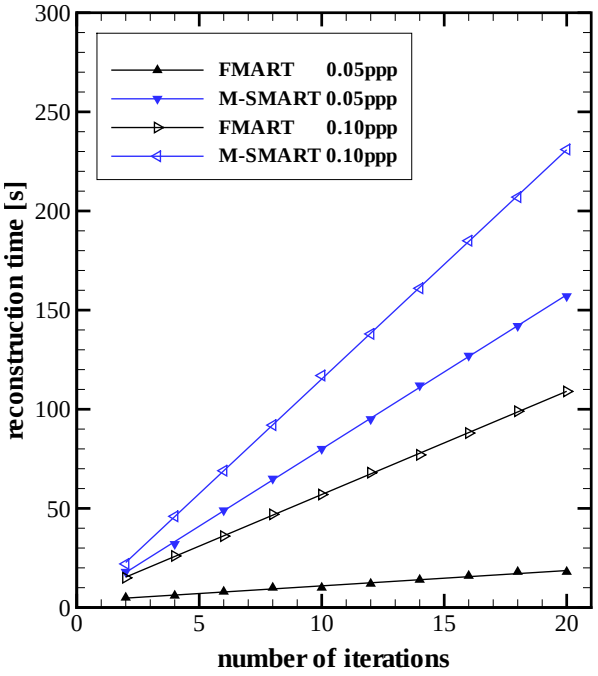

Figure 3.17: Computation time versus number of iterations for a FMART and a MLOS-SMART reconstruction at particle image densities of 0.05 and 0.10 ppp

reconstruction quality of MENT as discussed in Sect. 3.3.1. Below 0.05 ppp, FMART still performs faster than MENT. The computation time demand of MENT rises linearly with increasing particle number density at a low rate of increase. This is because MENT iteratively evaluates image intensities instead of volumetric intensities and the number of occupied pixels increases linearly until saturation while the number of occupied voxels increases quadratically (see also Fig. 3.11).

The computation time versus number of iterations is shown in Fig. 3.17. Compared to MLOS-SMART, the reconstruction speed of 10 iterations of FMART is about 8 times faster at 0.05 ppp and still 2 times faster at 0.10 ppp. At a fixed number of iterations and a fixed particle image density the computation time gain of FMART originates from the precalculation of pixel positions of each occupied voxel and possibly also from the utilization of lookup table to obtain the Gaussian weighting coefficients as described in Sect. 3.1.3.

3.4 Conclusions

In summary, it can be ascertained that particle volume reconstructions obtained with FMART exhibit a considerably stronger suppression of ghost intensity than those obtained with MENT. Reconstructions with MLOS-SMART show the strongest ghost suppression which on the other hand also rejects the intensity at a few valid particle positions.

With regard to volumetric particle tracking, the accuracy of recovered 3-D particle positions was evaluated for FMART by comparison of the center-of-mass of each reconstructed blob with its target position. The positioning error shows no dependency on the discretization level of the Gaussian weighting function from sub pixel increments smaller than 1/40th pixel. The uncertainty of the recovered particle position strongly depends on the viewing geometry and is highest for the depth position (along z). For the present viewing geometry and particle image densities between $0.05 - 0.10$ ppp, the RMS values of recovered positions in x, y and z were $0.24 - 0.31$ voxel, $0.21 - 0.27$ voxel and $0.31 - 0.42$ voxel. At 0.05 ppp the positioning error along x and y is comparable to the mean positioning error for tomographic PIV and MART, reported by Wieneke [178] for cameras in a square-like viewing geometry, whereby simulations by the author involved a 50% lower source density.

When looking at the error of the displacement estimates at intermediate particle image densities between $0.04 - 0.06$ ppp, FMART and MLOS-SMART exhibit rather similar RMS values of the displacement magnitude of 0.11 voxel and 0.10 voxel while cross-correlation of a reference containing no ghosts ('ground truth') exhibits an RMS value of 0.09 voxel. Given the maximum displacement of 5 voxel, the velocity measurement error (related to full scale) is 2.2% for FMART, 2% for SMART and 1.8% for the noise-free reference. With increasing image density the RMS of the magnitude grows faster for MLOS-SMART than for FMART which is accompanied by a higher uncertainty on the displacement z-component. At a particle image density of 0.1 ppp the RMS value of Δz is 0.17 voxel for FMART and 0.21 voxel for MLOS-SMART. The maximum entropy technique exhibits less accurate displacement fields including RMS values of Δz of 0.20 voxel at 0.05 ppp and of 0.37 voxel at 0.10 ppp.

From 0.05 ppp, the higher accuracy of FMART comes at the cost of a longer computation time compared with MENT. However, the FMART time consumption remains significantly below that of the present MLOS-SMART implementation. Depending on particle image density, the computation time required to achieve similar levels of reconstruction quality is $1.5 - 20$ times longer for MLOS-SMART in comparison to FMART. The computation time needed for 10 iterations is eight times longer at 0.05 ppp and still twice as long at 0.10 ppp of MLOS-SMART in comparison to FMART.

The results indicate that FMART is sufficiently accurate and computational efficient. Evaluation of FMART on the basis of experimental data is provided in Chap. 5 where tomographic PIV is applied in the high-speed flow of a transonic cascade wind tunnel.

Chapter 4

Studies on imaging and seeding in a transonic cascade

This chapter describes the first PIV implementation in the Transonic Cascade Wind Tunnel (TGK) at DLR Köln. In order to enable PIV, several improvements had to be made with respect to earlier laser velocimetry applications in the wind tunnel. These efforts are of direct use for the implementation of tomographic PIV in the facility and therefore presented here. Parts of the findings and results presented in this chapter enabled experimental studies of the transonic flow around the fan blade of an existing turbo fan engine to investigate the effect of leading edge deterioration. These studies are published in Experiments in Fluids [196].

Tracer particles are essential for PIV and their response time and size are of significance when applying the technique in transonic flows. The tracer particle should exhibit a fast response in order to follow sudden flow changes around edges or across shocks. Fast response times require small particles of a low Stokes number which on the other hand exhibit poor Mie scattering respectively a week PIV signal. This latter point is particularly problematic in TPIV where lens apertures need to stopped down in order to increase image sharpness at the cost of light-sensitivity.

The chapter is arranged as follows: The first section introduces the Transonic Cascade Wind Tunnel (TGK) facility. The second section describes the imple-

mentation of a PIV light-sheet probe and a seeding injection device for PIV. The third section of this chapter is dedicated to determining the particle time response on the basis of PIV data. Based on the response time the average droplet diameter is estimated using a modified version of the Stokes' drag law. The last section of this chapter describes a TPIV mock up setup to assess laser power requirements of the most suitable viewing geometry which maximizes the field of view with respect to a sufficient range of viewing angles.

4.1 The transonic cascade wind tunnel (TGK)

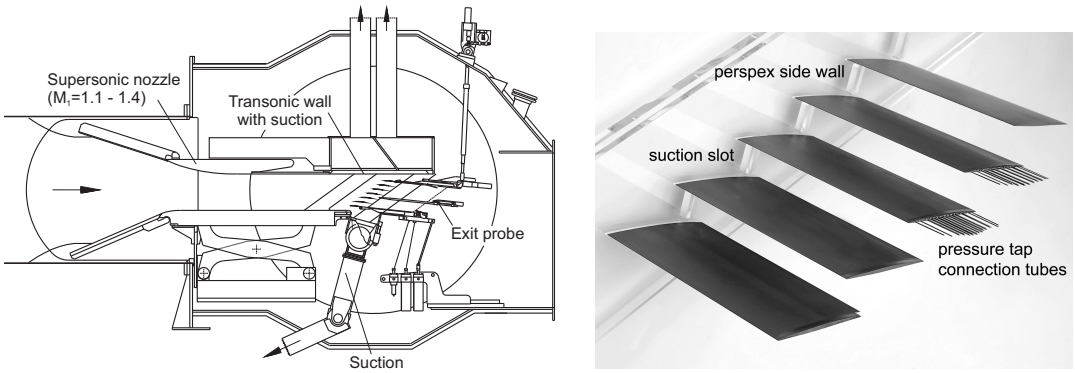

Figure 4.1: *Left*: The transonic cascade wind tunnel (adopted from [69]); *Right*: Cascade model (span=168 mm)

The facility (Fig. 4.1) is used to investigate the aerodynamic performance of turbomachinery compressor blade geometries. The incoming flow passes through a straight cascade of airfoils representing a portion of a ring of an actual blade row in an axial compressor or fan. The cascade blades are supported by side walls made of acrylic glass which provides suitable optical access for schlieren visualization and laser-two-focus velocity (L2F) [147] as well as tracer based shock visualisation (TSV)[55]. The test section has a span width of 168 mm and a variable height of $150 - 330$ mm. The inflow angle can be adjusted in a range between 80 and 160 degrees. A variable rectangular nozzle enables an inlet Mach number range of 0.2 to 1.4. Continuous operation in a closed loop allows a Reynolds number variation independent of the Mach number by adjustment of the total pressure and total temperature. Due to this flexibility, a wide range of cascade configurations can be tested [69].

Additional boundary layer suction capacities of the facility allow the control of the side wall boundary layer in front of the cascade test section, in the upper and lower bypass channels as well as on the upper and lower end walls. By controlling the latter, a homogeneous inflow representative of an "infinite blade cascade" can be achieved. In addition, suction slots in between the blades provide control of boundary layers on the side walls within the cascade passage. This allows the adjustment of specific axial velocity density ratios (AVDR) (c.f. [34]) at a controlled constriction to suppress or even enhance secondary flow effects. The throttle system is combined with two tailboards hinged to the trailing edges of the outermost blades.

The traversal of a combined 3-hole and static pressure probe in the wake allow measurements of exit flow conditions. During operation of the channel passage-to-passage flow periodicity is verified by traversing the wakes at mid span over the three middle passages as well as by measurement of the static pressure distribution across the inlet and outlet measurement plane. Additional static pressure tabs located at mid span on the suction and pressure sides of the middle airfoil enable the monitoring of the chord-wise pressure and isentropic Mach number distributions. Finally, the flow conditions are adjusted according to specific Mach number distributions on the airfoils pressure and suction side as described in [159] and [195].

4.2 Implementation of 2-C PIV

The wind tunnel geometry imposes a number of restrictions for the placement of cameras and a light sheet. The existing optical access was originally designed for optimal schlieren imaging such that additional access is required for the introduction of the light sheet normal to the viewing axis. This is realized by introducing a light sheet probe about 550 mm downstream from the cascade as illustrated in Fig. 4.2. The position of the PIV light sheet probe downstream of the trailing edge of the middle cascade passage is chosen to minimize disturbances of the flow in upstream direction. Before entering the probe the laser-beam is expanded with a lens doublet to roughly the inner tube diameter of 14 mm. This doublet also focuses the light sheet waist through the

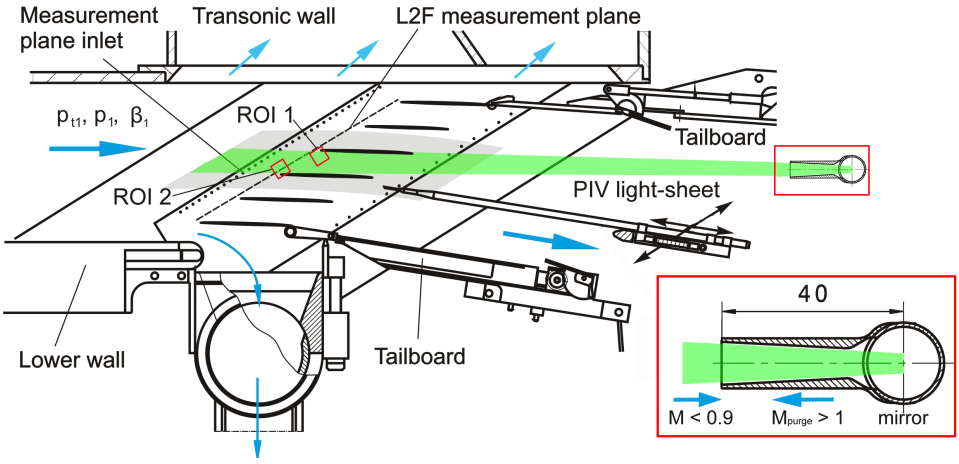

Figure 4.2: Light-sheet orientation and Laval nozzle contour of the probe tip

tube at an overall distance of 1 m. Within the viewing area the sheet thickness is 0.5 mm at $1/e^2$ intensity level and has a light sheet height of about 30 mm.

As the light-sheet probe is introduced downstream of the trailing edge, small cascade deflection angles at transonic configurations lead to a high aerodynamic loading of on the probe at high Mach numbers ($M_2 = 0.9$). First attempts have shown that the tunnel flow carries significant amounts of rust particles whose high momentum and abrasive nature leads to a fast erosion of the reflective coating on the 90 degree turning mirror at the tip of the light-sheet probe. As a consequence the light-sheet quality rapidly deteriorates to the point at which reliable PIV measurements are no longer possible. In order to improve the protection of the mirror surface from incoming particles (rust) the probe tip was retrofitted with a Laval nozzle (see Fig. 4.2) whose supersonic flow decelerates and deflects incoming particles. The inner contour of the nozzle is designed to match the beam shape. With this modification in place, PIV measurements can be performed for hours of continuous operation of the cascade wind tunnel operation without noticeable damage to the mirror.

Laser energy of 25 mJ per pulse provides sufficient light scattering from the sub-micrometer particles by producing particle images with a signal of approximately 900 counts of 14 bit dynamic range (16000 counts). The camera (PCO AG, pco.2000) is equipped with an $f = 180$ mm lens at an effective f-number of 9.2 (M=0.66, nominal $f_\# = 5.6$) and observes tracer particles in a classical normal viewing arrangement (see Fig. 4.3).

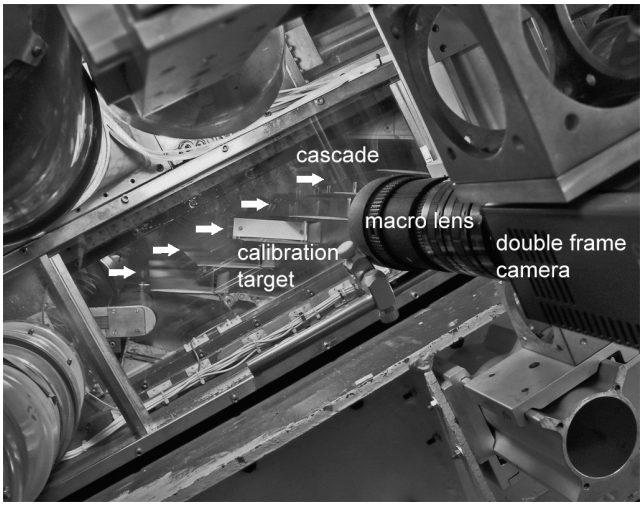

Figure 4.3: PIV double frame camera orientation, flow direction as indicated

Previous laser-2-focus measurement campaigns [147] employed a local stream-tube seeding in the form of the injecting the aerosol through a lance placed on the streamline upstream of the measurement area. This had the advantage of reduced window pollution by reducing droplet deposits to a minimum during a wind tunnel run. Closer investigation of acquired PIV images obtained in the wake of the seed probe resulted in irregular concentration distribution of the aerosol seeding. As a consequence regions of low particle density led to numerous spurious velocity vectors requiring extensive post-processing to avoid their unwanted contribution in subsequent statistical analysis of the acquired velocity data.

In an effort of improving the global seeding homogeneity a seeding injection rake of $300 \times 300\,\mathrm{mm}^2$ is installed within the settling chamber downstream of the diffusor screens about 3 m upstream of the test section. This ensured a more homogeneous distribution of the particles over a larger area and guaranteed a higher probability of sufficient and temporally constant tracer densities in the measurement domain even if the wake of the rake fluctuates temporally. With this configuration number densities of 6-8 particle images per interrogation-window could be obtained for imaging parameters provided in Table 4.1.

The droplet seeding consists of an atomized paraffin-ethanol mixture (1:2) that is dispersed by two atomizers. An impactor and a dryer unit between atomizer and the test section limit the initial maximum droplet diameter to

approximately $1\,\mu$m. The droplet time response and sizes are characterized experimentally in the following section.

4.3 Assessment of tracer response and size

The ability of the paraffin-ethanol droplet seeding to follow velocity changes in transonic flows is assessed by in situ step response measurements across a normal shock using PIV. Similar measurements of PIV tracer response across an oblique shock have been reported by Scarano et al. [137], Humble et al. [76] and Ragni et al. [129]. Following Stokes' drag law, Melling [106] predicted that the normal velocity U of a single particle across the shock follows an exponential decay.

$$\ln(U^*) = \ln\left(\frac{U - U_2}{U_1 - U_2}\right) = -Kt = -\frac{t}{\tau_p} \tag{4.1}$$

Here U_1 is the normal tracer velocity upstream of the shock and U_2 the downstream velocity. A particle crossing the shock needs the relaxation time τ_p to decelerate to the $1/e$ part of the velocity step across the shock. The distance traveled by the particle during the relaxation time is given by the relaxation length ξ_p.

$$\xi_p = \tau_p \left(U_1 - \frac{U_1 - U_2}{e}\right) \tag{4.2}$$

Measurements are performed near the leading edge of a single cascade airfoil within the region highlighted in Fig. 4.4. The cascade is operated at $M_1 = 1.25$ near stall. Under these operating conditions the flow is throttled and due to the increased back pressure the passage shock is shifted toward the leading edge and merges with the bow shock. Thus, near the leading edge the normal shock has a relatively stable position.

The PIV parameters of response evaluation are listed in Table 4.1. The temporal resolution is given by the pulse separation which is set to 250 ns. This value is well below the expected particle response time of $1 - 2\,\mu$s [129]. Within this pulse separation displacements of 9 pixel are obtained at $U_1 = 400\,\mathrm{m/s}$. The images are interrogated at a spatial resolution of $0.54 \times 0.54\,\mathrm{mm}^2$ (48×48 pixel

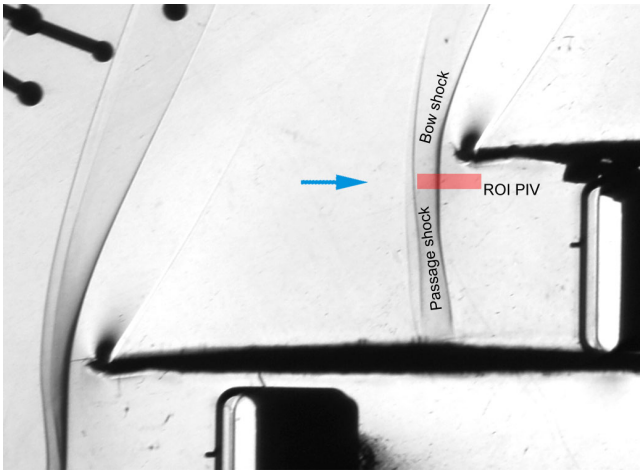

Figure 4.4: Schlieren image of the shock system in front of the leading edge at $M_1 = 1.25$ near stall

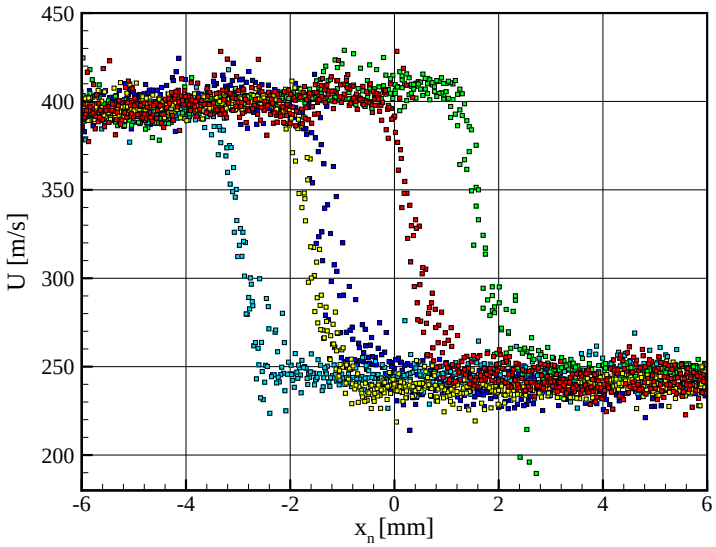

Figure 4.5: Velocity profiles across the normal shock of 5 separate PIV measurements within the highlighted region in Fig. 4.4

at 50% overlap) which is on the order of the expected particle relaxation length of 0.7 mm (Eq. (4.2) for $\tau = 2\,\mu$s) as measured for example in [129]. The spatial smoothing of the particle velocity decay across the normal shock is still at an acceptable level at this window size (c.f. Fig. 4.6).

Additional spatial resolution limitations such as aero-optical distortions [41] due to density gradients and the curvature of the shock were not observed in the PIV images. This is probably due to the low constriction of the flow at an AVDR of 1.12 where the span-wise shock curvature with respect to the side walls is low. Another reason for the low level of distortion might be the small field angle of the PIV imaging lens which does not exceeds 1.6° along x_n. The compression across the shock leads to an increase of particle image densities which leads to a higher weighting of correlation signal toward

Table 4.1: PIV parameter of response evaluation

Field of view		23×23	mm^2
		2048×2048	pixel
Magnification	M	0.65	
		88.6	pixel/mm
Pulse delay	Δt	250	ns
Inflow axial velocity	U_1	400	m/s
		8.8	pixel
Window size		0.54×0.54	mm
		48×48	pixel
Sampling		0.27×0.27	mm
		24×24	pixel
Interrogation method		Multi-grid+ Image deform.	
Peak detection		Gauss fit (3×3)	
Vector validation test		max. displacement (16 pixel)	
		max. displacement diff. (7 pixel)	
		normalized median (7)	

downstream velocities but seems to have no further drawbacks in terms of spatial resolution.

In order to infer the relaxation time of the droplet seeding, single shot PIV velocity profiles across the passage shock are extracted within a narrow stripe of $w = 15.0\,\text{mm}$ and $h = 3.6\,\text{mm}$ as shown in Fig. 4.5. Each velocity profile is ensemble averaged along h. Along x_n this corresponds to a maximum density of 55 PIV samples per mm at a sampling distance of r=0.27 mm. The validation rate of all sampled velocity data within N=1000 single shot PIV evaluations is 91% using the validation parameter provided in Table 4.1.

As the passage shock position fluctuates by $4 - 8\,\text{mm}$ or $350 - 700$ pixels in image space, time-averaging of all profiles would lead to very strong smoothing of the velocity gradients. Therefore each single shot velocity profile is fitted against an exponential velocity profile according to Eq. (4.2). For this purpose, the shock position was first estimated by the steepest velocity gradient in order to obtain upstream and downstream velocities U_1 and U_2 at a certain distance to the position (see Fig. 4.6, left). The velocities upstream and downstream are respectively averaged within a 3 mm interval at 1 mm distance to the estimated shock position in order to obtain average values for u_1 and u_2. The velocity slope in the logarithmic representation was linearly interpolated within a range of $-2.5 \leq \ln(U^*) \leq -0.5$ (Fig. 4.6, middle). This slope includes 26 ± 4 sampling points which lay in an interval of 1.6 mm along x_n. Finally, the

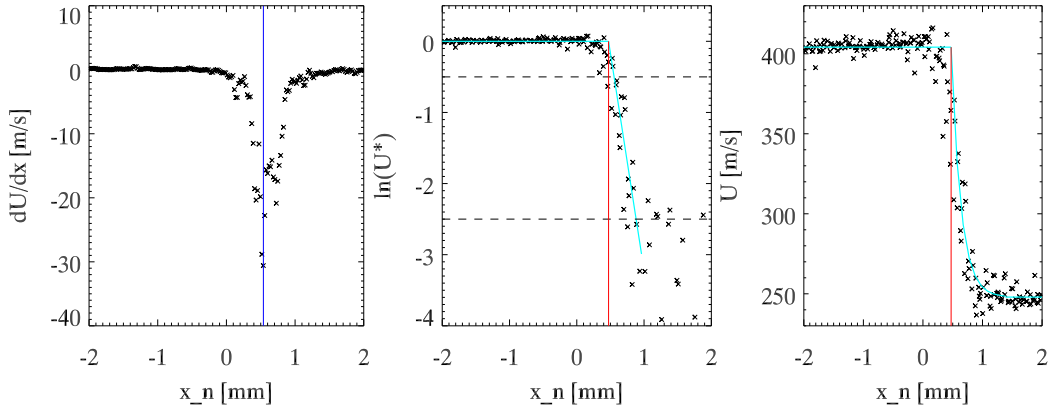

Figure 4.6: Single shot velocity profile across the shock; left: approximation of shock position with steepest gradient (blue vertical line); middle: normalized logarithmic representation, right: fit of the velocity decay across the shock

chord-wise shock position is given by the intersection of the linear slope with the upstream velocity level in the logarithmic scale representation of tracer velocity as proposed by Ragni et al. [129] (see Fig. 4.6, middle). The result of the exponential tracer velocity decay of each single shot is plotted in Fig. 4.6, right.

Gathering the response information from all evaluated profiles allows to build normalized PDFs of relaxation length (Fig. 4.7, left) and relaxation time (Fig. 4.7, right). Both PDFs are in line with standard normal distributions within the range of $\pm 4\sigma$. The characteristic relaxation length of paraffin tracer deceleration to the 1/e part of the velocity step across the normal shock is $\xi_p = 0.23 \pm 0.05\,\mathrm{mm}$. The average relaxation time of particles within 915 instant PIV measurements was $\tau_p = 0.76 \pm 0.15\,\mu\mathrm{s}$. This indicates an acceptable time response of the paraffin droplet seeding in comparison to values reported in literature. For example, measured relaxation times reported from Ragni et al. [129] are $\tau_p = 1.92 - 2.02\,\mu\mathrm{s}$ for DEHS seeding dispersed by Laskin atomizer and $\tau_p = 1.36 - 1.67\,\mu\mathrm{s}$ for titanium dioxide solid particles of 50 nm primary crystal size dispersed by a fluidized bed seeder.

Based on the equation of motion of spherical particles in gaseous flows (c.f. Soo [154]) the measured relaxation time can be used to infer an average particle droplet diameter d_p. If the particle density is much larger than fluid density

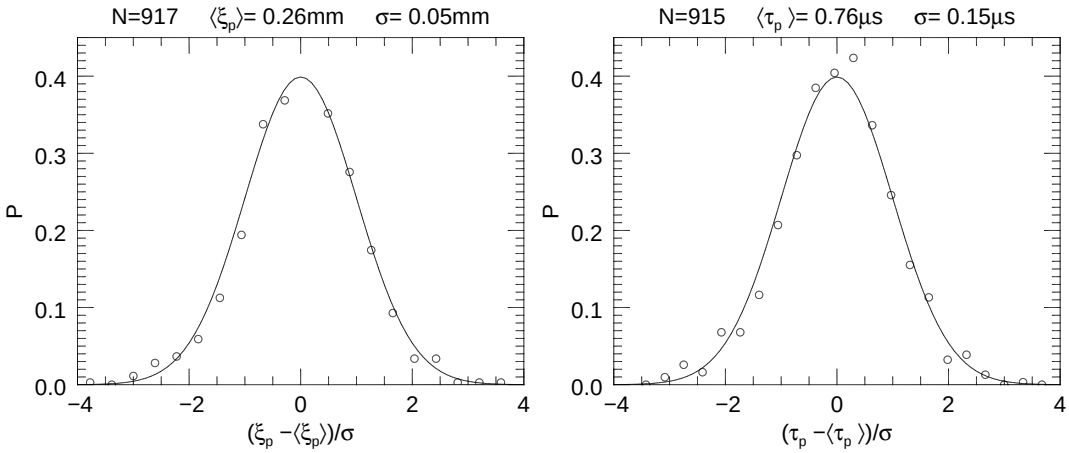

Figure 4.7: Normalized PDFs of particle relaxation length ξ_p (left) and relaxation time τ_p (right) and standard normal distributions (lines)

the equation of motion simplifies [106]:

$$\tau_p = \frac{4}{3}\frac{\rho_p d_p^2}{\mu C_D \mathrm{Re}_p}\,, \tag{4.3}$$

where C_D represents the drag coefficient of a sphere and Re_p the local particle Reynolds number which depends on the difference between fluid and particle velocity [51]:

$$\mathrm{Re}_p = \frac{\rho_2 d_p}{\mu_2}|\overrightarrow{U_f} - \overrightarrow{U_p}|\,. \tag{4.4}$$

Here ρ_2 and μ_2 represent the gas density and viscosity downstream of the shock.

Different empirical models of the drag coefficient C_D of a sphere have been reported in literature. For a Mach number of $\mathrm{Ma}_1 = 1.5$ Melling [106] applies a modified Stoke's drag law in the form of:

$$C_D = \frac{24}{\mathrm{Re}_p(1+\mathrm{Kn}_p)} \tag{4.5}$$

The particle Knudsen number Kn_p is related to the degree of rarefaction and is the ratio of the molecular mean free path length to the particle immediately downstream of the shock. Assuming an isentropic flow, the particle Knudsen number can be calculated from gas dynamics equations as described by Forney et al. [51]. At present flow conditions $T_t = 293K$ and $M_1 = 1.25$ and $\kappa = 1.4$

(air) and a particle diameter range between $d_p = 0.5 - 1\,\mu$m the particle Knudsen number downstream of the normal shock is in between $0.1 - 0.2$.

Substituting C_D in Eq. (4.3) by the modified Stoke's drag law Eq. (4.5) and applying a paraffin density of $\rho_p = 0.85\,\mathrm{g/cm^3}$ with the ethanol part fully evaporated results in an average particle diameter of $d_p = 0.5\,\mu$m.

A particle diameter estimation with Hendersons model of the drag coefficient [67] inserted in Eq. (4.3) results in a slightly smaller particle diameter of $d_p = 0.42\,\mu$m. The Henderson model requires prior knowledge of the particle Reynolds number (c.f. Thomas [163]). Following calculations provided by Forney et al. [51] the particle Reynolds number is estimated to be 1.9.

4.4 Viewing geometry and laser energy requirements for tomographic PIV

Tomographic measurements within this corner region of cascades are of particular interest to enable studies of secondary flow phenomena, for example, corner separation and its interaction with the passage vortex. Preparatory work involves estimation of laser power requirements for volumetric imaging in the TGK using a mock-up (see Fig. 4.8). Four PCO1600 cameras (Δpix= $7.4\,\mu$m) with 14bit dynamic range (DR) are arranged in a quadrangular fashion to observe a volumetric region near the side wall and the suction side of a OGV cascade.

All mock-up imaging parameters can be found in Table 4.2. Two cameras observe the volume of interest along the suction side at zero pitch with respect to blade span while the other camera pair observes the measurement volume from above at a pitch of 30°. The horizontal and vertical angular apertures of the system are both 30° (15° to the left, 15° to the right). With regard to the transonic cascade wind tunnel, these are approximately the maximum vertical and horizontal angular apertures due to constraints on optical access of the test rig. Geometric estimations yield a maximum angular apertures of $\beta = 45°$ along the diagonals between camera no. 1 and no. 3 and between camera no. 2 and no. 4. Thus, according to Eq. (2.11), particle reconstructions would be

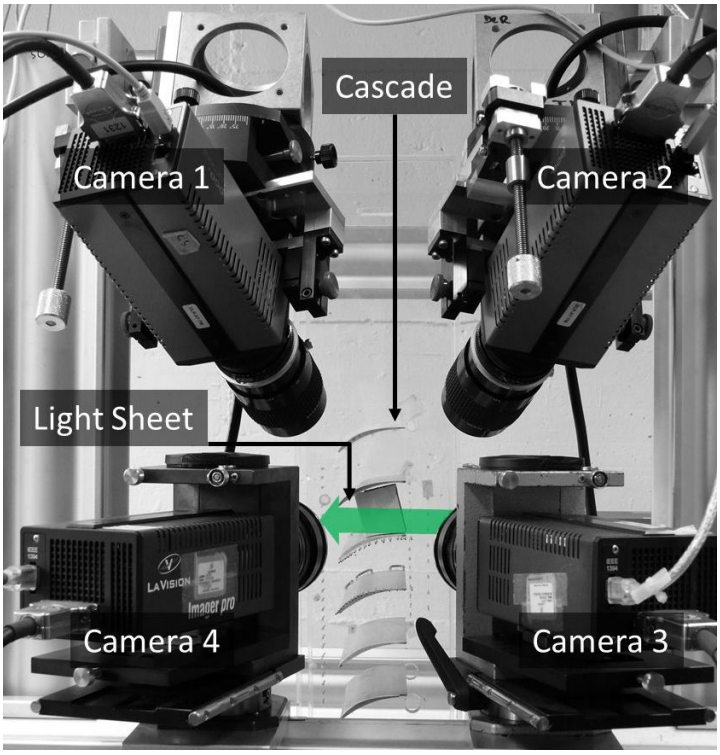

Figure 4.8: Mock-up of the tomographic PIV setup for measurements of the corner flow in a transonic cascade

elongated by a factor of 2.6 along the vector that bisects both observation vectors of camera no. 2 and no. 4. (or camera no. 1 and no. 3). Estimations of the aperture size using Eq. (2.10) yield a f-number of 11 to enables a depth of focus of 4.2 mm if a blur circle of $d_b = 2.6$ pixel is seen as sufficient which is approximately the size of the Airy disc (see Table 4.2).

Table 4.2: Imaging parameter of mock up setup

cam	φ	ψ	$DOF[mm]$	f [mm]	$f_\#$	$\approx M$	d_A [pixel]
1	-15°	30°	4.2	100	11	0.34	2.61
2	15°	30°	4.2	100	11	0.34	2.61
3	15°	0°	3.6	85	11	0.35	2.58
4	-15°	0°	3.6	85	11	0.35	2.58

A free jet nozzle provides an arbitrary flow along the trailing edge of a single blade suction within the region of interest. The flow is seeded using the previously characterized paraffin-ethanol droplet tracers having a mean particle diameter of $d_p = 0.5\,\mu$m as described in the previous section. A dual-cavity Nd:Yag laser (New Wave Gemini) with 80 mJ pulse energy provides thick sheet illumination of the paraffin droplet seeding. The sheet has a height of 24 mm and a thickness of 3.5 mm. The cameras no. 1 and no. 4 observe the sheet

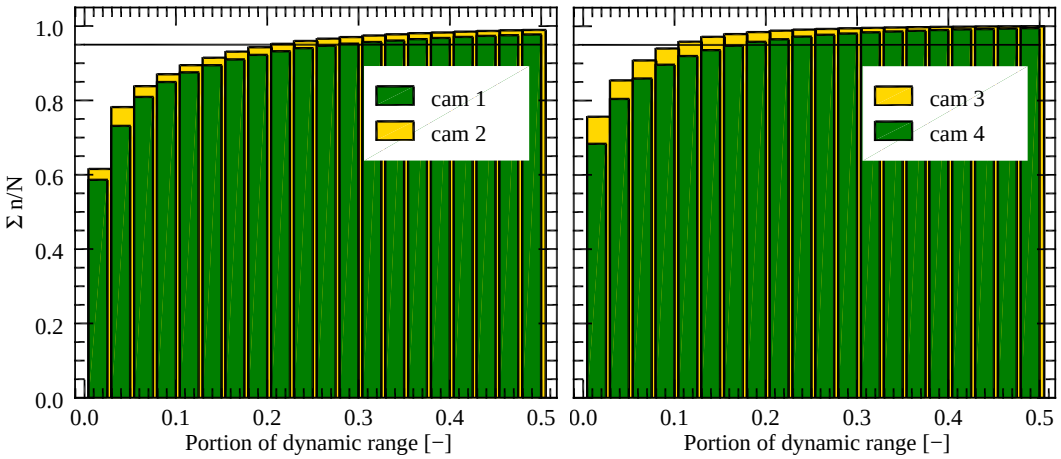

Figure 4.9: CDFs of peak intensities of 20.000 particle images in view no. 1 and no. 2 (left) and view no. 3 and no. 4 (right)

in forward scattering whereas camera no. 2 and no. 3 operate in backward scattering.

For signal intensity evaluation, particles are recorded at low seeding density to enable segmentation of particle images. Prior to image segmentation, a local minimum intensity of 9×9 pixel neighbors is subtracted form the intensity of each pixel to remove background intensity. After thresholding, the peak intensities of 20.000 particle images are evaluated for each view using connected component labeling (IDL routine *label_region*).

In order to assess whether laser energy is sufficient, it is appropriate to examine first the minimum particle image intensity which can be distinguished from the image background. Local background intensity variations are mainly generated from scattered light that is back-reflected by the blade surface as well as from fluctuations of the camera dark current. The local threshold t_{min} of visibility is estimated by calculating the mean local minimum over 100 images within the 9×9 neighbors of each pixel in exemplary particle image regions of the light sheet. A value of 2σ is added to the mean local minimum to account for fluctuations. This procedure yields background level of $0.07 - 0.1\%$ of the camera DR.

Fig. 4.9 shows cumulated distributions (CDFs) of the peak intensities of each single particle image obtained from segmentation. About 95% of all particle images recorded with camera no. 1 reach peak intensities up to 27% of the

camera dynamic range (DR). For camera no. 2 95% of all particle images only reach up to 22% of the DR due to backscattering. Cameras no. 3 and no. 4 are equipped with standard lenses and close-up extension rings which leads to a slightly lower light sensitivity compared to camera no. 1 and no. 2 (macro lenses). Due to this sensitivity loss, 95% of all particle images of camera no. 3 (backward scattering) and camera no. 4 (forward scattering) respectively utilize 12% and 18% of the camera DR. On the lower bound about 60% of all particle images of camera no. 1 and no. 2 and about $67 - 75\%$ of all particle images of camera no. 3 and no. 4 have peak intensities between $0.5 - 3.0\%$ of the camera DR. This value is at least five times above the background intensity threshold t_{min} which allows particle intensities to be distinguished from background noise. These findings indicate that under given imaging conditions 80 mJ laser energy per pulse are sufficient to illuminate the atomized paraffin-ethanol seeding within volume dimensions of $36 \times 24 \times 3.5\,\mathrm{mm}^3$.

Chapter 5

Application of tomographic PIV to the high-speed corner flow in a compressor cascade

Within this chapter tomographic PIV (TPIV) [42] and conventional stereoscopic PIV (SPIV) [5, 125] are utilized in order to measure the corner flow within a linear compressor cascade at $\mathrm{Ma}_1 = 0.60$. Parts of the content of this chapter have been published in conference proceedings [207, 204].

The oil-streak image shown in Fig. 5.1 provides an impression of the complex flow pattern at the intersection between the endwall and the blade's suction side in the cascade under investigation. The secondary flow on the endwall is dominated by the passage vortex which is driven by the pitch-wise pressure gradient between pressure and suction side.

The time-averaged location of the passage vortex can be predicted using a RANS (Reynolds-averaged Navier Stokes) simulation as visualized in Fig. 5.2. Slow-momentum fluid from the endwall moves toward the suction side leading to a transverse flow. In this region the axial flow travels against an adverse pressure gradient and separates. Such a corner separation has influence on the flow turning near the wall and leads to blockage effects which limit the mass flow capacity of the cascade. Secondly, the corner separation induces strong shear and velocity fluctuations which are responsible for the majority

of pressure losses in an axial compressor cascade [68].

The application of tomographic PIV near the trailing edge of a cascade blade is intended to demonstrate the technique's potential of instantaneously resolving secondary flow structures within the separation region of the cascade. To correctly measure velocities of the relatively slow transverse flow in the corner region or near the wall remains a challenging task, given the fact that the main flow component is at least one order of magnitude higher. Moreover, to derive three-dimensional statistical data of fluctuations of velocity in the turbulent flow region requires a large number of samples whose evaluation can be (computational) time-consuming. Thus, fast particle volume reconstruction algorithms become attractive for evaluation of large sets of data. Thus, both, the fast multiplicative algebraic reconstruction technique (FMART, see Sect. 3.1.3) and the maximum entropy technique (MENT, see Sect. 3.1.1) are validated against a conventional simultaneous multiplicative algebraic reconstruction technique (SMART) [8] on the basis of the experimental data.

This chapter is structured as follows: The first section 5.1 gives an overview of the cascade geometry and the main flow parameters. In section 5.2, various aspects of the adaption of the tomographic PIV setup to the restricted optical access on the cascade wind tunnel are described. This includes the optical setup of a light-sheet probe and imaging parameters of multiple views using four cameras. Section 5.3 provides details on the calibration procedure and evaluates image shifts due to tunnel vibrations. Section 5.4 describes the

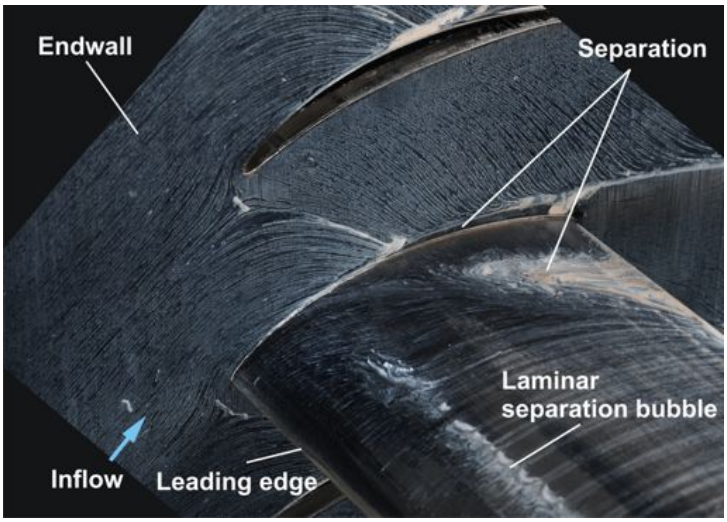

Figure 5.1: Oil streak pattern of surface shear [70]

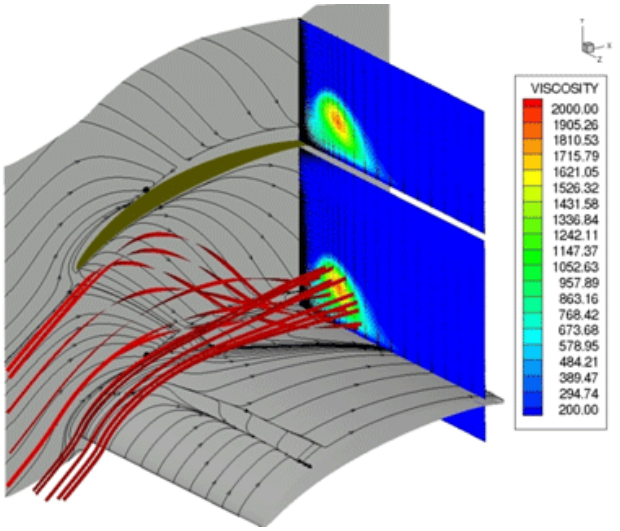

Figure 5.2: RANS simulation, color represents eddy viscosity [70]

image evaluation to finally obtain 3-D displacement vectors. A comparison of tomographic and stereoscopic PIV results is provided at the end of this chapter.

5.1 Cascade geometry and flow parameter

The corner flow is investigated in the DLR low Reynolds number OGV cascade whose geometry and aerodynamic characteristics are described in detail by Hergt et al. [70]. The cascade consists of seven airfoils with 70 mm chord and 168 mm blade span that are supported by transparent acrylic side walls of 16 mm thickness. The cascade is operated under realistic operation conditions, which can also be found in real OGV turbomachinery geometries [200]. Geometric parameters and operation conditions of the cascade are summarized in Table 5.1.

PIV Measurements are carried out near the suction side of a single passage

Table 5.1: Cascade and flow parameter

Chord length		70.0	mm
Pitch		40.4	mm
Span width		168	mm
Deflection angle		43°	
Mach number at aerodynamic design point	Ma_1	0.60	
Inflow axial velocity	u_1	206	m/s
Reynolds number based on chord length	Re	900,000	

near the trailing edge of the blade in a volume coincident with the numerically predicted location of the passage vortex. CFD results of the corresponding corner region flow are published by Hergt et al. [200]. In Fig. 5.3, an oil streak visualization on the suction side is overlaid with positions of the three TPIV measurement volumes. Each subvolume has a size of $36 \times 24 \times 4\,\mathrm{mm}^3$.

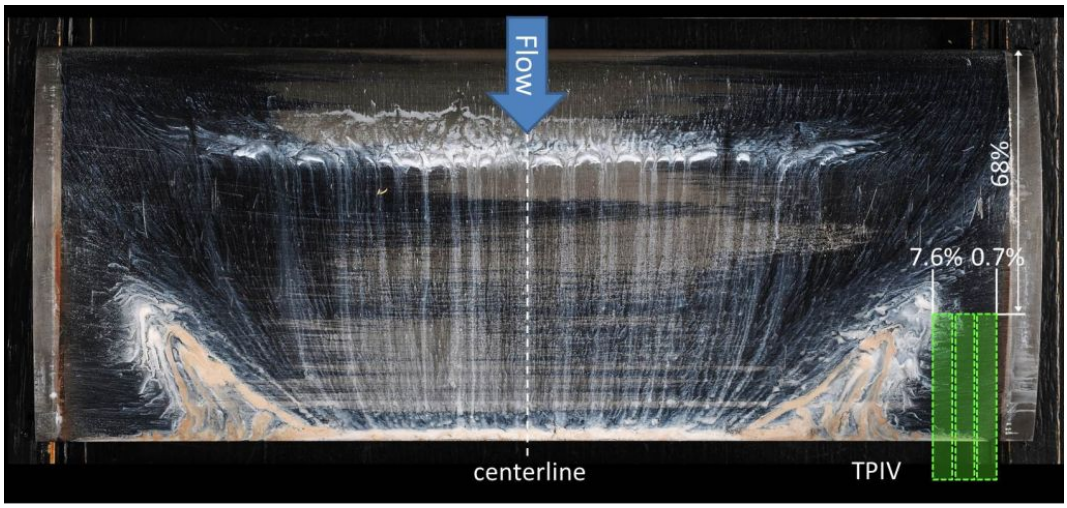

Figure 5.3: Oil streak visualization of the suction side of a single cascade blade overlaid with positions of TPIV measurement areas. Vertical measures based on chord length, horizontal measures based on span width

5.2 Optical setup

5.2.1 Implementation of thick-sheet illumination

A light sheet probe is positioned 450 mm downstream of the trailing edge of the cascade as depicted in Fig. 5.4. The beam enters the cascade through a 16 mm diameter probe whose tip contains a 90° deflecting mirror. As measurement domain and light sheet access are not on the same side of the wind tunnel, the laser beam is guided through the wind tunnel by a tube of 500 mm length. The probe is additionally supported from the inside of the tunnel in order to reduce aerodynamically induced bending and vibrations which would affect the light sheet position. To improve the protection of the mirror surface from incoming particles (rust) the light-sheet probe's tip is retrofitted with a Laval

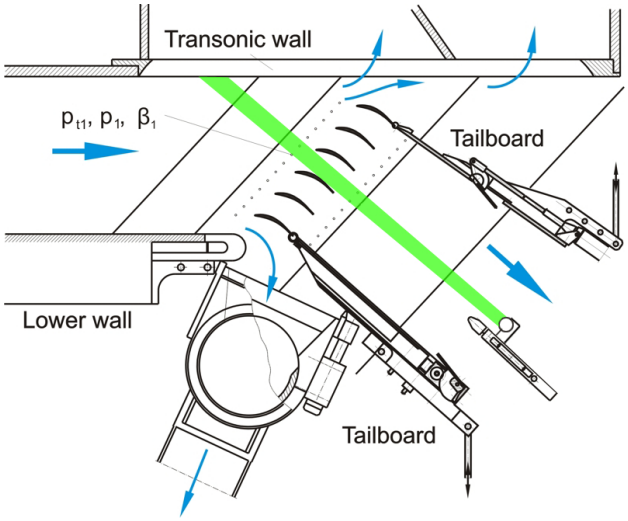

Figure 5.4: The TGK test section with OGV cascade and light-sheet orientation

nozzle which redirects and accelerates the purge flow against the tunnel flow as described in Sect. 4.2. Thereby incoming particles are sufficiently decelerated and prevent erosion of the mirror surface.

As illustrated in Fig. 5.5 the optical setup of the probe contains two doublets at the probe entry, the first of which reduces the laser-beam diameter to inner tube diameter. Together with a cylindrical lens positioned inside of the probe the beam is enlarged in one dimension to achieve a height of the sheet of 24 mm in the FOV. The two cylindrical lenses of the second doublet focus the sheet waist at varying distances depending on the spacing between the lenses. This leads to a variable thickness of the sheet within the FOV. With the aid of spacers a reliable and quick variation of sheet thickness can be achieved even while the wind tunnel is operating.

In order to increase the light sheet thickness in the FOV and at the same time prevent damage to optical components in the probe, the beam waist is shifted upstream of the FOV, away from the probe itself. In conjunction with the limited aperture of $6.6 \times 9.4\,\mathrm{mm}^2$ provided by the Laval nozzle at the probe tip, the maximum achievable sheet thickness is limited to about 4 mm in the probe volume.

The maximum light sheet thickness, as measured with a beam profiler, is 3.5 mm FWHM within the FOV at 450 mm distance from the probe tip (Fig. 5.6). The higher order transverse modes of the flash lamp pumped laser result in a more flat top profile of the thick sheet and therefore strongly deviates from the

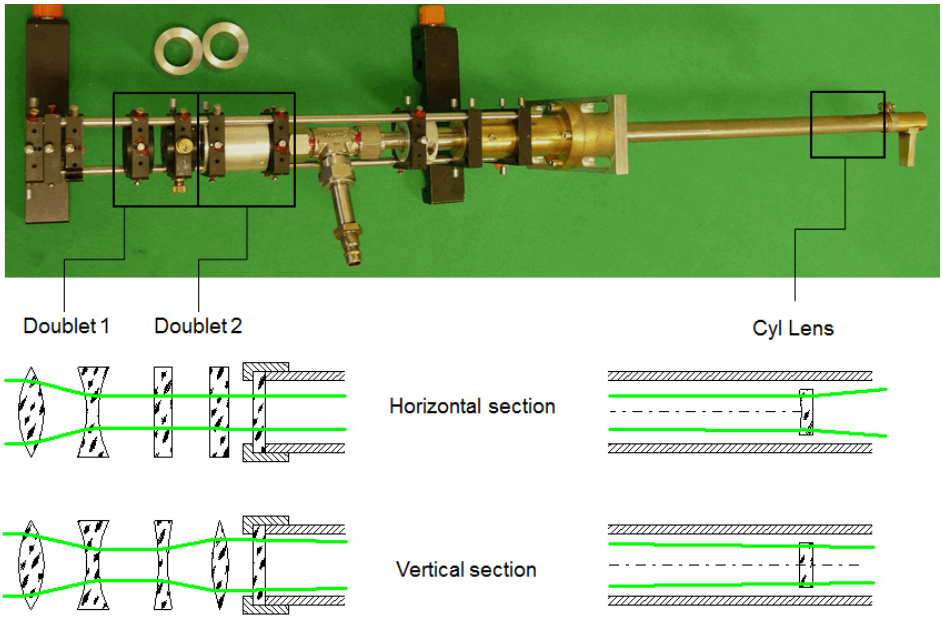

Figure 5.5: Optical design of the light-sheet probe

Gaussian fit. The minimum achievable light sheet thickness is 1.1 mm FWHM which is used for the stereo PIV reference measurements. The integral pulse energy is 50 mJ within the FOV.

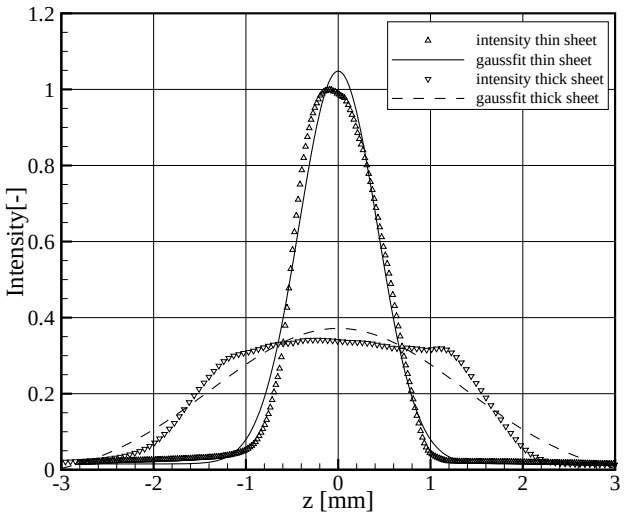

Figure 5.6: Light sheet intensity profile vs. volume depth of the thick and the thin sheet

5.2.2 Viewing geometry and imaging conditions

Fig. 5.7 shows a photograph of the tomographic PIV setup which involves four double-frame (PIV) cameras fitted with Scheimpflug mounts to account for the oblique imaging arrangement. The view parameters are summarized in Table 5.2. Camera positions and viewing angles are estimated using Tsai's camera model [164] as implemented in *PIVmap 3.5.9* (PIVTec GmbH). Two cameras observe the volume of interest along the suction side at zero pitch while the other camera pair observes the measurement volume from above at 26° and 34° pitch. In comparison with the preliminary study (c.f. section Sect. 4.4) the horizonal angular aperture is increased from 30° to $41 - 45°$ to fully exploit the optical accessibility of the side window and reduce elongation of particle reconstruction as much as possible. The maximum angular apertures is $\beta = 50°$ along the diagonals between camera no. 2 and no. 4. Thus, according to Eq. (2.11), particle reconstructions would roughly be elongated by a factor of 2.4.

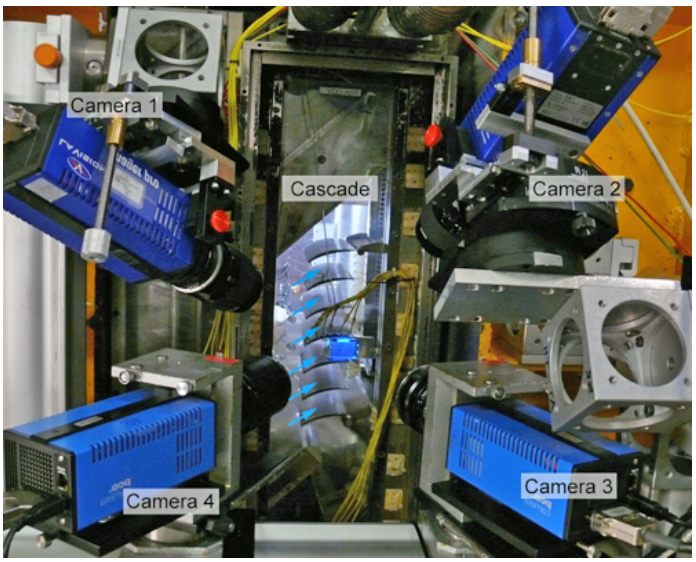

Figure 5.7: Tomographic PIV camera setup and back-illuminated calibration target on a micro traverse

Both single-axis and two-axis Scheimpflug mounts are used to optimize the depth of focus of each camera. The f-numbers range from $8 - 16$ to have a sufficient depth of focus and to reduce optical distortions due to the oblique viewing through the perspex window. Cameras no. 2 and no. 3 observe the illuminated volume with a backward scattering angle of $-15°$ at f-numbers of 11 and 8, respectively. Therefore these cameras have the lowest sensitivity in

the present imaging configuration. At 3.5 mm sheet thickness these cameras deliver a minimum net signal of about 150 counts per particle (after background intensity subtraction) which corresponds to only a few percent of the camera's dynamic range (14 bit for camera models pco.1600 / pco.2000). The common FOV has a size of approximately $36 \times 24\,\mathrm{mm}^2$ with corresponding camera resolutions ranging from 1600×1030 pixel (camera no. 2) to 2048×1800 pixel (camera no. 4).

The pulse separation Δt was set to $2\,\mu$s inducing maximum particle displacements of about 15 pixel on the camera sensors. The thickness of the illuminated volume was successively adjusted to approximately 1 and 3.5 mm FWHM during each wind tunnel run. Volumetric image data were acquired in three regions at distances of 4, 8 and 11 mm with respect to the side wall in order to cover the entire passage vortex. Each region has a size of $36 \times 24 \times 4\,\mathrm{mm}^3$. Within each region three additional thin sheet stereo PIV measurements were recorded and later used for comparison.

Table 5.2: Imaging parameter of the tomographic setup

cam	φ	ψ	DOF $[mm]$	f $[mm]$	$f_\#$ [-]	$\approx M$ [-]	$[^{pixel}/_{mm}]$	d_I [pixel]	D_I $[ppp]$
1	-30°	26°	4.5	100	16	0.37	50	3-5	0.018
2	15°	34°	4.4	100	11	0.31	42	2-4	0.024
3	15°	0°	3.6	85	8	0.38	51	2-4	0.022
4	-26°	0°	3.9	100	11	0.46	62	3-4	0.015

In the thick sheet configuration the measured particle image density in the separated corner flow ranges between $0.015 - 0.024$ ppp (particle per pixel) depending on the view's magnification. The particle image size varies between 2 and 5 pixels and is partially elliptical due to astigmatic effects within each particular view.

5.3 Calibration technique and accuracy of image registration

Volume calibration is achieved with lithographic photomasks of calibration points on soda-lime glass that are backlit with a display LED for homogenous

Table 5.3: Residuals of world-to-image mapping (fwd.) in [*pixel*] and image-to-world mapping (rev.) in [μm] after least squares minimization of the reprojection error $\bar{\varepsilon}$ Eq. (A.3)

Camera model	Camera 1		Camera 2		Camera 3		Camera 4	
	fwd. [*pixel*]	rev. [μm]	fwd. [*pixel*]	rev. [μm]	fwd. [*pixel*]	rev. [μm]	fwd. [*pixel*]	rev. [μm]
Pinhole w/o. distortions	0.24	-	0.29	-	0.25	-	0.20	-
Ratio of 2^{nd} order poly.	0.12	2.8	0.21	5.9	0.19	4.1	0.16	2.68
3^{rd} order poly.	0.21	4.6	0.24	5.9	0.16	3.1	0.22	3.8

illumination (Fig. 5.7). Opaque regions consist of a 100 nm thick layer of chromium oxide and have a lateral dimensional tolerance of ±300 nm. The points have a diameter of 0.4 mm and a spacing of 2 mm. The traversal of the calibration target along z-axis by a motorized translation stage allows the sequential recording of 3-D points in space at a manufacturer specified positioning accuracy of better than ±2 μm. Seven calibration planes at 1 mm z-spacing were recorded. Point correspondences are detected using PIVmap 3.5 (PIVTEC GmbH, Germany).

The measured point correspondences of world and camera coordinates are used to fit mapping functions according to world-to-image and image-to-world projection. The averaged residuals of the least squares optimization can be found in Table 5.3. The residuals of the world-to-image projection range from 0.12 to 0.3 pixel depending on the mapping function and camera. The averaged residuals per calibration plane are consistently lower. An explanation for this effect might be a slight nonlinearity in the travel of the traverse (see Sect. 6.3.2). This is also confirmed by the fact that the residuals increase as the camera viewing angle increases with respect to the normal of the plate.

Volume self-calibration [176] is applied to estimate rotational and translational calibration errors. This is achieved by triangulation of particle positions from each view using the *Matlab Calibration Toolbox* provided by S.Gesemann (DLR AS-EXV). The disparity magnitudes within the bounding planes of a calibration domain obtained in this way are shown in Table 5.4.

Global image shifts due to tunnel vibrations were monitored simultaneously with tomographic measurements. The particle image recordings additionally contain images of laser illuminated small reference marks on the perspex side-

Table 5.4: Averaged disparity magnitude within the bounding planes of the calibration domain obtained from volume self-calibration of the world-to-image mapping (fwd.) and image-to-world mapping (rev.)

Calibration plane	Camera 1		Camera 2		Camera 3		Camera 4	
	fwd. $[pixel]$	rev. $[\mu m]$	fwd. $[pixel]$	rev. $[\mu m]$	fwd. $[pixel]$	rev. $[\mu m]$	fwd. $[pixel]$	rev. $[\mu m]$
$z = 5mm$	0.45	8.9	0.67	16.1	0.80	15.8	0.49	7.9
$z = 11mm$	0.60	12.0	1.03	24.6	1.16	22.8	0.58	9.3

walls. These small marks were correlated with appropriate regions of the ensemble averaged intensity image of the PIV recording. This a posteriori evaluation is only possible for the measurement volumes at 4 and 8 mm distance from the sidewall, where both marks and particles still are within camera focus. Fig. 5.8 shows the image shifts due to tunnel vibrations. The shifts are on the order of ≈ 0.5 pixel for cameras no. 3 and no. 4 and of ≈ 1 pixel for camera no.1. By comparison, the sizes of particle images vary between $2 - 6$ pixel depending on the camera view (see Table 5.2).

5.4 Image evaluation

An overview of the involved processing steps is given in Table 5.5. Both SPIV and TPIV are very susceptible to laser flare, such as light reflected by the blades or light scattering by slight scratches or seeding deposits on the windows. Therefore each image is preprocessed using background subtraction and spatial filtering to enhance overall contrast thereby improving the visibility of particle images.

5.4.1 Stereoscopic PIV evaluation

Stereo PIV measurements are acquired from a thin light sheet setup using cameras no. 1 and no. 3 at a combined viewing angle of 50°. Stereo image data was processed with PIVview 3.5 (PIVTEC GmbH, Germany) using the PIV processing parameters summarized in Table 5.5.

In order to enable comparison between SPIV and TPIV results, the z po-

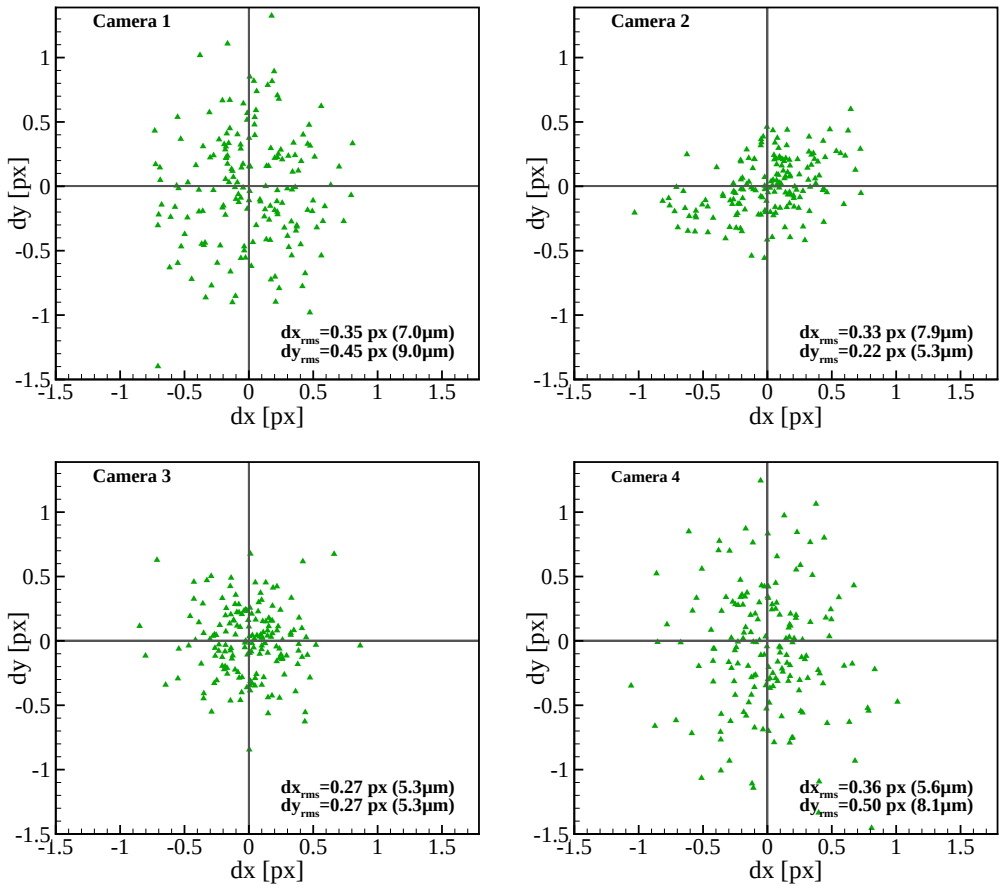

Figure 5.8: Global image shifts due to tunnel vibrations. Numbers in brackets indicate the approximate object space shifts

sition of the thin sheet within the volumetric domain was obtained from a tomographic reconstruction using all four images of the thin sheet. This z position was estimated by the intensity maximum of the mean particle field reconstruction of the thin sheet.

5.4.2 Tomographic particle volume reconstruction

The tomographic image data has been processed by FMART, MLOS-SMART and MENT according to the processing scheme provided in Table 5.5. For FMART, still lacking a procedure to calibrate the point spread function experimentally, a constant Gaussian weighting function of a width of $\sigma = 0.5$ pixel is applied for image sampling. According to tests performed in Sect. 3.3.3, the sub-pixel accuracy for the precalculation of weights was set to 1/50 pixel. To

Table 5.5: Evaluation parameters of stereoscopic PIV and tomographic PIV

	Stereo PIV (thin sheet)	Tomographic PIV (thick sheet)
field of view (FOV)	$\approx 36 \times 24\,\mathrm{mm}^2$	$\approx 36 \times 24\,\mathrm{mm}^2$
sheet thickness (FWHM)	1.1 mm	3.5 mm
size of ROI	1800×1200 pixel	$1800 \times 1200 \times 300$ voxel
resolution	50 pixel/mm	50 voxel/mm
image enhancement	min. image subtraction 3x3 median filter 7x7 high pass filter 3x3 low-pass filter	min. image and local min. subtraction (5x5 kernel) normalization by avg. image intensity clipping
mapping algorithm	2^{nd} order projection map and disparity correction	**A,B**: Ratio of 2^{nd} order poly. **C**: Two-plane-model and volume self calibration [176]
particle reconstruction	-	**A**: FMART, **B**: MENT **C**: MLOS-SMART
image interpolation	4^{th} order B-Spline	**A**: Gaussian weighting **B**: bi-linear, **C**: OTF [144]
interrogation method	multi-resolution (3 levels) image deformation (3 passes)	multi-resolution (3 levels) volume deformation (3 passes)
peak search	Whittaker reconstruction	3-point Gauss fit
interrogation window (IW)	64×32 pixel	$64 \times 32 \times 32$ voxel
particle images per IW	$\approx 10 - 16$	$\approx 6 - 9$
sampling grid	32×16 pixel	$32 \times 16 \times 16$ voxel
validation	displacement diff. < 5 pixel normalized median filter (≤ 3)	normalized median filter (≤ 3) light sheet intensity $> 40\%$
final data grid	54×74 vectors	$54 \times 74 \times 13$ vectors

reduce the effect of tunnel vibrations on camera alignment, the initial voxel volume was smoothed by a 3-D Gaussian filter of sigma values of $1.5 \times 1.5 \times 0.1$ voxel prior to the iterative refinement of intensities. Fig. 5.9 shows the reconstructed intensity versus volume depth and averaged over 100 realizations, cumulated along $100 \times 1000 \times 1$ voxel and normalized by the maximum intensity. For FMART, the relative ghost intensity background level in front and behind the thick sheet are 0.34 and 0.37 after four iterations. Further iterations did not reduce the ghost background level. These background intensity levels reach almost those of MLOS-SMART after 5 iterations whereby the latter exhibits ghost intensity levels in the order of 0.30 in front and of 0.35 behind the thick sheet after 5 iterations. After another 3 SMART iterations the background level further reduces and reaches values of 0.26 in front and 0.32 on the back of the thick sheet. For comparison, after a single iteration MENT exhibits significantly higher ghost background intensities of 0.44 in front and 0.39 behind the thick sheet. Additional MENT iterations did not improve the

signal.

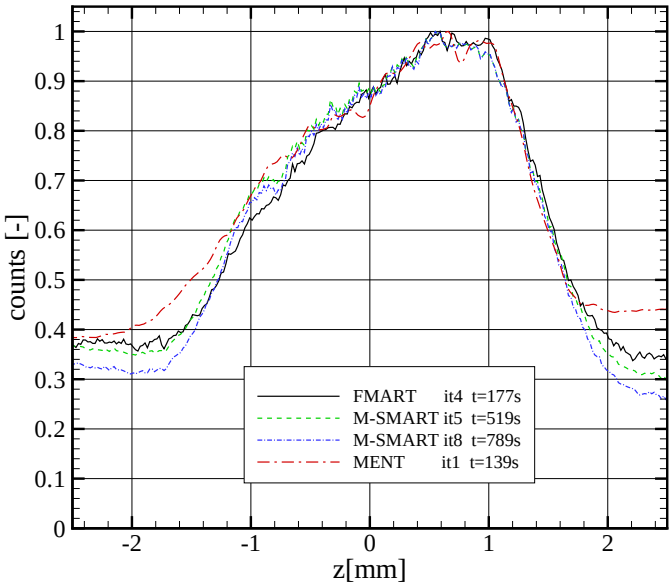

Figure 5.9: Reconstructed intensity within slices of 100 × 1000 × 1 voxel and Processing time of volume reconstruction on a Xeon Workstation, 12 cores at 2.4Ghz, 12GB RAM

Concerning the remaining ghost background, the reason for differences between MLOS-SMART on the one hand and FMART and MENT on the other hand might be that neither particle image distortions nor misalignments of the cameras were corrected for the latter techniques. During the MLOS-SMART processing image distortions and camera misalignments can be corrected to some extend by image interpolation on the basis of the optical transfer function [144] and by a volume self calibration [176].

In Fig. 5.9 the computation time needed for reconstruction of both time-steps is added (excluding the time needed for volume transfer to disc). The lower background intensity level of MLOS-SMART in comparison to FMART comes at the cost of a 4.5 times longer processing time on the same Workstation.

5.4.3 Particle displacement recovery

State-of-the-art cross-correlation processing is used for particle displacement recovery in both planar and volume PIV (see Sect. 2.5). Both algorithms employ a resolution pyramid that starts at a rather coarse grid and stepwise increases resolution while continually updating a predictor field [135, 128]. To increase processing speed, factor N image or volume downsampling is applied

by summing N^2 adjacent pixels or N^3 voxels, respectively. At a given resolution level integer-based sample offsetting is applied in a symmetric fashion using the estimate from the previous resolution step [174, 170]. Intermediate validation relies on normalized median filtering as proposed by Westerweel & Scarano [175]. Once the desired final spatial resolution is reached image or volume deformation based on third-order B-splines [161] is applied at least twice to further improve the match between the image or volumes and thereby improving the displacement estimates. The processing code is highly parallelized using OpenMP [121] to achieve optimal data throughput.

5.5 Error analysis

The evaluation of particle displacements (i.e. velocities) is subject to measurement uncertainties that consist of systematic and random errors. Possible sources of systematic errors are peak-locking [140], background noise due to stray light, ghost particle as well as strong velocity gradients within the interrogation region [172, 128]. Peak locking effects have not been observed in the displacement PDFs which is due to the sufficiently large particle image diameter of $d_I = 2 - 5$ pixels. Both inclined camera views were affected by light scattering off the airfoil which can cause self-correlation and a loss of signal in regions near the blade surface. This has been taken into account by evaluating TPIV measurements only up to a blade-normal distance of 1-2 mm. The broadening of the correlation peak due to velocity gradients has a negligible effect if variations of tracer velocity are small with respect to the corresponding width of the interrogation volume [172]. Doorne and Westerweel [39] estimate the critical velocity gradient over the interrogation region by $M\,|\Delta U_{crit}|\,\Delta t/d_I \leqslant 0.5$ which translates to $|\Delta U_{crit}| \geq 15\,\mathrm{m/s}$ for a particle image diameter of $d_I = 3$ pixels. Such strong variations of velocity occur within the axial extension of the interrogation volume in regions of the separated flow 2-3 mm above the blade. Thus image or volume deformation techniques (see Sect. 2.5) are applied for SPIV and TPIV to minimize the bias.

The random error of velocity components is influenced by the uncertainty of displacement detection (so-called cross-correlation noise) as well as by the

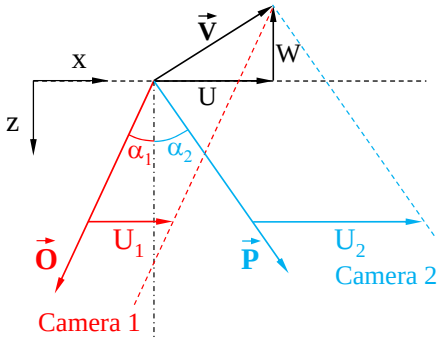

Figure 5.10: Stereoscopic measurement of U and W component from two projections (adopted from [128])

camera viewing geometry. In the following the dependence of the random error of each velocity components on the camera viewing geometry is determined.

In the present SPIV setup, velocity components U, V, W are recovered from particle image displacements in a thin sheet using two camera views. For example, Fig. 5.10 illustrates how each measured velocity component U_1, U_2 depends on Cartesian particle velocity components that is:

$$\begin{aligned} U_1 &= -\frac{\Delta X_{I1}}{M_1 \Delta t} = U - W \tan \alpha_1 \\ U_2 &= -\frac{\Delta X_{I2}}{M_2 \Delta t} = U - W \tan \alpha_2 \end{aligned} \tag{5.1}$$

Here, ΔX_{I1} and ΔX_{I2} are the image displacements along x in each camera, M_1 and M_2 describe both camera magnifications and Δt is the pulse delay. Furthermore, α_1 and α_2 describe the angels in the $x-z$ plane between the z axis and the lines of sight through the lens center to the recording plane of a particle [128]. The tangents of α_1 and α_2 can also be expressed in terms of components of the observation vectors $\mathbf{O}$ and $\mathbf{P}$ of each interrogation region:

$$\begin{aligned} \tan \alpha_1 &= \frac{O_x}{O_z} \\ \tan \alpha_2 &= \frac{P_x}{P_z}. \end{aligned} \tag{5.2}$$

In the same manner as provided in Eq. (5.1) and Eq. (5.2) equations can be found for velocity components U_i, V_i measured by each camera i. These equations can be combined to describe a general viewing geometry that is

defined through four observation vectors **O, P, Q, R**:

$$\mathbf{U}_{meas} = \begin{bmatrix} U_1 \\ V_1 \\ U_2 \\ V_2 \\ U_3 \\ V_3 \\ U_4 \\ V_4 \end{bmatrix} = \begin{bmatrix} 1 & 0 & -\frac{O_x}{O_z} \\ 0 & 1 & -\frac{O_y}{O_z} \\ 1 & 0 & -\frac{P_x}{P_z} \\ 0 & 1 & -\frac{P_y}{P_z} \\ 1 & 0 & -\frac{Q_x}{Q_z} \\ 0 & 1 & -\frac{Q_y}{Q_z} \\ 1 & 0 & -\frac{R_x}{R_z} \\ 0 & 1 & -\frac{R_y}{R_z} \end{bmatrix} \begin{bmatrix} U \\ V \\ W \end{bmatrix} . \tag{5.3}$$

Independent on whether two (i.e. SPIV) or four cameras are applied the velocity components U, V, W are over-determined, meaning that there are three unknown velocity components but either four (two cameras) or even eight (four cameras) known displacement components. Thus, equation Eq. (5.3) can be solved in a least-squares sense using the pseudo-inverse (c.f. [128]):

$$\begin{aligned} \mathbf{U}_{meas} =& \mathbf{A}\,\mathbf{V} \\ \Rightarrow\ \mathbf{V} =& (\mathbf{A}^T\,\mathbf{A})^{-1}\,\mathbf{A}^T\,\mathbf{U}_{meas} = \mathbf{A}^+\,\mathbf{U}_{meas} \end{aligned} \tag{5.4}$$

,

Because $\mathbf{V}$ depends linearly on the measurement vector $\mathbf{U}_{meas}$ each entry of $\mathbf{A}^+$ can be considered as first order partial derivative. Eq. (5.4) is explicitly solved for $\mathbf{A}^+$ using the Python library *SymPy*. Assuming that each of the components of $\mathbf{U}_{meas}$ is uncorrelated the partial derivatives can be used to estimate the combined velocity uncertainty [2]. For example, for SPIV the estimation of the combined standard deviation of the U-component is given by:

$$\sigma_U = \sqrt{\left[\frac{\partial U}{\partial U_1}\right]^2 \sigma_{U_1}^2 + \left[\frac{\partial U}{\partial V_1}\right]^2 \sigma_{V_1}^2 + \left[\frac{\partial U}{\partial V_2}\right]^2 \sigma_{U_2}^2 + \left[\frac{\partial U}{\partial V_2}\right]^2 \sigma_{V_2}^2} . \tag{5.5}$$

Here, $\sigma_{U_1}, \sigma_{V_1}, \sigma_{U_2}, \sigma_{V_2}$ are the standard deviations of measured velocities in each view. These uncertainties are estimated as follows:

$$\begin{aligned} \sigma_{U_1} = \sigma_{V_1} &= \frac{\sigma_{II}}{M_1\,\Delta t} \\ \sigma_{U_2} = \sigma_{V_2} &= \frac{\sigma_{II}}{M_2\,\Delta t} , \end{aligned} \tag{5.6}$$

Table 5.6: Uncertainties of velocity components based on observation vectors provided in Table 5.2 and a cross-correlation noise of $\sigma_{II} = 0.1$ pixel; uncertainties provided for TPIV does not include the effect of ghost particle

component	camera no. 1 & no. 3 (SPIV)		all cameras (TPIV)	
	σ [m/s]	σ/σ_u	σ [m/s]	σ/σ_u
U	0.73	1.00	0.52	1.00
V	0.79	1.08	0.55	1.06
W	1.46	2.00	1.03	1.98

where σ_{II} denotes the uncertainty of displacement detection. Due to the particle number densities and processing parameter provided in Table 5.5 a uncertainty of particle displacements of $\sigma_{II} = 0.1$ pixel can be assumed for regions without strong laser background [173].

Table 5.6 provides estimates of the measurement uncertainty for both the present SPIV setup (camera no. 1 and no. 3) and the present TPIV setup. Error estimation bases on observation vectors that coincides with the optical axis in each view which has been obtained through Tsai's camera model using *PIVmap 3.5.9*. Although TPIV bases on 3-D cross-correlation in voxel space rather than image space the uncertainties provided in Table 5.6 (column 4-5) are taken as an upper limit of measurement accuracy valid for a median z-plane of interrogation cells that is observed by all cameras. This 'upper accuracy limit' does not account for additional sources of error as, for example, elongation of particle reconstructions or the occurrence of ghost particle. The latter source of error depends on the applied reconstruction method and will be discussed in the following section on the basis of comparison of velocity results. Without these additional sources of error the uncertainty in velocity could be reduced by a factor of $1/\sqrt{2}$ if four cameras instead of two cameras are applied. On the other hand the uncertainty in the out-of-plane component W is twice the uncertainty of the axial component U independent on whether two or all four cameras are used.

Another aspect is that camera magnification varies over the measurement domain and is lower for interrogation positions located further away from the center of the measurement volume. Thus, for these regions, the uncertainty on the particle displacements measured by each camera is underestimated (Eq. (5.6)). The variation of the local magnification have been evaluated on the basis of

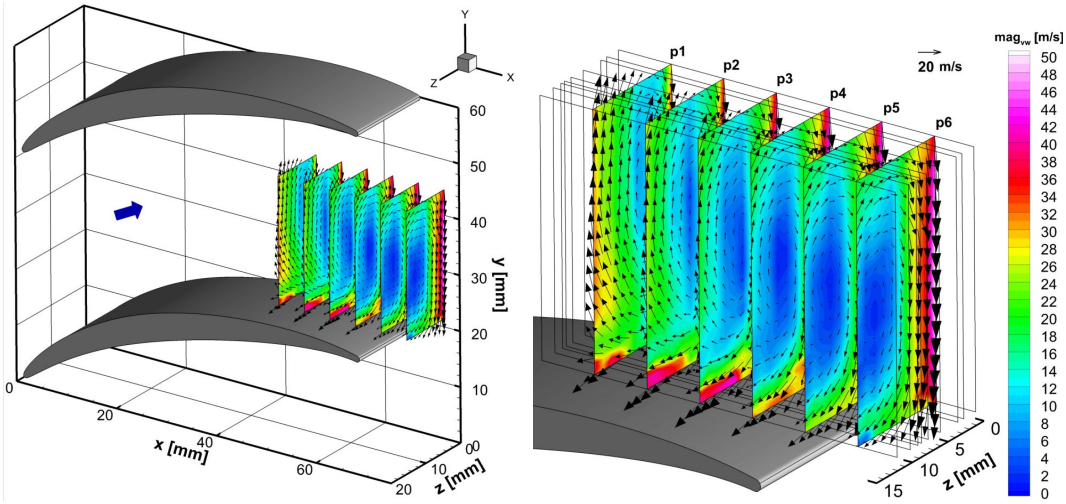

Figure 5.11: Time averaged secondary flow velocities obtained from SPIV measurements at 9 chord-wise planes each with 1mm sheet thickness; overview (left) and detailed flow field and boundaries of the SPIV planes (right)

calibration images. Near the rear corners of the measurement domain the uncertainties provided in Table 5.6 ar up to 1.9% higher for SPIV and up to 6% higher for TPIV due to this effect.

For the provided measurement setup the jitter of pulse separation time is below 50 ns which is considered as negligible in relation to a pulse delay of $\Delta t = 2\,\mu$s.

5.6 Discussion of results

Fig. 5.11 gives an overview of the secondary flow near the corner obtained by averaging $N = 510$ individual SPIV recordings from nine wall-parallel measurement planes. In order to emphasize the chordwise passage vortex evolvement, six orthogonal planes are extracted whose color represents the v, w magnitude while the vectors show the in-plane v, w velocity. Secondary flow velocities in-between the SPIV planes are obtained by inverse distance interpolation.

Due to interaction with the main flow the vortex is stretched along the end wall and velocities in the vicinity of the end wall are clearly increased. The separation region (see Fig. 5.1) causes an increase of secondary flow velocities near the blade's suction side.

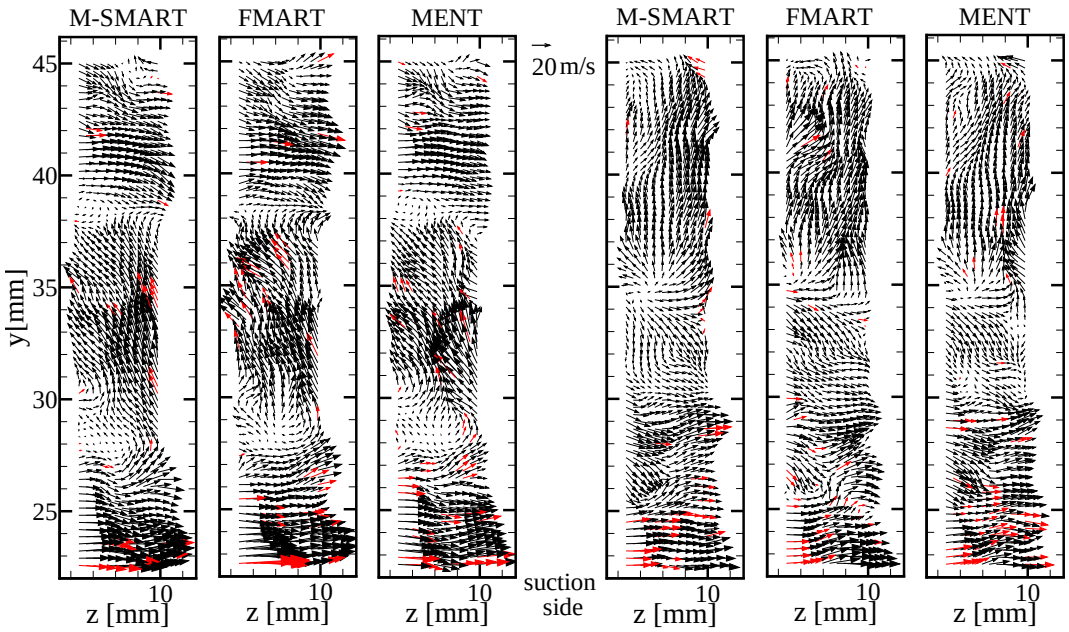

Figure 5.12: Two snap shots of secondary flow velocities in plane **p4** (see Fig. 5.11) obtained from TPIV using MLOS-SMART, FMART or MENT reconstruction techniques; the maximum out-of-plane velocity is 150 m/s; red vectors indicate interpolated outliers

Fig. 5.12 illustrates the turbulent character of the corner flow and compares single shots of secondary flow velocities obtained from TPIV involving MLOS-SMART, FMART and MENT reconstructions (boxcar average over $2 \times 2 \times 2$ nodes). The axial velocity component is about one order of magnitude faster and reaches up to 150 m/s. The instantaneous velocity fields obtained with MLOS-SMART and FMART contain more similarities with each other while MENT exhibits a few larger deviations.

Fig. 5.13 presents a comparison of the mean secondary velocity field obtained by SPIV and TPIV at $z = 6.25 - 9.75$ mm distance to the side wall. Again secondary flow velocities from SPIV are interpolated in between the actual measurement planes ($z = 6, 8, 10$ mm). Regions outside the common intersection of all cameras are blanked as well as regions where the light sheet intensity is clearly below 40%. Within each contour plane only the in-plane components are plotted to enhance the visibility of the secondary flow which otherwise would be lost in the presence of the strong out-of-plane component. The passage vortex can clearly be identified. The v, w magnitudes obtained by

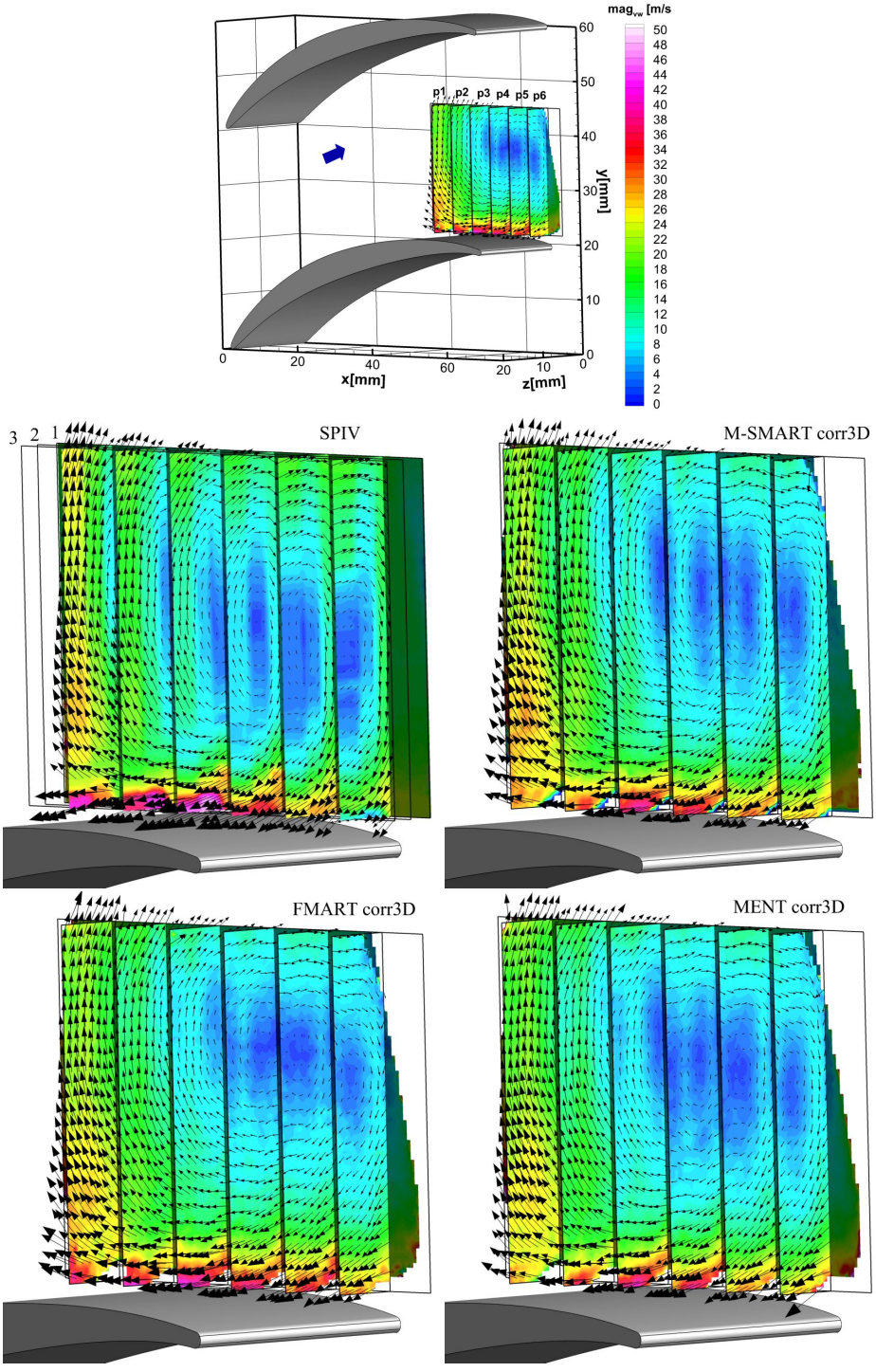

Figure 5.13: Secondary flow velocities of the corner flow; Average of $N = 500$ single shots at $z = 6.25 - 9.75\,\mathrm{mm}$ distance from the end wall; overview (top) and detailed flow field obtained with SPIV (middle left) and TPIV using MLOS-SMART (middle right), FMART (bottom left) and MENT (bottom right); vector skip: 3×2 in y and z

TPIV show a good qualitative agreement with the SPIV results. The increased secondary flow velocities near the blade's suction side can also be observed in SPIV results. The TPIV results exhibit lower magnitudes in this region due the greater susceptibility to background laser flare, especially for cameras no. 1 and no. 2. Both the FMART and MLOS-SMART reconstructions deliver very similar results in terms of secondary flow velocities. Velocity differences between MLOS-SMART and other tomographic reconstructions occur in regions near $z = 10\,\mathrm{mm}$ where the secondary flow velocities are slightly smaller for FMART and even smaller for MENT due to a higher number of ghost particles. Furthermore, the vortex core extension appears more stretched along y for MLOS-SMART in comparison to FMART. Possible sources of error are slight camera misalignments that lead to signal deterioration which will become particulary pertinent in regions of lower laser intensity (volume borders).

A more quantitative comparison of the velocity data, recovered by the respective methods was conducted by extracting coinciding profiles of velocity. Fig. 5.14 shows the mean velocity at $x = 60\,\mathrm{mm}$ located in front and on the back of the volume at $z = 6.25$, at $z = 9.75\,\mathrm{mm}$ and inside the light sheet at $z = 8\,\mathrm{mm}$, averaged over 500 samples. Stereoscopic PIV, FMART and MLOS-SMART reproduce the profile of the axial flow component u rather similar near $z = 8\,\mathrm{mm}$ and $z = 9.75\,\mathrm{mm}$. At the same z position, the u component obtained by MENT exhibits deviations of up to $5\,\mathrm{m/s}$ or 4% of the maximum mean axial velocity ($125\,\mathrm{m/s}$) while the w component shows deviations of up to $8\,\mathrm{m/s}$ probably due to the lower ghost suppression in comparison with FMART or MLOS-SMART (c.f. Sect. 3.3.3).

At $z = 6.25\,\mathrm{mm}$ the u-component measured by SPIV is up to $5\,\mathrm{m/s}$ slower in comparison to results obtained with MLOS-SMART and MART. The reason is probably a slight misalignment of the light-sheet position which does not fully coincide with the z plane under consideration. Additionally, the light sheet used for SPIV is almost twice as thick as the TPIV interrogation box, meaning that velocity gradients are spatially smoothed over a larger volume depth. This may also explain slight differences between SPIV and FMART and MLOS-SMART results regarding the secondary flow components v and w. Larger deviations between MLOS-SMART and FMART become visible at

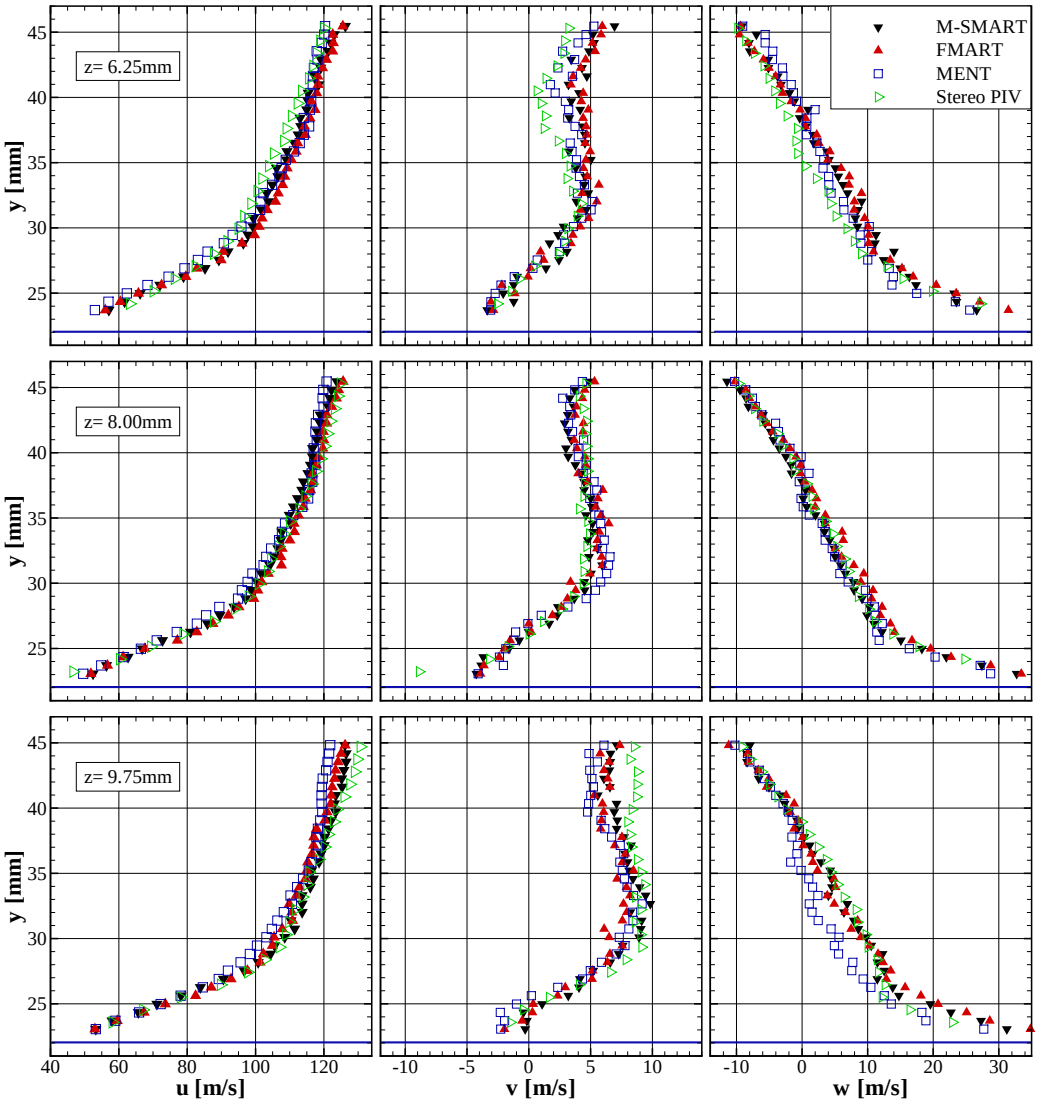

Figure 5.14: Comparison of mean velocity profiles extracted at $x = 60\,\mathrm{mm}$ and $z = 6.25\,\mathrm{mm}$ (top) $z = 8\,\mathrm{mm}$ (middle) $z = 9.75\,\mathrm{mm}$ (bottom) by the respective methods; the blue line marks the suction side blade surface

the back of the volume ($z = 9.75mm$) where both SNR and laser intensity are low (about 50% drop in intensity compared to center plane). Toward the back of the volume, correlation analysis of FMART and MENT reconstructions deliver significant lower v velocities in comparison to MLOS-SMART, as already observed in the qualitative comparison. The displacements are biased by up to $-3\,\mathrm{m/s}$ ($\Delta v = 0.3\,\mathrm{voxel}$). The reason for the deviation is probably the missing self-calibration (c.f. Sect. 2.2) which is not yet implemented in the camera model used for FMART and MENT. The self-calibration procedure that has

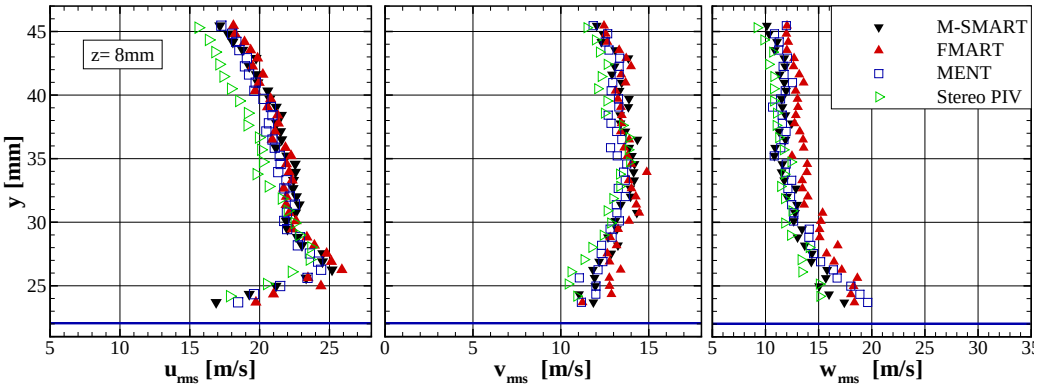

Figure 5.15: Comparison of RMS profiles extracted at $x = 60\,\text{mm}$ and $z = 8\,\text{mm}$ for SPIV and TPIV; the blue line marks the suction side blade surface

been applied for MLOS-SMART revealed disparities in the order of 1.0 and 1.2 pixel at $z = 11\,\text{mm}$ for cameras no. 2 and no. 3 (c.f. Table 5.4), which is not negligible compared to particle image sizes between $2 - 5$ pixels.

A comparison of velocity fluctuations in the middle of the thick light sheet at $z = 8mm$ reveals almost similar RMS values for MENT and MLOS-SMART (see Fig. 5.15). FMART exhibits slightly higher fluctuations regarding the w component and a wider dispersion of RMS values in both v and w. This is accompanied by slightly lower validation rates (87,6% instead of 89,3% for MLOS-SMART). The reason is probably that variations of the local particle image shape (blur or other distortions) are not taken into account for FMART due to a lack of a calibration procedure to determine the local point-spread function. It has been observed that the particle image size varies between 2 and 5 pixel over volume depth and is partially elliptical due to off-normal imaging through perspex windows (c.f. Table 5.2). By ignoring any local variation of the particle image size the FMART reconstruction is subject to increased noise. Axial velocity fluctuations (u_{rms}) obtained from SPIV deviate more than -12% in comparison with TPIV results. One reason for this could be that TPIV and SPIV results base on two different image data-sets each of both containing only 500 samples. To achieve comparability of both results would require statistical convergence of the RMS requiring significantly more than 500 samples [157, 180].

5.7 Conclusions

The investigation presented in this chapter demonstrates the applicability of volumetric PIV in a highly loaded compressor cascade at $\mathrm{Ma}_1 = 0.60$. By using a 50 mJ light-sheet probe and four simultaneous camera views it is possible to measure the high-speed corner flow in a volume of $36 \times 24 \times 3.5\,\mathrm{mm}^3$ at a final resolution of $54 \times 74 \times 13$ vectors at a spacing of 0.64 mm in x (chordwise direction) and a spacing of 0.32 mm in y and z using a window overlap of 50%. Aside from conventional particle volume reconstruction using MLOS-SMART, the fast multiplicative algebraic reconstruction technique (FMART) and the Maximum Entropy Technique (MENT) are applied with the intention to speed up reconstruction time. The measurements were complemented with stereoscopic PIV (SPIV) measurements at distinct planes to provide a basis for comparison between the employed volumetric techniques.

The instantaneous and time-averaged velocity fields obtained with MLOS-SMART and FMART contain more similarities with each other while MENT exhibits a few larger deviations. Averaged results of the corner flow from SPIV and volumetric PIV are presented to show qualitative conformance to the expected flow. Due to slight misalignments, the SPIV light-sheet position does not fully coincide with the TPIV z planes under consideration. This is considered to result in velocity deviations of up to 5 m/s between SPIV and TPIV at a maximum mean axial velocity of 125 m/s. The quantitative comparison of mean velocities revealed that MLOS-SMART and FMART reconstruction recover very similar velocity profiles except in regions of a low signal-to-noise ratio and a low laser intensity. These deviations occur near the outer boundaries of the light-sheet where SMART recovers mean velocities that are 3 m/s faster compared to FMART along y ($\Delta v = 0.3$ voxel). A probable reason seems to be differences of both camera calibration models. The SMART camera model includes a correction of particle image distortions (OTF calibration) and a disparity correction (volume self-calibration) which both are not yet implemented in the FMART and MENT camera model. The slightly higher velocity accuracy of SMART comes at the cost of a 4.5 times longer processing time in comparison to FMART which shows the potential saving in reconstruction time.

In the present case the camera views aligned with the span of the airfoil were only weakly affected by the laser light scattering off the airfoil, whereas the inclined camera views were strongly affected by light scattering off the airfoil which caused a loss of signal in these areas. Thus, TPIV measurements were possible up to a blade-normal distance of 1-2 mm. Similarly measurements in close proximity to the perspex endwall are hampered by light scattered by surface scratches and seeding residue. The reason for this seems to be slight vibrations of the Laval nozzle located at the light-sheet probe tip, which leads to stray light that is scattered off the endwall.

Chapter 6

Feasibility study on tomographic spray shadowgraphy

While the first part of this thesis is dedicated to implementation of TPIV in a transonic cascade wind tunnel the second part is aiming for instantaneous measurements of three-dimensional spray distributions and droplet velocities in fuel sprays. A similarity to TPIV is given by the fact that the technique proposed in this chapter draws upon reconstruction techniques similar to those for TPIV. *Tomographic shadowgraphy* relies on simultaneously acquired shadow images of a spray field obtained from different views using inline illumination with incoherent pulsed LED light for each view (see Fig. 6.1). After calibration of the multiple camera configuration, spray ligaments and droplets can be reconstructed by means of tomographic reconstruction techniques. Parts of the experimental results presented in this chapter are published in Experiments in Fluids [197].

One of the intentions of the study is to establish a methodology to characterize the smallest resolvable droplet size over the depth-of-field and to assess reconstruction algorithms known from TPIV for their suitability to determine the three-dimensional instantaneous spray distribution. In contrast to tomographic PIV which relies on a homogeneous distribution of particles within a well-defined volume, tomographic reconstruction of sprays has to deal with pronounced local variations of droplet number density and size. Depending on the atomization process, spray extensions can be irregular shaped and the

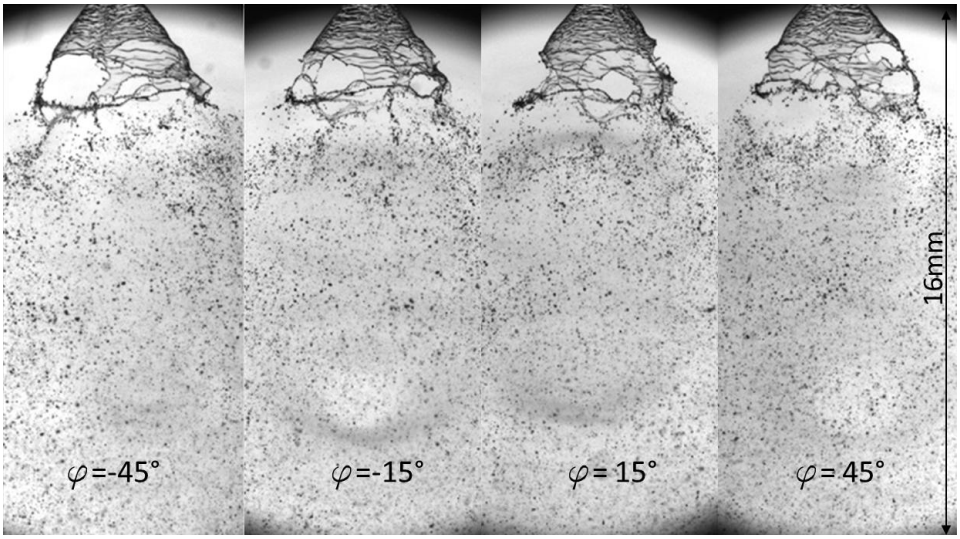

Figure 6.1: Simultaneous shadow images of a hollow cone spray obtained from different observation angles

depth-to-width aspect ratio of a droplet volume can be significantly larger than in a thick sheet TPIV experiment. Contrary to the edges of light sheet illumination in TPIV, the volume depth is bounded by the shape of the spray distribution, by the depth of field and the common intersection of all inline illumination pathes. Hence, parameter as source density or particle image density are difficult or even impossible to predict and does not allow a preliminary estimate of the expected reconstruction quality of an experimental setup. Therefore, in a first step, reconstruction quality is assessed on the basis of flat fan and hollow cone water sprays with known droplet sizes and known spatial spray distribution.

During this proof-of-concept study the technique's potential is evaluated with regard to a later application in swirled fuel sprays. In contrast to the cascade experiment (c.f. Sect. 5.2) with a depth-to-width aspect ratio of 0.1, camera calibration for swirled fuel sprays should be able to deal with deep volumes and aspect ratios up to 0.5. Therefore, within the present study camera calibration tests are performed to verify the accuracy of various mapping functions for deep volume camera calibration in fuel sprays.

Another aspect is that droplet velocities of swirled fuel sprays in injector representative environments can reach $80 - 150\,\mathrm{m/s}$ which does not allow time-

resolved acquisition with a sufficient spatial resolution. For example, state-of-the-art imaging technology achieve acquisition rates of 0.5 MHz at image resolution of about 30 Kpixel which is insufficient for reliable volume reconstruction. Hence, reconstruction algorithms which make use of multiple temporal samples [142] to improve ghost suppression are not considered here. Rather, only classic two-frame techniques are considered here. A comparison of MLOS, MENT and SMART volume reconstruction results is conducted on the basis of instantaneous and averaged reconstructed 3-D intensities of shadowgraphs of the hollow cone spray which has a well defined droplet distribution.

The chapter is arranged as follows: The first section (Sect. 6.1) discusses models of shadow image formation and derives relations between imaging parameter and droplet visibility. In section 6.2, the optical setup of the proof-of-concept study is presented. Section 6.3 describes the calibration procedure and evaluates effects of calibration marker type and spacing and effects of translation stage inaccuracies on calibration accuracy with regard to large depth-to-width aspect ratios. Within section 6.4 the smallest visible droplet sizes and their depth of field are derived for the previously described tomographic and setup. The spatial sampling rate is determined from a trade-off between required resolution and computational effort. Section 6.5 describes the image processing to finally obtain 3-D spray distributions. In Sect. 6.6 a qualitative comparison of different reconstruction techniques is presented on the basis of averaged 3-D intensities. The chapter ends with a discussion of results and conclusions.

6.1 Modelling of droplet image formation

If the spatial distributions of fuel sprays and droplet velocities shall be quantitatively captured using tomographic shadowgraphy, then the boundary conditions of the experiment have to be defined in terms of smallest visible droplet size and the depth of field. However, it is not obvious which part of a spray size fraction can be captured by the technique. The smaller the droplet or the more distant from the focal plane, the more blurred is the shadow image [17]. Large drops may have a higher image contrast and thus are visible over

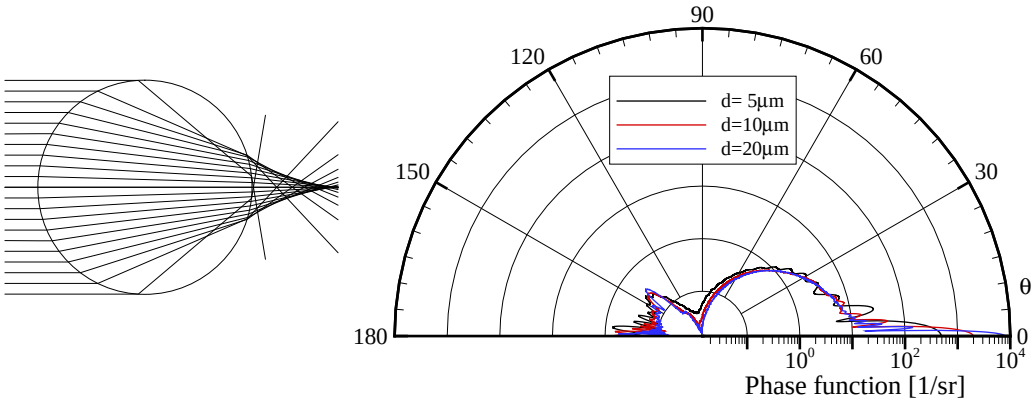

Figure 6.2: Light refraction of a spherical droplet (*left*) and Mie scattering of non-polarized polychromatic LED light ($\lambda = 460 - 600\,\mathrm{nm}$) by spherical kerosene droplets of different diameters in air (*right*)

a greater focal depth than small drops [50] and the depth-of-field of each view varies with the droplet diameter [86]. This raises the question on how optical resolution and image processing influence the shadow image contrast and how droplet visibility varies with the depth of the reconstructed domain. To answer these questions, physical aspects of droplet shadow image formation are discussed in this section.

Tomographic shadowgraphy relies on shadow images or shadowgraphs of a spray field using polychromatic inline illumination with pulsed LED light. The term 'shadow image' does not fully address the involved processes because, for example, the absorption coefficient of kerosene for visible light is rather low ($5.0e-07$ at $20°C$ and $1.7e-6$ at $280°C$ [127]). Due to low absorption, most of the photons impacting on a kerosene droplet are deflected by reflection, refraction and diffraction. Images of small droplets in forward scattering appear as dark spots on a bright background because the major part of the deflected light is not captured by the imaging lens. The light deflection is evident from light refraction of a spherical droplet as shown in Fig. 6.2 (left). The contribution of further individual reflections or refractions might be identified by the Debye series which gives an equivalent solution of the electromagnetic scattering of spheres as represented by the generalized Lorenz-Mie theory (GLMT) [73, 89].

The generalized Lorenz-Mie theory offers a comprehensive solution including all scattering processes caused by a spherical droplet, such as external and internal reflections, refractions and surface waves [18]. As an example of Mie calculations, Fig. 6.2, right, shows the angular intensity distribution of non-polarized polychromatic LED light ($\lambda = 460 - 600\,\mathrm{nm}$) by spherical kerosene droplets in air calculated with *MiePlot 4.5* [88]. The scattered intensity is expressed in terms of the so-called phase function which integrated over all scattering directions yields unity. Hence, the phase function can be seen as the angular distribution of a droplet transmission coefficient if absorption can be neglected. The transmission coefficient has direct influence on the shadow image contrast and visibility as discussed below.

A few modelling approaches of droplet shadow image formation can be found in literature. Ren et al. [132] simulated the droplet scattering within the lens aperture based on the GLMT followed by computation of the Huygens-Fresnel integral to find focused and unfocused droplet image intensities. Furthermore, the authors determine the local droplet image intensity by convolution of the irradiance distribution of the object with the point spread function (PSF) of the imaging system by following Goodmann [61]. The PSF approach as applied by Ren et al. bases on convolution of a Gaussian PSF and an opaque disc with the latter representing the ideal geometric droplet image. In case of forward scattering and polychromatic illumination, the results of GLMT simulations corresponded well with the PSF approach.

Blaisot and Yon [17] complemented the PSF approach of Ren et al. and developed a comprehensive spray imaging model to enable measurements of droplet sizes within diesel sprays with a single camera. Later on, this model was used by Fdida and Blaisot [50] to facilitate droplet sizing in thick volumes with a depth of one-tenth of the field-of-view width. In what follows the imaging model of Blaisot and Yon will be described in detail to provide better inside into droplet shadow image formation and the influence of imaging parameter on the droplet image contrast and size.

In the imaging model of Blaisot and Yon, the radial intensity distribution of a droplet shadow is modeled by the convolution of a ideal geometric droplet image and the point spread function in image space, with the latter describing

the resolving capability of the imaging system. The point spread function is considered as a Gaussian and was calibrated as a function of the object's position along the optical axis (z):

$$s(r,z) = s_0\, exp\left(-\frac{2r^2}{\chi^2(z)}\right). \tag{6.1}$$

In Eq. (6.1) s_0 represents a normalization factor, r is the radial droplet image coordinate and χ is the half-width of the point spread function. The geometric droplet image is represented by a slightly transmitting disc of radius $a_I = M\,a$ which intensity distribution is defined as follows:

$$o_g(x_I, y_I) = 1 - (1-\tau)\Pi(r)\,. \tag{6.2}$$

Here, τ is the contrast coefficient representing the droplet transmission within the bounds of the lens aperture, r is the radial image coordinate ($r = \sqrt{x_I^2 + y_I^2}$) and Π is the rectangle function:

$$\Pi(r) = \begin{cases} 1 \text{ for } \frac{r}{a_I} < 1.0 \\ 0 \text{ otherwise.} \end{cases} \tag{6.3}$$

In the imaging model of Blaisot and Yon, the image plane coordinates of each droplet are linearly related via magnification M $(x_I, y_I) = (x\,M, y\,M)$ and during their experimental verification telecentric lenses are used to achieve constant magnification along volume depth [50].

The convolution of the slightly transmitting disc and the Gaussian PSF finally leads to:

$$\tilde{i}(\tilde{r}) = 1 - 2\,(1-\tau)\,exp(-\tilde{r}^2) \int_0^{\tilde{a}} exp(-\rho^2)\, I_0\,(2\tilde{r}\rho)\, d\rho\,, \tag{6.4}$$

where $\tilde{r}$ is the non-dimensional radial image coordinate $\tilde{r} = \sqrt{2}r/\chi$ and $\tilde{a}$ is the non-dimensional droplet image radius $\tilde{a} = \sqrt{2}a_I/\chi$ both with regard to the half with of the PSF; I_0 is the Bessel function of the first kind and zero order and ρ denotes the integration argument.

While the PSF width depends on the optical setup and can be gained from calibration (e.g. knife edge technique [30, 29]) the contrast coefficient τ char-

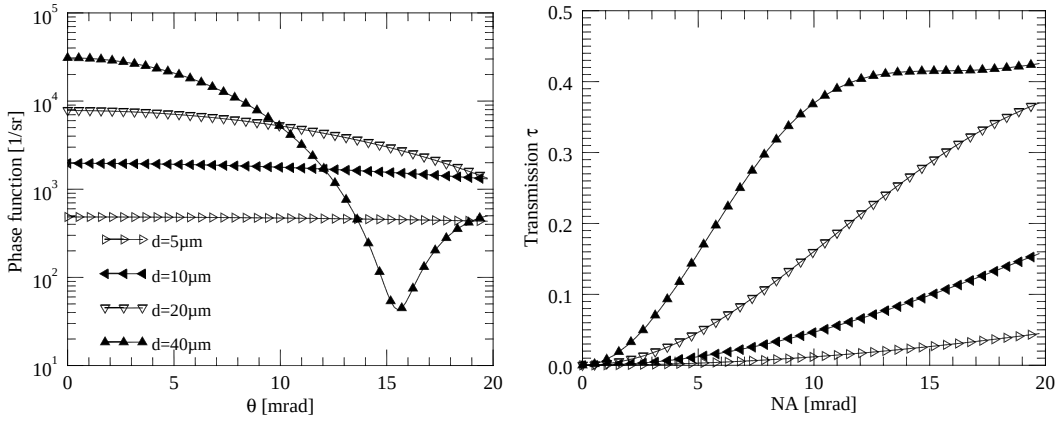

Figure 6.3: *Left* Angular distribution of forward-scattered intensity of non-polarized and polychromatic light ($\lambda = 460 - 600\,\mathrm{nm}$) upon spherical kerosene droplets in air ($T_k = 450K$,$T_a = 473K$), *Right* droplet transmission versus lens aperture (*right*)

acterizes the amount of transmitted light by the droplet [17] that is collected by the lens. In order to obtain the droplet transmission, the angular intensity distribution is simulated with *MiePlot 4.5* [88] for a typical size range in kerosene sprays, then normalized by the total amount of scattered light and then integrated numerically over the solid angle of the lens aperture.

For example, Fig. 6.3, left shows the simulated angular distribution of the forward-scattered intensity for polychromatic LED light ($\lambda = 0.46 - 0.60\,\mu\mathrm{m}$) of random polarization by spherical kerosene droplets at temperatures of $T_k = 450K$ and air temperatures of $T_a = 473K$. The range of scattering angles was set in a way that the maximum angle covers the object-sided lens aperture corresponding to $f_\# = 12$ at $M = 1$. The scattered intensity is expressed in terms of the phase function which integrated over all scattering directions yields unity. While forward scattering by small droplets of $d = 10\,\mu\mathrm{m}$ does not show a strong angular dependency, larger droplets of $d = 50\,\mu\mathrm{m}$ exhibit pronounced variations with a five times higher on-axis intensity and an additional intensity minimum at a scattering angle of 15.5 mrad. If absorption can be neglected, integration of the phase function over the solid angle yields the droplet transmission as a function of the object-sided numerical aperture which is plotted in Fig. 6.3 (right). Clearly, the transmission of a larger droplet shows a strong size dependency which is in contradiction with assumptions of Blaisot and Yon [17] who applied a constant transmission coefficient independent of

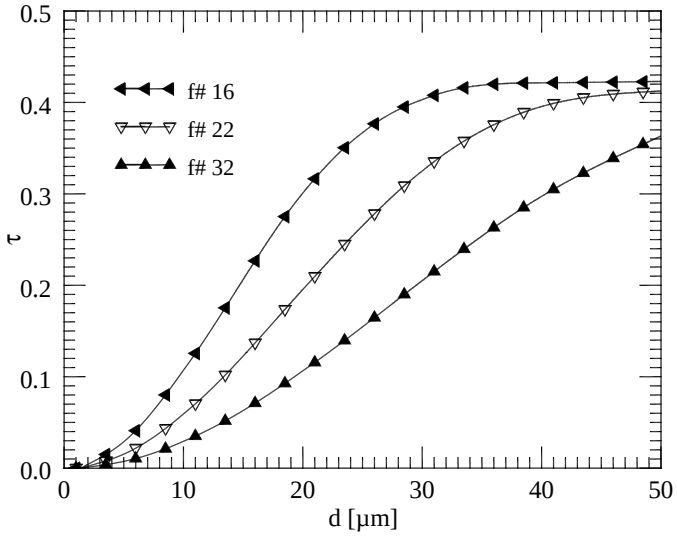

Figure 6.4: Transmission coefficient versus droplet diameter for different f-numbers at $M = 1$

droplet size.

Fig. 6.4 shows the transmission coefficient as a function of droplet diameter obtained from integration of the phase function over the object-sided solid angle of the numerical aperture. If the numerical aperture is small (NA $< 6°$), the object-sided numerical aperture of the lens can be expressed as:

$$\mathrm{NA} = \frac{1}{2\, f_{\#}\, (1 + 1/M)}\,, \tag{6.5}$$

where M is the magnification and $f_{\#}$ is the f-number of the lens. Eq. (6.5) is valid under the assumption that the position of the lens entrance pupil coincides with the object-sided principle plane.

Once the transmission coefficient is known, the shadow image intensity profile of kerosene droplets of different sizes can be calculated according to Eq. (6.4). For example, Fig. 6.5 shows simulated image profiles at a magnification of $M = 1$, a width of the point spread function of $\chi = 10\,\mu$m and $f_{\#} = 22$. Droplets which have a diameter which is five times larger than the half width of the point spread function (PSF) produce a flat-top shadow image with smoothed edges. The normalized minimum intensity of such flat top droplet images is given by the droplet transmission coefficient. Shadow images of droplets with a diameter considerably less than the PSF half-width are more smoothed with a much less pronounced intensity minimum.

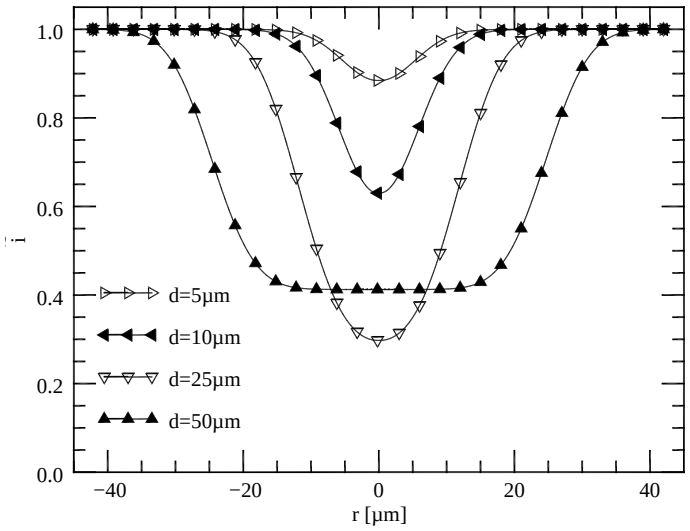

Figure 6.5: Droplet image profiles for different droplet diameter and a PSF half-width of $\chi = 10\,\mu$m at $f_\# = 22$ and $M = 1$

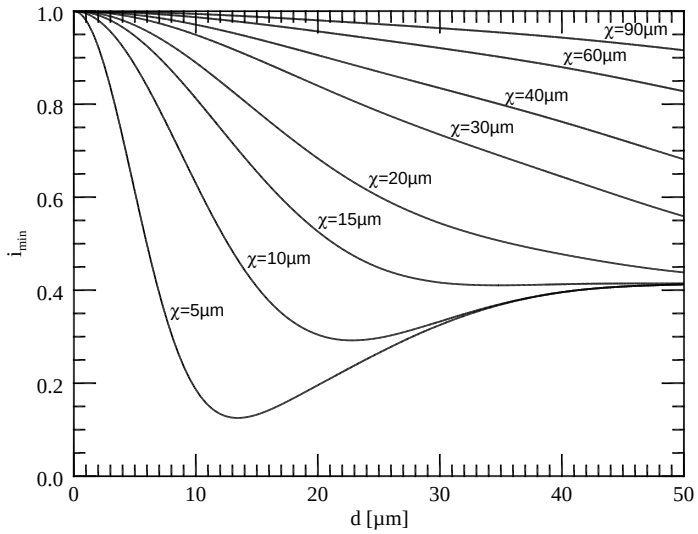

Figure 6.6: Minimum intensity of a droplet shadow image as a function of droplet diameter for different sizes of the PSF half-width at $f_\# = 22$ and $M = 1$

The normalized minimum image intensity of a droplet image profile or the shadow intensity attenuation can be calculated by the following equation (c.f. [17]):

$$\tilde{i}(0) = i_{min} = 1 - (1 - \tau)(1 - exp(-\tilde{a}^2). \tag{6.6}$$

The minimum intensity obtained with Eq. (6.6) can also be seen as the signal-strength of a droplet shadow image. Fig. 6.5 (right) shows the shadow intensity attenuation versus droplet diameter at $M = 1$, $f_\# = 22$ for different PSF widths and for droplet sizes up to $d = 50\,\mu$m. The intensity has a pronounced minimum if the PSF half-width is significant smaller than $\chi = 15\,\mu$m. At lower optical resolution ($\chi > 15\,\mu$m) the shadow image intensity decreases monotonously with increasing droplet diameter down to a boundary value

which is given by the transmission plateau shown in Fig. 6.4. That is in line with observations reported by Blaisot and Yon [17] who measured the strongest intensity decrease on the largest droplet images. In effect the shadow intensity attenuation or rather droplet contrast is a rough indicator of droplet size. This is valid as long as droplet diameter and lens apertures are small enough not to produce glare points in the shadow images. Aside from size dependency of the droplet contrast, the normalized minimum intensity of the shadow image given in Eq. (6.6) is a reasonable parameter in order to decide whether a droplet would be visible or not along volume depth. After image normalization (flat-field correction) a threshold of visibility can be defined from fluctuations of the LED background illumination and image noise.

The remaining unknown is the width of the point spread function which depends on the optical access, camera resolution and image processing and has to be gained from calibration of the tomographic setup as described in Sect. 6.4. The experimental setup of a proof-of-concept is described in the next section.

6.2 Experimental setup of feasibility tests

The proof-of-concept study is conducted with good optical accessibility to hollow cone and flat fan water sprays at ambient conditions.

The optical setup outlined in Fig. 6.7 involves four synchronized double-frame (PIV) cameras angled 30° with respect to each other. The water spray nozzle, either with flat fan or hollow cone spray geometry, is placed at the intersection of the camera views inside a 12-sided polygon-shaped chamber. The hollow cone spray is dispersed by a pressure-driven simplex swirl nozzle with $D_0 = 0.2\,\mathrm{mm}$ (spray angle 63°). The flat fan spray is created with a nozzle with $D_0 = 0.23\,\mathrm{mm}$ (spray angle 65°). The injection pressure is fixed at 6 bar which is below the optimal operating pressure but has the advantage of featuring the evolving spray within the imaged region downstream of nozzle exit. This allows the observation of all stages of liquid disintegration from film breakup into ligaments and further into droplets (see Fig. 6.8). For the given pressure of 6 bar the manufacturer of the hollow cone nozzle specifies a Sauter mean droplet diameter of 25 μm with a size distribution of 14...100 μm.

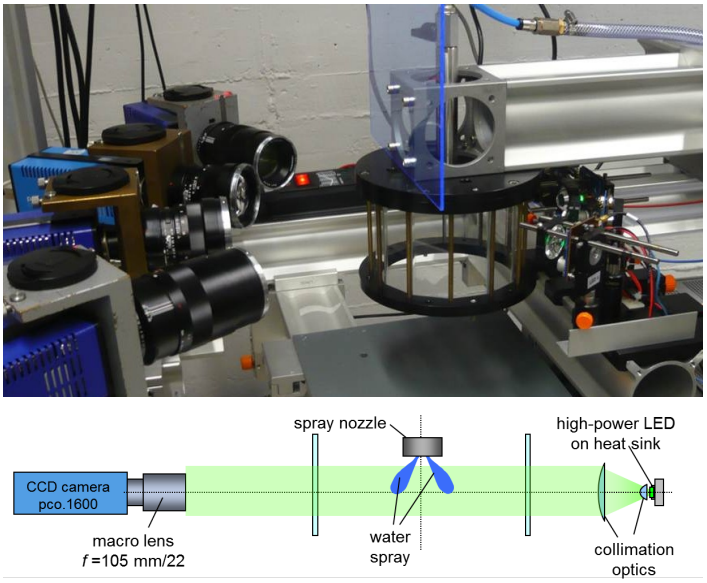

Figure 6.7: Photograph of the experimental setup for tomographic shadowgraphy; *bottom*: schematic of imaging configuration for one of four views

Table 6.1: Spray imaging parameters

View	$\approx \varphi$	$f_\#$	$f\,[mm]$	$\approx M$	$d_\mathrm{A}\,[\mu\mathrm{m}]$	$I_\mathrm{f,max}\,[\mathrm{A}]$
1	45°	22	100	0.45	41	25
2	15°	16	85	0.43	30	9.9
3	-15°	16	85	0.44	30	10
4	-45°	22	100	0.43	41	26

Inline illumination is provided for each camera by a current-pulsed, high power green LED (Luminus, SST-90, green) whose light is collimated with aspheric condenser lens of $f = 30\,\mathrm{mm}$ [183]. Peak currents between $I_\mathrm{f,max} = 10...25\,\mathrm{A}$ at $t_p = 1\,\mu\mathrm{s}$ were found sufficient to provide bright-field intensity levels at half camera dynamic range at lens apertures $f_\# = 16...22$. The pulse separation was set to $\Delta t = 6.4\,\mu\mathrm{s}$. At given peak current the light has a wavelength of about 525 nm at a bandwidth of 35 nm (FWHM).

With the aid of Scheimpflug camera mounts the focal planes of all cameras are aligned with the calibration target positioned at the center of the imaged volume. Using imaging lenses with small apertures, a common volume of approx. $18\times17\times9\,\mathrm{mm}^3$ ($w\times h\times d$) can be imaged with minimal blurring due to depth of field variations. The respective exposure parameters are summarized in Table 6.1. The two outer cameras are equipped with macro lenses (Zeiss Macro Planar, 100 mm) while the inner cameras use conventional lenses (Zeiss Planar, 85 mm) with close-up extension rings. The resolution of the focal plane array (CCD) for each view is 1600×1200 pixel at a mean magnification

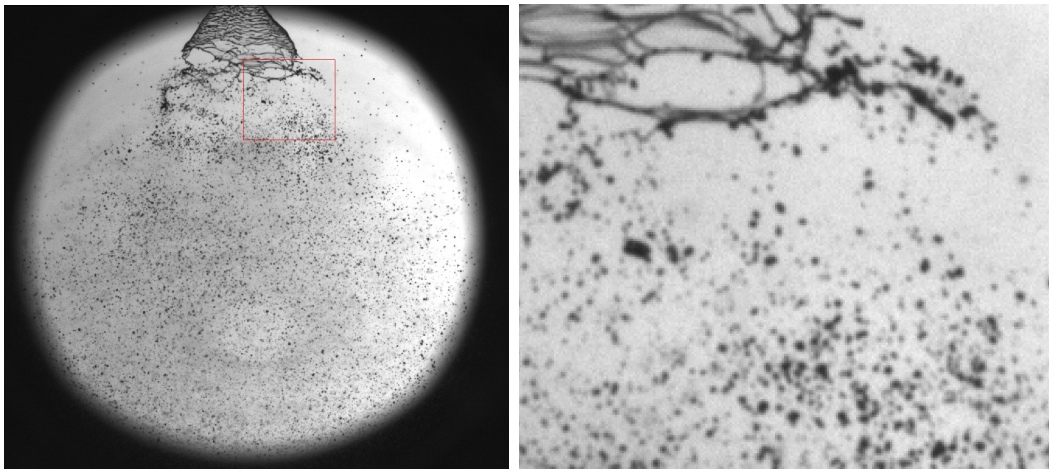

Figure 6.8: Sample droplet shadow image recording obtained for camera view no. 4 ($-45°$) of the hollow cone spray prior to contrast enhancement. The magnified region has a width of about 4 mm or 240 pixels.

of about 60 pixel/mm. The pixel size is 7.4 μm which is below the diffraction limited droplet image diameter d_A (see Eq. (2.5)). Below this size the true size of droplets can not be inferred from the shadowgraph images. In the present application this translates to droplet image diameter smaller than 4...5 pixel or $\approx 30\,\mu$m.

6.3 Implementation of camera calibration

The traversal of the calibration target along z-axis by a motorized translation stage allows the sequential recording of 3-D points in space at various depths. The procedure raises questions about which type of calibration marker and which calibration stage are the most appropriate for deep volumes in terms of accuracy. In order to answer these questions calibration tests are performed by application of different types of markers and extraction algorithms on the views no. 1 and 2 in the previously described spray imaging setup. The influence of positioning errors on calibration accuracy has already been observed in the thin sheet calibration described in Sect. 5.3. Pattern dimensions (e.g. marker spacing), depth of focus and the processing chain of feature extraction also may have influence on calibration accuracy.

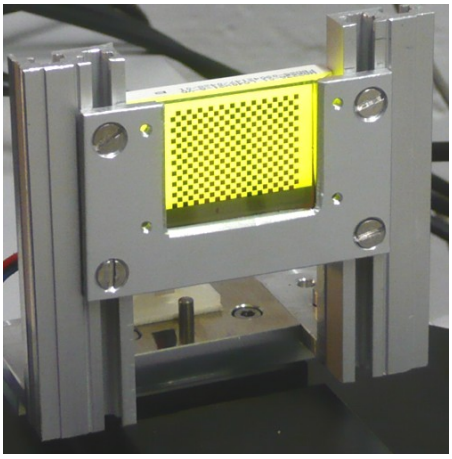

Figure 6.9: Micro-lithographic quality calibration target on traverse with LED back illumination

6.3.1 The effect of calibration marker type and spacing on calibration accuracy

Two types of calibration patterns are manufactured on lithographic photomasks: chessboards and transparent dots. The markers on glass are backlit with a display LED to obtain homogenous illumination (Fig. 6.9). Opaque regions of the pattern consist of a 100 nm thick layer of chromium oxide and have a lateral dimensional tolerance of ±300 nm. For the calibration tests described herein grids of regularly spaced dots or checkerboards were used. Two different isotropic spacings are used in a volume of about $22 \times 17 \times 9\,\mathrm{mm}^3$: $s_1 = 0.75\,\mathrm{mm}$ ($30 \times 23 \times 13$ markers) and $s_2 = 1.00\,\mathrm{mm}$ ($23 \times 18 \times 10$ markers).

Accuracy assessment of feature extraction bases on average residuals of the reprojection error Eq. (A.3) over all object-to-image correspondence in the calibrated volume. In this case, a pinhole camera model is fitted followed by a least squares minimization (see also Sect. A.2.1). Point correspondences are found using either *PIVmap 3.5.9* (PIVTec GmbH) or *OpenCV 2.4.9* [20]. In *PIVmap*, marker extraction is based on dot detection by cross-correlation with a similar-shaped template [179]. Prior template cross-correlation, chessboard corners are first converted into dots by a chain of partial derivatives as visualized in Fig. 6.10 and then smoothed by a low pass filter to suppress camera noise. During feature detection the particular template radius and the low pass kernel size are optimized in order to minimize the reprojection error.

In *OpenCV*, point correspondences in the checkerboard images are found in two

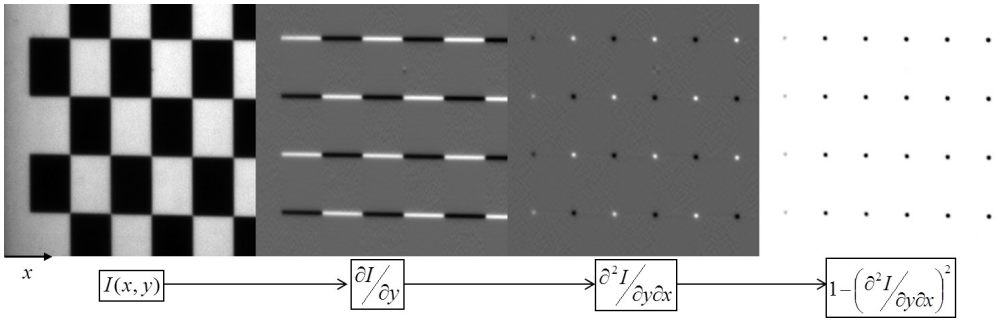

Figure 6.10: Processing on chessboard images prior sub-pixel corner detection, image intensities are scaled in the range of $0-1$ after each partial derivation

Table 6.2: Mean residuals of world-to-image pinhole mapping in [pixel] after least squares minimization of the reprojection error of a volume of $22 \times 18 \times 10\,\mathrm{mm}^3$

Pattern type	Spacing [mm]	Processing	View 1 $\varphi \approx 45°$			View 2 $\varphi \approx 15°$		
			$\overline{\lvert\varepsilon_x\rvert}$	$\overline{\lvert\varepsilon_y\rvert}$	$\bar{\varepsilon}$	$\overline{\lvert\varepsilon_x\rvert}$	$\overline{\lvert\varepsilon_y\rvert}$	$\bar{\varepsilon}$
Chessboard	0.75	PIVmap 3.5	0.056	0.048	0.080	0.076	0.049	0.099
Chessboard	0.75	OpenCV 2.4	0.059	0.050	0.084	0.0776	0.050	0.101
Points $d = 90\mu m$	0.75	PIVmap 3.5	0.057	0.048	0.082	0.081	0.048	0.103
Chessboard	1.00	PIVmap 3.5	0.052	0.050	0.079	0.073	0.050	0.097
Chessboard	1.00	OpenCV 2.4	0.054	0.052	0.082	0.075	0.051	0.099
Points $d = 120\mu m$	1.00	PIVmap 3.5	0.061	0.049	0.086	0.085	0.048	0.106

steps. After applying an adaptive thresholding, second order partial derivatives of the image are formed, followed by a local smoothing to find pixel positions of the corners using the function *cvFindChessboardCorners*. Corners coincide with local intensity peaks in the gradient filtered image. Sub-pixel accuracy in the vicinity of these peaks is achieved by iterative searching the radial saddle point of intensity by means of Harris corner detection [63] using the *OpenCV* function *cvFindCornerSubPix*.

Table 6.2 compares averaged residuals of the least squares minimization of the reprojection error of a pinhole camera mapping (views no. 1 and no. 2 in Table 6.1. If the average reprojection error $\bar{\varepsilon}$ of view no. 1 and no. 2 is considered, it can be seen, that in the majority of cases the lowest residuals are obtained if chessboard patterns are applied. Sub-pixel position detection by cross-correlating the postprocessed chessboards with a circular-shaped template (*PIVmap*) leads to slightly lower residuals in comparison to the Harris corner sub-pixel detection in *OpenCV*. The doubling of point correspondences

by lowering the feature spacing from 1 mm to 0.75 mm does not increase the accuracy of the camera calibration. The 4140 point correspondences at 1 mm spacing are sufficient to solve the system. If dots are used the residual reprojection error decreases slightly with increasing dot number. The reason for this is that the dot diameter also decreases proportional to the dot spacing. Larger dots and therefore larger template diameter can produce higher uncertainties in the position detection by cross-correlation especially at oblique viewing. This is because perspective projection is not shape preserving and distorts dot images into ellipses depending on the viewing angle. This distortion can bias sub-pixel position detection by cross-correlation with circular templates [66]. The bias error increases with dot diameter which is also confirmed by simulations published in [109]. This bias error is one reason why the chessboard patterns should be used instead of dots because positions of line crosses will be unbiased unlike any circular or rectangular shaped marker [66]. Moreover, no marker diameter has to be defined if chessboards are used.

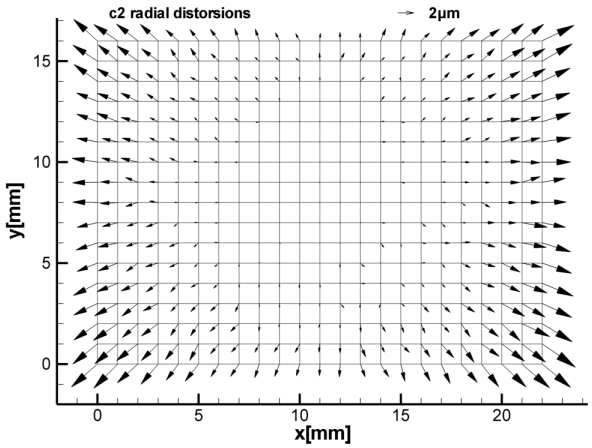

Figure 6.11: Influence of lens cushion distortion for a given calibration plane of view no. 2

It can also be seen from Table 6.2 that after subtracting average disparities per plane the mean absolute residual $\overline{|\varepsilon_x|}$ decreases with increasing camera yaw angle φ around y. The reason might be larger field angles in x-direction at less oblique viewing, thereby increasing influences of radial distortions. Lens cushion or barrel distortions strongly depend on the field angle and are not corrected in the pinhole model. Lens cushion distortions are made visible by a coplanar calibration of a single calibration plane of view no. 2 using the OpenCV radial distortion model implemented in the function *cvCalibrateCamera2*. Fig. 6.11 shows the difference vectors between radial distorted and

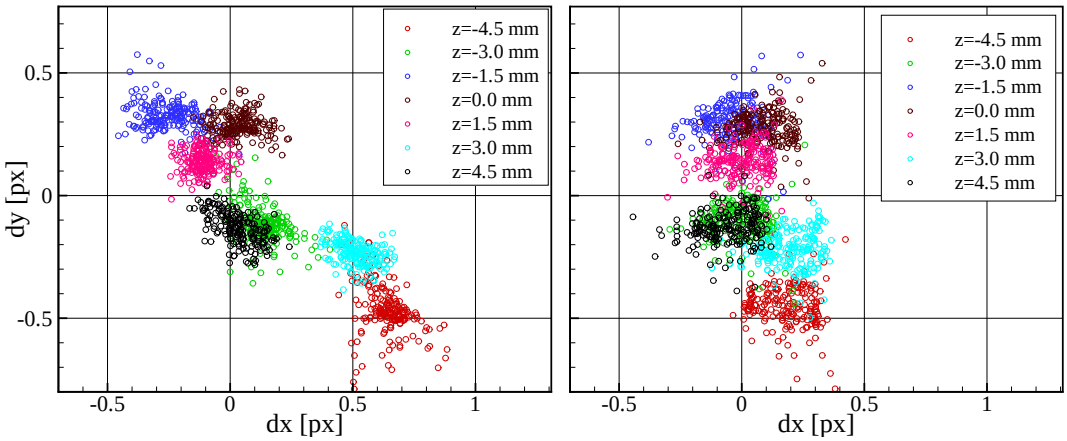

Figure 6.12: Projection disparities of point correspondences of view no. 1 (left) and view no. 2 at several target positions

undistorted back-projected calibration points of view no. 2 in order to document the influence of radial lens distortions of the 85 mm lens which is not designed as a macro lens. The differences have a maximum deviation of 2 μm in physical space which corresponds to approximately 0.12 pixel in the image plane. In the present thesis, lens distortions are corrected to some degree by application of polynomial mapping functions (see Sect. A.2.2) during volumetric (non-coplanar) camera calibration.

6.3.2 The influence of the stage positioning errors on calibration accuracy

The sequential recording of 3-D points in space is done by traversing the calibration target (photomask) along volume depth (z-axis) by a motorized translation stage. The stage used herein (*Thorlabs MTS-25*) is screw-driven and actuation bases upon a DC servo motor coupled with a planetary gear head. The moving platform is running on a dual set of linear rails with continuously recirculating ball bearings. Aside from encoder resolution each mechanical component may influence the positioning uncertainty respectively calibration accuracy.

The stage manufacturer specifies an absolute on-axis accuracy in between 75 – 145 μm at a maximum stage travel of 25 mm, a home location accuracy of

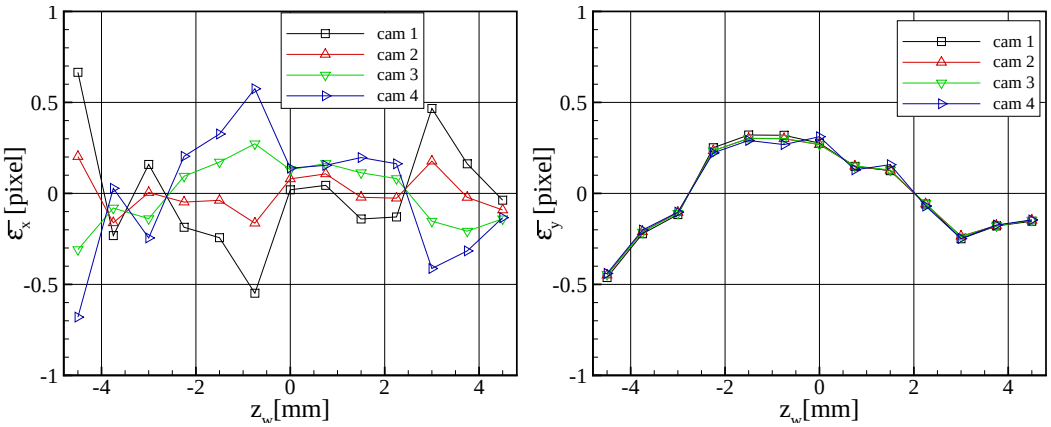

Figure 6.13: Mean disparities in x (left) and in y (right) direction at each photomask position indicating positioning inaccuracies of the translation stage

$\pm 4\,\mu$m and a backlash of $< 6\,\mu$m. The sum of these positioning errors can result in a significant bias of calibration data and becomes visible in scatter plots of projection disparities as shown in Fig. 6.12. Disparity point clouds from each plate position are clustered but show an individual offset from the origin. Fig. 6.13 shows the average disparities at each plate position over volume depth for all views. Disparities in x direction are in phase opposition for view no. 1 and no. 4 and for view no. 2 and no. 3 and are most probably connected with positioning errors along the z_{TS} axis (e.g. variations in screw pitch and motor step angle) because the error increases with the yaw angle φ The image disparities in y direction variate in unison and are most probably connected with positioning errors along the y_{TS} axis(e.g. variation of rail flatness). Maximum disparities occur at the calibration position ($z_{TS} = -4.5$) probably due to stage backlash upon reversing direction.

A numerical compensation of bias errors from stage inaccuracies is described in the following section.

6.3.3 Correction of stage positioning inaccuracies

A compensation of positioning errors is implemented by a least squares minimization of the mean disparities from each calibration plate position by using a Levenberg-Marquardt algorithm (function *lmmin* [191]). After an initial fit of the pinhole camera model to all point correspondences, camera

parameter are kept constant while three additional displacement parameter (Δx_{TS}, Δy_{TS}, Δz_{TS}) are optimized sequentially for each plane i. The output of the optimization is than used to correct each calibration plate position. The whole procedure reads as follows:

1. Initial pinhole calibration using all world-to-image point correspondences
2. Determination of $\Delta x_{TS}(i)$, $\Delta y_{TS}(i)$, $\Delta z_{TS}(i)$ by disparity minimization
3. Shifting of point correspondences using $\Delta x_{TS}(i)$, $\Delta y_{TS}(i)$, $\Delta z_{TS}(i)$
4. Pinhole calibration using corrected point correspondences
5. Repetition of step 2-4 for a given number of cycles
6. If required, additional higher order camera calibration

Two iteration cycles were sufficient to significantly reduce the disparities $\bar{\varepsilon}_x(z_{TS})$ and $\bar{\varepsilon}_y(z_{TS})$.

Table 6.3 compares the displacement output of the disparity minimization in the z bounding planes of the calibrated volume. As expected from mean image disparities shown in Fig. 6.13, displacements in x_{TS} direction are very small. The estimated positioning error along y_{TS} direction is rather similar for all four views and is $-7.5\,\mu$m at stage position $z_{TS} = -5$ and $3.2\,\mu$m in front of the volume at $z_{TS} = +5$. This makes sense because calibration images at each position are recorded simultaneously. As expected in the previous section, largest displacements occur in z_{TS}-direction. The offset δz_{TS} of each view varies significantly which does not allow to predict an unison mean displacement of the calibration stage for the given spatial direction. This stems from the fact that corresponding disparities may not only be associated with positioning errors but also depend on the sensitivity of each camera to out of plane displacements. This sensitivity should be almost zero at normal viewing ($\varphi = 0°$) and should be at maximum at a viewing angle of $\varphi = 90°$. Accordingly, displacements of each calibration plane are processed individually for each view and not averaged over all views.

Table 6.4 compares the average residuals of pinhole mapping functions with and without correction of traversing inaccuracies. Due to calibration point optimization average reprojection errors of all cameras decrease significantly to

Table 6.3: Correction values of the outer calibration plate positions estimated from least squares minimization of disparities using the pinhole camera model

z_{TS} $[mm]$	component	View 1 $[\mu m]$	View 2 $[\mu m]$	View 3 $[\mu m]$	View 4 $[\mu m]$
-5.0	Δx_{TS}	$+0.32$	$+0.58$	-0.18	-0.20
$+5.0$	Δx_{TS}	$+0.03$	$+0.25$	$+0.02$	$+0.06$
-5.0	Δy_{TS}	-7.60	-7.73	-7.63	-7.05
$+5.0$	Δy_{TS}	-3.21	-3.35	-3.19	-2.91
-5.0	Δz_{TS}	$+13.2$	$+12.0$	$+16.2$	$+22.1$
$+5.0$	Δz_{TS}	$+3.50$	-0.32	$+7.60$	$+13.4$

Table 6.4: Mean residuals of world-to-image (fwd.) and image-to-world mapping (rev.) after least squares minimization of the reprojection error ε Eq. (A.3) with and without correction of positioning inaccuracies

Calibration model	View 1		View 2		View 3		View 4	
	fwd. $[pixel]$	rev. $[\mu m]$	fwd. $[pixel]$	rev. $[\mu m]$	fwd. $[pixel]$	rev. $[\mu m]$	fwd. $[pixel]$	rev. $[\mu m]$
Pinhole	0.31	6.06	0.25	4.34	0.28	4.76	0.35	7.14
Pinhole w. corr.	0.07	1.39	0.10	1.70	0.05	0.90	0.05	1.03
Rat. 2^{nd} ord. poly.	0.10	3.01	0.10	1.57	0.09	1.69	0.10	2.61
Rat. 2^{nd} ord. poly. w. corr.	0.04	0.91	0.04	0.70	0.03	0.58	0.04	0.72

$\bar{\epsilon} \leq 0.1$ pixel or $\bar{\epsilon} \leq 1.7\,\mu$m. Residual errors due to lens distortions are corrected by an additional minimization of the reprojection error using a higher order camera model which applies ratios of 2^{nd} order polynomials (see Sect. A.2.2, Eq. (A.4)). Prior to fitting this higher order model is partially initialised using the optimized pinhole parameter. Table 6.4 also contains residuals of these higher order fits. Residuals without compensation of stage inaccuracies reach levels in the order of 0.1 pixel respectively $1 - 2\,\mu$m.

However, a higher order fit without correction or even avoidance of positioning errors is not recommended because the polynomial fit follows individual disparities at each plate position. This effect leads to a decrease of reprojection errors but can bias the tomographic reconstruction. On the other hand the application of the higher order calibration models with correction of disparities targets the compensation of other bias errors as optical distortions (c.f. Fig. 6.11). Due to positioning error correction followed by application of the higher order model the average reprojection error finally reduces to levels of < 0.05 pixel or $< 1\,\mu$m.

6.4 Estimation of the smallest visible drop size

In Sect. 6.1 models of shadow image formation have been introduced and discussed with regard to resolution capabilities of small droplets. It was demonstrated how shadow image visibility depends on droplet size and on imaging conditions. In this proof-of-concept study tomographic shadowgraphy is applied to a hollow cone pressure-driven simplex swirl nozzle whose size distribution is specified with $d = 14...100\,\mu$m at given operating pressure. Within this section the smallest visible droplet size and their depth is determined for the previously described tomographic setup. The voxel size is defined which allows resolution of the smallest droplets of the hollow cone spray, while keeping computational time demand as small as possible.

For this purpose the point spread function (PSF) of each view is determined using the knife edge technique [131, 30], which measures the response to step-like intensity gradients. Measurements of the step response are implemented on the basis of volumetric sets of chessboard calibration images of back-illuminated lithographic photomasks (see Fig. 6.9) which have already been used for camera calibration in the previous section. Opaque regions of the mask consist of a 100 nm thick layer of chromium oxide which leads to step-like intensity gradients across each edge. Ten calibration images taken at 1 mm z-spacing were used to estimate the PSF for each view.

The step response was measured in back-projected voxel-space to enable estimation of the overall point spread function. Hence, possible smoothing effects during reconstruction due to the finite voxel size and image interpolation are considered as well. For this reason, calibration images of each camera are back-projected onto their corresponding z-position using optimized mapping functions derived from camera calibration (see previous section). Back-projected and rectified images coincide with discrete $x - y$ voxel slices in the reconstruction. During back-projection, chessboard images were sampled either at 60 voxel/mm (approx. 1 voxel/pixel) or 120 voxel/mm (approx. 2 voxel/pixel) and all sub-pixel intensities are bilinearly interpolated between the 4-connected pixels.

After back-projection, chessboard images are normalized to correct inhomo-

geneities of the LED back-illumination. Therefore, the intensity in the center of the dark and the bright chessboard fields is extracted and separately interpolated by Kriging (*IDL* function *krig2d*) to obtain a background image and a bright field image. The background image is subtracted from the chessboard image and subtracted from the bright field image. Flat-field correction and normalization is achieved by dividing the chessboard image by the bright field image.

Fig. 6.14 (left) shows examples of the step response to a plate position in focus (top) and a position near the volume edge (bottom) after normalization. The direction of step response (y-axis) is aligned with the spray nozzle axis. The corresponding line spread functions are obtained by numerical differentiation of the edge spread functions [30] and are shown in Fig. 6.14 (right). Each line spread function (LSF) is matched with a Gaussian fit. The fit is in line with the LSF in focus (Fig. 6.14 (right,top)) but slightly mismatches the LSF out of focus near the volume edge (Fig. 6.14 (right,bottom)). However, the Gaussian fit is considered suitable for half-width estimation of the LSF. Fig. 6.15 (left) shows the mean LSF half-width at a 60 voxel/mm (approx. 1 voxel/pixel) sampling along the y axis in the $y-z$ center plane (coordinate system as shown in Fig. 6.20). The minima of the curves does not coincide (focus not exactly at the same $x-y$ plane). The defocussing of view no. 2 and no. 3 increases faster toward the volume edges which indicates a slightly smaller depth of focus compared with view no. 1 and no. 4. The reason for this is that lenses of both inner views no. 2 and no. 3 are stopped down to $f_{\#} = 16$ and while the lenes of both outer views are stopped down to $f_{\#} = 22$ to maintain a wider depth of field at larger focal length. The LSF half-width of both outer views no. 1 and no. 4 has a minimum of $\chi_y = 44 - 46\,\mu$m while both inner views no. 2 and no. 3 exhibit a smaller minimum near $\chi_y = 40 - 45\,\mu$m. The better resolution of the inner views within $-5 < z < 3$ is possibly due to the smaller f-number.

Fig. 6.15 (right) shows the mean LSF half-width at a doubled spatial sampling rate of 120 voxel/mm (approx. 2 voxel/pixel). All curves retain their shapes but the spread of the step response is about 11% less and therefore lead to a slightly better resolution compared to a sampling of 60 voxel/mm. On the

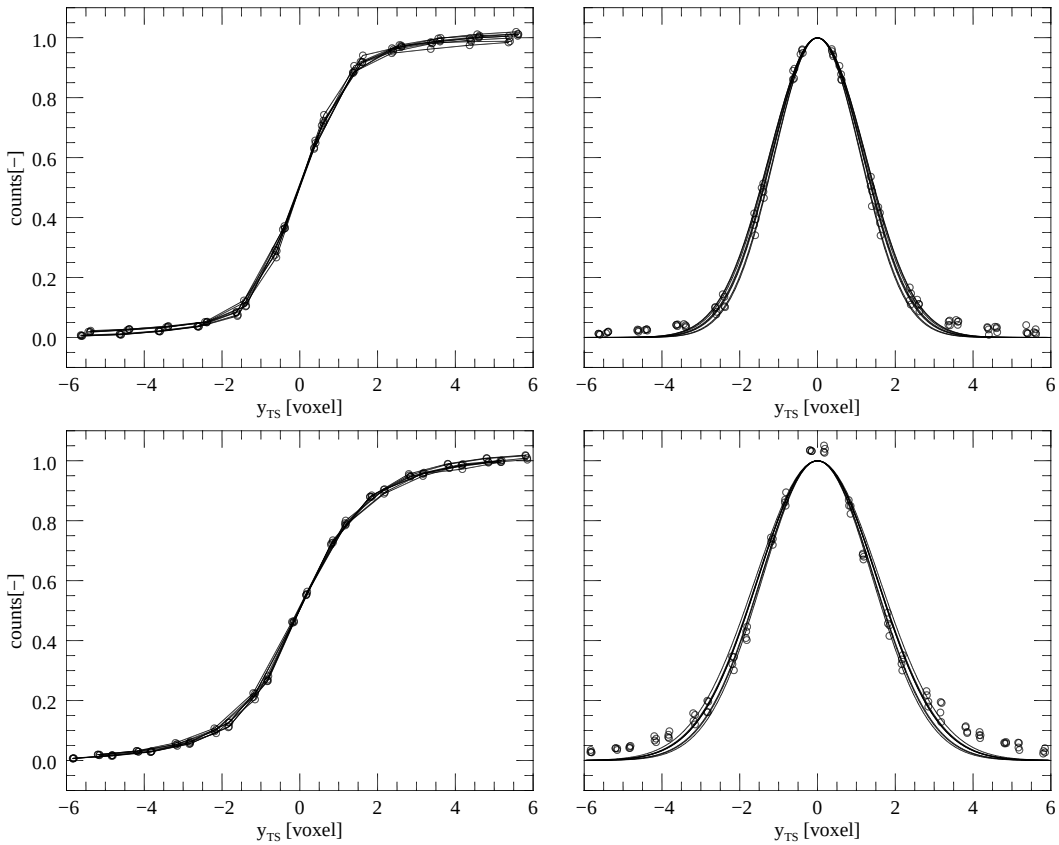

Figure 6.14: Step response of view no. 2 along the nozzle axis (8 chessboard edges of 2 mm spacing); edge spread (*left*) and line spread function+Gaussian fit (*right*) in focus at $z = 0$ mm (*top*) and near the volume edge at $z = -4.5$ mm (*bottom*)

other hand it must be noted that increasing the spatial sampling by a factor of two while retaining the size of volumetric domain considerably increases the computational effort approximately by a factor of eight.

Measurements of the LSF width are finally used to infer the minimum visible droplet diameter of the multiple view setup (see Fig. 6.7). Due to the use of Scheimpflug mounts, the focal planes of all views are parallel with respect to the calibration plate and due to a polygon-shaped spray chamber the optical axis of each view is orthogonal to each window. Hence, astigmatism effects are negligible and the PSF at each z position should have a circular Gaussian shape with its half-width being equal to the half-width of the LSF [130].

Based on the LSF half-width shown in Fig. 6.15 the shadow image depletion i_{min} can be estimated for a given droplet size range using Eq. (6.6). The

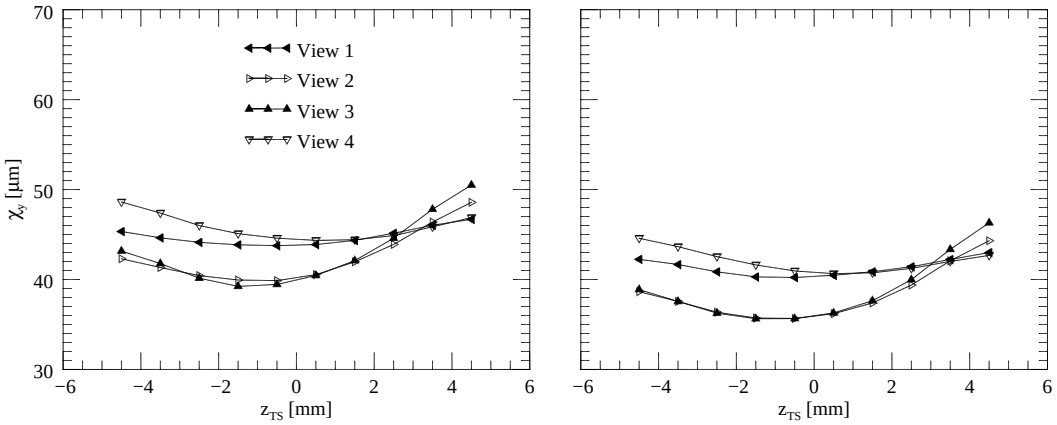

Figure 6.15: Mean half-width of the line spread function along the nozzle axis and in the $x-z$ center plane; 60 voxel/mm (approx. 1 voxel/pixel) (*left*), 120 voxel/mm (approx. 2 voxel/pixel) (*right*)

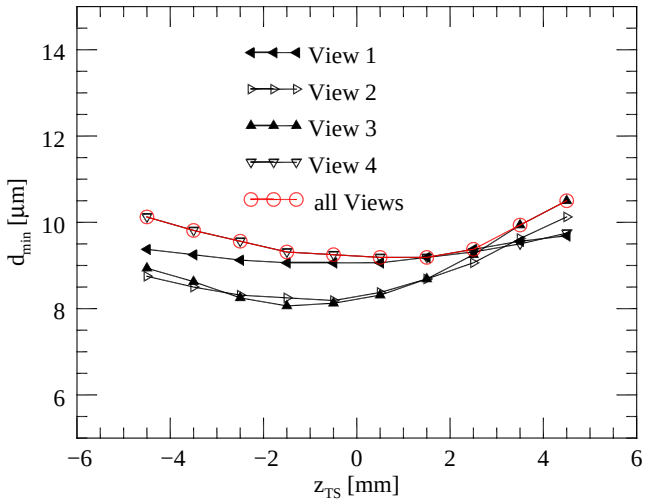

Figure 6.16: Smallest visible droplet diameter of the multiple view setup as a function of volume depth, at a spatial sampling of 60 voxel/mm

particular transmission coefficient is gained from Mie simulations of spherical water drops in air as described in Sect. 6.1. The minimum intensities of the droplets are then compared to the smallest detectable intensity depletion of the spray background illumination in order to decide whether a droplet would be visible or not.

This threshold of visibility is estimated from intensity fluctuations in 200 images recorded with LED light and without spray. After image normalization, all pixel intensities have a mean of $\tilde{i} = 1 \pm \sigma$ and the threshold of visibility was set to a values of $\tilde{i} = 1 - 2\sigma$. Fig. 6.16 shows the estimated smallest visible droplet sizes d_{min} for a spatial sampling of 60 voxel/mm. If one of the views can not detect a droplet because of low contrast it would not be visible

in the reconstructed volume. Therefore, the maximum of the size limits of all cameras at each calibration plate position gives the limit of the multiple view setup (red line in Fig. 6.16). The droplet visibility at 60 voxel/mm reduces to $d_{min} = 8\,\mu$m and therefore is more than sufficient to enable intensity reconstruction of the smallest droplets in the hollow cone spray of $d = 14\,\mu$m.

6.5 Shadow image processing and volume reconstruction

Prior to reconstruction the shadow image intensities are first inverted and then the minimum intensity image of the complete image sequence is subtracted. The remaining background is removed by subtracting the local minimum in a 11×11 pixel kernel followed by a subtraction of a constant offset of 200 counts.

According to considerations in the previous section, a volumetric domain of $18 \times 17 \times 9\,\text{mm}^3$ was reconstructed at 60 voxel/mm (total size of $1080 \times 1020 \times 540$ voxel). The observed intensities from each voxel are reconstructed according to its line-of-sight intersection with each image plane. These positions are calculated from higher order mappings obtained from calibration as described in Sect. 6.3 (ratios of 2nd order polynomials with correction). Sub-pixel intensities are bilinearly interpolated between the 4-connected pixels.

The observed intensities from each view are combined either by multiplication (MLOS) or by a maximum entropy approach (MENT) as described in Sect. 3.1.1. The single pass MLOS reconstruction of a double exposure of $1080 \times 1020 \times 540$ voxel from four views took about 30 s on a 12-core Intel Xeon workstation at 2.4 GHz (12 GByte RAM). A MENT reconstruction with two iteration took in the order of 117 s on the same workstation. Further iterations did not reduce the reconstruction residual ϵ (c.f. Eq. (3.3)) as already observed during numerical assessment Sect. 3.3.1. The peak RAM usage of both reconstruction schemes is 725 MByte.

As a benchmark for a comparison of reconstruction techniques the simultaneous multiplicative algebraic reconstruction technique (SMART) [112] is applied (c.f. Sect. 3.1.2). SMART iteratively refines voxel intensities obtained with

single pass MLOS [8] by repeated projection of voxel intensities onto each image plane followed by a simultaneous voxel intensity correction according to recorded image intensities. Projecting, comparing and updating the voxel intensity for all views is performed in one iteration loop and repeated until the differences between projected volume intensities and image intensities converge.

Fig. 6.17 shows the convergence and computational time demand of MLOS-SMART to reconstruct one double-volume of the hollow cone spray (average over 133 single shots). After seven iterations, the residual is constant within the 5% neighborhood. The seven SMART iterations on average take 404 s on a 12-core Intel Xeon workstation (2.40 GHz). The peak RAM usage of SMART is 2043 MByte.

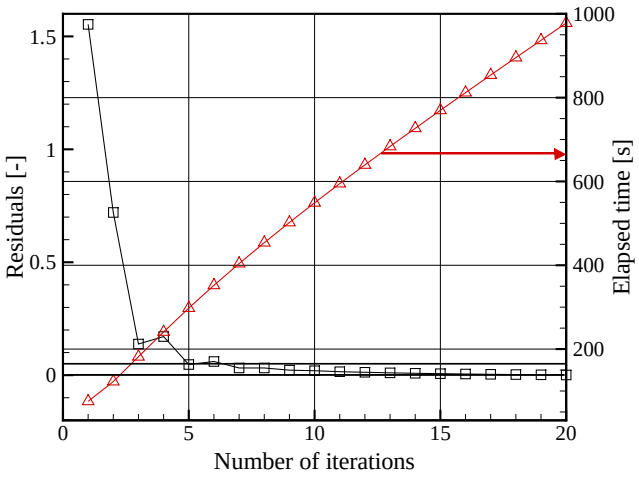

Figure 6.17: Reprojection residuals (□) and computational time demand (△) of MLOS-SMART on a 12-core Intel Xeon workstation running at 2.40 GHz

6.6 Reconstruction results

6.6.1 Instantaneous intensity distributions

Fig. 6.18, right, shows a MLOS reconstruction of a single realization of the fan spray for a $4 \times 4 \times 4\,\mathrm{mm}^3$ partial volume at a resolution of $240 \times 240 \times 240$ voxel. The corresponding location of this region is indicated in the shadowgraph image. Single droplets and parts of ligaments can be identified showing the

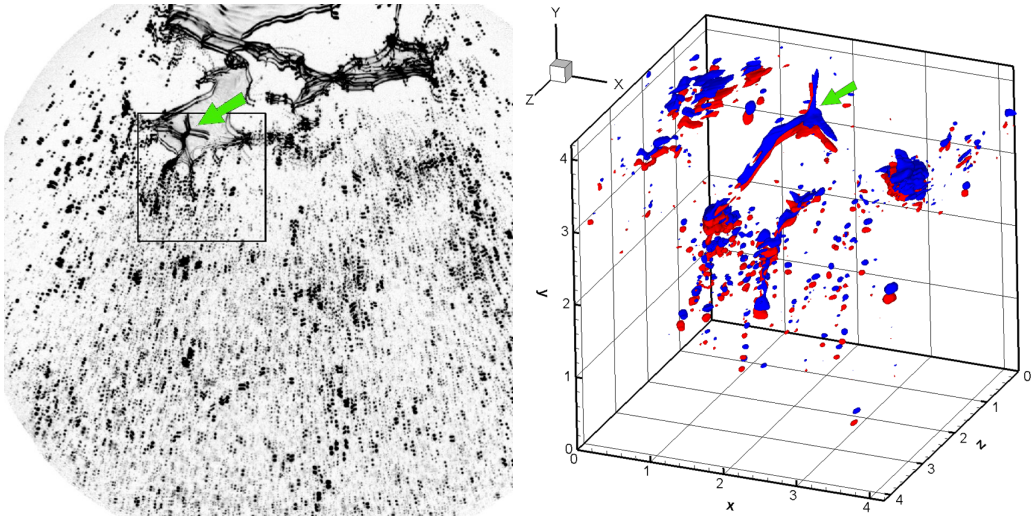

Figure 6.18: Left: Shadowgraph image pair of a flat fan spray, one of four simultaneous views. Right: iso-intensity plot of the reconstructed spray within region indicated by the rectangle in the shadowgraph. Blue represents the reconstruction obtained for the first recording while red was acquired 6.3 μs later in time

liquid sheet disintegration in three dimensions. The arrow marks comparable shapes on the edge of the liquid film.

Fig. 6.19 shows a more quantitative comparison of reconstructions of a $x - z$ voxel slice of a single shot of the hollow cone spray in a region marked with a highlighted frame in Fig. 6.19. Comparable droplet positions in Fig. 6.19 are marked with equally placed ellipses. Intensities are globally scaled to have equal maxima at position *a*. Independent of reconstruction type, most blob shapes are elongated along the z axis which is caused by the angular apertures of the viewing geometry of 90° (outer cameras) and 30° (inner cameras). Slight deviations between droplet positions found by MLOS, MENT and MLOS-SMART originate from different camera models respectively different mapping functions and should have a minor influence on velocity accuracy as long as PIV or PTV droplet displacements are small in comparison to mapping inaccuracies. Both, MLOS and MENT reconstructions contain additional blobs in comparison to MLOS-SMART. These blobs are often of low intensity and occur in the vicinity of blobs with higher intensity and therefore are probably ghost particles (e.g. blobs in the vicinity of the positions *a*, *b*, *d*,*f*, *g* and *h*). MLOS-SMART exhibits stronger noise suppression in comparison

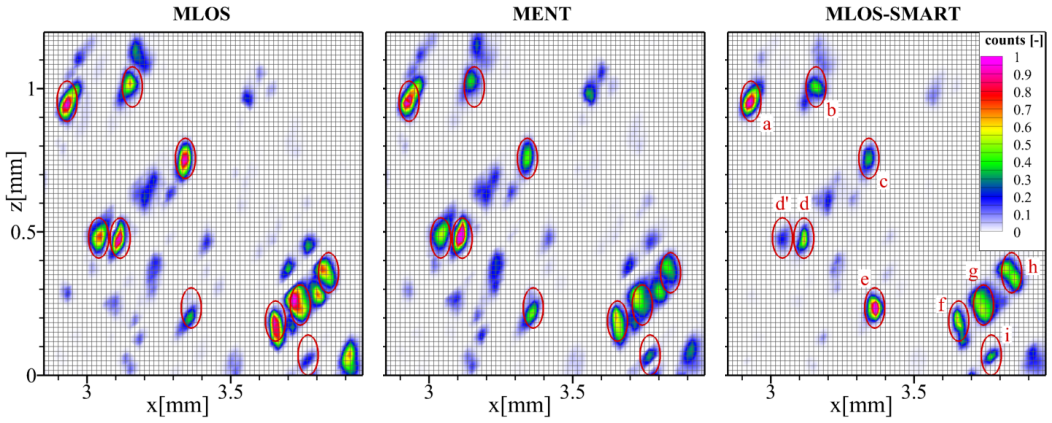

Figure 6.19: Comparison of reconstructed droplets (single shot) obtained with MLOS, MENT and MLOS-SMART in a single slice of $66 \times 1 \times 72$ voxel of the hollow cone spray within the region indicated in Fig. 6.21; red ellipses mark comparable droplet positions

with MLOS or MENT, as already observed during synthetic image evaluation (c.f. Sect. 3.3.2). However, the intensity distribution obtained with MENT shows more resemblances to the SMART reconstruction as single pass MLOS. In comparison with MLOS, MENT shows a slightly better ghost suppression. For example, the suppression of blob *d'* (most probably a ghost) in relation to the nearby blob *d* is 1 : 3.3 for SMART, 1 : 2 for MENT and 1 : 1.6 for MLOS.

The applied SMART reconstruction [143] makes use of a two-plane camera model (see Sect. 2.2) and a self-calibration routine as described by Wieneke [176]. The self-calibration compensates deviations between camera calibration and triangulated droplet images. Otherwise, if this misalignment is on the same order as the droplet image, size reconstruction quality will deteriorate significantly. In the present case the magnitudes of the global disparity vectors obtained by self-calibration are 0.85, 0.21, 0.40, 0.92 pixel or approximately 14.2, 3.5, 6.7, 15.3 μm in physical space. These global disparity vectors are on the same order as inaccuracies of the bounding calibration plate positions provided in Table 6.3 which are used for calibration of the two-plane camera model. Beyond that, volume self-calibration compensates deviations that occur in the time span between calibration and experiment which is probably another reason for the slightly better ghost suppression of SMART in comparison to MENT.

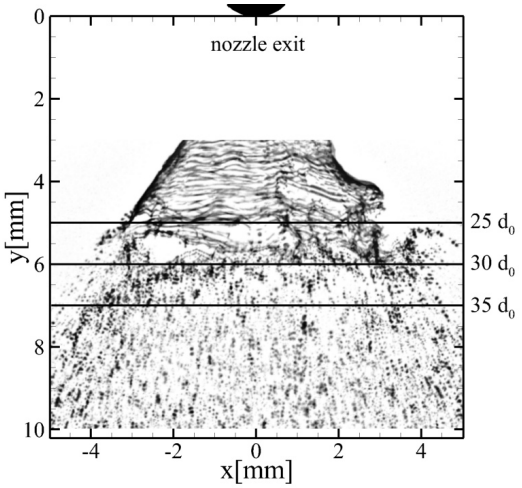

Figure 6.20: Portion of back-projected double exposed shadow image from view no. 2 showing the breakup of the liquid film near the top into droplets toward the bottom, horizontal lines mark positions of cross-sections shown in Fig. 6.21

6.6.2 Averaged cross-sectional intensity distributions

Fig. 6.21 compares cross sections of the hollow cone spray at $y = 25\,d_0$, $y = 30\,d_0$ and $y = 35\,d_0$ as processed with three different reconstruction methods using identical image preprocessing. The volume sections represent the average of 266 reconstructed 3-D shadowgraphs. The connected circular shape indicates regions where strong light deflection occur. This coincides with the rim of the liquid conical sheet and with regions where ligaments and droplets appear frequently.

Compared to the SMART reconstruction at $y = 25\,d_0$, MLOS exhibits a more blurred intensity distribution (c.f. Fig. 6.21, top). The reconstructed intensity is partially spread along lines of sight even into regions without significant droplet presence. The MENT reconstruction shows a better suppression of these artifacts and the intensity values within the circular shape are very similar to the result obtained with SMART. The averaged iterative SMART reconstruction shows a clear circular shape with higher intensity gradients close to the ring. However this involves roughly a four times longer computational effort in comparison to the MENT reconstruction. Further downstream (see Fig. 6.21) from $y \geq 35\,d_0$ the degree of atomization increases and the droplets are spread over a larger circular area. This region is characterized with locally lower droplet number densities and seems to be particularly well suited for a MENT reconstruction.

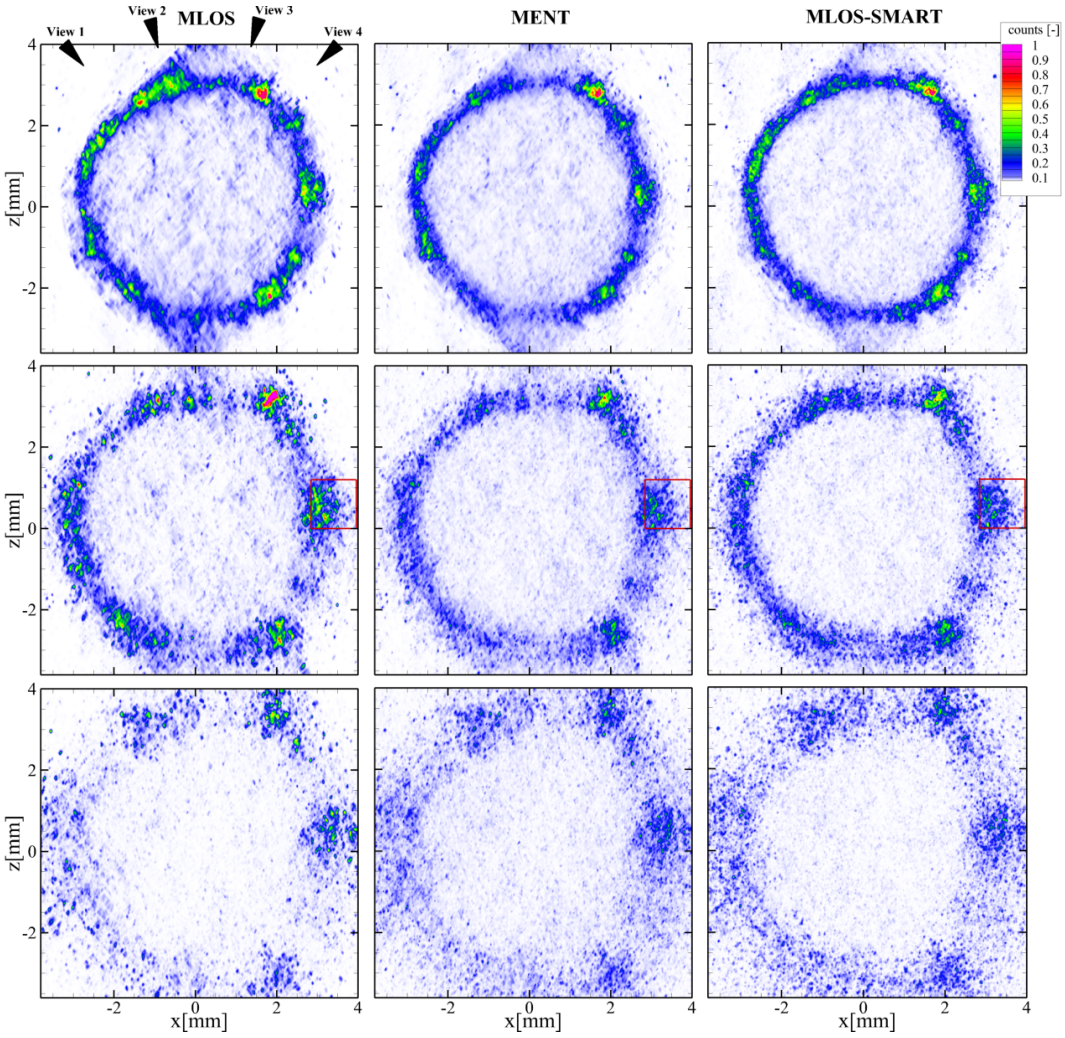

Figure 6.21: Extracted slices of 266 averaged volume reconstructions of the hollow cone spray at $y = 25\,d_0$ (*top*), $y = 30\,d_0$ (*middle*) and $y = 35\,d_0$ (*bottom*) obtained with MLOS, MENT and MLOS-SMART; the red box indicates the region shown in Fig. 6.19

6.7 Discussion

The tomographic reconstruction from multiple shadowgraphs intends to locate droplets in three-dimensional space due to a light intensity decrease within the observation path of each view which is driven by Mie scattering by the droplet. Due to resolution limits the true size of the droplets cannot be estimated geometrically for the majority of the droplets. In the described macroscopic imaging setup this translates to droplet images smaller than about 4 to 5 pixels or about $70\,\mu$m in physical space while the nozzle manufacturer specifies

a Sauter mean droplet size of 25 μm in the spray and a size range between $14 - 100\,\mu$m. On the other hand the great majority of the droplet shadows in the acquired images have diameters in the range of 3 to 6 pixels which indicate the presence of droplets with diameters well below 70 μm (c.f. Fig. 6.8). These smaller or more unfocused droplets have a significant lower contrast. In the present study it has been shown how droplet contrast and visibility depends on droplet size as well as on imaging parameters such as lens aperture, magnification, resolution and distance from the focal plane. These dependencies allow to estimate the minimum droplet diameter which a specific macroscopic imaging system can resolve if multiple scattering between droplets and is neglected. Estimations regarding resolution capabilities yield a visibility limit for droplets of a diameter of $d = 8\mu m$.

The three-dimensional intensity reconstruction finally yields an estimate of the instantaneous droplet position in space with intensity being a rough indicator of droplet size. The indication of size bases on the fact, that for a given size range and resolution the shadow intensity decrease monotonously with droplet size (see Fig. 6.6). As long as droplet diameter and lens apertures are small enough not to produce glare points, the droplet image in each view appears as a homogeneous dark spot. The similarity of the shadow image of a given droplet in each view allows a reconstruction of the droplet position by superposition of the lines of sight.

The continuous liquid sheet and ligaments close to the spray nozzle will be imaged quite differently by each camera depending on how the light is refracted through the complex liquid structures. Therefore the shape of fragments and ligaments can only roughly be identified in the reconstruction (see arrow in Fig. 6.18). In a similar manner the nearly transparent region of the continuous liquid film cannot be recovered three-dimensionally.

6.8 Summary

A technique called *tomographic shadowgraphy* was demonstrated by reconstructing the instantaneous 3-D spray distributions of hollow cone and flat fan water sprays at ambient conditions in a volume of up to $18 \times 17 \times 9\,\mathrm{mm}^3$.

The proof-of-concept study relies on a four-camera setup with inline illumination provided by current pulsed LEDs which results in droplet shadows being projected onto multiple sensor planes. Each camera records image pairs with short inter-framing times which allows the trajectories of the individual droplets to be estimated using conventional three-dimensional correlation or particle tracking approaches.

The observed volume is calibrated with a traversed micro target. Calibration tests have been performed to study the influence of marker type, feature extraction algorithms and translation stage accuracy on the reprojection error in volumes with a large depth-to-width aspect ratio of 0.5. In the majority of cases the lowest residuals are obtained if chessboard patterns are applied instead of bright circular spots on a dark background. Sub-pixel position detection by cross-correlating the preprocessed chessboards with a circular-shaped template leads to slightly lower residuals in comparison to the Harris corner sub-pixel detection, whereby preprocessing of chessboard images consists of a chain of partial derivatives followed by Gaussian smoothing.

Furthermore, the influence of stage positioning inaccuracies on volume calibration has been verified. A numerical correction of those positioning inaccuracies is proposed which reduces the 3-D spatial disparities at each calibration plate position by a least squares minimization. The algorithm was successfully demonstrated on the basis of camera calibration data.

The influence of imaging and spray parameters on the depth of field have been characterized. It was derived how the droplet shadow image contrast of each view depends on droplet size and spatial resolution. It was shown that the depth of field of a droplet shadow image strongly depends on droplet diameter and the local point spread function (PSF). From PSF measurements using the knife-edge technique the smallest visible droplet sizes and their depth of field are being derived for the presented spray volume reconstruction. The minimum resolvable droplet diameter approaches $d = 8\,\mu$m in focus and increases to $d = 11-13\,\mu$m near the rear and front boundaries of the reconstructed domain for the described imaging configuration and processing.

Instantaneous and time-averaged three-dimensional spray distributions obtained from MLOS, MENT and SMART algorithms are compared. With in-

creasing droplet number densities the utilization of the SMART reconstruction technique provides a better suppression of ghost droplet intensities in comparison with MENT and MLOS but has the disadvantage of a considerably higher computational effort. However this involves roughly a four times longer computational effort in comparison with MENT excluding the time needed for particle volume storage. Further downstream (from $y \geq 35\,d_0$) the degree of atomization increases and the droplets are spread over a larger circular area. This region is characterized with locally reduced droplet number densities and seems to be particularly well suited for a MENT reconstruction. In comparison with MLOS, MENT shows a slightly better ghost suppression.

While not presented herein the reconstructed volume data is well suited to extract additional information such as droplet velocities and trajectory using existing 3-D correlation or particle tracking velocimetry (PTV) methods.

Chapter 7

Tomographic shadowgraphy of swirled spray injection in a generic aero engine burner

Based on feasibility tests in the previous chapter the reminder of the thesis will report on the first implementation of tomographic shadowgraphy at elevated pressure and temperature in a spray test rig for aero engine burners. Parts of the content are published in conference proceedings [201].

The optimization of aero engine combustors requires a detailed knowledge of the fuel atomization process including fuel placement, breakup length scales, spray penetration depth, droplet sizes and velocities. Providing relevant experimental data on kerosene atomization on the other hand raises some serious challenges such as deployment of realistic operating conditions and sufficient optical access. Another obstacle is that the dispersion of liquid kerosene by aero engine combustors is driven by a highly three-dimensional swirl flow. Frequently, air-blast atomization of liquid kerosene films or jets is applied. The jet or film breakup itself is unsteady due to turbulence of the surrounding air flow. Therefore, a better insight into the phenomenon can only be provided by diagnostic methods capable of mapping the instantaneous three-dimensional velocity and placement of atomized fuel within the combustion volume both spatially and temporally.

The study presented in this chapter is aimed at applying *tomographic shadowgraphy* under rough operating conditions in a non-reacting kerosene spray in a high pressure environment with preheated airflow which is representative of air-blast atomization under realistic conditions. Tomographic shadowgraphy is used to measure instantaneous droplet velocities in the non-reactive flow of the generic aero engine burner model. The generic burner employs air-blast atomization of a single jet in cross-flow in the main stage. Of particular interest to spray investigation is the near field where the fragments of the kerosene jet leave the annular gap of the burner plate. The present application intends to provide insight into the instantaneous spray tail trajectory and the spatial distribution of liquid phase above the resolution limit.

Various aspects concerning the adaption of the tomographic setup to the facility are described. After tomographic reconstruction of the droplet field, droplet velocities are obtained by 3-D cross-correlation analysis of small interrogation volumes from two consecutive time steps as known from conventional tomographic particle image velocimetry [42]. Exemplary profiles of axial and tangential droplet velocities near the burner plate are compared with PDA measurements.

7.1 Breakup of a plain liquid jet in cross flow

The phenomenon under investigation is that of a liquid jet in cross flow. Some fundamental mechanisms involved in the jet breakup are be explained in the following. Fig. 7.1 schematically illustrates the atomization process of such a transverse liquid jet. The aerodynamic drag force causes the jet to curve in a downstream direction while droplets are stripped from the lateral liquid surfaces. Surface waves develop above the jet exit and larger amplitudes may be caused by so-called Rayleigh-Taylor and/or Kelvin-Helmholtz instabilities [145]. Ongoing growth of the wave amplitudes finally induce fracture of the liquid column into irregular shaped clumps of liquid. Further downstream, the liquid packets disintegrates into smaller ligaments which are finally dispersed into small droplets and comprise a mixing region of small droplets and air.

In general, the breakup of a liquid column or of a single droplet is controlled by

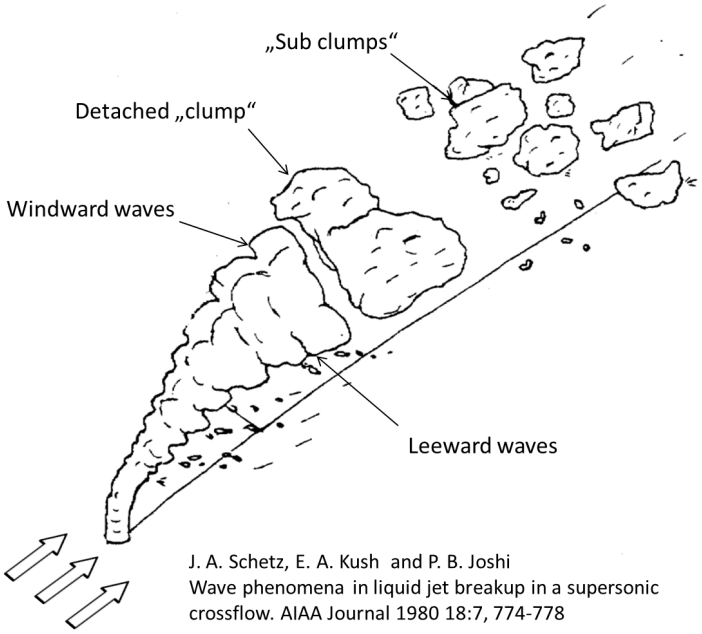

Figure 7.1: Schematic illustration of atomization of a plain liquid jet in cross-flow; reprinted from [145]

disruptive forces due to dynamic pressure and by surface tension and viscous forces. An important number that describes the ratio of aerodynamic forces to the consolidating surface tension force is the Weber number. In a fuel spray, the aerodynamic Weber number is defined as:

$$\mathrm{We}_{\mathrm{aero}} = \frac{\rho_a \, U_r^2 \, d_k}{\sigma_k} \,, \tag{7.1}$$

where ρ_a is the air density, U_r denotes the relative velocity between liquid and air, d_k is the representative diameter of the liquid (e.g. droplet diameter or nozzle diameter) and σ_k is the surface tension. For a spherical droplet, the initial breakup condition is met if the aerodynamic drag is equal to the surface tension force [92]:

$$\begin{aligned} C_D \, \frac{\pi \, d_k^2}{4} \, \frac{1}{2} \, \rho_a \, U_r^2 &= \pi \, d_k \, \sigma_k \\ \left(\frac{\rho_a \, U_r^2 \, d_k}{\sigma_k} \right)_{crit} &= \frac{8}{C_D} = \mathrm{We}_{\mathrm{crit}} \,, \end{aligned} \tag{7.2}$$

where C_D is the drag coefficient of the drop and $\mathrm{We}_{\mathrm{crit}}$is the critical Weber number of the onset of breakup.

The shape of the jet trajectory primarily depends upon the liquid to air momentum flux ratio:

$$q = \frac{\rho_k U_k^2}{\rho_a U_a^2} \tag{7.3}$$

Empirical models for trajectory and penetration depth for the transverse kerosene jet at elevated pressure are determined experimentally by Becker and Hassa [13] and Freitag and Hassa [54].

Different breakup regimes can be observed depending on q. At a low momentum flux ratio, *column breakup* is dominant, where the liquid jet body breaks into larger irregular-shaped fragments and ligaments. When q is high, *surface breakup* occurs before liquid column instabilities and ligaments and drops are continuously sheared-off of the jet surface mainly from the lateral sides of the jet [78]. The transition Weber number at which surface breakup occurs has been determined experimentally by Wu et al. [189] and subsequently by Becker and Hassa [13] and can be expressed as:

$$\mathrm{We}_{\mathrm{sb}} \approx 10^{(3.1-log(q))/0.81} \tag{7.4}$$

7.2 Test facility and operation conditions

Spray measurements are performed in a non-reactive kerosene-air flow in the optical swirling spray injector test rig (OSSI) at the DLR Institute of Propulsion Technology in Cologne. The design of the test rig and the generic burner model geometry are described in detail in [53].

Fig. 7.2 shows a longitudinal section of the test rig. The spray chamber has a length of 200 mm and a square cross-section of internal width of 102 mm. Pressure windows of 35 mm thickness and liner windows of 7 mm thickness provide optical access to the test-section from four sides. Additional cooling air is blown through the gap between pressure and liner window to protect the glass from thermal loading and to keep the external pressure casing at ambient temperature levels. The burner model is supplied with preheated and pressurized air through an upstream settling chamber (plenum). Inside the plenum a baffle with interchangeable screens provides flow conditioning and control of

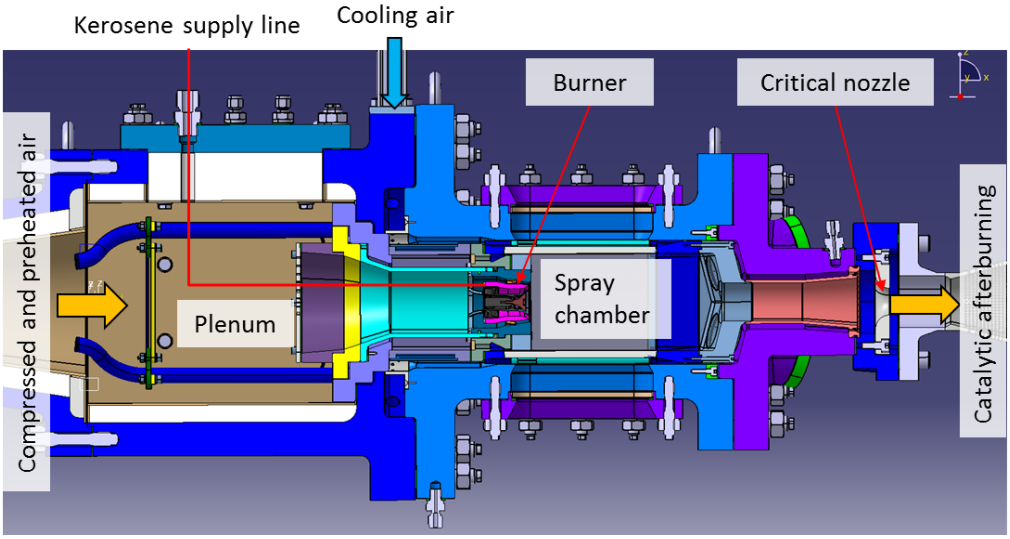

Figure 7.2: Schematic of the optical swirling spray injector test rig(c.f. [53])

the burner pressure loss. The kerosene supply line of the burner model passes through the preheated air flow and thus kerosene is preheated prior to injection to temperatures provided in Table 7.1. An exchangeable critical nozzle downstream of the spray chamber builds up pressure and provides mass flow control. For safety and environmental reasons the fuel air mixture is guided through a catalytic combustor after leaving the critical nozzle.

The generic aero engine burner model represents that of a lean staged industrial burner with the pilot part replaced by a solid center body (see Fig. 7.3). The burner model employs air-blast atomization of a single jet in cross-flow in the main stage. Kerosene is injected through a single bore of 0.88 mm length and a diameter of 0.29 mm (L/D=3). The injector is located in a conical main module which is placed between two co-rotating swirl generators. The liquid jet of kerosene is injected orthogonal to the conical surface 6 mm upstream of the burner exit. Downstream, the liquid jet fragments propagate in swirl direction and leave the annular passage premixed with air.

Table 7.1: Operation conditions of single jet in cross-flow atomization

No.	$p_a\,[bar]$	$T_a\,[K]$	$U_{auv}\,[m/s]$	$T_k\,[K]$	$\dot{m}_k\,[g/s]$	q_{UV}	$\mathrm{We}_{\mathrm{aero}}$
1	4	440	86	348	0.8	8	360
2	4	570	92	422	0.7	8	438
3	7	440	86	347	1.0	8	625
4	7	570	98	396	1.0	8	770

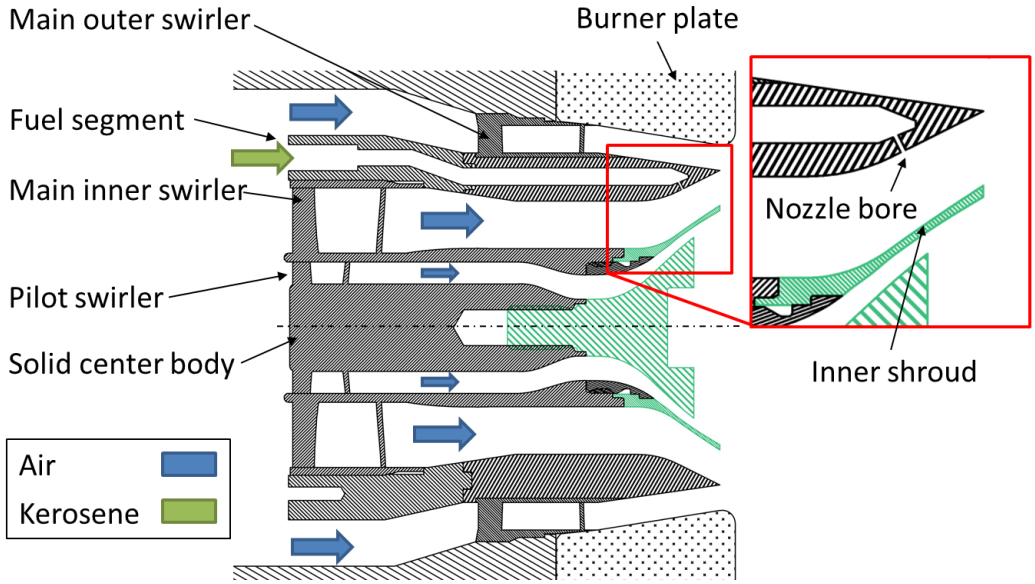

Figure 7.3: Aero engine burner model with single fuel injector (adopted from [52])

Table 7.1 summarizes the operation conditions. During the experiments described herein the pressure inside the spray chamber was varied between 4 and 7 bar and the burner air flow was preheated in a range between 440 K and 570 K. The liquid-to-air momentum flux ratio was kept constant while the aerodynamic Weber number ranged from 360 to 770.

Estimations of the aerodynamic Weber number (see Eq. (7.1)) base on the nozzle diameter D_0 and on slightly cooler kerosene temperatures measured about 5 mm upstream of the injection port. The Weber number therefore might be slightly underestimated due to an overestimation of kerosene surface tension.

7.3 Tomographic shadowgraphy setup for swirled fuel sprays

The experimental setup outlined in Fig. 7.4 and Fig. 7.5 involves four synchronized double-frame cameras (ILA.sCMOS) capable of acquiring 5 Mpixel double-images at a frame rate of 25 Hz. The cameras are angled with $-45°$, $-20°$, $25°$

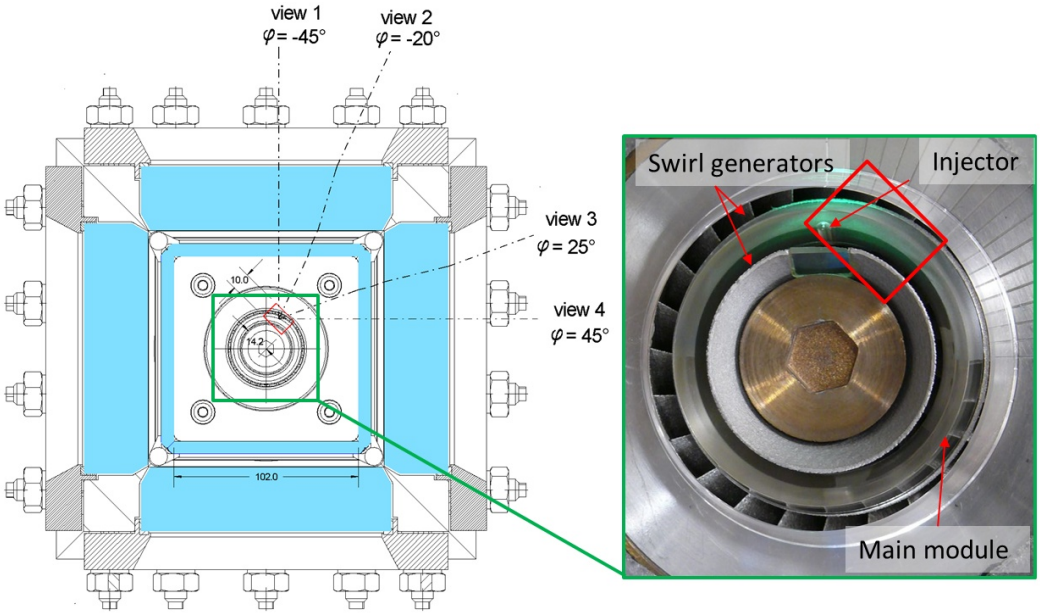

Figure 7.4: Test section of the optical swirling spray injector rig; *Left* camera orientation and volume of interest (red box); *Right* generic burner with a transparent main module (used for spray visualization) and injector bore

and 45° so that each field of view matches the spatial spray distribution downstream of the annular passage. Inline illumination is provided for each camera by a current-pulsed, high power green LED (Luminus, SST-90, green) [183] whose light is collimated with an aspheric condenser lens of $f = 30\,\mathrm{mm}$. Peak currents of $I_{\mathrm{f,max}} = 270\,\mathrm{A}$ at $t_p = 400\,\mathrm{ns}$ were found sufficient to provide bright-field intensity levels at 5% of the camera dynamic range (16bit) at lens aperture $f_\# = 22$. At given peak current the LED's emission spectrum has a bandwidth of 37 nm (FWHM) with a peak emission at $\lambda_{\mathrm{max}} = 514\,\mathrm{nm}$. To achieve droplet image displacements up to 10 pixel the pulse separation was set to $\Delta t = 1.7\,\mu\mathrm{s}$.

The imaging parameter of each camera are summarized in Table 7.2. All cameras are equipped with macro lenses (Nikkor Micro) at average magnifications ranging from $M = 0.85 - 0.95$ corresponding to $6.8 - 7.4\,\mu\mathrm{m/pixel}$ at image sizes of 2560×2160 pixel. The two outer cameras no. 1 and no. 4 use lenses of $f = 105\,\mathrm{mm}$ focal length and 35 mm close-up extension rings. The two inner cameras are both equipped with $f = 200\,\mathrm{mm}$ lenses in order to accommodate the additional compensator plates in the optical path and to maintain similar magnification compared to view no. 1 and no. 4. Purpose and working

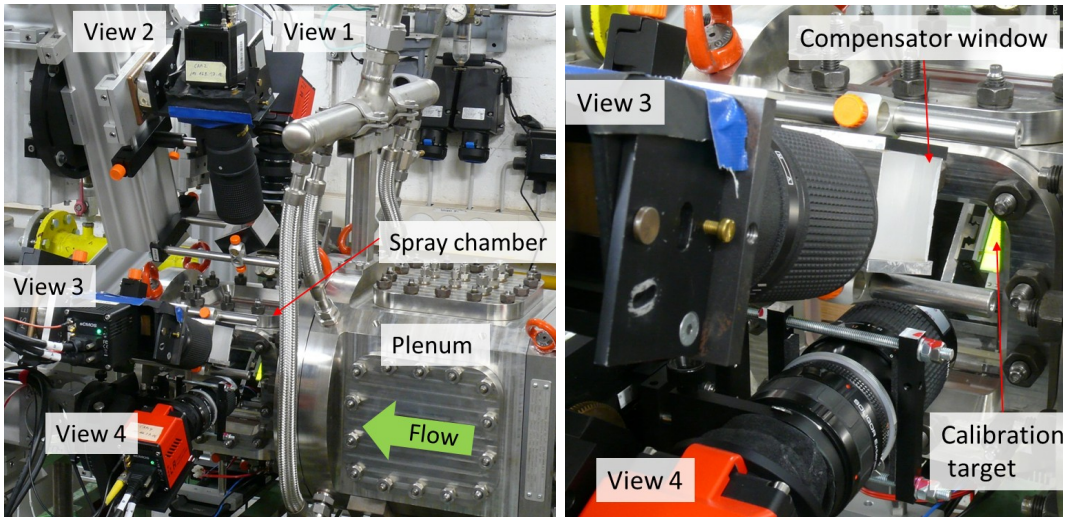

Figure 7.5: Optical swirling spray injector test rig and imaging setup; *Left* camera arrangement; *Right* detail with calibration equipment

Table 7.2: Imaging parameters

view	$\approx \varphi$	$f_\#$	$f\,[mm]$	$\approx M$	$d_\mathrm{A}\,[\mu\mathrm{m}]$
1	-45°	22	100	0.85	51
2	-20°	22	200	0.95	54
3	25°	22	200	0.93	53
4	45°	22	100	0.91	53

principle of those compensators are described in the following subsection.

With the aid of Scheimpflug tilt mounts, the focal planes of the cameras are aligned with the calibration target positioned at the center of the imaged volume so that the optical axis of each view coincides with the volumes's z axis. All apertures are stopped down to $f_\# = 22$ to maintain a depth of field of approximately 10 mm. Estimations of the depth of field and droplet visibility along volume depth are reported in Sect. 7.3.3.

7.3.1 Compensation of optical aberrations imparted by thick test rig windows

While the viewing directions of the outer cameras no. 1 and no. 4 are perpendicular to the windows, cameras no. 2 and no. 3 have to be tilted with respect to the test rig windows. Thus, droplet images of both inner cameras would exhibit elliptical distortions due to optical aberrations (see also Fig. 2.4). An-

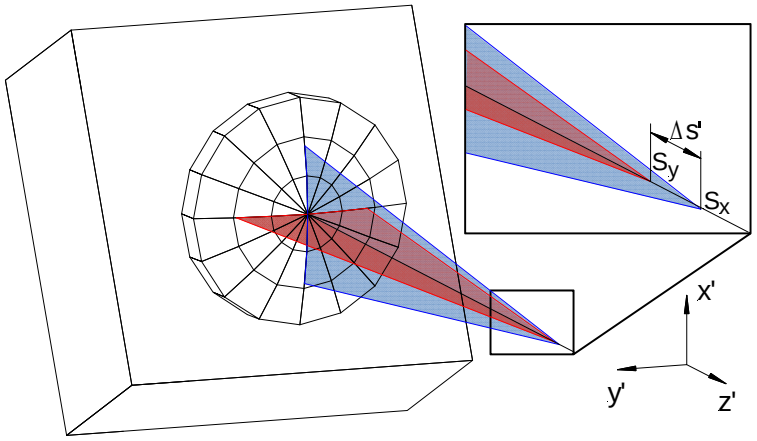

Figure 7.6: Astigmatism in the image plane due to observation through a thick tilted window

alytical expressions for such aberrations imparted by a tilted plane-parallel plate to a converging pencil of rays are given by J. Braat [19]. Aside from spherical and coma aberrations, at given tilt angles of $\beta = 20 - 25°$ the by far strongest optical aberration is astigmatism for which the wavefront aberration coefficient (see [19]) is proportional to $l\,\mathrm{NA}^2$ with l being the window thickness and NA being the numerical aperture. The astigmatism of the tilted window causes orthogonal lines in a object plane to focus sharply at different distances in the image space. This aberration effect is illustrated in Fig. 7.6, where a ray tracing has been conducted in air through a tilted quartz plate of 42 mm thickness ($\beta = 25°$, $n = 1.46157$) and through a biconvex lens ($f = 2\,l$, $M = 1$, $\mathrm{NA} = 0.1$). It turns out that the pencil of rays which lays in the $x' - z'$ plane has a different focus as the pencil of rays in the $y' - z'$ plane. Both foci are displaced by $\Delta s'$. Given the imaging parameter of view no. 2 (see Table 7.2), a total window thickness of $l = 42\,\mathrm{mm}$ and a tilt angle of $\beta = 25°$, the tracing of the extreme rays in the numerical aperture of the lens would result in a back-focal displacement of 1.4% of the focal length or $\Delta s' = 2.8\,\mathrm{mm}$. The corresponding lateral defocussing would be in the order of $2\,\mathrm{NA}\,\Delta s' = 65\,\mu\mathrm{m}$ or about 10 pixel.

Thus, optical compensation of astigmatism of pressure and liner windows is implemented by an additional tilted flat plate made of the same glass and having the same total thickness of both liner and pressure windows. The optical compensators are mounted in front of the lenses of views no. 2 and no. 3 (see Table 7.5, right). Each compensator plate generates additional elliptical droplet image distortions which are rotated around the optical axis by 90°

compared to image distortions from the test rig windows which leads to a near cancelation of droplet image ellipticity. The working principle of the compensator is evident from the ray tracing in Fig. 7.7. Here, the beam path of two extreme rays originating from the same point in image space are shown in perpendicular propagation planes and with and without compensation. The tilt angle β of the plate is equal to the tilt angle of the windows but while the camera tilt axis is parallel with the y-direction the compensator tilt axis is parallel with the x-direction. This leads to cancelation of the focal displacement Δs.

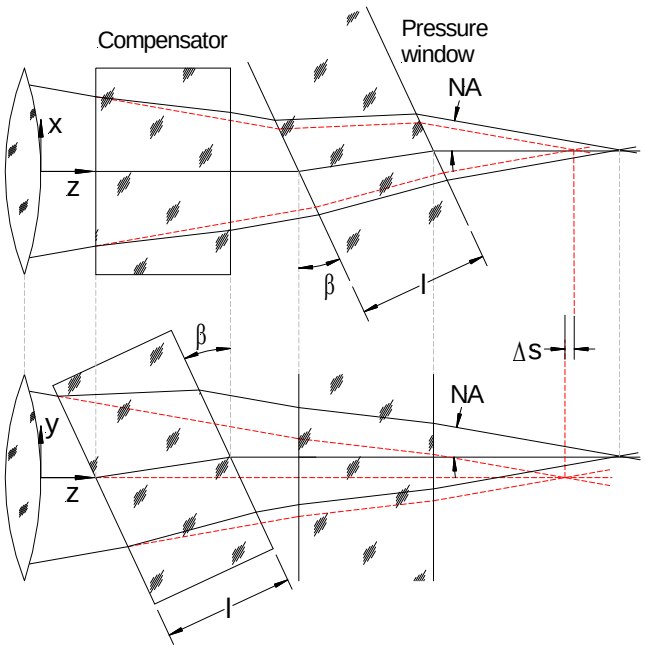

Figure 7.7: Working principle of astigmatism compensation; dashed red line: beam path without compensator; black lines: beam path with compensation

7.3.2 Camera calibration procedure

Camera calibration is achieved using a lithographically manufactured checkerboard pattern on a clear glass substrate (see Sect. 6.3) containing 22×21 corners of 0.75 mm spacing. The glass plate is backlit with a green display LED and is traversed by a small motorized translation stage to record sequentially object-to-image point correspondence inside the spray chamber.

Unlike in the feasibility study (see Sect. 6.3.2), a different miniature translation stage has been used for translation which runs on a precise single rail with cal-

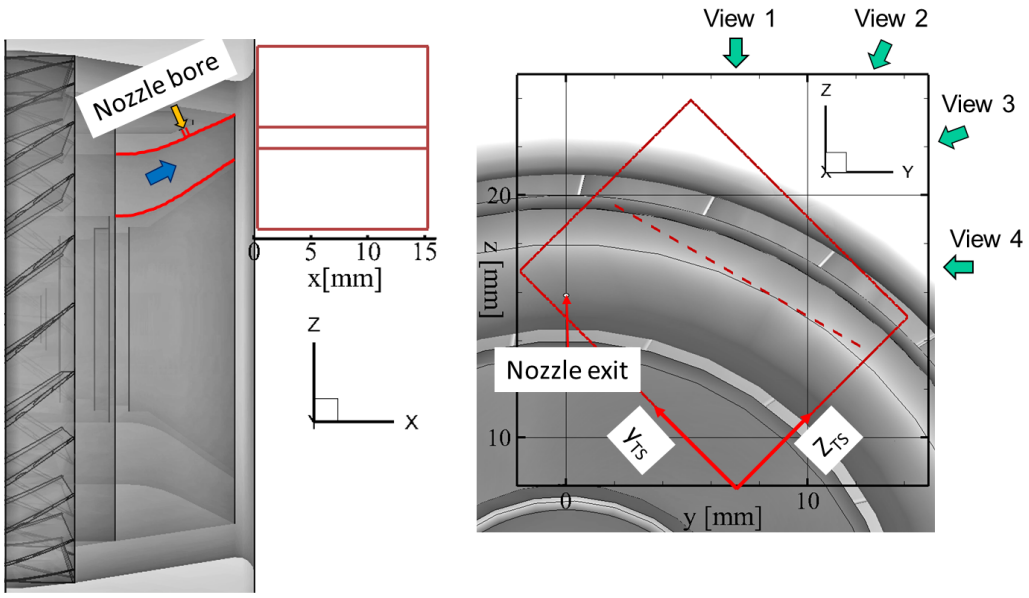

Figure 7.8: Orientation of the measurement volume ; *left* side view with annular passage and injector; *right* axial view; PDA measurements were performed along the dashed line

ibrated, pre-stressed bear ball bearings (*Newport Agilis AG-LS25-27P*). Moving parts consist of thermally matched stainless steal. The translation stage is driven by a piezo motor in closed loop operation with position feedback by a linear encoder. The vendor states a on axis accuracy of 20 μm (travel range 27 mm), an origin repeatability of 0.2 μm and a bidirectional repeatability of 0.2 μm.

The volume within which camera calibration has been conducted is located 6 mm downstream of the injection bore right next to the burner plate. The calibration plate is aligned parallel to the $x_{TS} - y_{TS}$ plane and translated along the z_{TS} (see Fig. 7.8). The latter axis is being rotated by 45° in relation to the burner y-axis to achieve visibility of the calibration plate in each view. Each calibration set consists of seven z positions of 1.5 mm spacing.

Table 7.3 shows the average residuals of the least squares minimization of the reprojection error and the maximum calibration plate disparities (see Sect. 6.3.3). When using a pinhole mapping function, residuals of the outer cameras no. 1 and no. 4 are in the order of $0.14 - 0.33$ pixel or $1.0 - 2.3\,\mu$m within a volume of $16.5 \times 15.8 \times 10.5\,\text{mm}^3$. The residuals of both inner views

Table 7.3: Residuals of world-to-image (fwd.) and image-to-world (rev.) mapping and calibration plate disparities after least squares minimization of the reprojection error with prior correction of positioning inaccuracies

View	Pinhole		Rat. 2^{nd} ord. poly.		maximum plate disparity		
	fwd. [*pixel*]	rev. [μm]	fwd. [*pixel*]	rev. [μm]	$\lvert\Delta x_{TS}\rvert$ [μm]	$\lvert\Delta y_{TS}\rvert$ [μm]	$\lvert\Delta z_{TS}\rvert$ [μm]
1	0.15	1.12	0.06	0.58	0.37	0.02	3.77
2	0.33	2.28	0.11	0.81	0.96	0.05	10.1
3	0.29	2.04	0.09	0.71	0.96	0.03	4.75
4	0.14	1.03	0.09	0.72	0.56	0.06	4.00

no. 2 and no. 3 are about twice as for the outer views no. 1 and no. 4 probably due to the smaller focal depth of the inner cameras resulting in a higher uncertainty of chessboard corner detection near the volume edges. Lens distortions are corrected by an additional minimization of the reprojection error using a higher order camera model which applies ratios of 2^{nd} order polynomials (see Sect. A.2.2). Prior to fitting, the higher order model is initialised using the optimized pinhole mapping coefficients. Calibration plate disparities, especially in z_{TS}, are noticeably smaller compared with disparities obtained during the feasibility study (see Table 6.3) which is mainly due to a higher positioning accuracy of the *Newport Agilis* translation stage.

7.3.3 Depth of field and smallest visible drop size

In the following the visibility of droplet shadows as a function of droplet size and volume position z_{TS} are estimated for the previously described multiple view setup. The underlying spray imaging model is described in Sect. 6.1. The depth of field depends on the resolution capability of each view and can be determined by the two-dimensional point spread function (PSF). If the ellipticity of the 2-D PSF is aligned with the major axes the PSF can be decomposed in two one-dimensional line spread functions (LSF).

The mean width variation of the LSF along x_{TS} over volume depth z_{TS} is estimated using the knife edge technique as described in Sect. 6.4. Measurements of the step response are implemented on the basis of volumetric sets of chessboard calibration images which have already been used for camera calibration (see previous section). Chessboard calibration images were recorded

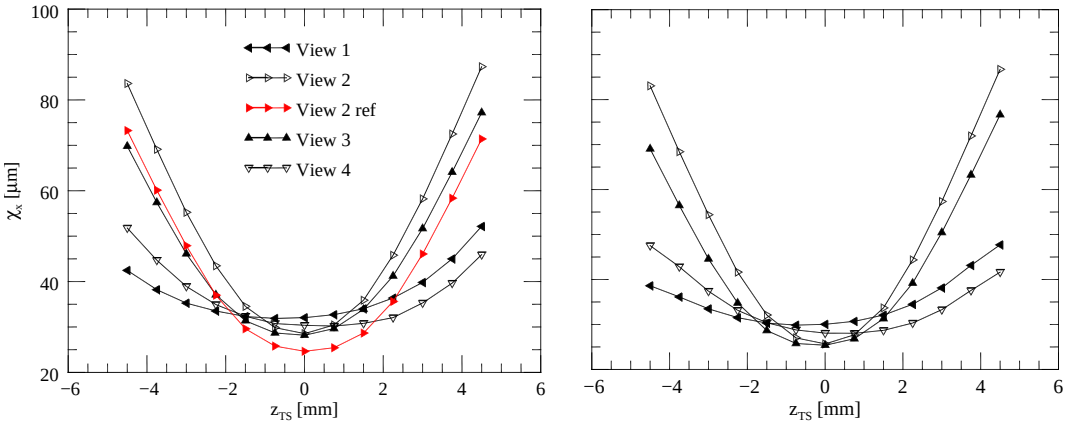

Figure 7.9: Mean half-width of the line spread function along the z_{TS} axis (see Fig. 7.8); *Left*: 83 voxel/mm (approx. 1.5 voxel/pixel); *Right*: 125 voxel/mm (approx. 1 voxel/pixel)

at 13 depth positions with 0.75 mm spacing within the spray chamber. The images are back-projected into the volume and flat-field corrected to enable an estimation of the width of the point spread function in voxel-space which includes possible smoothing effects during reconstruction due to the finite voxel size and image interpolation.

The left subfigure of Fig. 7.9 shows the mean half-width of the line spread function obtained from edge response measurements at a sampling of 83 voxel/mm (approx. 1.5 voxel/pixel) along the x_{TS} axis (coordinate system as shown in Fig. 7.8). The image sharpness of the two inner views no. 2 and no. 3 decreases stronger towards the volume edges as compared to view no. 1 and no. 4. The reference curve (red line) is measured for view no. 2 without windows and without compensator plates. The reference exhibits nearly the same shape meaning that the stronger blurring toward the volume edges is not caused by windows but seems to be specific for the particular lens that has been used for view no. 2 and no. 3 (Nikkor micro $f = 200$ mm) although magnification and f-number are similar compared to view no. 1 and no. 4 (Nikkor micro $f = 100$ mm).

Only minor improvements can be achieved by increasing the sampling to 125 voxel/mm (approx. 1.5 voxel/pixel) because the resolution is limited by the optical arrangement as shown in Fig. 7.9, right.

Due to the use of Scheimpflug mounts, focal planes of all views are almost

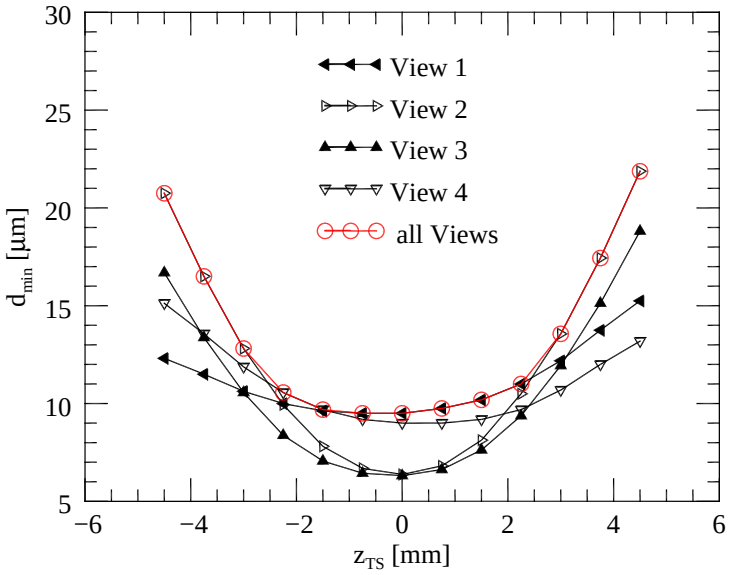

Figure 7.10: Smallest visible droplet diameter of the spray imaging setup as a function of volume depth, at a spatial sampling of 83 voxel/mm

parallel with respect to the calibration plate. Astigmatic aberrations are minimized by compensator plates. Hence, the PSF at each depth position should have almost a circular Gaussian shape with its half-width being equal to the LSF half-width [130]. Therefore, the LSF can be used to infer the minimum visible droplet diameter of the setup shown in Fig. 7.5.

Based on the LSF half-width the shadow image depletion i_{min} can be estimated for a given droplet size range from Eq. (6.6) as described in Sect. 6.4. The transmission coefficient is gained from Mie simulations of spherical kerosene drops in air as described in Sect. 6.1. The threshold of visibility is estimated from intensity fluctuations in 200 images recorded with LED back-illumination and without spray. After image normalization, all pixel intensities have a mean of $\tilde{i} = 1 \pm \sigma$ and the threshold of visibility was set to a values of $\tilde{i}_{thres} = 1 - 2\sigma$ yielding values of 0.980, 0.988, 0.988 and 0.980 for the view no. 1-4. Fig. 7.10 shows the estimated smallest visible droplet sizes d_{min} for a spatial sampling of 83 voxel/mm. If one of the views can not detect a droplet because of low contrast it would not be visible in the reconstructed volume. Therefore, the combined maximum of the size limits of all cameras at each calibration plate position gives the limit of the multiple view setup (red line in Fig. 7.10). For a given volume size of $16 \times 13 \times 10\,\mathrm{mm}^3$ it turns out that the minimum resolvable droplet diameter approaches $d = 10\,\mu$m within the focus and increases up to $d = 20\,\mu$m towards the volume edges.

The droplet visibility is only slightly improved if the spatial sampling rate is increased to 125 μm (approx. 1 voxel/pixel) so a sampling of 83 voxel/mm (voxel size of 12 μm) was chosen to reduce the computational time of volume processing as much as possible.

7.4 Image processing and volume reconstruction

After dark image subtraction, shadowgraphs are median filtered within the 3×3 neighborhood to reduce pixel artifacts of the sCMOS camera sensor. Then, images are flat-field corrected and normalized by division by a bright field image without spray. Prior to reconstruction the image intensities are inverted and a constant offset of 2σ is subtracted to clip intensities close to pixel noise (preprocessing **A** in Fig. 7.11 middle). The remaining unstructured background between droplet shadows seems to originate from small vaporized kerosene droplets with sizes below the smallest visible droplet size or from droplets which are completely out-of-focus. Unstructured background intensity around droplet images is partially removed by subtracting the local minimum in a 20×20 pixel kernel followed by clipping of a constant threshold (preprocessing **B** in Fig. 7.11 bottom). The removal of unstructured background between droplet images is not complete meaning that not all droplet shadow images are segmented. A further increase of the threshold would clip the smallest or most unfocused droplets images that exhibit the lowest contrast. Preprocessing **A** without sliding minimum subtraction and thresholding is applied prior reconstructions which are used to gain information about the placement of liquid phase in the spray (spatial intensity distribution). Preprocessing **B** is optimized to enhance gradients near the droplet shadow border and to improve the correlation signal height for droplet velocity estimation.

Resolution estimations from the preceding section have shown that a voxel size of 12 μm represents a sufficient spatial sampling during reconstruction. At a volumetric domain of $18 \times 17 \times 9\,\mathrm{mm}^3$ this corresponds to a total size of $1312 \times 1088 \times 864$ voxel. The observed intensities from each voxel are reconstructed according to its line-of-sight intersection with each image plane. These positions are calculated using mapping functions of ratios of 2nd order

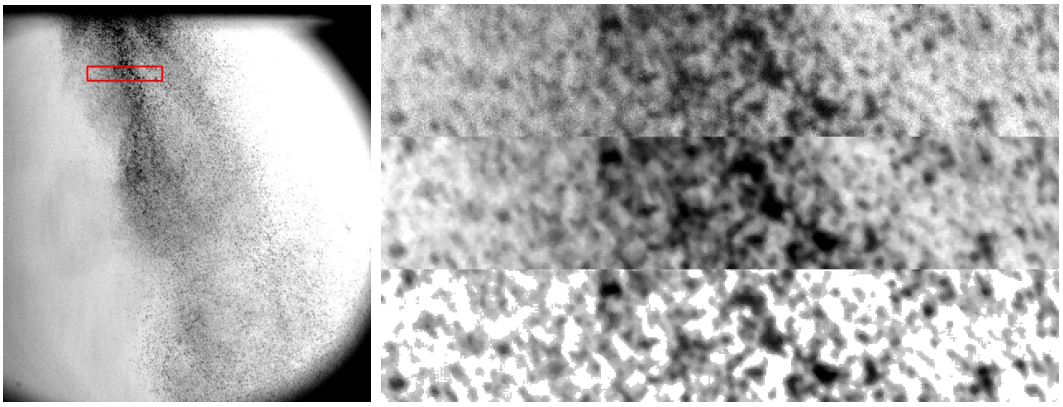

Figure 7.11: *Left*: Sample spray image obtained from view no. 1 at $p_a = 4\,\mathrm{bar}$, $T_a = 440\,\mathrm{K}$, $q_{UV} = 8$, $\mathrm{We}_{\mathrm{aero}} = 360$. *Right*: Magnified region of $410 \times 80\,\mathrm{pixel}$ ($\approx 3.11 \times 0.61\,\mathrm{mm}$) from the red box. Top: raw image; *Middle*: after contrast enhancement (processing **A**); *Bottom*: after local minimum subtraction (20×20 neighborhood) and thresholding (processing **B**).

polynomials which are obtained from camera calibration (see Sect. 7.3.2). The observed intensities from each view are combined by the maximum entropy technique (MENT) described in Sect. 3.1.1. Sub-pixel intensities are bilinearly interpolated between the 4-connected pixels. The FMART reconstruction technique (see Sect. 3.1.3) so far has not been applied and would require implementation of non-uniform weighting functions due to large variations of the PSF along the depth of field (see Fig. 7.9).

7.5 Droplet velocimetry by 3-D cross-correlation and error analysis

Droplet displacement recovery in the volume is achieved through the 3-D cross-correlation scheme as described in Sect. 5.4.3. A multi-grid algorithm is used, which employs a resolution pyramid that starts at a rather coarse grid of $128 \times 32 \times 32$ voxel and stepwise increase resolution to $64 \times 16 \times 16$ voxel while continually updating a predictor field. Intermediate validation is based on normalized median filtering. Once the final spatial resolution is reached volume deformation based on third-order B-splines is applied at least twice to further improve the match between volumes and thereby improving the displacement

estimates. The final vector spacing is $0.38 \times 0.19 \times 0.19$ mm ($32 \times 16 \times 16$ voxel) at a interrogation volume size of $0.77 \times 0.38 \times 0.38$ mm ($64 \times 32 \times 32$ voxel). Clearly, the resulting velocity field is not directly transferable to single droplets but at least provides estimates of the mean velocity of groups of droplets inside each interrogation box. Single droplet velocities can be obtained by subsequent tracking of each droplet reconstruction using matching techniques (e.g. nearest neighbour, neural network or the relaxation technique [124]).

An error analysis for the results of 3-D cross-correlation is hardly feasible because the cross-correlation noise depends on both the number of droplets per interrogation volume and the 3-D size of droplet reconstructions (c.f. [173]). Both parameter are unknown and depend on the spatial spray distribution, the local size distribution and the local PSF. The maximum of the cross-correlation coefficient Eq. (2.16) within each interrogation box at least provides a combined measure of both the number and the image contrast of contributing droplets, ligaments and ghost particle. Thus, each vector is validated based on the maximum correlation coefficient in order to exclude regions of low droplet number density and/or low image contrast. The vector is accepted only if the maximum cross-correlation coefficient is larger than 0.1.

The influence of viewing geometry on the relative accuracy of velocity estimates can be derived using the methodology provided in Sect. 5.5. According to the present viewing geometry (see Table 7.2 and Fig. 7.8) the uncertainty on the velocity component W (along z_{TS}) is 1.3 times larger compared to velocity components U and V along x_{TS} and y_{TS} which both are almost equal.

7.6 Results and discussion

The shadowgraph in Fig. 7.11 confirms that the spray is at a late state of air-blast atomization when it leaves the annular gap. Most of the liquid is already dispersed into droplets. The droplet distribution is not homogeneous and wavy streaks of larger droplets appear in the jet.

Fig. 7.12 (left) shows the instantaneous intensity-inverted shadow intensity within a spray volume at $p_A = 4$ bar, $T_A = 440$ K, $q_{uv} = 8$, $\mathrm{We}_{\mathrm{aero}} = 360$

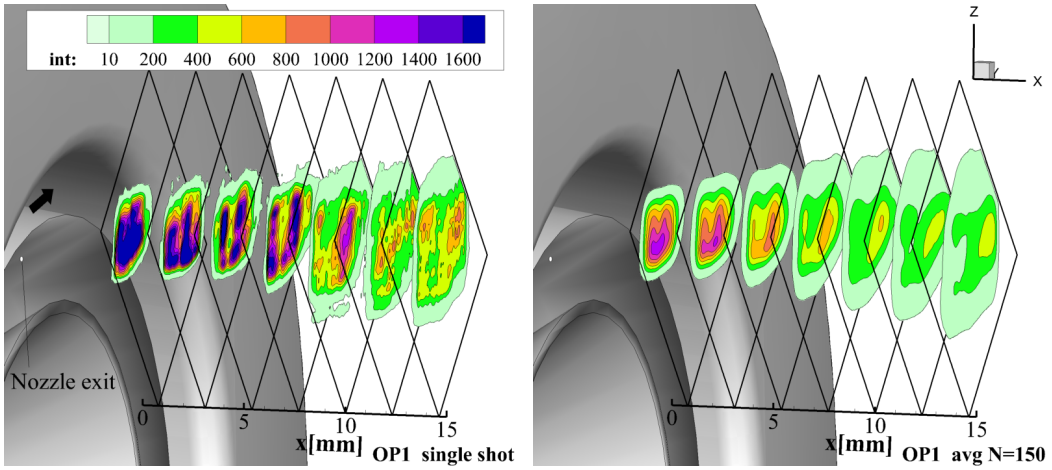

Figure 7.12: Volumetric intensity distributions obtained with tomographic shadowgraphy at $p_a = 4\,\mathrm{bar}$, $T_a = 440\,\mathrm{K}$, $q_{UV} = 8$, $\mathrm{We}_{\mathrm{aero}} = 360$; Single shot smoothed over 32^3 voxel(*left*) and average of 150 tomographic reconstructions (*right*)

at equidistant slices obtained from tomographic reconstruction of images with preprocessing **A**. Intensities are smoothed over 32^3 voxel ($0.38^3\,\mathrm{mm}^3$) to reduce the granularity from single droplet reconstructions. The result gives a qualitative impression of the spatial spray distribution with intensity being a rough indicator of droplet size.

The average intensity distribution shown in Fig. 7.12 (right) exhibits a u-shaped structure at ($x = 1 - 8\,\mathrm{mm}$) which indicates regions where droplets appear frequently. These regions seem to arise from the jet shear layer, where ligaments and drops are shed during surface break-up. At given operation conditions the Weber number $\mathrm{We}_{\mathrm{aero}} = 360$ is close to the transition Weber number (see Eq. (7.4) indicating that surface break-up is the dominant breakup mechanism of the kerosene jet. Further downstream the windward leg of the u-shaped structure disintegrates faster possibly due to stronger interaction with the swirled flow. Prior to evaporation, larger droplets are radially conveyed further outward in comparison to smaller droplets. The u-shaped structure of the mean droplet distribution has been confirmed by visualizations of Mie-scattering using a planar light-sheet[52].

Reconstruction ambiguities ('ghost particles' [42]) lead to a slight elongation of the u-shaped structure along volume depth near the burner plate due to

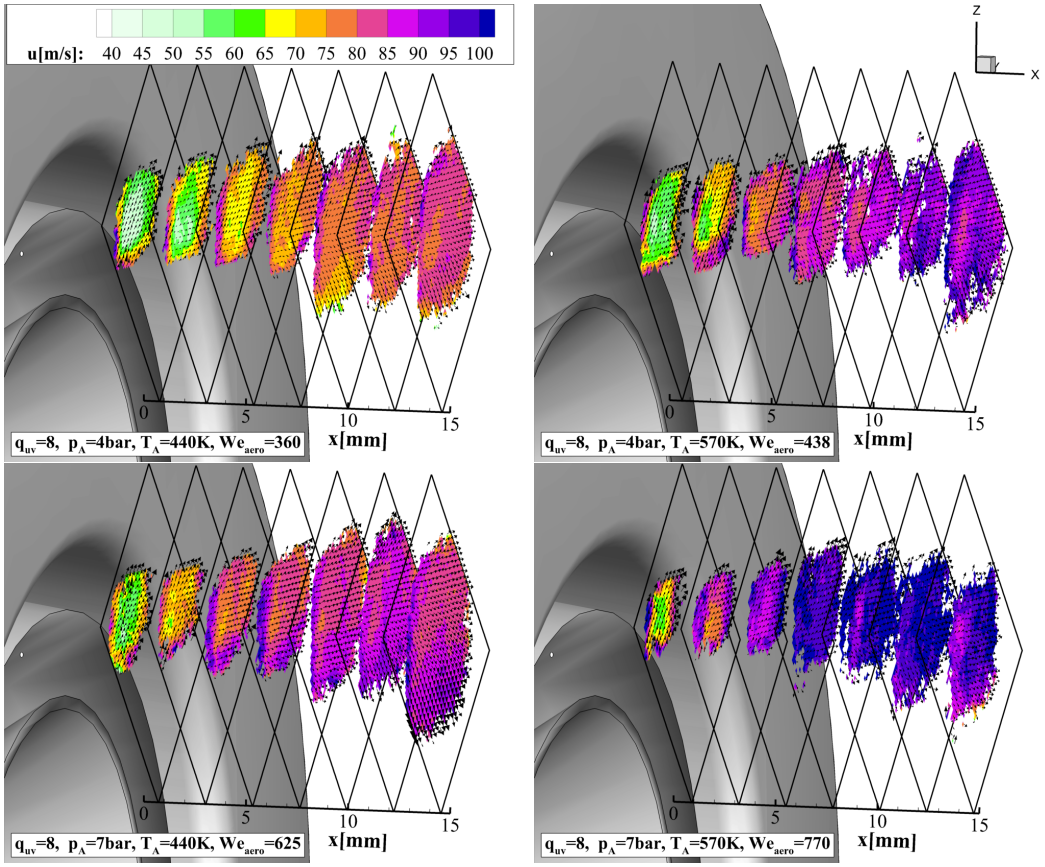

Figure 7.13: Snap shots of droplet velocities obtained from 3-D cross-correlation of single shots at different operation conditions (see Table 7.1). Vectors show the in-plane V, W components.

high droplet image densities. These ambiguities were also observed during the feasibility study at ambient conditions (see Sect. 6.6.2). Ambiguities could be partially suppressed by using additional cameras or more advanced reconstruction algorithms (e.g. FMART) which is subject of ongoing research.

Interaction of the hot, pressurized air flow with the spray can be studied by single shot velocity fields obtained from 3-D correlation analysis. Fig. 7.13 shows equidistant slices of the spray velocity field at increasing Weber number obtained from single shot results. Signal peaks that involve a correlation coefficient below 10% are blanked. The contour shape (axial velocity) can also be seen as a region, where droplets above the resolution limit of $d = 10\,\mu$m appear in coherent motion. The contour size and position can be used to track the spray trajectory and extension in space at fixed time.The size of the contoured area clearly decreases with rising air and fuel temperature indicating a signif-

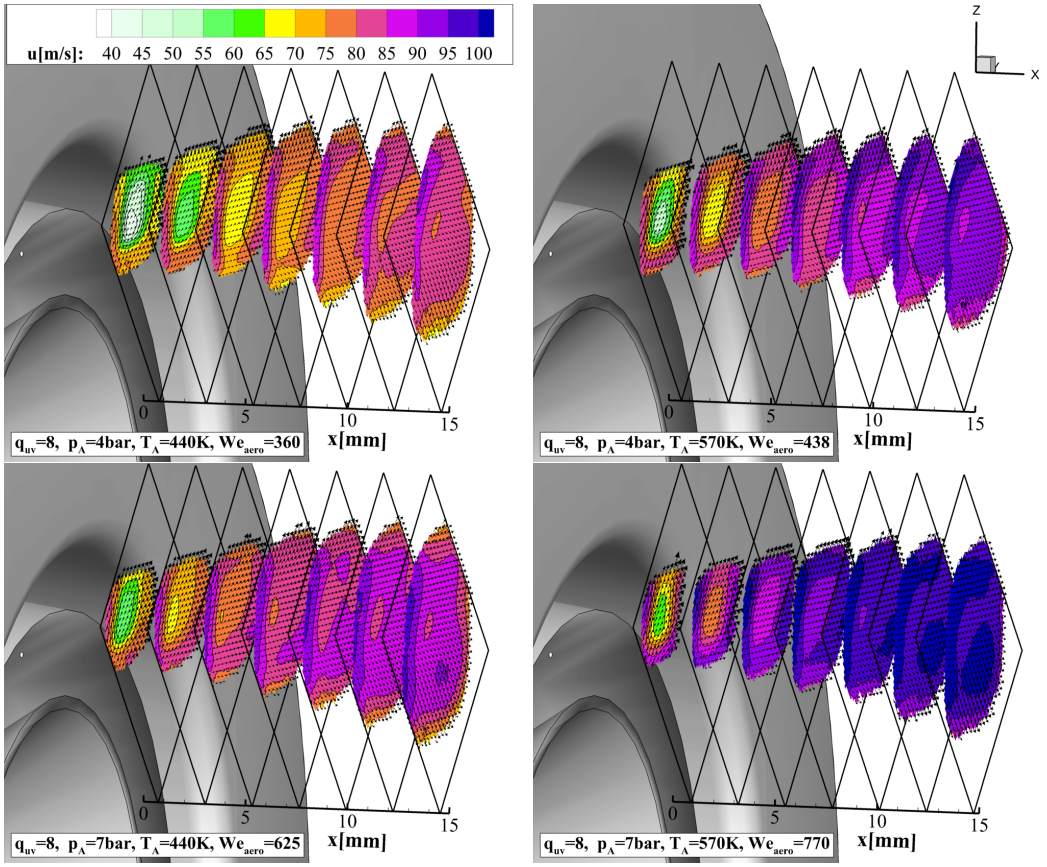

Figure 7.14: Mean droplet velocities obtained by averaging over 500 samples at different operation conditions (see Table 7.1). Vectors show the in-plane V, W components.

icant droplet size reduction which is also evident from PDA measurements of liquid jet in cross flow atomization at elevated temperature (c.f. [65]).

Averaged spray velocities are shown in Fig. 7.14 and reveal slightly higher axial spray velocities on the windward side of the spray. Near the burner plate both, instantaneous and time-averaged measurements show lower axial velocities inside the spray tail in comparison to outer regions. This might be due to the higher aerodynamic drag which the incoming air has to overcome until it reaches inner spray fragments, ligaments and droplets (c.f. [190]). There are clear differences of the sizes of contoured areas between average (Fig. 7.14) and instantaneous results (Fig. 7.13) which indicates fluctuations of the spray tail position. These differences are more pronounced at $T_a = 570\,\mathrm{K}$.

At $x = 10\,\mathrm{mm}$ distance to the burner plate, mean velocities are compared to

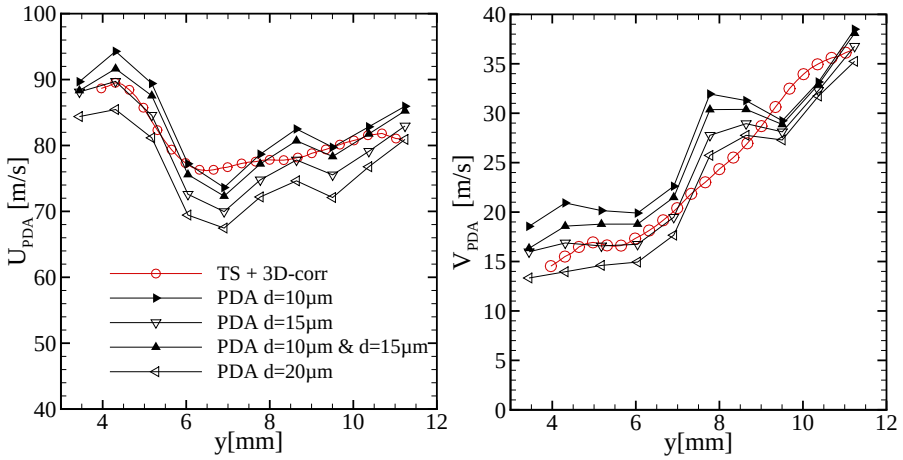

Figure 7.15: Comparison of velocity profiles obtained by PDA and tomographic shadowgraphy (TS) at $x = 10\,\mathrm{mm}$ along the dashed line in Fig. 7.8 (v_{PDA} runs parallel to the dashed line), $p_A = 4\,\mathrm{bar}$, $T_A = 440\,\mathrm{K}$, $q_{UV} = 8$, $\mathrm{We}_{\mathrm{aero}} = 360$

2-D PDA measurements acquired along the dashed line in Fig. 7.8. Fig. 7.15 shows axial and tangential velocity profiles of different size classes in comparison with profiles obtained from 3d correlation of two reconstructed volumes. Axial velocities are in agreement with velocities obtained from the $d = 10\,\mu\mathrm{m}$ and $d = 15\,\mu\mathrm{m}$ size classes except in regions with strong gradients (e.g. $y = 7\,\mathrm{mm}$). Velocities obtained from 3D correlation drop off near the edges, probably due to spatial averaging within the interrogation volume. Differences in tangential velocity are also present in regions with larger velocity gradients. Two possible explanations are: Either velocities are smoothed due to the correlation over varying droplet sizes within one interrogation volume or there is an additional bias due to reconstruction ambiguities ('ghost particles'). On the other hand PDA data might be biased to some degree by positioning inaccuracies or deviations of operation conditions during sequential acquisition of measurement points.

7.7 Summary

Tomographic shadowgraphy was applied in a non-reactive kerosene spray in a pressurized environment with preheated swirled airflow. Measurements rely on

the tomographic reconstruction of four views that image a combined volume of $16 \times 13 \times 10\,\mathrm{mm}^3$ at a magnification close to unity using pulsed LED illumination. The use of compensator plates to correct for astigmatism induced by the thick windows of the pressure casing has been described.

Estimations of the droplet shadow image contrast on the basis of the local point spread function revealed that the depth of focus strongly depends upon the droplet diameter. The minimum resolvable droplet diameter of the described multiple view setup approaches $d = 10\,\mu\mathrm{m}$ within a depth of field of $-2\,\mathrm{mm} < z_{TS} < 2\,\mathrm{mm}$ and than increases to $d = 20\,\mu\mathrm{m}$ within the depth range $2\,\mathrm{mm} < |z_{TS}| < 5\,\mathrm{mm}$. Velocities of droplets above the resolution limit were retrieved by 3-D cross-correlation of two consecutive spray volumes using small interrogation volumes of $0.77 \times 0.38 \times 0.38\,\mathrm{mm}$ at a vector spacing of $0.38 \times 0.19 \times 0.19\,\mathrm{mm}$. In this way, three-dimensional instantaneous spray velocities of jet-in-cross-flow atomization could be estimated at Weber numbers of $\mathrm{We}_{\mathrm{aero}} = 360 - 770$, air pressures of p_A=4-7 bar and air temperatures of T_A=440-570 K. Extracted slices of the instantaneous axial velocity indicate increasingly motion (undulations) and fluctuations of the spray tail with increasing temperature.

Validation against PDA velocity data revealed good agreement at size classes $d = 10\,\mu\mathrm{m}, 15\,\mu\mathrm{m}$ but some deviations in regions with strong velocity gradients. Deviations are probably caused by spatial smoothing over droplets within the finite size of each interrogation volume and by the presence of reconstruction ambiguities ('ghost particles'). The latter shortcoming might be improved by more advanced reconstruction techniques such as FMART. Application of FMART to the present data would require implementation of non-uniform weighting functions for droplet image sampling. The reason are large variations of the PSF across the volume for the required volume depth of 10 mm at a magnification close to unity.

Chapter 8

Conclusions and perspectives

Regarding volume resolving velocimetry for turbomachinery test facilities the most important results of the thesis are summarized below and presented in perspective.

8.1 Fast reconstruction of particle fields: performance evaluation using synthetic data

A novel Fast Multiplicative Algebraic Reconstruction Technique (FMART) has been introduced which performance has been assessed in comparison to a maximum entropy technique (MENT) and to conventional simultaneous MART (SMART) on the basis of a synthetic swirl flow.

Error distributions are presented that base on the differences between the measured displacement component and the analytical solution of the flow field taken at the center of each interrogation volume. At intermediate particle image densities of 0.05 ppp both FMART and SMART exhibit rather similar uncertainties of the displacement magnitude of 0.11 voxel and 0.10 voxel while cross-correlation of a reference containing no ghosts ('ground truth') exhibits uncertainties of 0.09 voxel. The latter represents the accuracy limit due to spatial filtering of the finite interrogation volume. The corresponding global velocity measurement error with regard to a displacement maximum of

5 voxels is 2.2% for FMART, 2% for SMART and 1.8% for the noise-free reference. Cross-correlation on the basis of MENT revealed a higher uncertainty of 0.13 voxel (2.6%). With increasing particle image density the uncertainty of displacement estimates grows faster for SMART than for FMART which is accompanied by a higher uncertainty of the displacements along volume depth for SMART. At a particle image density of 0.1 ppp the uncertainties on displacements along volume depth are 0.17 voxel (3.4%) for FMART, 0.21 voxel (4.2%) for SMART and 0.25 voxel (5%) for MENT. The slightly better accuracy of FMART at high image densities is probably due to the tendency to produce less extensive ('spiky') particle reconstructions. In summary, it can be ascertained that reconstructions obtained with FMART or SMART exhibit a considerably stronger suppression of ghost intensity than those obtained with MENT. From 0.05 ppp, the higher accuracy of FMART comes at the cost of a longer computation time compared with MENT. On the other hand the FMART time consumption remains significantly below that of SMART. Within the tested range of image densities ($0.03\,\text{ppp} - 0.13\,\text{ppp}$), the computation time required to achieve a similar reconstruction quality is $1.5 - 20$ times longer for SMART in comparison to FMART.

8.2 Experimental performance evaluation in a transonic cascade wind tunnel

The experimental performance of TPIV and different reconstruction techniques have been evaluated by measurements of the corner flow of a highly loaded compressor cascade at $\text{Ma}_1 = 0.60$. Velocities obtained with FMART and MENT are compared to those obtained by SMART as well as to SPIV measurements at three selected planes. Measurements are conducted in a volumetric domain of $36 \times 24 \times 3.5\,\text{mm}^3$ using four simultaneous camera views. The error analysis revealed uncertainties on span-wise components of velocity that are two times larger in comparison to axial components. Mean axial flow velocities show broad consistency with stereoscopic PIV with improved depth resolution. A comparison of secondary flow velocities revealed systematic deviations from SPIV of up to 5 m/s at a maximum axial velocity of 125 m/s. The probable

reason seems to be that the thin sheet is almost twice as thick as the TPIV interrogation box, resulting in reduced depth resolution for SPIV. Another reason might be a slight misalignment between the thin light sheet (SPIV) and the z planes under consideration. Instantaneous secondary velocity fields obtained with SMART and FMART reveal more similarities with each other while MENT exhibits larger deviations. Cross-correlation of MENT reconstructions underestimates the axial velocities by up to 4% and span-wise component by up to 6% both with regard to the maximum mean axial velocity in the measurement domain (125 m/s). Both SMART and FMART reconstructions reveal very similar velocities except in regions that exhibit a halving of laser irradiance (near the front and the back of the measurement domain). In these regions the blade-normal velocities obtained with FMART deviate by $2-3\,\mathrm{m/s}$ ($\delta Y = 0.2-0.3\,\mathrm{voxel}$) from the the reference (SMART). Regarding RMS values, FMART exhibits $20-25\%$ ($2-3\,\mathrm{m/s}$) higher span-wise fluctuations compared to SMART. This is accompanied by a slightly lower validation rate for FMART. Higher fluctuations are probably due to variations of the local particle image shape (blur or other distortions) which are not yet taken into account during FMART image sampling. Another probable reason is considered to be differences of both camera models. The SMART camera model additionally includes a correction of particle image distortions and a disparity correction (volume self-calibration). The slightly higher velocity accuracy of SMART comes at the cost of a 4.5 times longer processing time. The speed gain is about twice as low as predicted by numerical studies. The reason seems to be a larger particle image diameter compared to the numerical studies ($2-5\,\mathrm{pixels}$ instead of $3\,\mathrm{pixels}$), resulting in a higher number of occupied voxels which intensity has to be refined iteratively.

Laser flare due to light scattering within the facility poses some problems since it affects each camera view differently. In the present case the camera views aligned with the span of the airfoil were only weakly affected, whereas the inclined camera views were strongly affected by light scattering off the airfoil which caused a loss of signal in these areas. Due to these reflections, application of TPIV was only possible up to a blade-normal distance of 1-2 mm.

8.3 3-D spray reconstructions using tomographic shadowgraphy

The development of tomographic shadowgraphy has been described in the second part of the thesis. The technique bases on inline illumination provided by pulsed LEDs while each camera records image pairs at a fixed time increment. Three-dimensional droplet positions are obtained by means of a tomographic reconstruction. The instantaneous velocity of droplet ensemble is estimated through three-dimensional cross-correlation between both voxel volumes. Compared to holographic methods the instrumentation effort is considerably less complex to implement but requires a multiple view access to the spray. In particular the use of pulsed LED illumination in place of lasers further reduces complexity and cost.

During a preparatory study at ambient conditions instantaneous 3-D spray distributions of hollow cone and flat fan water sprays are reconstructed. The study revealed that droplet positions can be obtained by superposition of the lines of sight while the shape of fragments and ligaments at the primary stage of atomization can only roughly be identified in the reconstruction. The reason for this is that complex liquid structures are imaged quite differently by each camera depending on how the light is refracted through the liquid structures. With increasing droplet number densities SMART provides a better suppression of ghost intensities inside the hollow cone in comparison to MENT. SMART has the disadvantage of roughly a four times longer computational time in comparison to MENT for the present data.

Tomographic shadowgraphy was used for the first time to measure droplet velocities and spatial spray distributions of a generic aero-engine atomizer in a pressurized environment with preheated swirled airflow. Using four double-frame cameras and pulsed LEDs air-blast atomization of a non-reactive single kerosene jet in a swirl-flow have been investigated immediately downstream of the burner exit in a measurement domain of $16 \times 13 \times 10\,\mathrm{mm}^3$. The use of compensator plates to correct for astigmatism induced by the thick windows of the pressure casing has been demonstrated. For the present setup, an error analysis revealed uncertainties on radial components of velocity that are 1.3

times larger in comparison to axial components. The minimum resolvable droplet diameter of the described multiple view setup is estimated with $d = 10\,\mu$m.

Immediately downstream of the burner exit the fuel spray mainly consist of droplets and a few larger ligaments. Thus, velocities of droplets above the resolution limit have been retrieved by 3-D cross-correlation of two consecutive spray volumes. In this way, three-dimensional instantaneous spray velocities of jet-in-cross-flow atomization could be estimated at Weber numbers of $\mathrm{We}_{\mathrm{aero}} = 360 - 770$, air pressures of p_a=4-7 bar and air temperatures of T_a=440-570 K. Extracted slices of the instantaneous axial velocity indicate increasingly motion (undulations) and fluctuations of the spray tail with increasing temperature. Validation against PDA velocity data revealed good agreement at size classes $d = 10\,\mu\mathrm{m}, 15\,\mu\mathrm{m}$. Deviations are probably caused by spatial smoothing over droplets within the finite size of each interrogation volume and by the presence of reconstruction ambiguities ('ghost particles'). The latter shortcoming might be improved by more advanced reconstruction techniques such as FMART.

8.4 Perspectives

The application of tomographic and other multi-view imaging techniques on facilities with limited optical access presents a number of challenges some of which are difficult if not impossible to solve. Geometric constraints imposed by windows limit not only the maximum possible viewing angles but more importantly frequently constrain the commonly viewed domain (volume of interest), in particular if this domain is located further inside the facility. Given these challenges the choice of applying tomographic methods to turbomachinery facilities has to be carefully assessed in the context of the physics to be investigated. Foremost, the application of these methods only is justified if the flow itself is highly unsteady and cannot be adequately mapped using planar techniques, whose implementation generally is significantly less complex. On the other hand the access to three-dimensional, three-component unsteady velocity data alongside with the fully resolved three-dimensional strain tensor makes tomographic velocimetry very attractive to reliably capture the flow

physics and to provide important validation data. Research results in the present thesis suggest the following actions and improvements during future work on volume resolving velocimetry for turbomachinery test facilities at realistic operation conditions:

Enhanced particle reconstruction with FMART

- Implementation of non-uniform weighting of particle images on the basis of calibration images
- Compensation of camera vibrations by global improvements of 3-D particle positions on the basis of residual images

3-D 3-C Velocimetry in cascade wind tunnels

- Improvement of mechanical stability of thick-sheet laser illumination to achieve near-wall measurements
- Improvement of cross-sectional shape of the thick sheet volume illumination (ideally flat top) and at least doubling of laser irradiance

Optimization of fuel injectors using tomographic shadowgraphy

- Visualization of single droplet velocities at a fixed time using predictor fields from 3-D cross-correlation followed by particle tracking velocimetry (PTV)
- Derivation of unsteady 3-D distributions of spray penetration and velocity at preheating temperatures up to 750 K and air pressures of 12 bar ($We_{aero} > 1500$) in order to approach typical cruise conditions of fuel atomization

Appendix A

Camera calibration

A.1 Normalization of point correspondences

The result of camera calibration depends upon the coordinate frame in which point correspondences are expressed [64]. Thus a normalization of calibration points is conducted to avoid truncation errors during estimation of the camera parameters. The latter originates from combinations of very small and very large numbers (e.g. at very small magnifications). Apart from improved accuracy of parameter estimation, normalization provides a second benefit, namely that resulting mapping functions are invariant with respect to an arbitrary choice of the scale and coordinate origin [64]. The applied normalization method consists of translation and scaling of world and image coordinates of calibration points as follows:

$$\begin{bmatrix} \tilde{x} \\ \tilde{y} \\ \tilde{z} \end{bmatrix} = \frac{1}{s} \begin{bmatrix} x - c_x \\ y - c_y \\ z - c_z \end{bmatrix}$$
$$\begin{bmatrix} \tilde{x}_I \\ \tilde{y}_I \end{bmatrix} = \frac{1}{s_I} \begin{bmatrix} x_I - c_{Ix} \\ y_I - c_{Iy} \end{bmatrix}, \tag{A.1}$$

where c_x, c_y and c_z denote the coordinates of the centroid of the point cloud which is observed by all cameras and c_{Ix}, c_{Iy} are image coordinates of the centroid in each camera. Thus all coordinates are translated so as to bring

the centroid of the set of all points to the origin. The scaling factors s and s_I are set to the mean euclidian distance of the centered world and image point cloud. Thus, the "average" world and image point becomes $(1,1,1)^T$ respectively $(1,1)^T$.

A.2 Estimation of camera parameters

A.2.1 First order camera model (DLT)

The parameter of the DLT matrix Eq. (2.1) are computed from normalized calibration points. These points are arranged in a set of linear equations of the form $0 = \mathbf{La}$, where $\mathbf{L}$ is obtained from Eq. (2.2) and has the shape $2N \times 12$ with N being the number of point correspondences:

$$\mathbf{L} = \begin{bmatrix} \tilde{x}_1 & \tilde{y}_1 & \tilde{z}_1 & 1 & 0 & 0 & 0 & 0 & -\tilde{x}_1\tilde{x}_{I1} & -\tilde{y}_1\tilde{x}_{I1} & -\tilde{z}_1\tilde{x}_{I1} & -\tilde{x}_{I1} \\ 0 & 0 & 0 & 0 & \tilde{x}_1 & \tilde{y}_1 & \tilde{z}_1 & 1 & -\tilde{x}_1\tilde{y}_{I1} & -\tilde{y}_1\tilde{y}_{I1} & -\tilde{z}_1\tilde{y}_{I1} & -\tilde{y}_{I1} \\ \vdots & \vdots & \vdots & \vdots & \vdots & \vdots & \vdots & \vdots & \vdots & \vdots & \vdots & \vdots \\ \tilde{x}_i & \tilde{y}_i & \tilde{z}_i & 1 & 0 & 0 & 0 & 0 & -\tilde{x}_i\tilde{x}_{Ii} & -\tilde{y}_i\tilde{x}_{Ii} & -\tilde{z}_i\tilde{x}_{Ii} & -\tilde{x}_{Ii} \\ 0 & 0 & 0 & 0 & \tilde{x}_i & \tilde{y}_i & \tilde{z}_i & 1 & -\tilde{x}_i\tilde{y}_{Ii} & -\tilde{y}_i\tilde{y}_{Ii} & -\tilde{z}_i\tilde{y}_{Ii} & -\tilde{y}_{Ii} \\ \vdots & \vdots & \vdots & \vdots & \vdots & \vdots & \vdots & \vdots & \vdots & \vdots & \vdots & \vdots \\ \tilde{x}_N & \tilde{y}_N & \tilde{z}_N & 1 & 0 & 0 & 0 & 0 & -\tilde{x}_N\tilde{x}_{IN} & -\tilde{y}_N\tilde{x}_{IN} & -\tilde{z}_N\tilde{x}_{IN} & -\tilde{x}_{IN} \\ 0 & 0 & 0 & 0 & \tilde{x}_N & \tilde{y}_N & \tilde{z}_N & 1 & -\tilde{x}_N\tilde{y}_{IN} & -\tilde{y}_N\tilde{y}_{IN} & -\tilde{z}_N\tilde{y}_{IN} & -\tilde{y}_{IN} \end{bmatrix} \tag{A.2}$$

Initially, the solution $\mathbf{a} = (a_{11}, a_{12}, a_{13}, a_{14}, a_{21}, a_{22}, a_{23}, a_{24}, a_{31}, a_{32}, a_{33}, a_{34})^T$ can be estimated in a least squares fashion using singular value decomposition (SVD) of $\mathbf{L}$ as described by Faugeras and Toscani [49] (see also Hartley and Zisserman [64]). Within this thesis, the SVD implementation from OpenCV [21] is used. In order to provide a homogeneous solution, $\mathbf{a}$ is divided by a_{34}. To improve the accuracy of $\mathbf{a}$ in a second step, a iterative maximum likelihood estimation is applied [194, 57] by minimizing the reprojection error function:

$$\varepsilon_i = \sqrt{(\widehat{x_{Ii}} - x_{Ii})^2 + (\widehat{y_{Ii}} - y_{Ii})^2}\,, \tag{A.3}$$

where the residual ε_i denotes the magnitude of the difference vector between estimated point projections $(\hat{x_I}, \hat{y_I})$ and measured pixel coordinates (x_I, y_I). Minimizing the reprojection error is a nonlinear minimization problem, which can be solved with the Levenberg-Marquardt algorithm (LM) [126]. The LM

algorithm was implemented using the C library *lmfit* [191].

The resulting DLT matrix of each camera is modified by an additional affine transformation to include normalization parameter (c.f. Sect. A.1) and to finally obtain a direct mapping between world and image coordinates.

A.2.2 Higher order camera models

Following C. Willert [179], three-dimensional mapping functions are applied that involve ratios of 2nd order polynomials. Those functions are obtained by extending numerator and denominator in Eq. (2.2):

$$\begin{aligned}\tilde{x}_I &= \frac{(b_{11}\tilde{x} + b_{12}\tilde{y} + b_{13}\tilde{z} + b_{14})\tilde{x} + (b_{15}\tilde{y} + b_{16}\tilde{z} + b_{17})\tilde{y} + (b_{18}\tilde{z} + b_{19})\tilde{z} + b_{110}}{(b_{31}\tilde{x} + b_{32}\tilde{y} + b_{33}\tilde{z} + b_{34})\tilde{x} + (b_{35}\tilde{y} + b_{36}\tilde{z} + b_{37})\tilde{y} + (b_{38}\tilde{z} + b_{39})\tilde{z} + b_{310}} \\ \tilde{y}_I &= \frac{(b_{21}\tilde{x} + b_{22}\tilde{y} + b_{23}\tilde{z} + b_{24})\tilde{x} + (b_{25}\tilde{y} + b_{26}\tilde{z} + b_{27})\tilde{y} + (b_{28}\tilde{z} + b_{29})\tilde{z} + b_{210}}{(b_{31}\tilde{x} + b_{32}\tilde{y} + b_{33}\tilde{z} + b_{34})\tilde{x} + (b_{35}\tilde{y} + b_{36}\tilde{z} + b_{37})\tilde{y} + (b_{38}\tilde{z} + b_{39})\tilde{z} + b_{310}}\end{aligned} \tag{A.4}$$

Initially, 12 parameter of the model are set to the outcome of the previously described DLT parameter estimation. That is: $b_{14} = a_{11}$, $b_{17} = a_{12}$, $b_{19} = a_{13}$, $b_{110} = a_{14}$, $b_{24} = a_{21}$, $b_{27} = a_{22}$, $b_{29} = a_{23}$, $b_{210} = a_{24}$, $b_{34} = a_{31}$, $b_{37} = a_{32}$, $b_{39} = a_{33}$, $b_{310} = 1$. To find the best match to the 29 unknowns, a nonlinear least squares minimization of the reprojection error in Eq. (A.3) is applied using the Levenberg-Marquardt method [126, 191]. The inverse mapping function from pixel to world coordinates requires the evaluation of two additional functions $\tilde{x} = f'_x(\tilde{x_I}, \tilde{y_I}, \tilde{z})$ and $\tilde{y} = f'_y(\tilde{x_I}, \tilde{y_I}, \tilde{z})$. The parameters of these inverse mappings are obtained by an additional non-linear least squares optimization of 29 parameters using all point correspondences and by interchanging the image coordinates and the world-coordinates of all point correspondences.

By following Soloff et al. [153], a further higher order polynomial mapping model is implemented and tested during this thesis. The mapping functions consist of three-dimensional 3rd order polynomials:

$$\begin{aligned}\tilde{x}_I =& a_0 + a_1\tilde{x} + a_2\tilde{y} + a_3\tilde{z} + a_4\tilde{x}^2 + a_5\tilde{y}^2 + a_6\tilde{z}^2 + a_7\tilde{x}\tilde{y} + a_8\tilde{x}\tilde{z} + a_9\tilde{y}\tilde{z} \\ &+ a_{10}\tilde{x}^3 + a_{11}\tilde{y}^3 + a_{12}\tilde{z}^3 + a_{13}\tilde{x}^2\tilde{y} + a_{14}\tilde{x}^2\tilde{z} + a_{15}\tilde{y}^2\tilde{x} + a_{16}\tilde{y}^2\tilde{z} \\ &+ a_{17}\tilde{z}^2\tilde{x} + a_{18}\tilde{x}\tilde{y}\tilde{z} \\ \tilde{y}_I =& a_{19} + a_1\tilde{x} + a_{20}\tilde{y} + a_{21}\tilde{z} + a_4\tilde{x}^2 + a_{22}\tilde{y}^2 + a_{23}\tilde{z}^2 + a_{24}\tilde{x}\tilde{y} + a_{25}\tilde{x}\tilde{z} + a_{26}\tilde{y}\tilde{z} \\ &+ a_{27}\tilde{x}^3 + a_{28}\tilde{y}^3 + a_{29}\tilde{z}^3 + a_{30}\tilde{x}^2\tilde{y} + a_{31}\tilde{x}^2\tilde{z} + a_{32}\tilde{y}^2\tilde{x} + a_{33}\tilde{y}^2\tilde{z} \\ &+ a_{34}\tilde{z}^2\tilde{x} + a_{35}\tilde{x}\tilde{y}\tilde{z}\end{aligned} \tag{A.5}$$

Initially, the parameter a_1 and a_{20} are set to unity. To find the best match to the 36 unknowns, again a nonlinear least squares minimization of the reprojection error (c.f. Eq. (A.3)) is applied using the LM method. The procedure for inverse mapping is the same as for the camera model of ratios of 2^{nd} order polynomials and requires a further non-linear least squares optimization of 34 parameters using all normalized point correspondences.

Bibliography

[1] European Aeronautics: A Vision for 2020. Office for Official Publications of the European Communities, Luxembourg (2001)

[2] Evaluation of measurement data - guide to the expression of uncertainty in measurement GUM, JCGM 100:2008 (2008)

[3] Adrian, R.J.: Particle-imaging techniques for experimental fluid mechanics. *Annual Review of Fluid Mechanics* **23**(1), 261–304 (1991)

[4] Akhmetbekov, Y.K., Lozhkin, V., Markovich, D., Tokarev, M.: Multiset triangulation 3D PTV and its performance compared to tomographic PIV. In: 9th International Symposium on Particle Image Velocimetry – PIV 11 (2011)

[5] Arroyo, M.P., Greated, C.A.: Stereoscopic particle image velocimetry. *Measurement Science and Technology* **2**(12), 1181 (1991)

[6] Arroyo, P., Lobera, J., Recuero, S., Woisetschläger, J.: Digital image plane holography for three-component velocity measurements in turbomachinery flows. In: 13th Int Symp on Applications of Laser Techniques to Fluid Mechanics (Lisbon, Portugal) (2006)

[7] Atkinson, C., Coudert, S., Foucaut, J.M., Stanislas, M., Soria, J.: The accuracy of tomographic particle image velocimetry for measurements of a turbulent boundary layer. *Experiments in Fluids* **50**(4), 1031–1056 (2011)

[8] Atkinson, C., Soria, J.: An efficient simultaneous reconstruction technique for tomographic particle image velocimetry. *Experiments in Fluids* **47**, 553–568 (2009)

[9] Avallone, F., Ye, Q., Schrijer, F., Scarano, F., Cardone, G.: Tomographic PIV investigation of roughness-induced transition in a hypersonic boundary layer. *Experiments in Fluids* **55**(11), 1852 (2014)

[10] Aziz, A.Y.I., Karara, H.M.: Direct linear transformation into object space coordinates in close-range photogrammetry. In: Proc. of the Symposium on Close-Range Photogrammetry, pp. 1–18. Urbana, Illinois (1971)

[11] Bachalo, W.D., Houser, M.J.: Development of the phase/doppler spray analyzer for liquid drop size and velocity characterizations. *Optical Engineering* **23**, 583–590 (1984)

[12] Baek, S.J., Lee, S.J.: A new two-frame particle tracking algorithm using match probability. *Experiments in Fluids* **22**(1), 23–32 (1996)

[13] Becker, J., Hassa, C.: Breakup and atomization of a kerosene jet in crossflow at elevated pressure. *Atomization and Sprays* **12**(1-3), 49–67 (2002)

[14] Behr, T., Kalfas, A.I., Abhari, R.S.: Control of rotor tip leakage through cooling injection from the casing in a high-work turbine. *Journal of Turbomachinery* **130**(3), 031,014–031,014–12 (2008)

[15] Bilsky, A.V., Lozhkin, V.A., Markovich, D.M., Tokarev, M.P.: A maximum entropy reconstruction technique for tomographic particle image velocimetry. *Measurement Science and Technology* **24**(4), 045,301 (2013)

[16] Bilsky, A.V., Markovich, D.M., Tokarev, M.P., Lozhkin, V.A.: Low computation cost reconstruction technique for tomo-PIV. In: 16th Int Symp on Applications of Laser Techniques to Fluid Mechanics (2012)

[17] Blaisot, J.B., Yon, J.: Droplet size and morphology characterization for dense sprays by image processing: application to the diesel spray. *Experiments in Fluids* **39**(6), 977–994 (2005)

[18] Born, M., Wolf, E.: Principles of Optics. Oxford: Pergamon (1997)

[19] Braat, J.: Analytical expressions for the wave-front aberration coefficients of a tilted plane-parallel plate. *Appl. Opt.* **36**(32), 8459–8467 (1997)

[20] Bradski, G.: The OpenCV Library. *Dr. Dobb's Journal of Software Tools* (2000)

[21] Bradski, G., Kaehler, A.: Learning OpenCV, 1st edn. O' Reilly Media, Inc., Sebastopol (2008)

[22] Buchmann, N.A., Cierpka, C., Kähler, C.J., Soria, J.: Ultra-high-speed 3d astigmatic particle tracking velocimetry: application to particle-laden supersonic impinging jets. *Experiments in Fluids* **55**(11), 1842 (2014)

[23] Byrne, C.: Block-iterative algorithms. *International Transactions in Operational Research* **16**(4), 427–463 (2009)

[24] Cai, W., Powell, C.F., Yue, Y., Narayanan, S., Wang, J., Tate, M.W., Renzi, M.J., Ercan, A., Fontes, E., Gruner, S.M.: Quantitative analysis of highly transient fuel sprays by time-resolved x-radiography. *Applied Physics Letters* **83**(8), 1671–1673 (2003)

[25] Cao, L., Pan, G., de Jong, J., Woodward, S., Meng, H.: Hybrid digital holographic imaging system for three-dimensional dense particle field measurement. *Appl. Opt.* **47**(25), 4501–4508 (2008)

[26] Champagnat, F., Cornic, P., Cheminet, A., Leclaire, B., Besnerais, G.L., Plyer, A.: Tomographic PIV: particles versus blobs. *Measurement Science and Technology* **25**(8), 084,002 (2014)

[27] Cierpka, C., Rossi, M., Segura, R., Kähler, C.J.: On the calibration of astigmatism particle tracking velocimetry for microflows. *Measurement Science and Technology* **22**(1), 015,401 (2011)

[28] Cierpka, C., Segura, R., Hain, R., Kähler, C.J.: A simple single camera 3C3D velocity measurement technique without errors due to depth of correlation and spatial averaging for microfluidics. *Measurement Science and Technology* **21**(4), 045,401 (2010)

[29] Claxton, C.D., Staunton, R.C.: Measurement of the point-spread function of a noisy imaging system. *J. Opt. Soc. Am. A* **25**(1), 159–170 (2008)

[30] Clemens, N.T.: *Flow Imaging*, pp. 390–420. John Wiley & Sons, Inc. (2002)

[31] Coletti, F., Benson, M.J., Sagues, A.L., Miller, B.H., Fahrig, R., Eaton, J.K.: Three-dimensional mass fraction distribution of a spray measured by x-ray computed tomography. *Journal of Engineering for Gas Turbines and Power* **136**(5), 051,508–051,508–8 (2014)

[32] Cornic, P., Champagnat, F., Cheminet, A., Leclaire, B., Le Besnerais, G.: Computationally efficient sparse algorithms for tomographic PIV reconstruction. In: 10th International Symposium on Particle Image Velocimetry – PIV 13, Delft, The Netherlands, July 2-4, 2013 (2013)

[33] Cornic, P., Champagnat, F., Cheminet, A., Leclaire, B., Le Besnerais, G.: Fast and efficient particle reconstruction on a 3d grid using sparsity. *Experiments in Fluids* **56**(3), 62 (2015)

[34] Cumpsty, N.: Compressor Aerodynamics. Longman Scientific & Technical Harlow, Essex, England (1989)

[35] Damaschke, N., Nobach, H., Semidetnov, N., Tropea, C.: Optical particle sizing in backscatter. *Appl. Opt.* **41**(27), 5713–5727 (2002)

[36] Discetti, S., Astarita, T.: Fast 3D PIV with direct sparse cross-correlations. *Experiments in Fluids* **53**(5), 1437–1451 (2012)

[37] Discetti, S., Astarita, T.: A fast multi-resolution approach to tomographic PIV. *Experiments in Fluids* **52**(3), 765–777 (2012)

[38] Discetti, S., Natale, A., Astarita, T.: Spatial filtering improved tomographic PIV. *Experiments in Fluids* **54**(4), 1505 (2013)

[39] van Doorne, C.W.H., Westerweel, J.: Measurement of laminar, transitional and turbulent pipe flow using stereoscopic-PIV. *Experiments in Fluids* **42**(2), 259–279 (2007)

[40] Durst, F., Zaré, M.: Laser-doppler measurements in two-phase flow. In: Proceedings of the LDA-Symposium, Copenhagen, pp. 403–429 (1975)

[41] Elsinga, G., van Oudheusden, B., Scarano, F.: Evaluation of aero-optical distortion effects in PIV. *Experiments in Fluids* **39**(2), 246–256 (2005)

[42] Elsinga, G., Scarano, F., Wieneke, B., van Oudheusden, B.: Tomographic particle image velocimetry. *Experiments in Fluids* **41**, 933–947 (2006)

[43] Elsinga, G.E., Adrian, R.J., van Oudheusden, B.W., Scarano, F.: Three-dimensional vortex organization in a high-reynolds-number supersonic turbulent boundary layer. *Journal of Fluid Mechanics* **644**, 35–60 (2010)

[44] Elsinga, G.E., van Oudheusden, B.W., Scarano, F.: Experimental assessment of tomographic-PIV accuracy. In: 13th Int Symp on Applications of Laser Techniques to Fluid Mechanics (Lisbon, Portugal) (2006)

[45] Elsinga, G.E., Scarano, F., Wieneke, B., van Oudheusden, B.W.: Assessment of tomo-PIV for three-dimensional flows. In: 6th International Symposium on Particle Image Velocimetry – PIV (Pasadena, CA, USA) (2005)

[46] Elsinga, G.E., Scarano, F., Wieneke, B., van Oudheusden, B.W.: Tomographic particle image velocimetry. In: 6th International Symposium on Particle Image Velocimetry – PIV (Pasadena, CA, USA) (2005)

[47] Elsinga, G.E., Tokgoz, S.: Ghost hunting-an assessment of ghost particle detection and removal methods for tomographic-PIV. *Measurement Science and Technology* **25**(8), 084,004 (2014)

[48] Fahringer, T.W., Lynch, K.P., Thurow, B.S.: Volumetric particle image velocimetry with a single plenoptic camera. *Measurement Science and Technology* **26**(11), 115,201 (2015)

[49] Faugeras, O.D., Toscani, G.: Camera calibration for 3D computer vision. In: Proc. International Workshop on Industrial Applications of Machine Vision and Machine Intelligence, Silken, Japan, pp. 240–247 (1987)

[50] Fdida, N., Blaisot, J.B.: Drop size distribution measured by imaging: determination of the measurement volume by the calibration of the point spread function. *Measurement Science and Technology* **21**(2), 025,501 (2010)

[51] Forney, L.J., Dyke, D.B.V., McGregor, W.K.: Dynamics of particle-shock interactions: Part i: Similitude. *Aerosol Science and Technology* **6**(2), 129–141 (1987)

[52] Freitag, S.: Experimentelle Untersuchung der Kraftstoffaufbereitung in einer verdrallten Luftströmung unter realistischen Drücken und Vorwärmtemperaturen ohne Reaktion in einem Einzelsektor-Brennkammermodell mit punktuellem Kraftstoffeintrag. In: Deutscher Luft- und Raumfahrtkongress, 13.-15. September, Braunschweig (2016)

[53] Freitag, S., Behrendt, T.: Commissioning of the optical swirling spray injector: A new test section for investigations of atomization inside an aero engine burner at realistic operating conditions. In: 26th European Conference Liquid Atomization & Spray Systems (ILASS), 08.-10. Sept. 2014, Bremen, Germany (2014)

[54] Freitag, S., Hassa, C.: Spray characteristics of a kerosene jet in cross flow of air at elevated pressure. In: 22nd European Conference Liquid Atomization & Spray Systems (ILASS), 08.-10. Sept. 2008, Como Lake, Italy (2008)

[55] Gawehn, T.: Verdichtungsstoßvisualisierung mittels Laserlichtschnitt. Ph.D. thesis, Ruhr-Universität Bochum / DLR Köln AT-OTM (2005)

[56] Geisler, R., Novara, M., Schröder, A.: Volumetric multi-pulse particle tracking measurement for separated laminar transitional flow investigations. In: 18th Int Symp on Applications of Laser Techniques to Fluid Mechanics (Lisbon, Portugal) (2016)

[57] Gesemann, S.: Ein- und Mehrkamerakalibrierung. Master's thesis, University of Paderborn / German Aerospace Center DLR Göttingen AS-EXV (2007)

[58] Gesemann, S., Huhn, F., Schanz, D., Schröder, A.: From noisy particle tracks to velocity, acceleration and pressure fields using b-splines and penalties. In: 18th Int Symp on Applications of Laser Techniques to Fluid Mechanics (Lisbon, Portugal) (2016)

[59] Gesemann, S., Schanz, D., Schröder, A., Petra, S., Schnörr, C.: Recasting tomo-PIV reconstruction as constrained and L1-regularized nonlinear least squares problem. In: 15th Int Symp on Applications of Laser Techniques to Fluid Mechanics (Lisbon, Portugal) (2010)

[60] Glover, A.R., Skippon, S.M., Boyle, R.D.: Interferometric laser imaging for droplet sizing: a method for droplet-size measurement in sparse spray systems. *Applied Optics* **34**(36), 8409–8421 (1995)

[61] Goodman, J.: Introduction to Fourier Optics. McGraw Hill, New York (1968)

[62] Gordon, R., Bender, R., Herman, G.T.: Algebraic reconstruction techniques (ART) for three-dimensional electron microscopy and X-ray photography. *Journal of theoretical Biology* **29**(3), pp. 471–481 (1970)

[63] Harris, C., Stephens, M.: A combined corner and edge detector. In: 4th Alvey Vision Conference, pp. 147–151 (1988)

[64] Hartley, R., Zisserman, A.: Multiple View Geometry in Computer Vision, 2 edn. Cambridge University Press, New York (2003)

[65] Hassa, C., Wiesmath, P.: The effect of initial fuel temperature on vaporization in aero engine combustors with prevaporization. In: ICLASS 2012, 12th Triennial International Conference on Liquid Atomization and Spray Systems, Heidelberg, Germany, September 2-6 (2012)

[66] Heikkila, J., Silven, O.: A four-step camera calibration procedure with implicit image correction. In: Proceedings of the 1997 Conference on Computer Vision and Pattern Recognition (CVPR '97) (1997)

[67] Henderson, C.: Drag coeffcient of spheres in continuum and rarefied flows. *AIAA J* **14**, 707–708 (1976)

[68] Hergt, A., Dorfner, C., Steinert, W., Nicke, E., Schreiber, H.A.: Advanced nonaxisymmetric endwall contouring for axial compressors by generating an aerodynamic separator - part II: Experimental and numerical cascade investigation. *Journal of Turbomachinery* **133**(2), 021,027–021,027 (2010)

[69] Hergt, A., Grund, S., Steinert, W.: Webpage of the transonic cascade wind tunnel. http://www.dlr.de/at/en

[70] Hergt, A., Steinert, W., Grund, S.: Design and experimental investigation of a compressor cascade for low Reynolds number conditions. In: 21th International Symposium on Air Breathing Engines, Busan (South Korea), ISABE-2013-1104 (2013)

[71] Herman, G.T., Lent, A.: Iterative reconstruction algorithms. *Computers in Biology and Medicine* **6**(4), 273 – 294 (1976)

[72] Hom, J., Chigier, N.: Rainbow refractometry: Simultaneous measurement of temperature, refractive index, and size of droplets. *Applied Optics* **41**(10), 1899–1907 (2002)

[73] Hovenac, E.A., Lock, J.A.: Assessing the contributions of surface waves and complex rays to far-field Mie scattering by use of the Debye series. *J. Opt. Soc. Am. A* **9**(5), 781–795 (1992)

[74] Huang, H.T., Fiedler, H.E., Wang, J.J.: Limitation and improvement of PIV. *Experiments in Fluids* **15**(4), 263–273 (1993)

[75] Humble, R.A., Elsinga, G.E., Scarano, F., van Oudheusden, B.W.: Three-dimensional instantaneous structure of a shock wave/turbulent boundary layer interaction. *Journal of Fluid Mechanics* **622**, 33–62 (2009)

[76] Humble, R.A., Scarano, F., van Oudheusden, B.W.: Particle image velocimetry measurements of a shock wave/turbulent boundary layer interaction. *Experiments in Fluids* **43**(2-3), 173–183 (2007)

[77] Jambunathan, K., Ju, X.Y., Dobbins, B.N., Ashforth-Frost, S.: An improved cross correlation technique for particle image velocimetry. *Measurement Science and Technology* **6**(5), 507 (1995)

[78] Jazi, M.B.: Surface breakup of a liquid jet injected into a gaseous crossflow. Ph.D. thesis, Graduate Department of Civil Engineering, University of Toronto (2014)

[79] Jermy, M., Greenhalgh, D.: Planar dropsizing by elastic and fluorescence scattering in sprays too dense for phase doppler measurement. *Applied Physics B: Lasers and Optics* **71**, 703–710 (2000)

[80] Jones, A.R., Sarjeant, M., Davis, C.R., Denham, R.O.: Application of in-line holography to drop size measurement in dense fuel sprays. *Appl. Opt.* **17**(3), 328–330 (1978)

[81] Kähler, C.J., Astarita, T., Vlachos, P.P., Sakakibara, J., Hain, R., Discetti, S., La Foy, R., Cierpka, C.: Main results of the 4th international PIV challenge. *Experiments in Fluids* **57**(6), 97 (2016)

[82] Kang, B., Poulikakos, D.: Holography experiments in a dense high-speed impinging jet spray. *Journal Of Propulsion And Power* **12**(2), 341–348 (1996)

[83] Katz, J., Sheng, J.: Applications of holography in fluid mechanics and particle dynamics. *Annual Review of Fluid Mechanics* **42**(1), 531–555 (2010)

[84] Kawaguchi, T., Akasaka, Y., Maeda, M.: Size measurements of droplets and bubbles by advanced interferometric laser imaging technique. *Measurement Science and Technology* **13**(3), 308 (2002)

[85] Keane, R.D., Adrian, R.J.: Theory of cross-correlation analysis of PIV images. *Applied Scientific Research* **49**(3), 191–215 (1992)

[86] Koh, K.U., Kim, J.Y., Lee, S.Y.: Determination of in-focus criteria and depth of field in image processing of spray particles. *Atomization and Sprays* **11**(4), 317–333 (2001)

[87] Kristensson, E., Berrocal, E., Richter, M., Pettersson, S.G., Aldén, M.: High-speed structured planar laser illumination for contrast improvement of two-phase flow images. *Opt. Lett.* **33**(23), 2752–2754 (2008)

[88] Laven, P.: Simulation of rainbows, coronas, and glories by use of Mie theory. *Appl. Opt.* **42**(3), 436–444 (2003)

[89] Laven, P.: Simulation of rainbows, coronas and glories using Mie theory and the Debye series. *Journal of Quantitative Spectroscopy and Radiative Transfer* **89**(1–4), 257 – 269 (2004)

[90] Le Gal, P., Farrugia, N., Greenhalgh, D.: Laser sheet dropsizing of dense sprays. *Optics and Laser Technology* **31**(1), 75 – 83 (1999)

[91] Lecordier, B., Lecordier, J., Trinié, M.: Iterative sub-pixel algorithm for the cross-correlation PIV measurements. In: 3rd International Workshop on Particle Image Velocimetry – PIV 99, Santa Barbara (1999)

[92] Lefebvre, A.H.: Atomization and Sprays. CRC Press Taylor & Francis Group (1989)

[93] Liu, X., Im, K.S., Wang, Y., Wang, J., Tate, M.W., Ercan, A., Schuette, D.R., Gruner, S.M.: Four dimensional visualization of highly transient fuel sprays by microsecond quantitative x-ray tomography. *Applied Physics Letters* **94**(8), 084,101 (2009)

[94] Lü, Q., Chen, Y., Yuan, R., Ge, B., Gao, Y., Zhang, Y.: Trajectory and velocity measurement of a particle in spray by digital holography. *Appl. Opt.* **48**(36), 7000–7007 (2009)

[95] Maas, H., Gruen, A., Papantoniou, D.: Particle tracking velocimetry in three-dimensional flows - part 1. photogrammetric determination of particle coordinates. *Experiments in Fluids* **15**(2), 133–146 (1993)

[96] Maas, H.G.: Complexity analysis for the determination of image correspondences in dense spatial target fields. *International Archives of Photogrammetriy and Remote Sensing* **29**, 102–107 (1992)

[97] Maeda, M., Kawaguchi, T., Hishida, K.: Novel interferometric measurement of size and velocity distributions of spherical particles in fluid flows. *Measurement Science and Technology* **11**(12), L13 (2000)

[98] Malek, M., Allano, D., Coëtmellec, S., Özkul, C., Lebrun, D.: Digital in-line holography for three-dimensional-two-components particle tracking velocimetry. *Measurement Science and Technology* **15**(4), 699 (2004)

[99] Malik, N., Dracos, T., Papantoniou, D.: Particle tracking velocimetry in three-dimensional flows - part ii: Particle tracking. *Experiments in Fluids* **15**(4-5), 279–294 (1993)

[100] Martins, F.J.W.A., Foucaut, J.M., Thomas, L., Azevedo, L.F.A., Stanislas, M.: Volume reconstruction optimization for tomo-PIV algorithms applied to experimental data. *Measurement Science and Technology* **26**(8), 085,202 (2015)

[101] Martins, H., Birk, J., Kelley, R.: Camera models based on data from two calibration planes. *Computer Graphics and Image Processing* **17**(2), 173 – 180 (1981)

[102] Meier, U., Freitag, S., Heinze, J., Lange, L., Magens, E., Schroll, M., Willert, C., Hassa, C., Bagchi, I.K., Lazik, W., Whiteman, M.: Characterization of lean burn module air blast pilot injector with laser techniques. *Journal of Engineering for Gas Turbines and Power* **135**(12), 121,508–121,508–7 (2013)

[103] Meinhart, C.D., Wereley, S.T.: The theory of diffraction-limited resolution in microparticle image velocimetry. *Measurement Science and Technology* **14**(7), 1047 (2003)

[104] Meinhart, C.D., Wereley, S.T., Gray, M.H.B.: Volume illumination for two-dimensional particle image velocimetry. *Measurement Science and Technology* **11**(6), 809 (2000)

[105] Melen, T.: Geometrical modelling and calibration of video cameras for underwater navigation. Ph.D. thesis, Norges Tekniske Hoegskole, Trondheim (1994)

[106] Melling, A.: Tracer particles and seeding for particle image velocimetry. *Measurement Science and Technology* **8**, 1406–1416 (1997)

[107] Meng, H., Hussain, F.: In-line recording and off-axis viewing technique for holographic particle velocimetry. *Appl. Opt.* **34**(11), 1827–1840 (1995)

[108] Meng, H., Pan, G., Pu, Y., Woodward, S.H.: Holographic particle image velocimetry: from film to digital recording. *Measurement Science and Technology* **15**(4), 673 (2004)

[109] Michaelis, D., Wieneke, B., Gomit, G., Calluaud, D., Chatellier, L., Thomas, L., David, L., Astarita, T., Discetti, S., Buchmann, N., Soria, J., Tokarev, M.: Deliverable 2.2 Calibration procedures for full volumetric and thin-volume (thick-sheet) configuration. Tech. rep., EU-FP7, AFDAR (2012)

[110] Miller, B., Sallam, K.A., Lin, K.C., Carter, C.: Digital holographic spray analyzer. In: ASME Conference Proceedings of 14th International Conference on Nuclear Engineering (FEDSM2006), vol. 2, pp. 1023–1028 (2006)

[111] Minerbo, G.: Ment: A maximum entropy algorithm for reconstructing a source from projection data. *Computer Graphics and Image Processing* **10**(1), 48 – 68 (1979)

[112] Mishra, D., Muralidhar, K., Munshi, P.: A robust MART algorithm for tomographic applications. *Numerical Heat Transfer, Part B: Fundamentals* **35**(4), 485–506 (1999)

[113] Mishra, Y.N., Kristensson, E., Berrocal, E.: Reliable lif/mie droplet sizing in sprays using structured laser illumination planar imaging. *Opt. Express* **22**(4), 4480–4492 (2014)

[114] Naumann, H., Schröder, G.: Bauelemente der Optik. C. Hanser Verlag München (1992)

[115] Needell, D., Tropp, J.: Cosamp: Iterative signal recovery from incomplete and inaccurate samples. *Applied and Computational Harmonic Analysis* **26**(3), 301 – 321 (2009)

[116] Nogueira, J., Lecuona, A., Rodríguez, P.A.: Local field correction PIV: on the increase of accuracy of digital PIV systems. *Experiments in Fluids* **27**(2), 107–116 (1999)

[117] Novara, M.: Advances in tomographic PIV. Ph.D. thesis, Delft University of Technology (2013)

[118] Novara, M., Batenburg, K.J., Scarano, F.: Motion tracking-enhanced mart for tomographic PIV. *Measurement Science and Technology* **21**(3), 035,401 (2010)

[119] Novara, M., Schanz, D., Kähler, C.J., Schröder, A.: Shake-the-box for multi-pulse tomographic systems: towards high seeding density particle tracking in high speed flows. In: 11th International Symposium on Particle Image Velocimetry – PIV 15, Santa Barbara, CA USA, September 14.-16. (2015)

[120] Ooms, T.A.: Digital holographic particle image velocimetry. Ph.D. thesis, Delft University of Technology (2008)

[121] OpenMP Architecture Review Board: OpenMP application program interface version 4.5 (2015)

[122] Pan, G., Meng, H.: Digital in-line holographic piv for 3d particulate flow diagnostics. In: 4th International Symposium on Particle Image Velocimetry – PIV01, Göttingen, Germany, September 17-19, 2001 (2001)

[123] Pereira, F., Gharib, M., Dabiri, D., Modarress, D.: Defocusing digital particle image velocimetry: a 3-component 3-dimensional DPIV measurement technique. application to bubbly flows. *Experiments in Fluids* **29**(1), S078–S084 (2000)

[124] Pereira, F., Stüer, H., Graff, E.C., Gharib, M.: Two-frame 3d particle tracking. *Measurement Science and Technology* **17**(7), 1680 (2006)

[125] Prasad, A., Adrian, R.: Stereoscopic particle image velocimetry applied to liquid flows. *Experiments in Fluids* **15**(1), 49–60 (1993)

[126] Press, W.H., Teukolsky, S.A., Vettering, W.T., Flannery, B.P.: Numerical Recipes in C, 2nd edn. Cambridge: Cambridge University Press (1992)

[127] Rachner, M.: Die Stoffeigenschaften von Kerosin Jet A-1. Tech. Rep. ISRN DLR-FB-98-01, DLR (1998)

[128] Raffel, M., Willert, C., Wereley, S., Kompenhans, J.: Particle Image Velocimetry, A Practical Guide. Springer Berlin-Heidelberg (2007)

[129] Ragni, D., Schrijer, F., van Oudheusden, B., Scarano, F.: Particle tracer response across shocks measured by PIV. *Exp Fluids* **50**(1), 53–64 (2011)

[130] Rao, U.V.G., Jain, V.K.: Gaussian and exponential approximations of the modulation transfer function. *J. Opt. Soc. Am.* **57**(9), 1159–1160 (1967)

[131] Reichenbach, S.E., Park, S.K., Narayanswamy, R.: Characterizing digital image acquisition devices. *Optical Engineering* **30**(2), 170–177 (1991)

[132] Ren, K.F., Lebrun, D., Özkul, C., Kleitz, A., Gouesbet, G., Gréhan, G.: On the measurements of particles by imaging methods: Theoretical and experimental aspects. *Particle & Particle Systems Characterization* **13**(2), 156–164 (1996)

[133] Salvi, J., Armangué, X., Batlle, J.: A comparative review of camera calibrating methods with accuracy evaluation. *Pattern Recognition* **35**(7), 1617 – 1635 (2002)

[134] Santangelo, P.J., Sojka, P.E.: Focused-image holography as a dense-spray diagnostic. *Appl. Opt.* **33**(19), 4132–4136 (1994)

[135] Scarano, F.: Iterative image deformation methods in PIV. *Measurement Science and Technology* **13**(1), R1 (2002)

[136] Scarano, F.: Tomographic PIV: principles and practice. *Measurement Science and Technology* **24**(1), 012,001 (2013)

[137] Scarano, F., van Oudheusden, B.: Planar velocity measurements of a two-dimensional compressible wake. *Experiments in Fluids* **34**, 430–441 (2003)

[138] Scarano, F., Poelma, C.: Three-dimensional vorticity patterns of cylinder wakes. *Experiments in Fluids* **47**(1), 69 (2009)

[139] Scarano, F., Riethmuller, M.L.: Iterative multigrid approach in PIV image processing with discrete window offset. *Experiments in Fluids* **26**(6), 513–523 (1999)

[140] Scarano, F., Riethmuller, M.L.: Advances in iterative multigrid PIV image processing. *Experiments in Fluids* **29**(1), S051–S060 (2000)

[141] Schäfer, W., Tropea, C.: Time-shift technique for simultaneous measurement of size, velocity, and relative refractive index of transparent droplets or particles in a flow. *Appl. Opt.* **53**(4), 588–597 (2014)

[142] Schanz, D., Gesemann, S., Schröder, A.: Shake-the-box: Lagrangian particle tracking at high particle image densities. *Experiments in Fluids* **57**(5), 70 (2016)

[143] Schanz, D., Gesemann, S., Schröder, A., Wieneke, B., Michaelis, D.: Tomographic reconstruction with non-uniform optical transfer functions (OTF). In: 15th Int Symp on Applications of Laser Techniques to Fluid Mechanics (Lisbon, Portugal) (2010)

[144] Schanz, D., Gesemann, S., Schröder, A., Wieneke, B., Novara, M.: Non-uniform optical transfer functions in particle imaging: calibration and application to tomographic reconstruction. *Measurement Science and Technology* **24**(2), 024,009 (2013)

[145] Schetz, J.A., Kush, E.A., Joshi, P.B.: Wave phenomena in liquid jet breakup in a supersonic crossflow. *AIAA Journal* **18**(7), 774–778 (1980)

[146] Schneiders, J.F.G., Scarano, F.: Dense velocity reconstruction from tomographic ptv with material derivatives. *Experiments in Fluids* **57**(9), 139 (2016)

[147] Schodl, R.: A laser-two-focus (L2F) velocimeter for automatic flow vector measurements in the rotating components of turbomachines. *Journal of Fluids Engineering* **102**(4), 412–419 (1980)

[148] Schrijer, F.F.J., Scarano, F.: Effect of predictor-corrector filtering on the stability and spatial resolution of iterative PIV interrogation. *Experiments in Fluids* **45**(5), 927–941 (2008)

[149] Schroll, M., Klinner, J., Lange, L., Willert, C.: Particle image velocimetry of highly luminescent, pressurized combustion flows of aero engine combustors. In: 10th International Symposium on Particle Image Velocimetry - PIV13 (2013)

[150] Sheng, J., Malkiel, E., Katz, J.: Digital holographic microscope for measuring three-dimensional particle distributions and motions. *Appl. Opt.* **45**(16), 3893–3901 (2006)

[151] Sheng, J., Malkiel, E., Katz, J.: Using digital holographic microscopy for simultaneous measurements of 3D near wall velocity and wall shear stress in a turbulent boundary layer. *Experiments in Fluids* **45**(6), 1023–1035 (2008)

[152] Sjolander, S.A.: Overview of tip-clearance effects in axial turbines. VKI Lecture Series 1997-01, Von Karman Institute for Fluid Dynamics, Rhode-St-Genése, Belgium. (1997)

[153] Soloff, S.M., Adrian, R.J., Liu, Z.C.: Distortion compensation for generalized stereoscopic particle image velocimetry. *Measurement Science and Technology* **8**(12), 1441 (1997)

[154] Soo, S.L.: Fluid dynamics of multiphase systems. Waltham : Blaisdell (1967)

[155] Soria, J.: An investigation of the near wake of a circular cylinder using a video-based digital cross-correlation particle image velocimetry technique. *Experimental Thermal and Fluid Science* **12**(2), 221 – 233 (1996)

[156] Soria, J., Atkinson, C.: Towards 3c-3d digital holographic fluid velocity vector field measurement - tomographic digital holographic PIV (Tomo-HPIV). *Measurement Science and Technology* **19**(7), 074,002 (2008)

[157] Stafford, J., Walsh, E., Egan, V.: A statistical analysis for time-averaged turbulent and fluctuating flow fields using particle image velocimetry. *Flow Measurement and Instrumentation* **26**(0), 1 – 9 (2012)

[158] Stanislas, M., Okamoto, K., Kähler, C.J., Westerweel, J.: Main results of the second international piv challenge. *Experiments in Fluids* **39**(2), 170–191 (2005)

[159] Steinert, W., Fuchs, R., Starken, H.: Inlet flow angle determination of transonic compressor cascade. *J. Turbomach.* **3**(114), 487–493 (1992)

[160] Swithenbank, J., Beer, J.M., Taylor, D.S., Abbott, D., McCreath, C.G.: A laser diagnostic technique for the measurement of droplet and particle size distribution. *Prog. Astronaut. Aeronaut.* **53**, 421 (1977)

[161] Thévenaz, P., Blu, T., Unser, M.: Interpolation revisited. *IEEE Transactions on Medical Imaging* **19**(7), 739–758 (2000)

[162] Thomas, L., Tremblais, B., David, L.: Optimization of the volume reconstruction for classical tomo-PIV algorithms (MART, BIMART and SMART): synthetic and experimental studies. *Measurement Science and Technology* **25**(3), 035,303 (2014)

[163] Thomas, P.: Experimentelle und theoretische Untersuchungen zum Folgeverhalten von Teilchen unter dem Einfluß großer Geschwindigkeitsgradienten in kompressibler Strömung. Ph.D. thesis, Universität Göttingen / DLR Göttingen AS-EV (1991)

[164] Tsai, R.: A versatile camera calibration technique for high-accuracy 3D machine vision metrology using off-the-shelf TV cameras and lenses. *IEEE Journal on Robotics and Automation* **3**(4), 323–344 (1987)

[165] Verhoeven, D.: Limited-data computed tomography algorithms for the physical sciences. *Appl. Opt.* **32**(20), 3736–3754 (1993)

[166] Voges, M., Beversdorff, M., Willert, C., Krain, H.: Application of particle image velocimetry to a transonic centrifugal compressor. *Experiments in Fluids* **43**(2), 371–384 (2007)

[167] Voges, M., Schnell, R., Willert, C., Mönig, R., Müller, M.W., Zscherp, C.: Investigation of blade tip interaction with casing treatment in a transonic compressor part i: Particle image velocimetry. *Journal of Turbomachinery* **133**(1), 011,007–011,007–11 (2010)

[168] Wang, H., Gao, Q., Wei, R., Wang, J.: Intensity-enhanced MART for tomographic PIV. *Experiments in Fluids* **57**(5), 87 (2016)

[169] Wei, G.Q., Ma, S.D.: A complete two-plane camera calibration method and experimental comparisons. In: 4th International Conference on Computer Vision, pp. 439–446 (1993)

[170] Wereley, S.T., Meinhart, C.D.: Second-order accurate particle image velocimetry. *Experiments in Fluids* **31**(3), 258–268 (2001)

[171] Wernet, M.P.: Application of tomo-PIV in a large-scale supersonic jet flow facility. *Experiments in Fluids* **57**(9), 144 (2016)

[172] Westerweel, J.: Fundamentals of digital particle image velocimetry. *Measurement Science and Technology* **8**(12), 1379 (1997)

[173] Westerweel, J.: Theoretical analysis of the measurement precision in particle image velocimetry. *Experiments in Fluids* **29**, S003–S012 (2000)

[174] Westerweel, J., Dabiri, D., Gharib, M.: The effect of a discrete window offset on the accuracy of cross-correlation analysis of digital PIV recordings. *Experiments in Fluids* **23**(1), 20–28 (1997)

[175] Westerweel, J., Scarano, F.: Universal outlier detection for PIV data. *Experiments in Fluids* **39**(6), 1096–1100 (2005)

[176] Wieneke, B.: Volume self-calibration for 3d particle image velocimetry. *Experiments in Fluids* **45**, 549–556 (2008)

[177] Wieneke, B.: Iterative reconstruction of volumetric particle distribution. In: 9th International Symposium on Particle Image Velocimetry – PIV 11 (2011)

[178] Wieneke, B.: Iterative reconstruction of volumetric particle distribution. *Measurement Science and Technology* **24**(2), 024,008 (2013)

[179] Willert, C.: Assessment of camera models for use in planar velocimetry calibration. *Experiments in Fluids* **41**, 135–143 (2006)

[180] Willert, C.: High-speed particle image velocimetry for the efficient measurement of turbulence statistics. *Experiments in Fluids* **56**(1), 17 (2015)

[181] Willert, C., Hassa, C., Stockhausen, G., Jarius, M., Voges, M., Klinner, J.: Combined PIV and DGV applied to a pressurized gas turbine combustion facility. *Measurement Science and Technology* **17**(7), 1670 (2006)

[182] Willert, C., Heinze, J., Klinner, J., Stockhausen, G., Voges, M.: Development and application of laser-based diagnostics for combustion research at DLR cologne. In: 5th Australian Conference on Laser Diagnostics in Fluid Mechanics and Combustion (2008)

[183] Willert, C., Stasicki, B., Klinner, J., Moessner, S.: Pulsed operation of high-power light emitting diodes for imaging flow velocimetry. *Measurement Science and Technology* **21**(7), 1–12 (2010)

[184] Willert, C., Stockhausen, G., Voges, M., Klinner, J., Schodl, R., Hassa, C., Schürmans, B., Güthe, F.: Selected Applications of Planar ImagingVelocimetry in Combustion Test Facilities, Topics in Applied Physics, *vol. 112*, pp. 283–309. Springer Berlin Heidelberg, Berlin, Heidelberg (2008)

[185] Willert, C.E., Gharib, M.: Digital particle image velocimetry. *Experiments in Fluids* **10**(4), 181–193 (1991)

[186] Willert, C.E., Gharib, M.: Three-dimensional particle imaging with a single camera. *Experiments in Fluids* **12**(6), 353–358 (1992)

[187] Woisetschläger, J., Göttlich, E.: Recent Applications of Particle Image Velocimetry to Flow Research in Thermal Turbomachinery, Topics in Applied Physics, *vol. 112*, pp. 311–331. Springer Berlin Heidelberg, Berlin, Heidelberg (2008)

[188] Worth, N.A., Nickels, T.B.: Acceleration of tomo-PIV by estimating the initial volume intensity distribution. *Experiments in Fluids* **45**(5), 847 (2008)

[189] Wu, P.K., Kirkendall, K.A., Fuller, R.P., Nejad, A.S.: Breakup processes of liquid jets in subsonic crossflows. *Journal of Propulsion and Power* **13**(1), 64–73 (1997)

[190] Wu, P.K., Kirkendall, K.A., Fuller, R.P., Nejad, A.S.: Spray structures of liquid jets atomized in subsonic crossflows. *Journal of Propulsion and Power* **14**(2), 173–182 (1998)

[191] Wuttke, J.: lmfit - a C library for Levenberg-Marquardt least-squares minimization and curve fitting. http://apps.jcns.fz-juelich.de/doku/sc/lmfit

[192] Yang, Y., Kang, B.: Measurements of the characteristics of spray droplets using in-line digital particle holography. *Journal of Mechanical Science and Technology* **23**, 1670–1679 (2009)

[193] Zhang, J., Tao, B., Katz, J.: Turbulent flow measurement in a square duct with hybrid holographic piv. *Experiments in Fluids* **23**(5), 373–381 (1997)

[194] Zhang, Z.: A flexible new technique for camera calibration. Technical report, Microsoft Research (1999)

List of journal publications

[195] Hergt, A., Klinner, J., Steinert, W., Beversdorff, M., Giebmanns, A., Schnell, R.: The effect of an eroded leading edge on the aerodynamic performance of a transonic fan blade cascade. *J. Turbomach.* **137**(2), 021,006 (2014)

[196] Klinner, J., Hergt, A., Willert, C.: Experimental investigation of the transonic flow around the leading edge of an eroded fan airfoil. *Experiments in Fluids* **55**(9), 1800 (2014)

[197] Klinner, J., Willert, C.: Tomographic shadowgraphy for three-dimensional reconstruction of instantaneous spray distributions. *Experiments in Fluids* **53**(2), 531–543 (2012)

[198] Klinner, J., Willert, C., Schneider, A., Mack-Gardner, A.: Messung der Strömungsverteilung am Austritt der Bipolarplatten eines Brennstoffzellen-Stacks. *tm - Technisches Messen* **78**(5), 246–252 (2011)

[199] Klinner, J., Willert, C.E.: Measurements of turbulent jet mixing in a turbulent co-flow including the influence of periodic forcing and heating. *Flow, Turbulence and Combustion* **98**(3), 751–779 (2017)

Conferences

[200] Hergt, A., Klinner, J., Morsbach, C., Franke, M., Grund, S.: Advanced study of secondary flow structures in a highly loaded compressor cascade. In: 11th European Turbomachinery Conference, Madrid, Spain, March 23-27 (2015)

[201] Klinner, J., Freitag, S., Hassa, C., Willert, C.: Tomographic shadowgraphy of swirled non-reactive spray injection in a generic aero engine burner under realistic operating conditions. In: 18th Int Symp on Applications of Laser Techniques to Fluid Mechanics, Lisbon, Portugal, July 4-7 (2016)

[202] Klinner, J., Hergt, A., Beversdorff, M., Willert, C.: Visualization and PIV measurements of the transonic flow around the leading edge of an eroded fan airfoil. In: 16th Int Symp on Applications of Laser Techniques to Fluid Mechanics, Lisbon, Portugal, July 9-12 (2012)

[203] Klinner, J., Mayer, V., Heinze, J., Willert, C.: Simultaneous measurements of mixing fraction and velocities of a coaxial jet in a turbulent channel flow. In: 17th Int Symp on Applications of Laser Techniques to Fluid Mechanics, Lisbon, Portugal, July 7-10 (2014)

[204] Klinner, J., Voges, M., Willert, C.: Application of tomographic PIV on a passage vortex in a transonic compressor cascade. In: 21th Conference of the German Association for Laser Anemometry (GALA), München, Germany, Sept. 3-5 (2013)

[205] Klinner, J., Willert, C.: Tomographic shadowgraphy for spray diagnostics. In: 24th European Conference on Liquid Atomization & Spray Systems (ILASS), Estoril, Portugal, Sept. 5-7 (2011)

[206] Klinner, J., Willert, C.: Tomographic spray shadowgraphy - a feasibility study. In: Forum on recent developments in Volume Reconstruction techniques applied to 3D fuid and solid mechanic (FVR11), Poitiers, France, Nov. 29- Dec.01. (2011)

[207] Klinner, J., Willert, C.: Application of tomographic PIV in a transonic cascade. In: 10th International Symposium on Particle Image Velocimetry (PIV13), Delft, The Netherlands, July 2-4 (2013)

[208] Klinner, J., Willert, C., Förster, W., Beversdorff, M., Mayer, V.: Simultaneous PLIF/PIV measurements of pulsating and heated coaxial jets in a turbulent channel flow. In: 8th International Symposium on Turbulence, Heat and Mass Transfer (THMT-15), Sarajevo, Bosnia and Herzegovina, Sept. 15-18 (2015)